UNIVERSITÀ
DEGLI STUDI
DI TRIESTE

UNIVERSITÀ DEGLI STUDI DI TRIESTE

XXXVII CICLO DEL DOTTORATO DI RICERCA IN NANOTECNOLOGIE

DESIGN, SYNTHESIS AND APPLICATION OF NOVEL 1D AND 2D-NANOCOMPOSITES FOR BIOSENSING

Settore scientifico-disciplinare: **CHIM/06**

DOTTORANDO / A
GIUSEPPE MISIA

COORDINATORE
PROF. ALBERTO MORGANTE

SUPERVISORE DI TESI
PROF. MAURIZIO PRATO

CO-SUPERVISORE DI TESI
DR. ALESSANDRO SILVESTRI

ANNO ACCADEMICO 2023/2024

Table of Contents

Abbreviations 4

Abstract 7

Chapter I Introduction 9

1.1 The Necessity for New Sensing Platforms and the Advent of Nanostructured Sensors 9

1.2 Definition of Sensor and Classification 10

1.3 Nanomaterials and their Classification 12

1.3.1 Carbon Nanomaterials 14

1.3.2 Carbon Nanotubes 14

1.3.3 Graphene 22

1.3.4 Molybdenum Disulfide 25

1.4 Electrocatalysis 29

1.5 Electrochemical Techniques 32

1.5.1 Voltammetry 32

1.5.2 Chronoamperometry 34

1.5.3 Electrochemical Impedance Spectroscopy 35

1.6 References 40

Chapter II Nanocomposite based on Multiwalled Carbon Nanotubes and Gold Nanoparticles from Metal Vapor Synthesis for Voltammetric detection of Monoamine Neurotransmitters in Complex Biological Systems 62

Abstract 62

2.1 Introduction 62

2.1.1 Monoamine Neurotransmitters as Analytes 62

2.1.2 Carbon Nanotubes as Transducers for Neurotransmitters 65

2.1.3 Gold Nanoparticles from Metal Vapor Synthesis for Heterogeneous Catalysis 65

2.1.4 Molecularly Imprinted Polymers as Artificial Receptors 66

2.1.5 Aim of the Project 67

2.2 Results and Discussions 68

2.2.1 Functionalization of MWCNTs 68

2.2.2 Characterization of MWCNT-S-Au 76

2.2.3 Electrocatalytic Activity 78

2.2.4 Design of Electrochemical Sensor for Serotonin in Human Serum 80

2.2.5 Design of Electrochemical Sensor for Dopamine at Cellular Level 101

2.3 Conclusions 108

2.4 Experimental Section 110

2.4.1 Materials and Instruments 110

2.4.2 Synthesis of 4,4'-dithiodibenzenediazonium tetrafluoroborate 112

2.4.3 Metal Vapor Synthesis of AuNPs 114

2.4.4 Synthesis of MWCNT-S-Au 114

2.4.5 Electrochemical Characterization of MWCNT-S-Au 115

2.4.6 Design of Experiment for Sensing of Serotonin 115

2.4.7 Manufacture of the Electrochemical Sensor for Serotonin 115

2.4.8 Detection of Serotonin and Evaluation of Sensing Performances 118

2.4.9 Manufacture of the Electrochemical Sensor for Dopamine 118

2.5 References 119

Chapter III Electrocatalytic Properties of Crystalline Phases of Molybdenum Disulfide for Hydrogen Peroxide Reduction and Non-Covalent Functionalization of 1T Nanosheets 130

Abstract 130

3.1 Introduction 130

3.1.1 Molybdenum Disulfide as Sustainable Electrocatalyst 130

3.1.2 The Role of Hydrogen Peroxide in the Human Body 131

3.1.3 Molybdenum Disulfide as Peroxidase Mimic 132

3.1.4 Aim of the Project 133

3.2 Results and Discussion 134

3.2.1 Synthesis and Characterization of Molybdenum Disulfide 134

3.2.2 Evaluation of Electrocatalytic Activity of Different Crystalline Phases 138

3.2.3 Electrochemical Impedance Spectroscopy Study 143

3.2.4 Colorimetric Assay 151

3.2.5 Non-Covalent Functionalization of 1T-Molybdenum Disulfide 154
3.3 Conclusions 165
3.4 Experimental Section 167
3.4.1 Materials and Instruments 167
3.4.2 Synthesis of 2D-Molybdenum Disulfide in different crystalline phases and morphologies 168
3.4.3 Electrochemical Measurements 169
3.4.4 Colorimetric assay 170
3.4.5 Non-covalent Functionalization of 1T-MoS_2 171
3.5 References 176
Chapter IV Ultrasound-aided Exfoliation of Few-layered Graphene in a Sustainable Alternative Solvent 184
Abstract 184
4.1 Introduction 184
4.1.1 Cyrene as a Sustainable Alternative Solvent for Graphene Exfoliation 184
4.1.2 Aim of the Project 186
4.2 Results and Discussion 186
4.2.1 Effect of the Amplitude 186
4.2.2 Effect of the Flask Size 187
4.2.3 Comparison with NMP 189
4.2.4 Pulsed Sonication 191
4.2.5 Comparison of Different Graphite Types 192
4.3 Conclusions 196
4.4 Experimental Section 196
4.4.1 Materials and Instruments 196
4.4.2 Exfoliation of Graphene 197
4.5 References 199

Abbreviations

0D	Zero-dimensional
1D	Monodimensional
2D	Bidimensional
3D	Tridimensional
5-HT	5-hydroxytryptamine/serotonin
AA	Ascorbic acid
AFM	Atomic Force Microscopy
ATR-FTIR	Attenuated total reflectance Fourier transform infrared spectroscopy
AuNPs	Gold nanoparticles
CA	Chronoamperometry
CNTs	Carbon nanotubes
CPE	Constant phase element
CV	Cyclic voltammetry
CVD	Chemical vapor deposition
DA	Dopamine
DMF	N,N-Dimethylformamide
DoE	Design of experiment
DOP	Dopaminergic neurons
DPV	Differential pulse voltammetry
DSC	Differential scanning calorimetry
EDC	1-ethyl-3-(3-dimethylaminopropyl)carbodiimide
EDX	Energy-dispersive X-ray spectroscopy
EG	Exfoliated graphene
EIS	Electrochemical impedance spectroscopy
FBS	Fetal bovine serum
FET	Field effect transistor
FoM	Figure of merit
GCE	Glassy carbon electrode
G-FET	Graphene field effect transistor
GLUT	Glutamatergic neurons

GO	Graphene oxide
HER	Hydrogen evolution reaction
HPLC	High-performance liquid chromatography
HPRR	Hydrogen peroxide reduction reaction
ICP	Inductively coupled plasma
iPSC	Induced pluripotent stem cells
ITO	Indium tin oxide
LOD	Limit of detection
LPE	Liquid phase exfoliation
LSV	Linear sweep voltammetry
MA	Modulation amplitude
MIP	Molecularly imprinted polymer
MNPs	Metal nanoparticles
MS	Mass spectrometry
MT	Modulation time
MVS	Metal vapor synthesis
MWCNTs	Multi-wall carbon nanotubes
MWCNT-S-Au	Multi-wall carbon nanotubes functionalized with gold nanoparticles from metal vapor synthesis
MWCNT-SH	Multi-wall carbon nanotubes functionalized with thiol moieties
MWCNT-SS	Multi-wall carbon nanotubes functionalized with disulfide moieties
NHS	*N*-hydroxysuccinimide
NIP	Non-molecularly imprinted polymer
NMP	N-Methylpyrrolidone
NMR	Nuclear magnetic resonance
NRR	Nitrogen reduction reaction
OCP	Open circuit potential
OER	Oxygen evolution reaction
ORR	Oxygen reduction reaction
PANI	Polyaniline

PBS	Phosphate buffer solution
PCR	Polymerase chain reaction
PEDOT	Poly(3,4-ehtylenedioxythiophene)
pFBA	P-fluorobenzaldehyde
POCT	Point-of-care
PPy	Polypyrrole
PTFE	Polytetrafluoroethylene
PUNA	Primitive undifferentiated cells
R_{CT}	Resistance to charge transfer
RFID	Radio frequency identification
rGO	Reduced graphene oxide
R_S	Electrolyte ionic resistance
SEM	Scanning electron microscopy
SERS	Surface-enhanced Raman scattering
SMA	Solvated metal atoms
SPCE	Screen-printed carbon electrode
STEM	Scanning transmission electron microscopy
SWCNTs	Single-wall carbon nanotubes
TCEP	Tris(2-carboxyethyl)phosphine
TEM	Transmission electron microscopy
TGA	Thermogravimetric analysis
TH	Tyrosine hydroxylase
TMB	3,3',5,5'-tetramethylbenzidine
TMDs	Transition metal dichalcogenides
TRP	Tryptophan
UA	Uric acid
XPS	X-ray photoelectron spectroscopy

Abstract

Electrochemical sensors and biosensors are self-contained integrated devices that enable to get quantitative information on the concentration of biomolecules of interest in real time, with high sensitivity. Advance in electrochemical sensing technology is beneficial for several applications, from detection of pollutants in environmental matrices to point-of-care testing and clinical analysis, to food safety. Electrochemical sensors have been greatly fostered by the development of new electrocatalytic materials and nanostructured electrodes. Electroactive nanomaterials, like carbon nanotubes, metal nanoparticles, graphene and other 2D materials, can boost performances of electrochemical sensors, by enhancing the total contact surface area, improving charge transfer and catalyzing redox processes involved in the sensing mechanism.

The objective of this thesis is to develop novel 1D and 2D nanomaterials and nanocomposites to implement in electrochemical sensing platforms for biomolecules of interest, as electrocatalysts. The properties of the used nanomaterials have been tuned by different approaches, involving functionalization of their surface, phase engineering and optimization of synthetic strategies, to improve their performance in terms of electrocatalytic activity, sensitivity, selectivity and conductivity.

Specifically, the first chapter will focus on the modification of Multiwalled Carbon Nanotubes (MWCNTs) with gold nanoparticles (AuNPs) from metal vapor synthesis (MVS) for the detection of monoamine neurotransmitters like dopamine and serotonin. The obtained nanocomposite (MWCNT-S-Au) was then implemented in a sensor based on screen-printed carbon electrodes (SPCE) for sensing of serotonin in complex biological matrices and in an indium tin oxide (ITO) electrode for *in situ* real-time detection of neurotransmitters in neuronal cultures.

The second chapter revolves around phase engineering and functionalization of molybdenum disulfide (MoS_2) for detection of hydrogen peroxide (H_2O_2). In this case, attention was focused on the influence of different crystalline phases on the electrocatalytic properties of the material and the design of a functionalization strategy based on non-covalent interactions with alkylammonium salts.

Finally, the third chapter describes a study on the exfoliation of graphene in Cyrene, a green alternative to commonly used DMF and NMP. In this study, we observed the effect of

experimental and instrumental parameter for ultrasound assisted exfoliation of graphene from graphite, to find optimal conditions for exfoliation of few-layers graphene nanosheets.

Chapter I

Introduction

1.1 The Necessity for New Sensing Platforms and the Advent of Nanostructured Sensors

Research and innovation in sensing and nanomaterial science have a huge impact on several aspects of human life. For instance, technologies for point-of-care testing (POCT) and self-diagnosing are pivotal for the development of modern society. The demographic growth and the occurrence of globally diffused diseases impose the necessity for faster and more efficient diagnostic tools that can be used without expensive equipment or specialized personnel.[7] Implementation of nanomaterials has greatly fostered self-diagnosis technologies. A renown example are colorimetric immunosensors based on gold nanoparticles widely used for pregnancy tests or antigen immunoassays for viral infections.[8,9] During COVID-19 pandemic, these tools have proven extremely important in the overall control of infection, allowing quick domiciliary self-monitoring. Moreover, the low cost of these technologies enables mass production and wide distribution of these sensors, which can be used without specific equipment, thus extending basic healthcare to larger portions of the population.[10]

Environmental analysis for detection of pollutants derived from anthropic activity is another huge problem that human society is facing, which benefits from the flourishing research activity on sensing technologies. The contamination of various natural matrices with contaminants constitutes a serious threat that human society has to face,[11,12] and monitoring technologies is a fundamental tool to control the impact of human activity over environment.[13–15]

Finally, sensors find application in industrial applications for monitoring of toxic volatile compounds[16,17] and quality control.[18]

1.2 Definition of Sensor and Classification

Following the official definition provided by IUPAC,[19] a chemical sensor is "a device that converts chemical data, ranging from the concentration of a single sample component to complete composition analysis, into an analytically usable signal". Two are the main components of a sensor: a receptor, which transforms the chemical information of interest into a form of energy, through a specific interaction, and the transducer, which measures/transforms the energy carrying the chemical information into a useful analytical signal.

The functioning principle of the sensor may be physical, if no chemical reaction takes place, as in measurements of absorbance, temperature or conductivity. Chemical sensors base their recognition ability on selective chemical interactions between the receptor the analyte. Among chemical receptors, biochemical receptors are those specifically related to biochemical processes, like enzymatic reactions or immune-targeting.

Chemical sensors are categorized based on the transducing mechanism and the type of signal: in optical sensors, the interaction between analyte and receptor produces changes in optical phenomena like variation of absorbance or quenching of fluorescence. Electrical sensors base their analytical response on the change of electrical properties (conductivity, permittivity, charge carrier density) of the transducer. These sensors are not to be mistaken with electrochemical sensors, as the phenomena leading to the recognition event do not involve redox processes.

Electrochemical sensors transform the effect of electrochemical reaction (i.e. the charge transfer and variation of oxidation state of species at the electrode interface) into a useful signal. They comprehend different subgroups, depending on the used electrochemical technique: voltammetric sensors include devices based on voltammetric techniques (cyclic voltammetry, linear sweep voltammetry, differential pulse voltammetry, square wave voltammetry), in which current is measured upon application of scanning, and amperometric sensors, in which current is measured upon application of constant potential. In potentiometric sensors, potential between the working electrode and the reference electrode is measured.

Electrochemical sensors constitute a powerful tool to face modern challenges posed to our society, thanks to their low cost, high sensitivity and accuracy, versatility and rapid response.

In the last 60 years, the advance in equipment miniaturization has greatly fostered electrochemical technology, allowing electrochemistry to get out of the laboratories in the form of portable devices.[20,21] Before 1990s, electrochemistry was confined to laboratory setups, due to bulky instrumentation and large volumes of sample required. Miniaturization of the electrodes and the advent of novel manufacturing techniques like screen-printing allowed for electroanalysis to get out of the chemistry lab and reach common users, in the form of compact analytical systems.[22] In the early 2000s, the implementation of nanomaterials like carbon nanotubes[23] and graphene[24] in the design of functional sensors furtherly fostered the field of electrochemical portable analysis, allowing for better performances and fabrication of flexible compact designs. This rapid evolution of electrochemistry stimulated the research and development of nanostructured electrochemical sensors and biosensors for various applications: in environmental analysis for detection of pesticides[14,25], antibiotic and drug residues[15,26] and heavy metals;[13,27] in industrial processes for real-time monitoring of gases[28] and food contaminations;[18] in healthcare for detection of biomolecules of interest like neurotransmitters,[29] and for immunosensors.[30,31]

1.3 Nanomaterials and their Classification

Nanomaterials differ from their bulk counterparts in that they have at least one dimension in the range of 1 to 100 nm. While size and shape have little effect on bulk material's physical or chemical characteristics, they are crucial in influencing a material's behavior at the nanoscale. Nanomaterials' exceptionally high surface-to-volume ratio increases the probability of interaction with other materials, chemical species, and biological interfaces. Simultaneously, their electronic structures undergo noteworthy changes due to the quantum confinement effect, which arises when particles are too tiny to be compared with the wavelength of excitons. As a result, nanomaterials exhibit exotic behaviors, including improved catalytic performances, particular interactions with biological surfaces and cells, as well as special optical and electrical qualities.

Based on their dimensions, nanomaterials can be divided in three categories: 0D, 1D and 2D nanomaterials. 0D nanomaterials are spherical or quasi-spherical materials with all dimensions in the range of few nanometers. Typical examples of 0D nanomaterials are metal nanoparticles (MNPs), metal oxide nanoparticles (MONPs), metal nanoclusters (MNCs), inorganic quantum dots (QDs), carbon dots (CDs) and fullerenes (C_{60}).[32]

1D nanomaterials possess a high length-to-diameter ratio, which influences their electrical, chemical, optical and mechanical properties.[32] Metal nanowires (MNWs), metal nanorods (MNRs), carbon nanofibers (CNFs), carbon nanotubes (CNTs) and carbon nanohorns (CNHs) belong to this category. CNTs are one of the most studied materials of this class, thanks to their peculiar electronic properties[33] and outstanding mechanical strength.[34,35]

Nanomaterials that possess one dimension much smaller than the other two are defined as 2D nanomaterials. This group comprises many materials that share the structural arrangement of atomically thin planar layers stacked on top of each other. Strong covalent bonds bind the atoms of each layer, while the interlayer interactions are weaker van der Waals forces. Graphene is considered the archetype of this category,[36] which includes as well transition metal dichalcogenides (TMDs),[37] hexagonal boron nitride (HBN), black phosphorus (BP), carbon nitride (CN) and MXenes.[38]

Three-dimensional nanomaterials are also mentioned in literature, as materials that exceed the nanometer range in any dimension, but are made up of individual blocks in the nanoscale.[7,39] This definition appears to be inconsistent with the primary definition of nanomaterial, which stipulates that a nanomaterial must have size in the nanometric scale

for at least one of its three dimensions. A better definition for this class of materials is bulk nanostructured materials[40] and describes bulk solids with nanoscale or partly nanoscale microstructures. Zeolites,[41] metal organic frameworks (MOFs),[42] three-dimensional covalent organic frameworks (COFs),[43,44] fullerites,[45] porous carbon black (CB),[46,47] hierarchically self-entangled carbon nanotubes networks[48] belong to this family of materials.

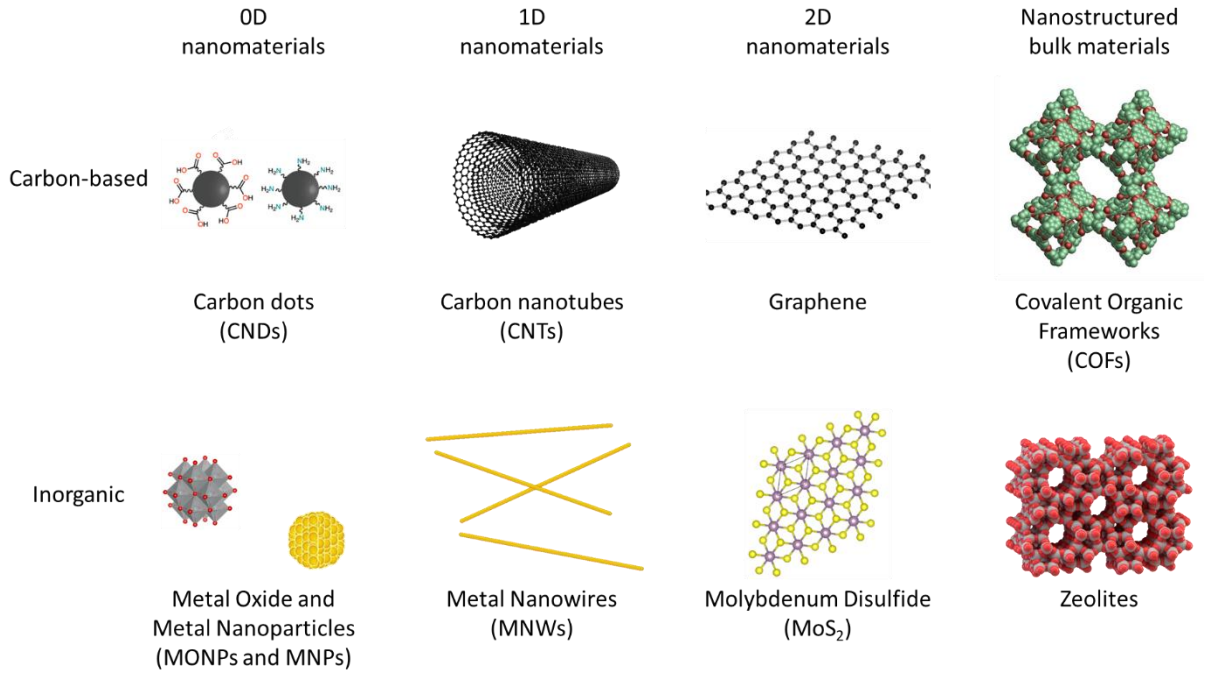

Figure 1 *Examples of carbon-based and inorganic materials classified by dimension.*

This classification is based only on dimensions, thus each class is extremely heterogeneous in the type of properties it displays, and can be considered as a rich toolbox in the design of highly sensitive devices. In electrochemical sensors, nanomaterials and nanocomposites fulfil different functions, typically concurring in enhancing or transducing specific biological processes into a signal appropriate for determining an analyte concentration.[49] The role of a nanomaterial in the electrochemical device depends on its specific properties, in terms of conductivity, reactivity, shape and morphology.

Discussion will now focus on nanomaterials that have been used in this thesis, giving a detour on their synthesis, functionalization and peculiar properties.

1.3.1 Carbon Nanomaterials

Since the discovery of fullerenes in 1985,[50] there has been a significant amount of study focused on carbon nanomaterials. The discovery of these unusual "soccer ball" shaped nanoparticles fueled the field of nanomaterials research, in a time in which only known allotropes of carbon were diamonds and graphite. After the isolation of CNTs by Ijiima in 1991,[51] the interest in these materials has continuously grown, and they quickly rose to the top of the list of nanomaterials utilized for energy storage, photovoltaic, sensing, and even X-ray sources. Ultimately, Novoselov and Geim's isolation of graphene in 2004 transformed the field of nanoscience once more and ushered in the era of two-dimensional nanomaterials.[52]

It is simple to understand why these nanomaterials are so successful and why there is so much research revolving around them: their physical and chemical characteristics allow them to compete with inorganic nanoparticles in a wide range of applications, but with a significantly lower cost of production and environmental impact. From a single element, carbon, it is possible to synthesize all classes of materials: zero-dimensional (i.e. Fullerenes and CDs), one-dimensional (i.e. CNTs, CNFs), two-dimensional (i.e. Graphene, Graphyne) and nanostructured bulk materials (i.e. CB). Furthermore, by tuning their dimensions, spatial organization, and organic chemistry functionalization, it is possible to modify their reactivity, mechanical and electrical properties, and biocompatibility.

1.3.2 Carbon Nanotubes

CNTs are seamless, open- or closed-ended cylinders made of one or more layers of sp^2 carbon (named respectively single-wall, or SWCNT, or multiwall, or MWCNT). The structure of ideal CNTs consists of a hexagonal lattice except at their ends, but typically, mass-produced CNTs are characterized by structural defects, like pentagons, heptagons, and other imperfections in the sidewalls. The diameters of SWCNTs and MWCNTs are typically 0.8 to 2 nm and 5 to 20 nm, respectively, although MWCNT diameters can exceed 100 nm. CNT lengths go from less than 100 nm to several centimeters, bridging molecular and macroscopic scales.[53]

Arc discharge, laser ablation, and chemical vapor deposition (CVD) are the three primary synthetic processes used to produce CNTs. All three methods use a source of carbon atoms

that is vaporized and then condensed on a metal catalyst at high temperatures, where growth of CNTs takes place.

Historically, arc discharge was the first method used to synthesize and isolate CNTs: this technique was already used to produce C_{60} fullerene, when in 1991 Iijima used it to synthesize and isolate the first known CNTs, with diameters ranging from 2 to 50 nm.[54] The arc discharge is generated between two graphite electrodes, producing extremely high temperatures (up to 6000°C) causing graphite from the anode to sublimate. In low Ar or He pressure, sublimated carbon deposits on the cathode (in the presence of Fe, Ni or Co as catalysts), leading to growth of CNTs.

In the laser ablation method, the sublimation of graphite is laser-induced, in a heated furnace (2700-3200°C) under He or Ar atmosphere. A flux of gas delivers sublimated carbon to a cooled catalytic surface (usually Fe, Ni or Co), where the growth of CNTs takes place.[55] This technique provides more control over the final quality of CNTs, as the modulation of the temperature of the furnace[56] and of the cooled catalytic collector[57] allows control over the size and amount of the of defects of CNTs.

On an industrial scale, high temperatures involved in arc discharge and laser ablation methods can be problematic; moreover, these methods suffer from low yields that are not compatible with large-scale production.[58] CVD is the technique of choice for industrial-grade production of nanotubes, thanks to more practical and less expensive setup and lower operative temperatures. Typically, a carbon precursor (acetylene, ethylene, methane, etc.) is injected in the reactor and carried by an inert gas toward a thin layer of silica decorated with MNPs that serve as catalysts for the growth of CNTs. The operational temperature usually goes from 600 to 1200°C.[59] A variation of CVD that is commonly used is plasma-enhanced CVD (PECVD), in which working temperatures are even lower, and a plasma of carbon precursor and carrier gas is generated.[58,60]

The diameter, length, and structure of CNTs have a significant impact on their chemical, physical, and electrical characteristics. To better understand their structural organization, it is useful to imagine CNTs as folded graphene sheets (**Figure 2a**): the width of the initial graphene sheet determines the diameter and the number of layers of graphene (single-layer or few-layer) determines if the final CNT is a SWCNT or MWCNT.

The direction along which the graphene is folded is defined as chiral vector (**Figure 2b**), and is expressed as:

$$\vec{C} = n\overrightarrow{a_1} + m\overrightarrow{a_2}$$ **(Equation 1)**

Where $\overrightarrow{a_1}$ and $\overrightarrow{a_2}$ are the two vectorial components of $\vec{C}$ along *x* and *y*, *n* and *m* are integers. The outcome of the wrapping can be a zig-zag CNT (*m* = *i*, *n* = 0, with *i* = 1, 2, 3), an armchair CNT (*m* = *i*, *n* = *i*, with *i* = 1, 2, 3) or a chiral CNT (*m* = *i*, *n* = *j*, with $i \neq j$ = 1, 2, 3).

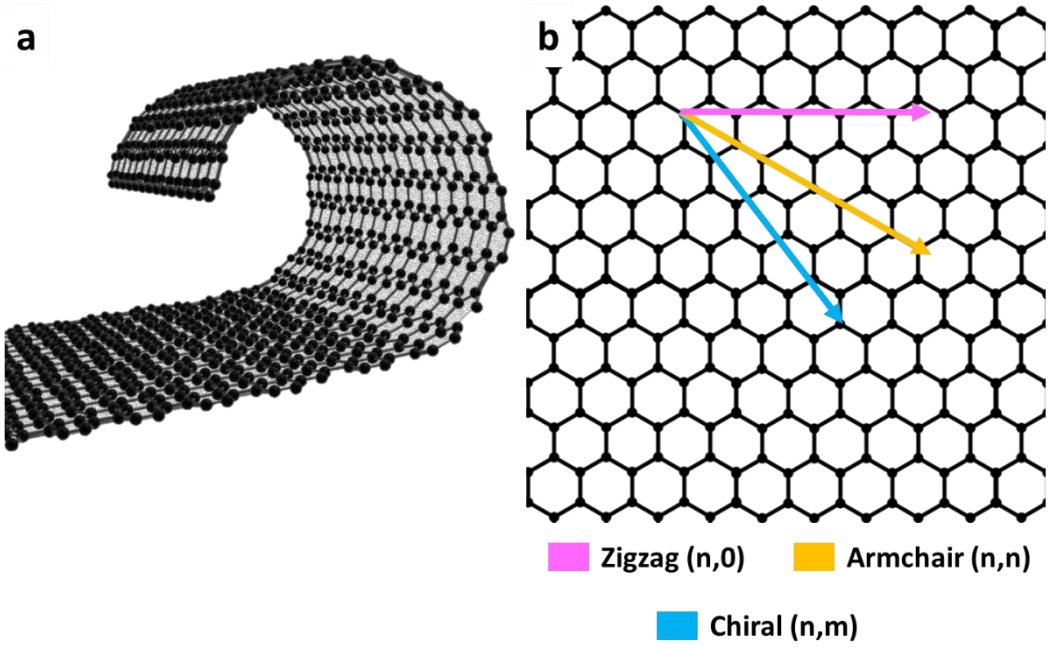

Figure 2 *a) Folding of single-layer graphene; b) chiral vector of CNT.*

In SWCNTs, the values of the parameters *n* and *m* are associated with the electronic properties of the material. For values of *m*-*n* = 3*i* (*i* = 1, 2, 3), SWCNTs present a metallic behavior, with high conductivity, up to 2×10^7 S m^{-1}, comparable with values previously reported for MNPs.[33] For values of *m*-*n* = 3*i* ± 1 (*i* = 1, 2, 3), SWCNTs behave as semiconductors.[61] Separation of SWCNTs with different chirality is one main topic in nanomaterials science,[62,63] as efficient sorting of SWCNTs by chirality will allow to fully exploit the potential of this material in future electronics[64] and biotechnologies.[65]

On the other hand, MWCNTs, being composed of different concentrical SWCNTs, exhibit properties that lie in between the two cases, with a maximum electrical conductivity of 2×10^5 S cm^{-1}.[66]

As already mentioned, organic chemistry can be used to modify the surface of CNTs, introducing task-specific functional groups. Surface modification increases the applicability

of CNTs exponentially, introducing control over solubility,[67,68] aggregation,[69] dispersibility in polymeric matrices,[70,71] selective interaction with chemical species[72] and biological interfaces.[73,74]

Functionalization can proceed through covalent organic functionalization or supramolecular approach. The first provides a more stable functionalization of CNTs, but introduces defects and changes their structure, potentially compromising their electrical characteristics.[75] On the other hand, supramolecular functionalization is weaker and more labile, over time and at high temperatures, but does not modify the CNT lattice, maintaining its electronic properties intact.[76,77]

Oxidation, fluorination, cycloadditions and direct arylation with aryl diazonium are examples of covalent methods (**Figure 3**). Oxidation is one of the simplest methods for altering and modifying CNTs. This method was first described in 1993 by Ajayan et al.,[78] who employed Pb_3O_4 at high temperatures to oxidize CNTs only at the level of the caps, opening their ends. Oxidation is a helpful method to improve the solubility of CNTs and to introduce oxygenated moieties as precursors for additional modifications. Using different oxidative agents and different experimental conditions it is possible to modulate the degree of oxidation: for example, by treating CNTs with concentrated HCl, it is possible to open the caps of CNTs and remove metal impurities from synthesis, without damaging the CNT structure, as HCl has not enough oxidative power to attack sp^2 carbon.[79,80] Mixtures of NH_4/H_2O_2 can be employed as weak oxidants that attack only defective sites without compromising the sp^2 carbon lattice, while stronger oxidants like HNO_3 or HNO_3/H_2SO_4 mixtures can oxidize also the walls of CNTs.[81] Oxidation of CNTs leads to formation of carboxylate groups on the surface that can subsequently be used for further derivatizations, through activation with thionyl chloride,[82] amidation,[83] esterification.[84]

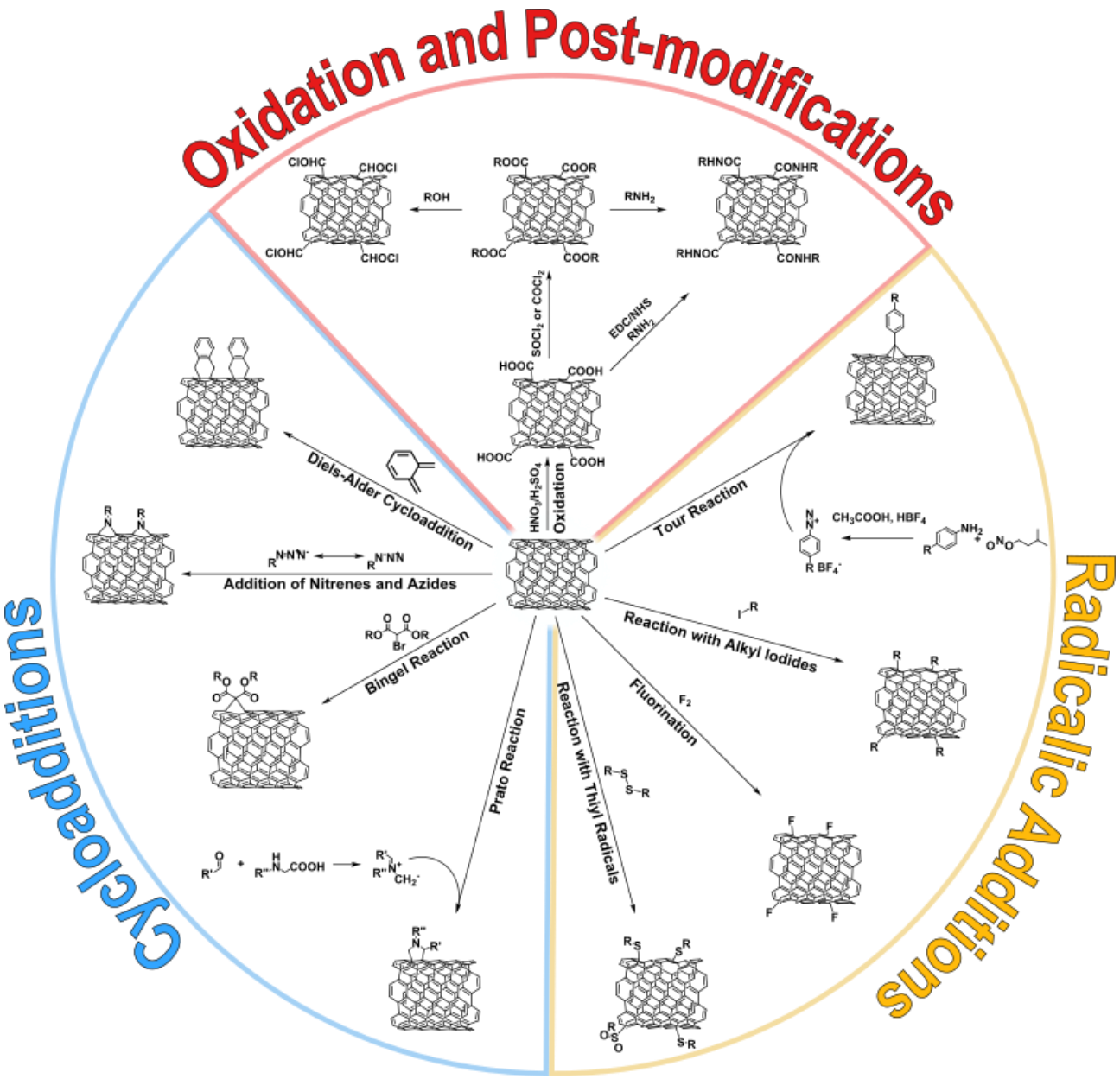

Figure 3 *Covalent approaches for functionalization of CNTs.*

Fluorination is another method that can serve as a propaedeutic step to introduce functionalizations on the sidewalls of CNTs, as the introduction of fluorine atoms greatly increases their reactivity. Fluorination is carried out by treating CNTs with F_2 gas at temperatures between 150 and 400°C[85] and subsequent sidewall alkylation is feasible, using organolithium, Grignard or metal alkoxide reagent.[75]

Cycloadditions are a versatile strategy to functionalize CNTs with multiple moieties. X. Lu et al. already predicted the possibility of using the Diels-Alder reaction to functionalize the sidewall of CNTs in 2002, with CNTs acting as dienophile.[86,87] Later J. Delgado et al. were

among the first to demonstrate the viability of this reaction for functionalization of CNT sidewalls.[88] However, Diels-Alder presents a major drawback that is reversibility due to the low thermodynamic stability of the formed adduct.[89] 1,3-dipolar cycloadditions of azomethine ylides (Prato reaction) represent a more suitable option for the controlled functionalization of CNTs.[90] The azomethine ylide is generated in situ by thermal condensation of an aldehyde and an α-amino acid, and subsequently attacks the sidewall of CNT, forming a pyrrolidine ring fused on the C-C bonds. By opportunely selecting the side chain of the amino acid, it is possible to obtain a vast library of functionalized CNTs.[91]

The chemistry of diazonium salts represents one of the most valuable and well-studied tools for functionalization of CNTs. The group of James M. Tour pioneered this approach in 2001,[92] proposing a simple and efficient method to functionalize CNTs with a high degree of functionalization, based on electrochemical reduction of various aryl diazonium tetrafluoroborates. The reaction mechanism involves the decomposition of the diazonium salt, with formation of the corresponding aryl radical and a molecule of N_2. The free radicals proceed then to attack the surface of CNTs. Diazonium salts can be previously synthesized[93–96] or generated in situ,[97,98] and their decomposition can be induced electrochemically,[92,93] thermally[97–100] or triggered by acids.[100] As a consequence, this approach emerges as extremely versatile for many different applications. One main drawback is related to safety issues, as most diazonium salts are extremely reactive and even explosive.[95] This problem can be addressed by choice of suitable counter anions, like tetrafluoroborate, which enhance stability of the salts.[101] The second issue with diazonium chemistry is the poor control and the tendency to polymerization;[102] however, this phenomenon can be limited by opportune control of experimental conditions and diazonium concentration[95] or tuning of the molecular structure.[103,104]

Several other covalent approaches can be found in literature, as research on derivatization and manipulation of CNTs benefits from decades of study in the nanoscience community. Some examples are the addition of carbenes and nitrenes, nucleophilic additions, and electrophilic additions.[75]

Non-covalent functionalization typically relies on weak supramolecular interactions like π-π stacking between the surface of CNTs and polycyclic aromatic compounds like pyrene[105,106] and porphyrins,[107,108] or on hydrophobic interactions with surfactants like sodium dodecyl sulfate.[109,110] This strategy is recommended when preserving the electrical and optical

properties of CNTs is crucial for specific applications, like field effect transistors.[111] The non-covalent functionalization can be less stable when compared to covalent one, as the weak interactions between CNTs and the adsorbed species can be easily broken upon washing, filtration and dialysis.[112]

The same supramolecular interactions can be employed to promote polymer adsorption on the surface of CNTs. This will cause the polymeric network to wrap around the sidewalls of CNTs.[113] The multi-point enthalpy-driven interactions between CNTs and the polymeric network greatly enhance the stability of functionalization allowing for its resistance to washing processes.[114] The array of eligible polymers for CNT wrapping is extremely vast and their selection depends on the final application of the functionalized material: for example, polymers with extended π-conjugated have strong affinity for the polyolefinic surface of CNTs, and have been used for sorting of CNT of different chirality[115] and composites of aromatic polymers like poly(3-alkylthiophenes) and CNTs proved extremely interesting for photovoltaic applications.[116] Biopolymers like proteins[117] and DNA[112] have been widely explored as wrapping agents for CNTs, to increase dispersibility in water, enhance biocompatibility[118] and to modulate selective interactions with target molecules.[119]

Finally, an interesting strategy that reunites covalent and non-covalent approaches is based on the use of mechanical bonds between CNTs and organic macrocyclic rings.[120,121] Similarly to CNT wrapping, SWCNTs are encapsulated in organic macrocycles that interact with their sidewalls through weak supramolecular interactions (typically π-π), resulting in a rotaxane-like structure.[122] Typically, thin SWCNTs (diameter ≤1 nm) are first functionalized non-covalently with "nano-horseshoe" precursors of the macrocycle, and subsequently clipping is carried out to close the macrocycle around the tube.[121] This approach boasts advantage of leaving intact the surface and electronic properties of CNTs, typical of non-covalent functionalization, but at the same time benefits of greater stability, thanks to covalent bonds that hold together the structure of the macrocycle.[120]

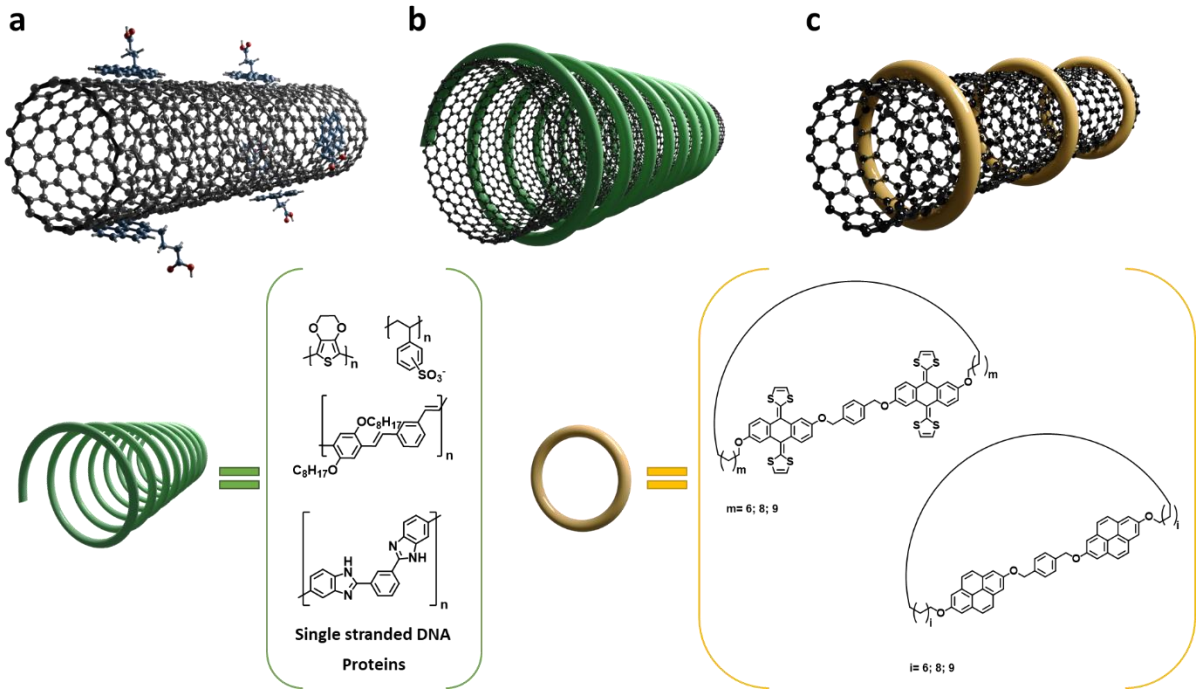

Figure 4 *Non-covalent approaches for functionalization of CNTs: a) functionalization by single molecule adsorption; b) CNT wrapping with polymers; c) mechanically interlocked CNTs.*

The possibility of finely tuning properties of CNTs, by modulating their dimensions and chirality, and the wide range of functionalization strategies that have been developed to modify their surface chemistry, makes CNT extremely versatile for a many applications. Due to their excellent electric conductivity and the possibility of introducing specific receptors on their surface, CNTs emerge as optimal transducers for electrochemical sensors in sensing technology.

Taking advantage of their high electroactive area, CNTs can be used to create tags for radio frequency identification (RFID) or CNT-based Field Effect Transistors (CNT-FET), which detect hazardous gases like NO_2 and NH_3 [123,124] or CO_2,[125] based on the change in conductivity of CNTs upon adsorption of the analytes. Additionally, bare CNTs are ideal candidates for the electrochemical stripping examination of metal ions. Their high surface area makes them ideal for the adsorption of the analyte, allowing pre-concentration of metallic species at the electrode surface and increasing sensitivity.[126]

Selectivity can be implemented in CNT-based sensors after they have been properly functionalized. For instance, D. Fu et al. were able to distinguish CO from other gases

including NO and NO_2 by functionalizing the surface of CNTs with carboxylic moieties.[127] Bioreceptors, like enzymes or aptamers, can be immobilized on the surface, by both covalent and non-covalent approaches.[128,129] For example, Li et al. immobilized glucose oxidase on CNTs to design an amperometric sensor for detection of glucose.[130] Briefly, through an oxidation-amidation functionalization pathway, they introduced primary amines on the surface of MWCNTs, which reacted with aldehyde from the enzyme forming imine groups. In another work, Zhan et al. reported an amperometric sensor for H_2O_2 based on myoglobin immobilized on MWCNTs.[131] In this case, a non-covalent approach based on hydrophobic interactions, hydrogen bonding and electrostatic interactions was used to functionalize MWCNTs with a polymer (P(MMA-co-AAM)) and myoglobin was dispersed in the polymeric matrix.

A possible disadvantage of free CNTs can be their toxicology, although more research is still needed on this matter. Depending on their size, carbon nanotubes could be toxic and cause asbestosis if breathed in. However, not all CNTs are systematically harmful, and toxicity is frequently associated with metallic impurities that are produced during the CNT manufacturing process rather than the CNTs themselves.

1.3.3 Graphene

With good reason, the discovery and isolation of graphene is regarded as a turning point in the advancement of nanotechnology and nanoscience. This material is one of the most promising choices for the development of nanoelectronics in the future because of its chemical and physical features.[24,132,133] Graphene is a 2D nanomaterial made of a single atomic layer of graphite, which was isolated in 2004 by Nobel Prize awarded Andrej Gejm and Konstantin Novosëlov. It is the thinnest material to exist, one of the strongest known and it outcompetes highly conductive metals like copper, in terms of sustained current density.[36]

In first instance, graphene was isolated from naturally occurring graphite, by mechanical exfoliation.[52] This method yields the highest quality graphene, but is not scalable on an industrial scale. As previously seen for CNTs, CVD has become the technique of choice for production of high-quality supported graphene on an industrial scale.[134–136] On the other hand, colloidal suspensions of graphene nanosheets and nanoplatelets can be obtained by liquid phase exfoliation (LPE), which is the most convenient synthetic strategy in terms of

cost efficiency, at expense of final graphene quality.[137] LPE can proceed by different pathways that have in common the aim of breaking the weak interlayer interactions that hold together graphite crystals. In chemical LPE, strong oxidants are used to oxidize graphite to graphite oxide, disrupting its ordered structure to allow layers separation during a sonication step.[138] The obtained graphene oxide (GO) can be applied as it is or reduced to recover original properties of graphene, however the characteristics of reduced graphene oxide (rGO) never match those of pristine graphene.[137,139]

LPE can be carried out without the use of oxidants, as demonstrated by the Hernandez et al. in a 2008 research article that constitutes a fundamental milestone in the field.[137] In their work they demonstrate that suitable solvents like N-Methylpyrrolidone (NMP), N,N-Dimethylformamide (DMF), γ-butyrolactone and 1,3-dimethyl-2-imidazolinidone can favor exfoliation of graphene from graphite without the aid of surfactants or oxidants, thanks to their strong interaction with the surface of graphitic layers. The obtained graphene presented low number of defects on the surface, clearly demonstrating superior quality compared to the chemical approach.

The use of surfactants can improve the efficiency of LPE, increasing yield and colloidal stability.[140,141] Typically, surfactants used to favor LPE of graphene have an aromatic part that can interact via π-π interactions with the sp^2 surface of graphitic layers and a charged part that causes repulsion between layers, facilitating their separation.[142,143] The downside of using surfactants is their difficult removal from surface of graphene, as they would passivate and negatively affect graphene performances.[140] However, the strong interaction between the dispersant and graphene can be exploited to perform exfoliation and non-covalent functionalization in one step. For example, Shin et al. demonstrated that, by opportunely functionalizing pyrene derivatives used as dispersants, it is possible to tune stability of the obtained dispersion and modulate its biocompatibility.[140]

When compared to mechanically exfoliated or CVD graphene, both exfoliated graphene (EG) and rGO exhibit lower electronic qualities due to their numerous defects, limited extension, and few layers rather than a single sheet of carbon atoms. The final application determines whether to use EG, rGO, or CVD graphene: for some applications, such as field effect transistors (G-FET), CVD graphene is necessary to preserve electronic properties like the Dirac-like linear dispersion relation of its energy momentum, which allows for the extremely high charge transfer of the delocalized electrons.[144,145] LPE allows easy and scalable

production of liquid-processable colloidal graphene, which can be implemented in the design of conductive inks for printable devices.[146]

Furthermore, because of their defective nature, EG and rGO are significantly more reactive than CVD graphene, which is good for electrochemical sensing applications since it enables the addition of recognition elements by chemical modification.[147,148] Because of these advantages, research on LPE-graphene inks for electronics is incredibly abundant across a wide range of disciplines. EG-based inks have been used as both electrocatalytic and transducing elements in sensing technologies.

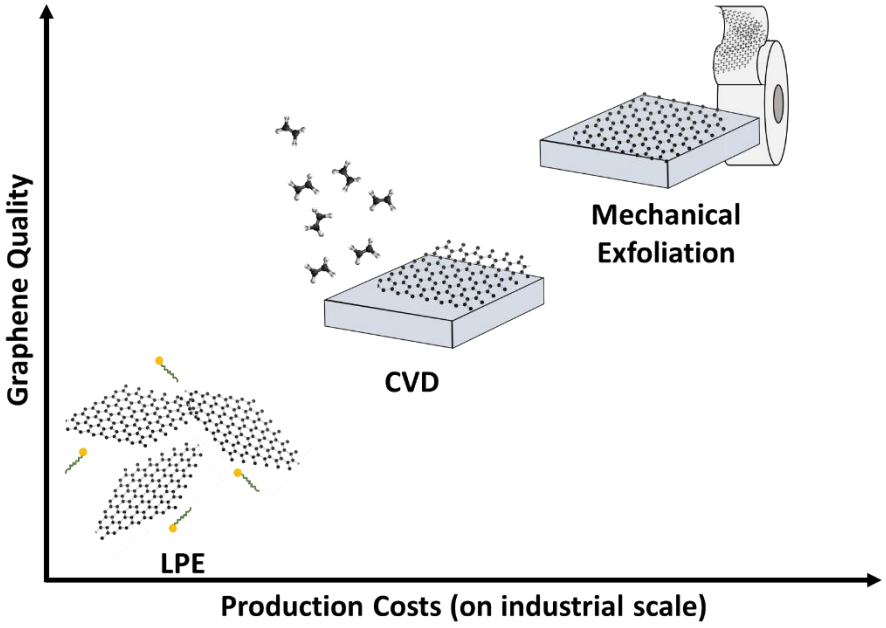

Figure 5 *Different synthetic strategies for graphene production, reported against the production costs on industrial scale and quality of final graphene.*

Covalent and non-covalent approaches previously described for CNTs can be applied to functionalize graphene as well.[102] Multiple covalent functionalization can be carried out on the surface of graphene, like reduction of diazonium salts,[104] cycloadditions[147,149] or photo-induced radicalic reactions.[150] Generally, graphene is less reactive than CNTs, due to the lack of pyramidalization of perfectly planar hexagonal lattice, and its reactivity mainly depends on the presence of defects on its surface.[55] As a consequence, rGO and EG are more reactive than CVD graphene. Non-covalent approaches may be preferred for functionalization of CVD graphene, both to face its low reactivity and to maintain its precious electronic properties.

For electrochemical biosensing devices, EG is a great transducer due to its large surface area. P. Labroo and Y. Cui have provided an excellent illustration of this use, having created an EG-based nano-ink for the examination of several metabolites.[151] In their work, four enzymes—glucose, lactate, xanthine, and cholesterol oxidases—have been immobilized on the surface of EG nanoplatelets through the use of EDC-NHS chemistry. These enzymes serve as bioreceptor, oxidizing selectively their substrates and producing H_2O_2 as a byproduct. Upon application of a positive potential of 0.5 V, the produced H_2O_2 oxidizes at the surface of the EG nanoplatelets, resulting in an electrical signal.

Silvestri et al. have shown that every component of a biosensor may be immobilized on graphene flakes, resulting in nano-assemblies suitable for use as the ink's active component.[152] Through a combination of covalent and non-covalent methods, the authors functionalized graphene using various enzymes and cobalt phthalocyanine (CoPC), resulting in inks that are specific to short-chain alcohols, glucose, and lactate. This strategy's main benefit is that it enables direct inkjet printing of electrodes, eliminating the need for post-functionalization with receptors and electrochemical mediators.

Another method for integrating every sensor component into an ink is self-assembling. The same authors suggested creating a self-assembling bio-ink for glucose and H_2O_2 sensing using EG and protein-stabilized metal nanoclusters as the basis for an ink-jet printable ink.[153] The primary function of the engineered proteins utilized in this work is templating the development of size-controlled metallic clusters, as well as self-assembling in a self-standing biofilm that immobilizes and stabilizes the enzymes introduced to the formulation. Graphene, on the other hand, increases the hybrid material's conductivity and significantly boosts its electrocatalytic qualities, increasing the sensors' sensitivity and detection limits.

1.3.4 Molybdenum Disulfide

Graphene opened a new era for nanoscience, opening new perspectives on layered materials and ushering research on two-dimensional nanomaterials. The family of 2D-nanomaterials rapidly expanded after 2004, incorporating nanomaterials with extremely various properties. The common element to these materials is the structural organization in stacked atomically thin planar layers, with strong covalent bonds binding the atoms of each layer, and weak Van der Waals interactions holding together the different layers.[154]

TMDs are a subgroup of the 2D-nanomaterial family, including around 40 different materials. All members of this group are characterized by their chemical composition in which one transition metal is bound to a chalcogen (**Figure 6a**). When TMDs are exfoliated to few-layer or monolayer nanosheets, electronic properties can change drastically, due to the modification of their band structures (**Figure 6b**).[155] Furthermore, each TMD can exist in several crystalline phases, and each phase exhibits different properties (**Figure 6c**).[37]

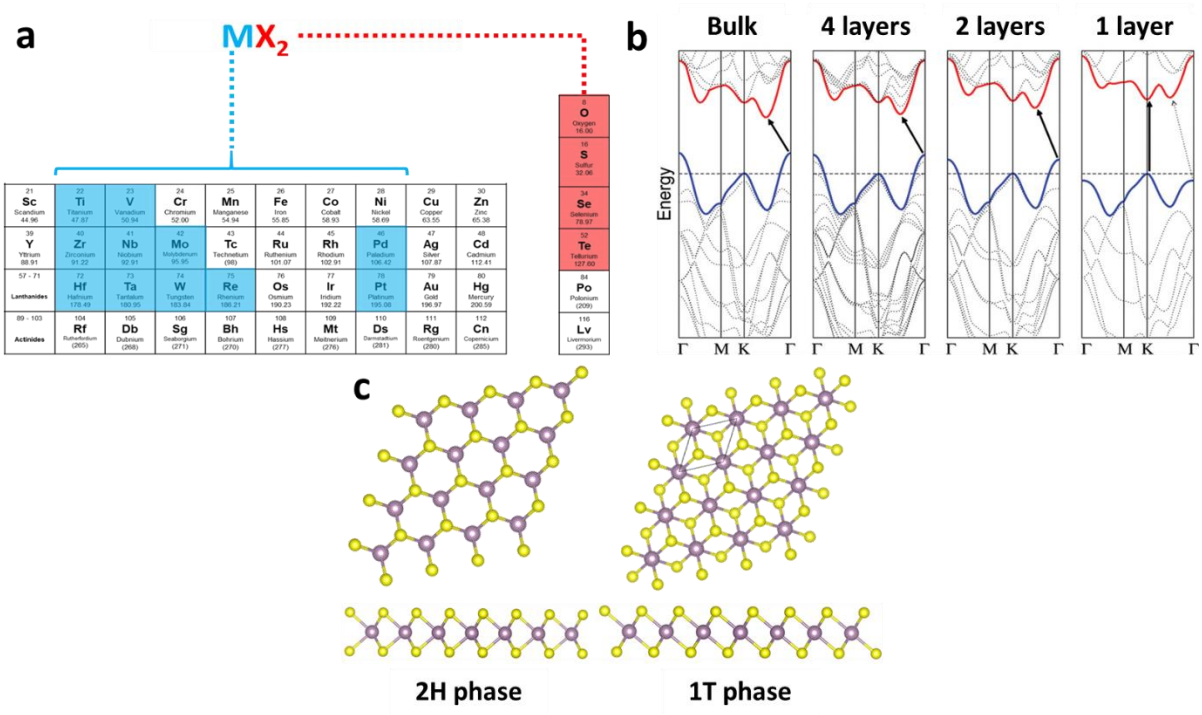

Figure 6 *a) Metals and chalcogens known to form TMDs; b) Thickness-dependent band structure of MoS_2; c) 2H and 1T phases of MoS_2. Panel b was adapted with permission from Nano Lett. 2010, 10, 4, 1271–1275. Copyright 2010 American Chemical Society.*

MoS_2 is probably the most studied material of TMD family. Isolation of monolayer MoS_2 actually traces back to 1986, almost twenty years before isolation of graphene,[156] but research on its electronic and optical properties exploded only in the 2010s, on the wave of excitement for the discovery of graphene. Bulk MoS_2 is commonly employed industrially as solid lubricant and behaves as a semiconductor with an indirect band gap of 1.23 eV.[157] Once exfoliated, modifications in its band structure lead to a new direct band gap of ≈ 1.8 eV (**Figure 6b**) and interesting properties like photoluminescence arise.[155] Bulk MoS_2 and physically exfoliated MoS_2 typically present a hexagonal lattice (2H phase), which is thermodynamically stable. Upon reduction of 2H phase, it is possible to induce a structural

change towards a metastable phase with octahedral structure (1T phase). 1T-MoS_2 is characterized by a metallic behavior, with high conductivity, and abundant active sites on both edges and basal plane.[158]

Similarly to graphene, MoS_2 can be synthesized using both top-down and bottom-up methods. Top-down approaches include mechanical exfoliation, LPE and ball milling, and remain the most promising strategies for production of 2D MoS_2, given the huge availability of the bulk precursor, known as molybdenite.[38,159]

On the other hand, hydrothermal synthesis from ionic precursors and CVD growth are effective bottom-up protocols for synthesis of MoS_2.[160,161]

Taking advantage of synthetic strategies already mentioned for CNTs and Graphene, it is possible to functionalize the surface of MoS_2, tuning its electronic properties and introducing specific moieties. The use of diazonium salt to covalently functionalize its surface is well represented in literature[162,163] as well as reaction with alkyl iodides.[164]

The strategy of "sulfur healing" (**Figure 7a**) is another covalent approach that is specific for MoS_2 and other sulfur-bearing TMDs. It takes advantage of naturally occurring and exfoliation-induced sulfur vacancies on the surface of MoS_2, replacing them with sulfur atoms of thiols.[165] However, doubts arose concerning the actual mechanism involved in this reaction, suggesting that functionalization may be occurring by simple formation of disulfide bonds between the thiol and sulfur atoms on the surface of MoS_2.[166]

It is also possible to exploit the nucleophilic character of sulfur atoms on the surface of MoS_2 to covalently functionalize the material with maleimide derivatives, through a simple click reaction (**Figure 7b**), as demonstrated by M. Vera-Hidalgo et al.[167] The reaction proceeds through Michael addition and allows to modify the surface of MoS_2 with a plethora of maleimide-based reagents.

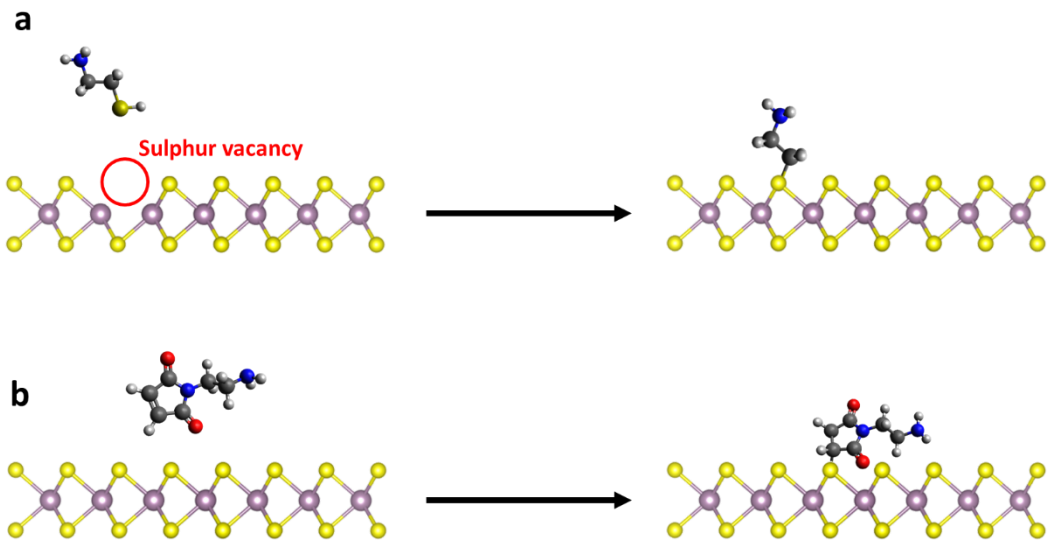

Figure 7 *Covalent functionalization of MoS_2 through a) Sulfur healing and b) Michael reaction with maleimides.*

Non-covalent functionalization approaches for MoS_2 rely on electrostatic interactions between the negative surface charge of MoS_2 and positively charged species[168] or on metal-ligand coordination between molecular species and Mo atoms of MoS_2.[169]

In sensing technologies, MoS_2 has been implemented for detection of gases, metals and biomolecules. Because of its charge-transfer characteristics, MoS_2 may interact with a variety of gaseous compounds. It can be used as an electron-donor towards gases that are electron-acceptors, such as CO, NO_2, NO, or H_2O, and it can also accept electrons from compounds that are electron-donors, such as NH_3.[170] These interactions determine as consequence changes in the resistance to charge transfer and can be exploited to design impedimetric or chemresistor-based sensors. Yao et al. used this strategy to design an electrochemical sensor for NH_3 vapor at concentrations of 5 ppm.[171] Later Chen et al. used AuNPs to modify the surface of MoS_2, improving this same technology and extending the range of analytes to different volatile organic compounds.[172]

The chalcogen atoms on the surface of TMDs provide helpful coordination sites for metal ions. Using this, Neethipathi et al. designed a Cu^{2+} ion sensor based on a SPCE functionalized with a MoS_2 suspension, having a linear range of 5µM to 5mM.[173] More selective coordination sites can be introduced by functionalization. For example, Zhuravlova et al. used Sulfur

healing to introduce 2,2′:6′,2′′-terpyridine-4′-thiol, which is selective for Co^{2+}, for specific chemresistive sensing of Co in water.[174]

Finally, MoS_2 has been applied to the sensing of small molecules such as glucose, dopamine, and H_2O_2, which are relevant to biological activities. Huang et al. doped MoS2 with NiNPs to design a non-enzymatic amperometric sensor for glucose at micromolar scale.[175] Wang et al. developed a sensor for H_2O_2 detection at nanomolar concentrations, using ultrasmall MoS_2 nanoparticles to modify a glassy carbon electrode.[176] MoS_2 modified with MNPs found application also for electrochemical sensing of dopamine, as reported by Chao et al. who used a nanocomposite based on PtNPs and MoS_2 to detect simultaneously dopamine and uric acid with linear ranges from 0.5 to 150 μmol L^{-1} and 5 to 1000 μmol L^{-1} respectively.[177] Switching to less expensive metals for MoS_2 doping can also reduce production costs. As an example, Lei et al. employed Mn single atom doping of MoS_2 to detect concentrations as low as 50 nM in artificial sweat.[178]

1.4 Electrocatalysis

The birth of the term electrocatalysis is generally referred to the work of Kobosev and Monblanova, in the early 1930s, as they were the first to use it to describe redox processes catalyzed upon adsorption of the substrate on the active surface of the working electrode.[179] Interest in this field increased sensitively in the last 40 years, as the influence of the nature of the electrode material on the kinetics of redox processes was further explored, mainly for energy storage and conversion.[180]

Electrocatalysis has emerged in the last decades as a powerful tool to face fundamental challenges on unprecedented scale. Energy storage and conversion probably is the field that benefited the most from application of electrocatalytic materials for oxygen reduction reaction (ORR), hydrogen evolution reaction (HER) or oxygen evolution reaction (OER).[181–183] Environmental remediation is another important application for electrocatalytic materials, that are used to favor elimination of water pollutants.[184–186]

The electrocatalyst can be either a solid material deposited at the interface between the electrode and the medium containing the substrate or a freely diffusing molecular species,[187] that facilitates an electrochemical reaction, typically by lowering the activation energy of the process and favoring the charge transfer from the electrode surface to the reactants. The

decrease of the activation energy results in the application of lower overpotentials to start the redox reaction,[188] while the more efficient charge transfer leads to higher current densities.[189]

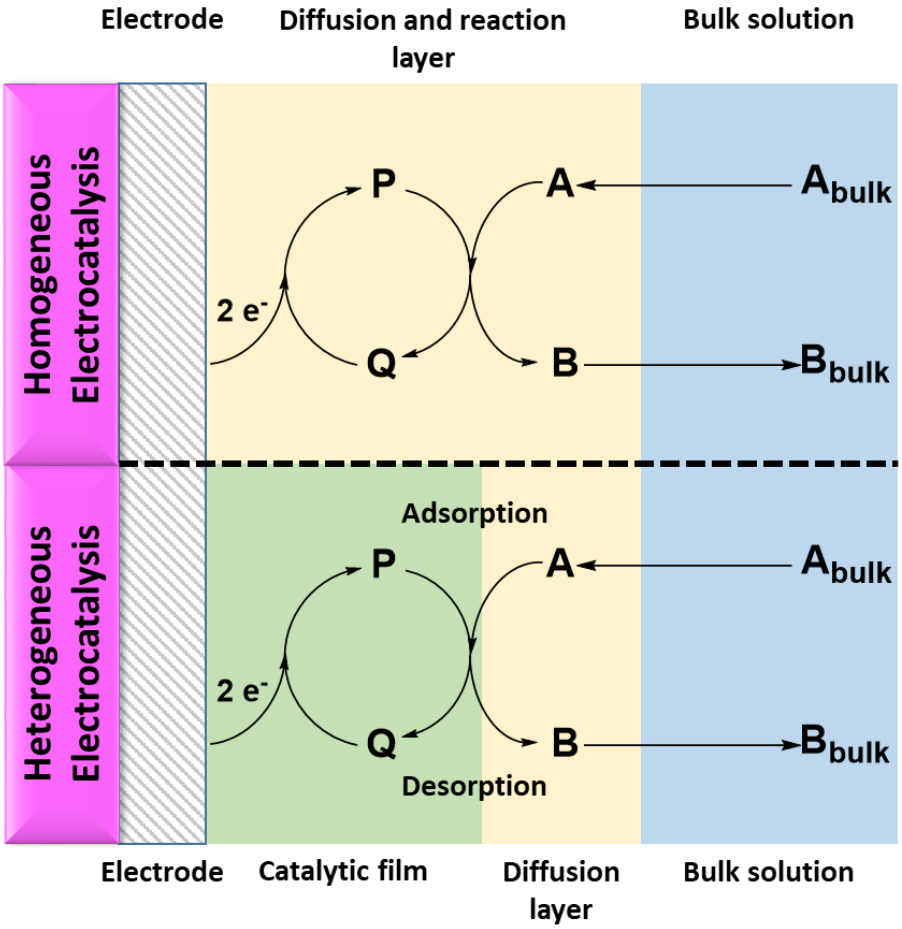

Figure 8 *Reaction scheme for homogeneous and heterogeneous electrocatalysis.*

Overpotential is defined as the additional potential (beyond the thermodynamic requirement) needed to drive a reaction at a certain rate.[190] Three components are primarily responsible for the bias between the thermodynamic potential and applied potential: ohmic overpotential is caused by inherent electric resistance that is imposed by every component of the electrochemical setup and is associated with the design of the cell (junction resistance, electrolyte resistance, capacitance). Mass-transport and concentration overpotential depends on the ability of all chemical species involved in the redox process to freely diffuse through the electrolyte, towards the surface of the electrodes. Finally, the potential difference over the equilibrium potential required to overcome the reaction's activation energy is known as the activation overpotential.[191,192] Electrocatalysts act on the latter form of overpotential, favoring adsorption of the substrate and charge transfer. A lower

overpotential means that less energy is needed to produce the same current, which is desirable for more efficient energy conversion.[193] Additionally, application of low potentials allows the use of aqueous electrolytes, which typically are characterized by a narrow electroactive window of 1.23 V,[193] eliminating the need for risky organic solvents with wider working voltage ranges.[194]

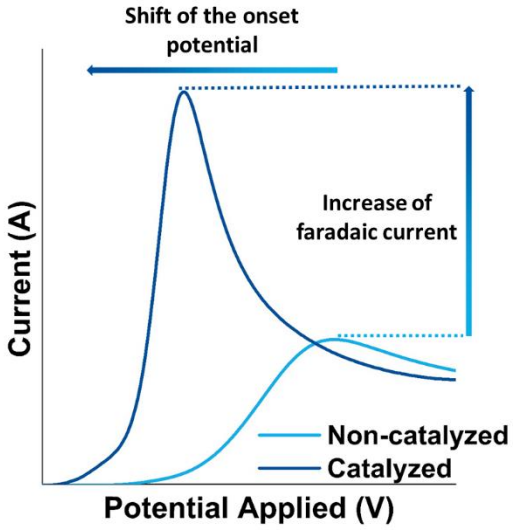

Figure 9 *Effect of electrocatalyst on voltammetric peak.*

Electrochemical sensing technology has been greatly fostered by the development of new electrocatalytic materials and nanostructured electrodes. Literature is full of examples of the application of electrocatalytic nanomaterials: from sensors for detection of biomolecules of interest like neurotransmitters,[29,195,196] glucose,, uric acid[197,198] or ascorbic acid,[199,200] to immunosensors.[30,31,201]

In sensing application, the possibility of modulating the overpotential for a specific redox reaction can enhance selectivity of the sensor for its target, while the higher current density concurs to higher sensitivity, allowing detection at lower concentrations.

1.5 Electrochemical Techniques

Various electrochemical techniques are used not only during the actual sensing process, but also to characterize electroactive nanomaterials that are used for the design of the sensors. Below, the techniques used within this PhD thesis are briefly listed and explained.

1.5.1 Voltammetry

Voltammetry is a set of electrochemical techniques that involve measurement of voltage-dependent and time-dependent current upon application of a controlled potential. The measured current is proportional to the concentration of one or more electroactive species at the electrode surface. Voltammetric techniques differ for the time-dependent function used to sweep the applied potential.

Linear sweep voltammetry (LSV) is the term for the technique when potential is swept linearly over time (**Figure 12a**). By plotting the current against the applied voltage, it possible to obtain a voltammogram. The voltammogram shows the occurrence of electrochemical reaction as current peaks: the scan begins from the left-hand side, and when a redox reaction takes place, a faradaic current begins to flow, reaching a peak before dropping (**Figure 12b**).

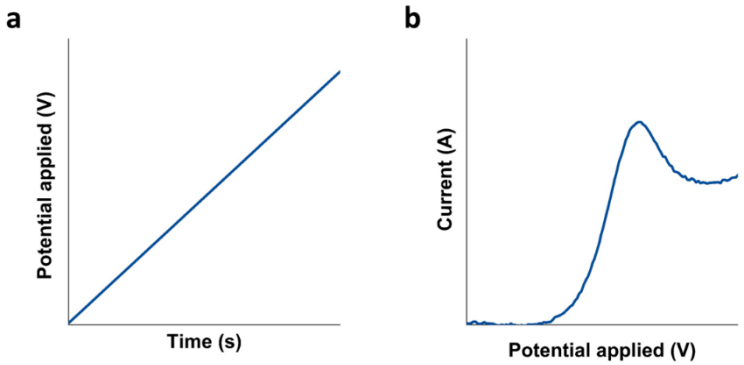

Figure 10 *a) Potential scan for LSV; b) Voltammogram obtained from LSV.*

The peak occurs because at some point the consumption of the reagent at the surface of the electrode generates a depletion layer and diffusion from the bulk of the solution to the electrode becomes rate-determining. The slope of the potential-time line determines the voltage scan rate, which has important effects on the final voltammogram.

Cyclic voltammetry (CV) is extremely similar to LSV. Also in this case voltage is swept linearly, but upon reaching a determined value of potential, the scan is reversed and voltage is swept back to initial potential with the same scan rate (**Figure 13a**). While the forward sweep produces the same response of LSV, when potential is swept back, it is possible to move back to equilibrium and study reversible processes (Figure 13b). CV is a simple yet powerful technique to explore an electrochemical system, highlighting cathodic and anodic phenomena, together with their reversibility, before proceeding to other more specific electrochemical measurements.

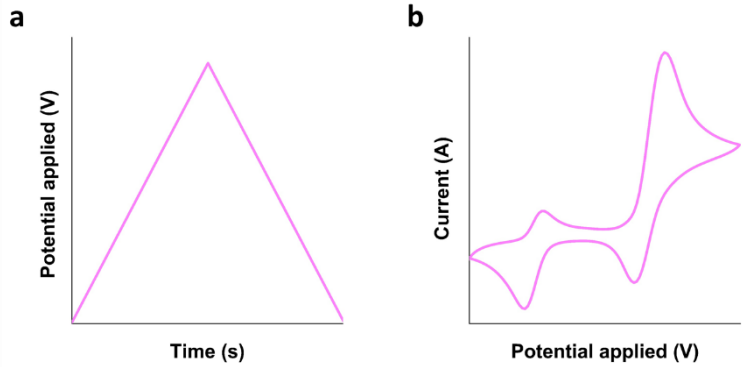

Figure 11 *a) Potential scan for CV; b) Voltammogram obtained from CV.*

The application of potential pulses over a linear or step-wise potential sweep is at the base of pulse voltammetry. Normal pulse voltammetry (NPV), differential pulse voltammetry (DPV) and square wave voltammetry (SWV) belong to this group of techniques. Pulse voltammetry allows to greatly enhance sensitivity by removing background capacitive current.[202]

In NPV a series of potential pulses of increasing amplitude are applied over a period of time and current is sampled at the end of each pulse, where capacitive current decays, isolating only the faradaic contribution. DPV is based on a similar series of potential pulses, however the amplitude of pulses is constant and small (10 to 100 mV), and is superimposed on a gradient of potential (which could be a linear sweep). In the case of DPV, current is sampled before and at the end of each pulse and the subtraction between the two currents allows eliminating the contribution of non-faradaic current. Finally, SWV is based on the application of symmetrical square-wave pulses superimposed on a staircase potential scan, and current is measured as the difference between the forward current and the reverse current of each

pulse. **Figure 14** illustrates the potential scan for DPV (**Figure 14a**) and the obtained voltammogram (**Figure 14b**).

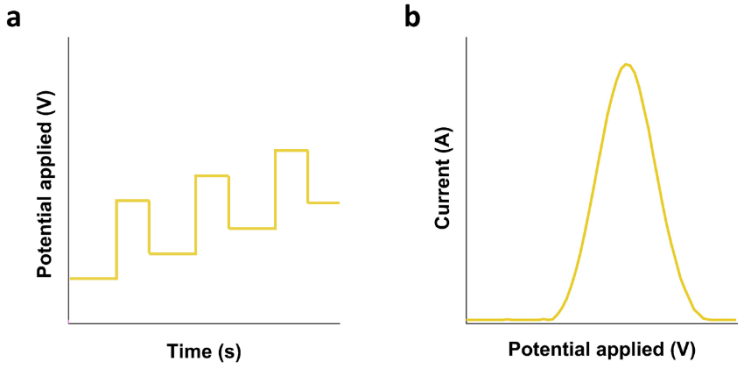

Figure 12 *a) Potential scan for DPV; b) Voltammogram obtained from DPV.*

While LSV and CV are useful tools for exploration of electrochemical properties and definition of the electrochemical system, pulse voltammetry techniques offer the best performances for sensing and biosensing, thanks to their superior sensitivity, higher resolution and accuracy.[203–205]

1.5.2 Chronoamperometry

Chronoamperometry is part of the voltammetric techniques, as it exploits the same working principles: a potential-dependent current that is function of the concentration of a species is measured upon application of a potential. The difference with the other voltammetric techniques is that the working potential here is constant and not scanned over time (**Figure 15a**).[206] In chronoamperometry, current is displayed against time instead of voltage, and is dependent only on the concentration of an electroactive species at electrode surface. The obtained graph is called amperogram and its shape depends on the experimental setup used for the measurement.

When amperometric measurements are carried out in continuum, in an electrochemical cell, and the analyte is added in small aliquots overtime, the obtained amperogram presents a typical staircase trend (**Figure 15b**). Alternatively, amperometry can be implemented in a flow system, for example as a detection technique for liquid chromatography[207] and the

resultant amperogram is characterized by the presence of peaks with intensity directly proportional to analyte concentration (**Figure 15c**).

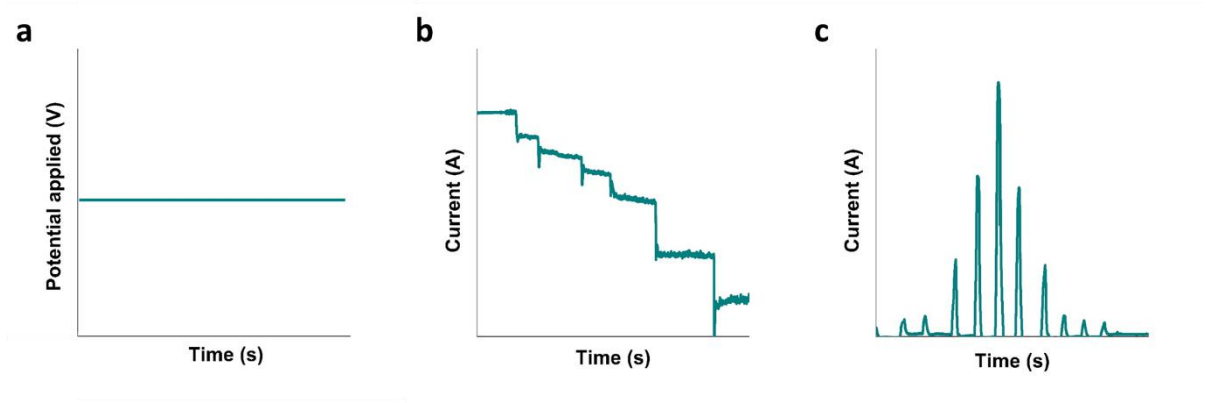

Figure 13 *a) Potential vs time for amperometry; b) Staircase amperogram (for a reduction reaction); c) Flow amperogram.*

1.5.3 Electrochemical Impedance Spectroscopy

Electrochemical systems can be complex and challenging to fully comprehend because of the various electrical and electrochemical processes that might happen at a given time. Upon application of voltage at the surface of an electrode, polarization, charging, faradaic and diffusion processes are triggered, and the measured current is a sum of all these contributions. In direct current systems, it is not possible to discern all these components of the measured signal. However, alternate current techniques, and specifically electrochemical impedance spectroscopy (EIS), are a powerful tool to deepen the understanding of an electrochemical system.[208]

EIS is an electrochemical technique in which a potentiostat applies a sinusoidal potential or current to an electrochemical system and detects the corresponding sinusoidal current or potential as a response. The approach is known as potentiostatic EIS when a sinusoidal potential is applied to produce a sinusoidal current (**Figure 16**); in the opposite situation, it is known as galvanostatic EIS.

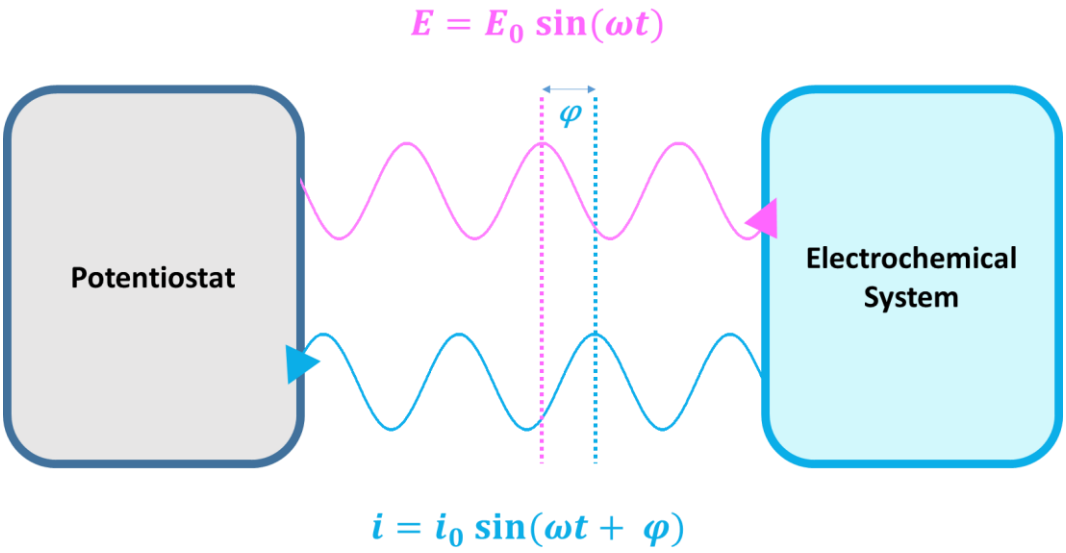

Figure 14 *Scheme of potentiostatic EIS measurement.*

The input and the output signal are both time-dependent by the same angular frequency ω and are characterized by an amplitude (E_0 and i_0). The output current wave may be offset from the sinusoidal function of the applied potential, by a phase shift or phase angle (φ).

In direct current systems, the ratio between E and i is defined by Ohm's law through a constant of proportionality that is the electric resistance, R. However, in alternate current system the resistance is replaced by a more generic term, which is electrical impedance, Z.

Impedance is the total opposition presented by an electrical circuit to alternating current and it includes the effect of classic resistors as well as other circuit elements like inductors and capacitors. From its definition, it is derived as it follows:

Equation 1 $$E = E_0 \sin(\omega t)$$

Equation 2 $$i = i_0 \sin(\omega t + \varphi)$$

Equation 3 $$Z = \frac{E}{i} = \frac{E_0 \sin(\omega t)}{i_0 \sin(\omega t + \varphi)} = Z_0 \frac{\sin(\omega t)}{\sin(\omega t + \varphi)}$$

Impedance therefore is expressed in terms of a magnitude Z_0 and phase shift φ and depends on ωt. Total impedance is the sum of all impedances of the system, which, in the case of an electrochemical cell, are related to different processes.

The difficulty in identifying the individual components stems from the near simultaneous occurrence of these events. However, what differentiates different electrochemical and electrical phenomena occurring in the electrochemical cell and at the surface of the electrode

is the different timescale at which they happen. For instance, it usually takes a tens of femtoseconds for charge transfer at the electrode interface,[209] while diffusion of species from bulk of solution is much slower, taking up to several seconds.

The Fourier transform allows moving from the time domain to the frequency domain, so that is possible to isolate single processes based on their timescale. By collecting data at different frequencies and performing a Fourier transform, it is possible to determine both E and i as functions of ω (**Figure17**). For each frequency, Z is determined as the ratio between E and i.

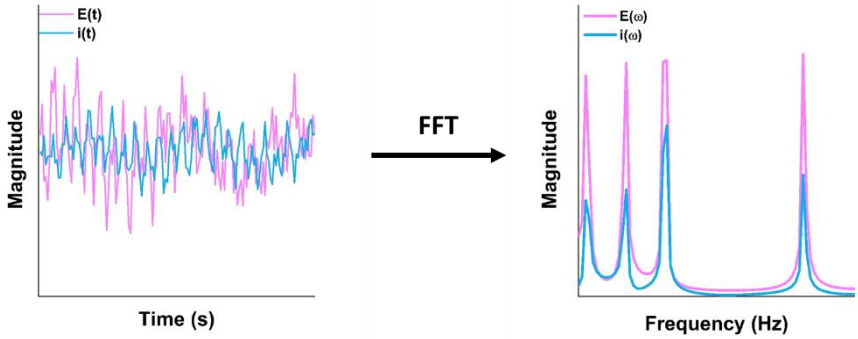

Figure 15 *Fast Fourier transform of EIS data, from time domain to frequency domain.*

There are different ways to represent EIS data. It is possible to plot the sinusoidal function of the current against the sinusoidal function of the potential to obtain the Lissajous plot. This plot gives information on the phase angle: when φ = 0°, the Lissajous plot consists of a straight line, while if the potential and the current are out of phase, its shape changes to a tilted ellipsis and finally to a perfect circle for φ = 90° (**Figure 18a**).

Data in the frequency domain can be represented with the Bode plot, in which both impedance magnitude Z and phase angle φ are reported as function of the applied frequency ω, displayed in logarithmic scale (**Figure 18b**).

Impedance can be expressed as a complex number, with a real component Z' and an imaginary one Z'', using Euler's formula:

$$\textbf{Equation 4} \quad e^{jx} = \cos x + j \sin x$$

By substituting x with $\omega t + \varphi$ and applying the Euler's formula to equations 1 and 2, it is possible to derive **equation 5**:

Equation 5 $Z = |Z|(\cos\varphi + j\sin\varphi)$

Where impedance Z is defined as linear combination of two components: real impedance ($Z' = |Z|\cos\varphi$) and imaginary impedance ($Z'' = |Z|\sin\varphi$).

Nyquist plot displays real impedance Z' on the x-axis and the negative imaginary impedance $-Z''$ on the y-axis (**Figure 18c**). The negative sign conventionally is used for the imaginary component because values of Z'' are normally less than zero. Moreover, by convention, Nyquist plot must be orthonormal. The various electrochemical and electrical processes that occur in the electrochemical system determine the shape of the Nyquist plot, and by opportune fitting, a significant quantity of valuable data can be extracted from it.

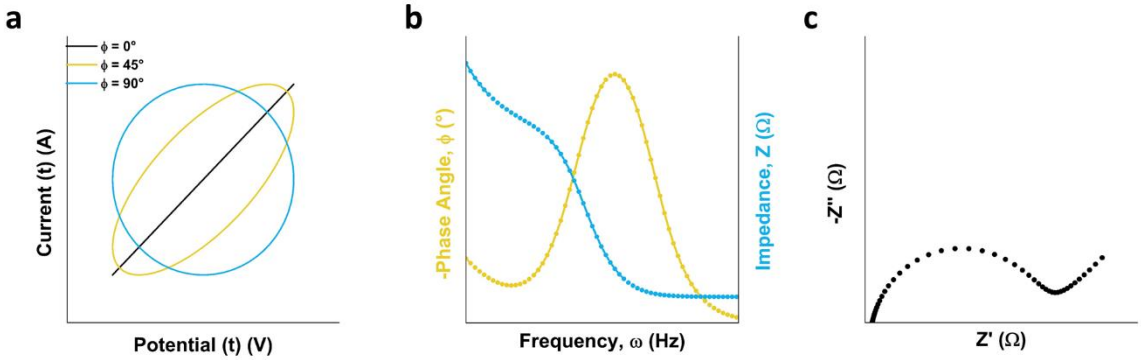

Figure 16 *Representation of EIS data. a) Lissajous plot of spectra with different phase angles, b) Bode plot and c) Nyquist plot.*

Analysis and interpretation of EIS spectra involve mathematical fitting of the data with circuit elements that model different components of the electrochemical system. Some of the most commonly used circuit elements are reported in **Table 1**.

Table 1 *Some known circuit elements used for fitting of EIS.*

Circuit Element	Symbol Used	Modelled Electrochemical Process
Resistor (R)		Resistance to charge transfer at the electrode-electrolyte interface; intrinsic resistance of the electrolyte.
Capacitor (C)		Electrical double layer charging; non-faradaic charging processes.
Constant Phase Element (CPE or Q)		Non-ideal capacitors.
Inductor (L)		Magnetic inductance.
Warburg Impedance (W)	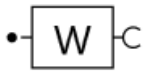	Diffusion processes in liquid phases, from bulk to electrode's surface.

These circuit elements are arranged in model circuits, simulating the whole electrochemical system. The most used circuit is Randles circuit (**Figure 19**), consisting of a resistor that models the electrolyte ionic resistance (R_S), connected in series to the parallel combination of a capacitor or a constant phase element for the double-layer charging and a resistance for the charge transfer associated with a redox reaction (R_{CT}).[210] The R_{CT} can be accompanied by a Warburg impedance, which takes into account the diffusion of the electroactive species to the surface of the electrode at low frequencies.

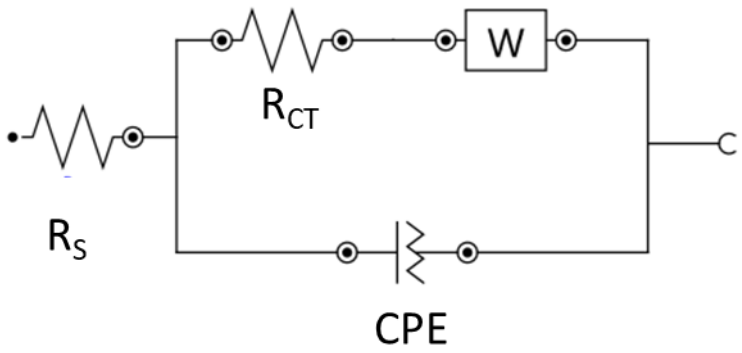

Figure 17 *Randles circuit.*

The fitting software uses the tentative circuit chosen to model the system, to perform the fitting. Finally, a value of impedance (as resistance, capacitance, etc.) is attributed to each circuit element. These data give precious insight on the processes that are taking place: for example, R_{CT} is correlated with kinetics of electrochemical processes, as lower values of R_{CT} mean higher current densities and faster reactions.[211]

1.6 References

(1) Maduraiveeran, G.; Jin, W. Nanomaterials Based Electrochemical Sensor and Biosensor Platforms for Environmental Applications. *Trends in Environmental Analytical Chemistry* **2017**, *13*, 10–23. https://doi.org/10.1016/j.teac.2017.02.001.

(2) Karthik, V.; Selvakumar, P.; Senthil Kumar, P.; Satheeskumar, V.; Godwin Vijaysunder, M.; Hariharan, S.; Antony, K. Recent Advances in Electrochemical Sensor Developments for Detecting Emerging Pollutant in Water Environment. *Chemosphere* **2022**, *304*, 135331. https://doi.org/10.1016/j.chemosphere.2022.135331.

(3) Campuzano, S.; Pedrero, M.; Yáñez-Sedeño, P.; Pingarrón, J. M. New Challenges in Point of Care Electrochemical Detection of Clinical Biomarkers. *Sensors and Actuators B: Chemical* **2021**, *345*, 130349. https://doi.org/10.1016/j.snb.2021.130349.

(4) Zhang, Z.; Sen, P.; Adhikari, B. R.; Li, Y.; Soleymani, L. Development of Nucleic-Acid-Based Electrochemical Biosensors for Clinical Applications. *Angewandte Chemie* **2022**, *134* (50), e202212496. https://doi.org/10.1002/ange.202212496.

(5) Li, T.; Shang, D.; Gao, S.; Wang, B.; Kong, H.; Yang, G.; Shu, W.; Xu, P.; Wei, G. Two-Dimensional Material-Based Electrochemical Sensors/Biosensors for Food Safety and Biomolecular Detection. *Biosensors* **2022**, *12* (5), 314. https://doi.org/10.3390/bios12050314.

(6) Gu, Y.; Li, Y.; Ren, D.; Sun, L.; Zhuang, Y.; Yi, L.; Wang, S. Recent Advances in Nanomaterial-Assisted Electrochemical Sensors for Food Safety Analysis. *Food Frontiers* **2022**, *3* (3), 453–479. https://doi.org/10.1002/fft2.143.

(7) Byakodi, M.; Shrikrishna, N. S.; Sharma, R.; Bhansali, S.; Mishra, Y.; Kaushik, A.; Gandhi, S. Emerging 0D, 1D, 2D, and 3D Nanostructures for Efficient Point-of-Care Biosensing. *Biosensors and Bioelectronics: X* **2022**, *12*, 100284. https://doi.org/10.1016/j.biosx.2022.100284.

(8) Spicuzza, L.; Campagna, D.; Maria, C. D.; Sciacca, E.; Mancuso, S.; Vancheri, C.; Sambataro, G.; Spicuzza, L.; Campagna, D.; Maria, C. D.; Sciacca, E.; Mancuso, S.; Vancheri, C.; Sambataro, G. An Update on Lateral Flow Immunoassay for the Rapid Detection of

SARS-CoV-2 Antibodies. *AIMSMICRO* **2023**, *9* (2), 375–401. https://doi.org/10.3934/microbiol.2023020.

(9) WHO-2019-nCoV-Ag-RDTs-Self-Testing-2022.1-Ara.Pdf.

(10) Kaittanis, C.; Santra, S.; Perez, J. M. Emerging Nanotechnology-Based Strategies for the Identification of Microbial Pathogenesis. *Advanced Drug Delivery Reviews* **2010**, *62* (4), 408–423. https://doi.org/10.1016/j.addr.2009.11.013.

(11) Keys, P. W.; Galaz, V.; Dyer, M.; Matthews, N.; Folke, C.; Nyström, M.; Cornell, S. E. Anthropocene Risk. *Nat Sustain* **2019**, *2* (8), 667–673. https://doi.org/10.1038/s41893-019-0327-x.

(12) Ruddiman, W. F. The Anthropocene. *Annual Review of Earth and Planetary Sciences* **2013**, *41* (Volume 41, 2013), 45–68. https://doi.org/10.1146/annurev-earth-050212-123944.

(13) Li, Z.; Xu, D.; Zhang, D.; Yamaguchi, Y. A Portable Instrument for On-Site Detection of Heavy Metal Ions in Water. *Anal Bioanal Chem* **2021**, *413* (13), 3471–3477. https://doi.org/10.1007/s00216-021-03292-w.

(14) Niu, K.; Zuo, Z.; Lu, X.; Zou, L.; Chen, J. Ultrathin Graphdiyne Nanosheets Confining Cu Quantum Dots as Robust Electrocatalyst for Biosensing Featuring Remarkably Enhanced Activity and Stability. *Biosensors and Bioelectronics* **2022**, *205*, 114111. https://doi.org/10.1016/j.bios.2022.114111.

(15) Ayankojo, A. G.; Reut, J.; Öpik, A.; Syritski, V. Sulfamethizole-Imprinted Polymer on Screen-Printed Electrodes: Towards the Design of a Portable Environmental Sensor. *Sensors and Actuators B: Chemical* **2020**, *320*, 128600. https://doi.org/10.1016/j.snb.2020.128600.

(16) Mishra, V. N.; Agarwal, R. P. Sensitivity, Response and Recovery Time of SnO2 Based Thick-Film Sensor Array for H2, CO, CH4 and LPG. *Microelectronics Journal* **1998**, *29* (11), 861–874. https://doi.org/10.1016/S0026-2692(98)00019-6.

(17) Persaud, K.; Dodd, G. Analysis of Discrimination Mechanisms in the Mammalian Olfactory System Using a Model Nose. *Nature* **1982**, *299* (5881), 352–355. https://doi.org/10.1038/299352a0.

(18) Mohan, B.; Priyanka; Singh, G.; Chauhan, A.; Pombeiro, A. J. L.; Ren, P. Metal-Organic Frameworks (MOFs) Based Luminescent and Electrochemical Sensors for Food Contaminant Detection. *Journal of Hazardous Materials* **2023**, *453*, 131324. https://doi.org/10.1016/j.jhazmat.2023.131324.

(19) Hulanicki, A.; Glab, S.; Ingman, F. Chemical Sensors: Definitions and Classification. *Pure and Applied Chemistry* **1991**, *63* (9), 1247–1250. https://doi.org/10.1351/pac199163091247.

(20) Hernández-Rodríguez, J. F.; Rojas, D.; Escarpa, A. Electrochemical Sensing Directions for Next-Generation Healthcare: Trends, Challenges, and Frontiers. *Anal. Chem.* **2021**, *93* (1), 167–183. https://doi.org/10.1021/acs.analchem.0c04378.

(21) Mahato, K.; Wang, J. Electrochemical Sensors: From the Bench to the Skin. *Sensors and Actuators B: Chemical* **2021**, *344*, 130178. https://doi.org/10.1016/j.snb.2021.130178.

(22) Wang, J. Decentralized Electrochemical Monitoring of Trace Metals: From Disposable Strips to Remote Electrodes. Plenary Lecture. *Analyst* **1994**, *119* (5), 763–766. https://doi.org/10.1039/AN9941900763.

(23) Balasubramanian, K.; Burghard, M. Biosensors Based on Carbon Nanotubes. *Anal Bioanal Chem* **2006**, *385* (3), 452–468. https://doi.org/10.1007/s00216-006-0314-8.

(24) Silvestri, A.; Wetzl, C.; Alegret, N.; Cardo, L.; Hou, H.-L.; Criado, A.; Prato, M. The Era of Nano-Bionic: 2D Materials for Wearable and Implantable Body Sensors. *Advanced Drug Delivery Reviews* **2022**, *186*, 114315. https://doi.org/10.1016/j.addr.2022.114315.

(25) Ezhil Vilian, A. T.; Mohammadi, A.; Han, S.; Tiwari, J. N.; Kumar, K.; Senthil Kumar, A.; Saravanan, A.; Huh, Y. S.; Han, Y.-K. Gold Nanoclusters Supported Molybdenum Diselenide-Porous Carbon Composite as an Efficient Electrocatalyst for Selective Ultrafast Probing of Chlorpyrifos-Pesticide. *Chemical Engineering Journal* **2023**, *472*, 145048. https://doi.org/10.1016/j.cej.2023.145048.

(26) Dinh, N. X.; Pham, T. N.; Huy, T. Q.; Trung, D. Q.; Tuan, P. A.; Khue, V. Q.; Quy, N. V.; Le, V. P.; Lam, V. D.; Le, A.-T. Ultrasensitive Determination of Chloramphenicol in Pork and Chicken Meat Samples Using a Portable Electrochemical Sensor: Effects of 2D Nanomaterials on the Sensing Performance and Stability. *New J. Chem.* **2021**, *45* (17), 7622–7636. https://doi.org/10.1039/D1NJ00582K.

(27) Liao, J.; Chang, F.; Han, X.; Ge, C.; Lin, S. Wireless Water Quality Monitoring and Spatial Mapping with Disposable Whole-Copper Electrochemical Sensors and a Smartphone. *Sensors and Actuators B: Chemical* **2020**, *306*, 127557. https://doi.org/10.1016/j.snb.2019.127557.

(28) Huang, L.; Sun, H.; Li, W.; Zhang, J.; Feng, S.; Lu, Q.; Wang, T.; Liang, X.; Liu, F.; Liu, F.; Lu, G. Pt Loading of Phosphorus-Doped Carbon Nanotube Aerogels in Fuel Cell-Type Gas Sensors for Ultrasensitive H2 Detection. *ACS Sens.* **2024**, *9* (7), 3763–3772. https://doi.org/10.1021/acssensors.4c00948.

(29) Kaur, H.; Siwal, S. S.; Saini, R. V.; Singh, N.; Thakur, V. K. Significance of an Electrochemical Sensor and Nanocomposites: Toward the Electrocatalytic Detection of Neurotransmitters and Their Importance within the Physiological System. *ACS Nanosci. Au* **2023**, *3* (1), 1–27. https://doi.org/10.1021/acsnanoscienceau.2c00039.

(30) Iglesias-Mayor, A.; Amor-Gutiérrez, O.; Novelli, A.; Fernández-Sánchez, M.-T.; Costa-García, A.; de la Escosura-Muñiz, A. Bifunctional Au@Pt/Au Core@shell Nanoparticles As Novel Electrocatalytic Tags in Immunosensing: Application for Alzheimer's Disease Biomarker Detection. *Anal. Chem.* **2020**, *92* (10), 7209–7217. https://doi.org/10.1021/acs.analchem.0c00760.

(31) Ding, H.; Yang, L.; Jia, H.; Fan, D.; Zhang, Y.; Sun, X.; Wei, Q.; Ju, H. Label-Free Electrochemical Immunosensor with Palladium Nanoparticles Functionalized MoS2/NiCo Heterostructures for Sensitive Procalcitonin Detection. *Sensors and Actuators B: Chemical* **2020**, *312*, 127980. https://doi.org/10.1016/j.snb.2020.127980.

(32) Paras; Yadav, K.; Kumar, P.; Teja, D. R.; Chakraborty, S.; Chakraborty, M.; Mohapatra, S. S.; Sahoo, A.; Chou, M. M. C.; Liang, C.-T.; Hang, D.-R. A Review on Low-Dimensional Nanomaterials: Nanofabrication, Characterization and Applications. *Nanomaterials* **2023**, *13* (1), 160. https://doi.org/10.3390/nano13010160.

(33) Ebbesen, T. W.; Lezec, H. J.; Hiura, H.; Bennett, J. W.; Ghaemi, H. F.; Thio, T. Electrical Conductivity of Individual Carbon Nanotubes. *Nature* **1996**, *382* (6586), 54–56. https://doi.org/10.1038/382054a0.

(34) Salvetat, J.-P.; Bonard, J.-M.; Thomson, N. H.; Kulik, A. J.; Forró, L.; Benoit, W.; Zuppiroli, L. Mechanical Properties of Carbon Nanotubes. *Appl Phys A* **1999**, *69* (3), 255–260. https://doi.org/10.1007/s003390050999.

(35) Treacy, M. M. J.; Ebbesen, T. W.; Gibson, J. M. Exceptionally High Young's Modulus Observed for Individual Carbon Nanotubes. *Nature* **1996**, *381* (6584), 678–680. https://doi.org/10.1038/381678a0.

(36) Geim, A. K. Graphene: Status and Prospects. *Science* **2009**, *324* (5934), 1530–1534. https://doi.org/10.1126/science.1158877.

(37) Manzeli, S.; Ovchinnikov, D.; Pasquier, D.; Yazyev, O. V.; Kis, A. 2D Transition Metal Dichalcogenides. *Nat Rev Mater* **2017**, *2* (8), 1–15. https://doi.org/10.1038/natrevmats.2017.33.

(38) Pinilla, S.; Coelho, J.; Li, K.; Liu, J.; Nicolosi, V. Two-Dimensional Material Inks. *Nat Rev Mater* **2022**, *7* (9), 717–735. https://doi.org/10.1038/s41578-022-00448-7.

(39) Mekuye, B.; Abera, B. Nanomaterials: An Overview of Synthesis, Classification, Characterization, and Applications. *Nano Select* **2023**, *4* (8), 486–501. https://doi.org/10.1002/nano.202300038.

(40) Koch, C. C. Nanostructured Materials: An Overview. In *Bulk Nanostructured Materials*; John Wiley & Sons, Ltd, 2009; pp 1–20. https://doi.org/10.1002/9783527626892.ch1.

(41) Anu Prathap, M. U.; Kaur, B.; Srivastava, R. Electrochemical Sensor Platforms Based on Nanostructured Metal Oxides, and Zeolite-Based Materials. *The Chemical Record* **2019**, *19* (5), 883–907. https://doi.org/10.1002/tcr.201800068.

(42) Giménez-Marqués, M.; Hidalgo, T.; Serre, C.; Horcajada, P. Nanostructured Metal–Organic Frameworks and Their Bio-Related Applications. *Coordination Chemistry Reviews* **2016**, *307*, 342–360. https://doi.org/10.1016/j.ccr.2015.08.008.

(43) Waller, P. J.; Gándara, F.; Yaghi, O. M. Chemistry of Covalent Organic Frameworks. *Acc. Chem. Res.* **2015**, *48* (12), 3053–3063. https://doi.org/10.1021/acs.accounts.5b00369.

(44) Tan, K. T.; Ghosh, S.; Wang, Z.; Wen, F.; Rodríguez-San-Miguel, D.; Feng, J.; Huang, N.; Wang, W.; Zamora, F.; Feng, X.; Thomas, A.; Jiang, D. Covalent Organic Frameworks. *Nat Rev Methods Primers* **2023**, *3* (1), 1–19. https://doi.org/10.1038/s43586-022-00181-z.

(45) Duclos, S. J.; Brister, K.; Haddon, R. C.; Kortan, A. R.; Thiel, F. A. Effects of Pressure and Stress on C60 Fullerite to 20 GPa. *Nature* **1991**, *351* (6325), 380–382. https://doi.org/10.1038/351380a0.

(46) Ma, C.; Wu, L.; Dirican, M.; Cheng, H.; Li, J.; Song, Y.; Shi, J.; Zhang, X. Carbon Black-Based Porous Sub-Micron Carbon Fibers for Flexible Supercapacitors. *Applied Surface Science* **2021**, *537*, 147914. https://doi.org/10.1016/j.apsusc.2020.147914.

(47) Vicentini, F. C.; Raymundo-Pereira, P. A.; Janegitz, B. C.; Machado, S. A. S.; Fatibello-Filho, O. Nanostructured Carbon Black for Simultaneous Sensing in Biological Fluids. *Sensors and Actuators B: Chemical* **2016**, *227*, 610–618. https://doi.org/10.1016/j.snb.2015.12.094.

(48) Schütt, F.; Signetti, S.; Krüger, H.; Röder, S.; Smazna, D.; Kaps, S.; Gorb, S. N.; Mishra, Y. K.; Pugno, N. M.; Adelung, R. Hierarchical Self-Entangled Carbon Nanotube Tube Networks. *Nat Commun* **2017**, *8* (1), 1215. https://doi.org/10.1038/s41467-017-01324-7.

(49) Kwon, O. S.; Song, H. S.; Park, T. H.; Jang, J. Conducting Nanomaterial Sensor Using Natural Receptors. *Chem. Rev.* **2019**, *119* (1), 36–93. https://doi.org/10.1021/acs.chemrev.8b00159.

(50) Kroto, H. W.; Heath, J. R.; O'Brien, S. C.; Curl, R. F.; Smalley, R. E. C60: Buckminsterfullerene. *Nature* **1985**, *318* (6042), 162–163. https://doi.org/10.1038/318162a0.

(51) Iijima, S. Carbon Nanotubes. *MRS Bulletin* **1994**, *19* (11), 43–49. https://doi.org/10.1557/S0883769400048405.

(52) Novoselov, K. S.; Geim, A. K.; Morozov, S. V.; Jiang, D.; Zhang, Y.; Dubonos, S. V.; Grigorieva, I. V.; Firsov, A. A. Electric Field Effect in Atomically Thin Carbon Films. *Science* **2004**, *306* (5696), 666–669. https://doi.org/10.1126/science.1102896.

(53) De Volder, M. F. L.; Tawfick, S. H.; Baughman, R. H.; Hart, A. J. Carbon Nanotubes: Present and Future Commercial Applications. *Science* **2013**, *339* (6119), 535–539. https://doi.org/10.1126/science.1222453.

(54) Iijima, S. Helical Microtubules of Graphitic Carbon. *Nature* **1991**, *354* (6348), 56–58. https://doi.org/10.1038/354056a0.

(55) Yellampalli, S. *Carbon Nanotubes: Synthesis, Characterization, Applications*; BoD – Books on Demand, 2011.

(56) Journet, C.; Bernier, P. Production of Carbon Nanotubes.

(57) Morales, A. M.; Lieber, C. M. A Laser Ablation Method for the Synthesis of Crystalline Semiconductor Nanowires. *Science* **1998**, *279* (5348), 208–211. https://doi.org/10.1126/science.279.5348.208.

(58) Lavagna, L.; Nisticò, R.; Musso, S.; Pavese, M. Functionalization as a Way to Enhance Dispersion of Carbon Nanotubes in Matrices: A Review. *Materials Today Chemistry* **2021**, *20*, 100477. https://doi.org/10.1016/j.mtchem.2021.100477.

(59) See, C. H.; Harris, A. T. A Comparison of Carbon Nanotube Synthesis in Fixed and Fluidised Bed Reactors. *Chemical Engineering Journal* **2008**, *144* (2), 267–269. https://doi.org/10.1016/j.cej.2008.06.002.

(60) Choi, Y. C.; Shin, Y. M.; Lee, Y. H.; Lee, B. S.; Park, G.-S.; Choi, W. B.; Lee, N. S.; Kim, J. M. Controlling the Diameter, Growth Rate, and Density of Vertically Aligned Carbon Nanotubes Synthesized by Microwave Plasma-Enhanced Chemical Vapor Deposition. *Applied Physics Letters* **2000**, *76* (17), 2367–2369. https://doi.org/10.1063/1.126348.

(61) Speranza, G. Carbon Nanomaterials: Synthesis, Functionalization and Sensing Applications. *Nanomaterials* **2021**, *11* (4), 967. https://doi.org/10.3390/nano11040967.

(62) Liu, H.; Nishide, D.; Tanaka, T.; Kataura, H. Large-Scale Single-Chirality Separation of Single-Wall Carbon Nanotubes by Simple Gel Chromatography. *Nat Commun* **2011**, *2* (1), 309. https://doi.org/10.1038/ncomms1313.

(63) Yang, F.; Wang, M.; Zhang, D.; Yang, J.; Zheng, M.; Li, Y. Chirality Pure Carbon Nanotubes: Growth, Sorting, and Characterization. *Chem. Rev.* **2020**, *120* (5), 2693–2758. https://doi.org/10.1021/acs.chemrev.9b00835.

(64) Yang, D.; Li, L.; Li, X.; Xi, W.; Zhang, Y.; Liu, Y.; Wei, X.; Zhou, W.; Wei, F.; Xie, S.; Liu, H. Preparing High-Concentration Individualized Carbon Nanotubes for Industrial Separation of Multiple Single-Chirality Species. *Nat Commun* **2023**, *14* (1), 2491. https://doi.org/10.1038/s41467-023-38133-0.

(65) Yomogida, Y.; Tanaka, T.; Zhang, M.; Yudasaka, M.; Wei, X.; Kataura, H. Industrial-Scale Separation of High-Purity Single-Chirality Single-Wall Carbon Nanotubes for Biological Imaging. *Nat Commun* **2016**, *7* (1), 12056. https://doi.org/10.1038/ncomms12056.

(66) Li, Q. W.; Li, Y.; Zhang, X. F.; Chikkannanavar, S. B.; Zhao, Y. H.; Dangelewicz, A. M.; Zheng, L. X.; Doorn, S. K.; Jia, Q. X.; Peterson, D. E.; Arendt, P. N.; Zhu, Y. T. Structure-Dependent Electrical Properties of Carbon Nanotube Fibers. *Advanced Materials* **2007**, *19* (20), 3358–3363. https://doi.org/10.1002/adma.200602966.

(67) Dyke, C. A.; Tour, J. M. Overcoming the Insolubility of Carbon Nanotubes Through High Degrees of Sidewall Functionalization. *Chemistry – A European Journal* **2004**, *10* (4), 812–817. https://doi.org/10.1002/chem.200305534.

(68) Tasis, D.; Tagmatarchis, N.; Georgakilas, V.; Prato, M. Soluble Carbon Nanotubes. *Chemistry – A European Journal* **2003**, *9* (17), 4000–4008. https://doi.org/10.1002/chem.200304800.

(69) Dossot, M.; Gardien, F.; Mamane, V.; Fort, Y.; Liu, J.; Vigolo, B.; Humbert, B.; McRae, E. Optical Parameter to Reveal the Interplay between Covalent Functionalization and the State of Aggregation of Single-Walled Carbon Nanotubes. *J. Phys. Chem. C* **2007**, *111* (33), 12199–12206. https://doi.org/10.1021/jp0719210.

(70) Lin, Y.; Meziani, M. J.; Sun, Y.-P. Functionalized Carbon Nanotubes for Polymeric Nanocomposites. *J. Mater. Chem.* **2007**, *17* (12), 1143–1148. https://doi.org/10.1039/B618344A.

(71) Sahoo, N. G.; Rana, S.; Cho, J. W.; Li, L.; Chan, S. H. Polymer Nanocomposites Based on Functionalized Carbon Nanotubes. *Progress in Polymer Science* **2010**, *35* (7), 837–867. https://doi.org/10.1016/j.progpolymsci.2010.03.002.

(72) Sun, Y.-P.; Fu, K.; Lin, Y.; Huang, W. Functionalized Carbon Nanotubes: Properties and Applications. *Acc. Chem. Res.* **2002**, *35* (12), 1096–1104. https://doi.org/10.1021/ar010160v.

(73) Shim, M.; Shi Kam, N. W.; Chen, R. J.; Li, Y.; Dai, H. Functionalization of Carbon Nanotubes for Biocompatibility and Biomolecular Recognition. *Nano Lett.* **2002**, *2* (4), 285–288. https://doi.org/10.1021/nl015692j.

(74) Ménard-Moyon, C.; Kostarelos, K.; Prato, M.; Bianco, A. Functionalized Carbon Nanotubes for Probing and Modulating Molecular Functions. *Chemistry & Biology* **2010**, *17* (2), 107–115. https://doi.org/10.1016/j.chembiol.2010.01.009.

(75) Singh, P.; Campidelli, S.; Giordani, S.; Bonifazi, D.; Bianco, A.; Prato, M. Organic Functionalisation and Characterisation of Single-Walled Carbon Nanotubes. *Chem. Soc. Rev.* **2009**, *38* (8), 2214–2230. https://doi.org/10.1039/B518111A.

(76) Crescenzo, A. D.; Ettorre, V.; Fontana, A. Non-Covalent and Reversible Functionalization of Carbon Nanotubes. *Beilstein J. Nanotechnol.* **2014**, *5* (1), 1675–1690. https://doi.org/10.3762/bjnano.5.178.

(77) Tuncel, D. Non-Covalent Interactions between Carbon Nanotubes and Conjugated Polymers. *Nanoscale* **2011**, *3* (9), 3545–3554. https://doi.org/10.1039/C1NR10338E.

(78) Ajayan, P. M.; Ebbesen, T. W.; Ichihashi, T.; Iijima, S.; Tanigaki, K.; Hiura, H. Opening Carbon Nanotubes with Oxygen and Implications for Filling. *Nature* **1993**, *362* (6420), 522–525. https://doi.org/10.1038/362522a0.

(79) Tohji, K.; Goto, T.; Takahashi, H.; Shinoda, Y.; Shimizu, N.; Jeyadevan, B.; Matsuoka, I.; Saito, Y.; Kasuya, A.; Ohsuna, T.; Hiraga, K.; Nishina, Y. Purifying Single-Walled Nanotubes. *Nature* **1996**, *383* (6602), 679–679. https://doi.org/10.1038/383679a0.

(80) Misia, G.; Evangelisti, C.; Merino, J. P.; Pitzalis, E.; Abelairas, A. M.; Mosquera, J.; Criado, A.; Prato, M.; Silvestri, A. Design and Optimization of an Electrochemical Sensor Based on Carbon Nanotubes for the Reliable Voltammetric Detection of Serotonin in Complex Biological Fluids. *Carbon* **2024**, *229*, 119550. https://doi.org/10.1016/j.carbon.2024.119550.

(81) Datsyuk, V.; Kalyva, M.; Papagelis, K.; Parthenios, J.; Tasis, D.; Siokou, A.; Kallitsis, I.; Galiotis, C. Chemical Oxidation of Multiwalled Carbon Nanotubes. *Carbon* **2008**, *46* (6), 833–840. https://doi.org/10.1016/j.carbon.2008.02.012.

(82) Philip, B.; Xie, J.; Chandrasekhar, A.; Abraham, J.; Varadan, V. K. A Novel Nanocomposite from Multiwalled Carbon Nanotubes Functionalized with a Conducting Polymer. *Smart Mater. Struct.* **2004**, *13* (2), 295. https://doi.org/10.1088/0964-1726/13/2/007.

(83) Niyogi, S.; Hamon, M. A.; Hu, H.; Zhao, B.; Bhowmik, P.; Sen, R.; Itkis, M. E.; Haddon, R. C. Chemistry of Single-Walled Carbon Nanotubes. *Acc. Chem. Res.* **2002**, *35* (12), 1105–1113. https://doi.org/10.1021/ar010155r.

(84) Sun, Y.-P.; Huang, W.; Lin, Y.; Fu, K.; Kitaygorodskiy, A.; Riddle, L. A.; Yu, Y. J.; Carroll, D. L. Soluble Dendron-Functionalized Carbon Nanotubes: Preparation, Characterization, and Properties,. *Chem. Mater.* **2001**, *13* (9), 2864–2869. https://doi.org/10.1021/cm010069l.

(85) Mickelson, E. T.; Huffman, C. B.; Rinzler, A. G.; Smalley, R. E.; Hauge, R. H.; Margrave, J. L. Fluorination of Single-Wall Carbon Nanotubes. *Chemical Physics Letters* **1998**, *296* (1), 188–194. https://doi.org/10.1016/S0009-2614(98)01026-4.

(86) Lu, X.; Tian, F.; Wang, N.; Zhang, Q. Organic Functionalization of the Sidewalls of Carbon Nanotubes by Diels–Alder Reactions: A Theoretical Prediction. *Org. Lett.* **2002**, *4* (24), 4313–4315. https://doi.org/10.1021/ol026956r.

(87) Lu, X.; Tian, F.; Xu, X.; Wang, N.; Zhang, Q. A Theoretical Exploration of the 1,3-Dipolar Cycloadditions onto the Sidewalls of (n,n) Armchair Single-Wall Carbon Nanotubes. *J. Am. Chem. Soc.* **2003**, *125* (34), 10459–10464. https://doi.org/10.1021/ja034662a.

(88) Delgado, J. L.; Cruz, P. de la; Langa, F.; Urbina, A.; Casado, J.; Navarrete, J. T. L. Microwave-Assisted Sidewall Functionalization of Single-Wall Carbon Nanotubes by Diels–Alder Cycloaddition. *Chem. Commun.* **2004**, No. 15, 1734–1735. https://doi.org/10.1039/B402375G.

(89) Hirsch, A. Addition Reactions of Buckminsterfullerene (C60). *Synthesis* **1995**, *1995* (8), 895–913. https://doi.org/10.1055/s-1995-4046.

(90) Georgakilas, V.; Kordatos, K.; Prato, M.; Guldi, D. M.; Holzinger, M.; Hirsch, A. Organic Functionalization of Carbon Nanotubes. *J. Am. Chem. Soc.* **2002**, *124* (5), 760–761. https://doi.org/10.1021/ja016954m.

(91) Tasis, D.; Tagmatarchis, N.; Bianco, A.; Prato, M. Chemistry of Carbon Nanotubes. *Chem. Rev.* **2006**, *106* (3), 1105–1136. https://doi.org/10.1021/cr050569o.

(92) Bahr, J. L.; Yang, J.; Kosynkin, D. V.; Bronikowski, M. J.; Smalley, R. E.; Tour, J. M. Functionalization of Carbon Nanotubes by Electrochemical Reduction of Aryl Diazonium Salts: A Bucky Paper Electrode. *J. Am. Chem. Soc.* **2001**, *123* (27), 6536–6542. https://doi.org/10.1021/ja010462s.

(93) Marcoux, P. R.; Hapiot, P.; Batail, P.; Pinson, J. Electrochemical Functionalization of Nanotube Films: Growth of Aryl Chains on Single-Walled Carbon Nanotubes. *New J. Chem.* **2004**, *28* (2), 302–307. https://doi.org/10.1039/B309509F.

(94) Strano, M. S.; Dyke, C. A.; Usrey, M. L.; Barone, P. W.; Allen, M. J.; Shan, H.; Kittrell, C.; Hauge, R. H.; Tour, J. M.; Smalley, R. E. Electronic Structure Control of Single-Walled Carbon Nanotube Functionalization. *Science* **2003**, *301* (5639), 1519–1522. https://doi.org/10.1126/science.1087691.

(95) Salice, P.; Fabris, E.; Sartorio, C.; Fenaroli, D.; Figà, V.; Casaletto, M. P.; Cataldo, S.; Pignataro, B.; Menna, E. An Insight into the Functionalisation of Carbon Nanotubes by Diazonium Chemistry: Towards a Controlled Decoration. *Carbon* **2014**, *74*, 73–82. https://doi.org/10.1016/j.carbon.2014.02.084.

(96) Dyke, C. A.; Tour, J. M. Unbundled and Highly Functionalized Carbon Nanotubes from Aqueous Reactions. *Nano Lett.* **2003**, *3* (9), 1215–1218. https://doi.org/10.1021/nl034537x.

(97) Bahr, J. L.; Tour, J. M. Highly Functionalized Carbon Nanotubes Using in Situ Generated Diazonium Compounds. *Chem. Mater.* **2001**, *13* (11), 3823–3824. https://doi.org/10.1021/cm0109903.

(98) Mitchell, C. A.; Bahr, J. L.; Arepalli, S.; Tour, J. M.; Krishnamoorti, R. Dispersion of Functionalized Carbon Nanotubes in Polystyrene. *Macromolecules* **2002**, *35* (23), 8825–8830. https://doi.org/10.1021/ma020890y.

(99) Abiman, P.; Wildgoose, G. G.; Compton, R. G. Investigating the Mechanism for the Covalent Chemical Modification of Multiwalled Carbon Nanotubes Using Aryl Diazonium Salts. *International Journal of Electrochemical Science* **2008**, *3* (2), 104–117. https://doi.org/10.1016/S1452-3981(23)15430-7.

(100) Hudson, J. L.; Casavant, M. J.; Tour, J. M. Water-Soluble, Exfoliated, Nonroping Single-Wall Carbon Nanotubes. *J. Am. Chem. Soc.* **2004**, *126* (36), 11158–11159. https://doi.org/10.1021/ja0467061.

(101) Souza, E. L. S. de; Chorro, T. H. D.; Correia, C. R. D. Thermal Analysis of Arenediazonium Tetrafluoroborate Salts: Stability and Hazardous Evaluation. *Process Safety and Environmental Protection* **2023**, *177*, 69–81. https://doi.org/10.1016/j.psep.2023.06.082.

(102) Wetzl, C.; Silvestri, A.; Garrido, M.; Hou, H.-L.; Criado, A.; Prato, M. The Covalent Functionalization of Surface-Supported Graphene: An Update. *Angewandte Chemie* **2023**, *135* (6), e202212857. https://doi.org/10.1002/ange.202212857.

(103) Greenwood, J.; Phan, T. H.; Fujita, Y.; Li, Z.; Ivasenko, O.; Vanderlinden, W.; Van Gorp, H.; Frederickx, W.; Lu, G.; Tahara, K.; Tobe, Y.; Uji-i, H.; Mertens, S. F. L.; De Feyter, S. Covalent Modification of Graphene and Graphite Using Diazonium Chemistry: Tunable

Grafting and Nanomanipulation. *ACS Nano* **2015**, *9* (5), 5520–5535. https://doi.org/10.1021/acsnano.5b01580.

(104) Wetzl, C.; Brosel-Oliu, S.; Carini, M.; Silvio, D. D.; Illa, X.; Villa, R.; Guimera, A.; Prats-Alfonso, E.; Prato, M.; Criado, A. Covalent Functionalisation Controlled by Molecular Design for the Aptameric Recognition of Serotonin in Graphene-Based Field-Effect Transistors. *Nanoscale* **2023**, *15* (41), 16650–16657. https://doi.org/10.1039/D3NR04153K.

(105) Nakashima, N.; Tomonari, Y.; Murakami, H. Water-Soluble Single-Walled Carbon Nanotubes via Noncovalent Sidewall-Functionalization with a Pyrene-Carrying Ammonium Ion. *Chemistry Letters* **2002**, *31* (6), 638–639. https://doi.org/10.1246/cl.2002.638.

(106) Tomonari, Y.; Murakami, H.; Nakashima, N. Solubilization of Single-Walled Carbon Nanotubes by Using Polycyclic Aromatic Ammonium Amphiphiles in Water—Strategy for the Design of High-Performance Solubilizers. *Chemistry – A European Journal* **2006**, *12* (15), 4027–4034. https://doi.org/10.1002/chem.200501176.

(107) Murakami, H.; Nomura, T.; Nakashima, N. Noncovalent Porphyrin-Functionalized Single-Walled Carbon Nanotubes in Solution and the Formation of Porphyrin–Nanotube Nanocomposites. *Chemical Physics Letters* **2003**, *378* (5), 481–485. https://doi.org/10.1016/S0009-2614(03)01329-0.

(108) Rahman, G. M. A.; Guldi, D. M.; Campidelli, S.; Prato, M. Electronically Interacting Single Wall Carbon Nanotube–Porphyrin Nanohybrids. *J. Mater. Chem.* **2006**, *16* (1), 62–65. https://doi.org/10.1039/B515394H.

(109) Xu, Z.; Yang, X.; Yang, Z. A Molecular Simulation Probing of Structure and Interaction for Supramolecular Sodium Dodecyl Sulfate/Single-Wall Carbon Nanotube Assemblies. *Nano Lett.* **2010**, *10* (3), 985–991. https://doi.org/10.1021/nl9041005.

(110) Blanch, A. J.; Quinton, J. S.; Shapter, J. G. The Role of Sodium Dodecyl Sulfate Concentration in the Separation of Carbon Nanotubes Using Gel Chromatography. *Carbon* **2013**, *60*, 471–480. https://doi.org/10.1016/j.carbon.2013.04.064.

(111) Altuntas, H.; Snashall, K.; Oke-Altuntas, F.; Jayawerdane, I.; Tas, M. O.; Silva, S. R. P. Effect of Pyrene-1 Boronic Acid Functionalization on the Electrical Characteristics of Carbon Nanotube Field-Effect Transistor. *Electron. Mater. Lett.* **2023**, *19* (5), 405–414. https://doi.org/10.1007/s13391-023-00415-6.

(112) Noguchi, Y.; Fujigaya, T.; Niidome, Y.; Nakashima, N. Single-Walled Carbon Nanotubes/DNA Hybrids in Water Are Highly Stable. *Chemical Physics Letters* **2008**, *455* (4), 249–251. https://doi.org/10.1016/j.cplett.2008.02.089.

(113) Fujigaya, T.; Nakashima, N. Non-Covalent Polymer Wrapping of Carbon Nanotubes and the Role of Wrapped Polymers as Functional Dispersants. *Sci. Technol. Adv. Mater.* **2015**, *16* (2), 024802. https://doi.org/10.1088/1468-6996/16/2/024802.

(114) O'Connell, M. J.; Boul, P.; Ericson, L. M.; Huffman, C.; Wang, Y.; Haroz, E.; Kuper, C.; Tour, J.; Ausman, K. D.; Smalley, R. E. Reversible Water-Solubilization of Single-Walled Carbon Nanotubes by Polymer Wrapping. *Chemical Physics Letters* **2001**, *342* (3), 265–271. https://doi.org/10.1016/S0009-2614(01)00490-0.

(115) Nish, A.; Hwang, J.-Y.; Doig, J.; Nicholas, R. J. Highly Selective Dispersion of Single-Walled Carbon Nanotubes Using Aromatic Polymers. *Nature Nanotech* **2007**, *2* (10), 640–646. https://doi.org/10.1038/nnano.2007.290.

(116) Cataldo, S.; Salice, P.; Menna, E.; Pignataro, B. Carbon Nanotubes and Organic Solar Cells. *Energy Environ. Sci.* **2012**, *5* (3), 5919–5940. https://doi.org/10.1039/C1EE02276H.

(117) Xie, H.; Ortiz-Acevedo, A.; Zorbas, V.; Baughman, R. H.; Draper, R. K.; Musselman, I. H.; Dalton, A. B.; Dieckmann, G. R. Peptide Cross-Linking Modulated Stability and Assembly of Peptide-Wrapped Single-Walled Carbon Nanotubes. *J. Mater. Chem.* **2005**, *15* (17), 1734–1741. https://doi.org/10.1039/B413262A.

(118) Calvaresi, M.; Zerbetto, F. The Devil and Holy Water: Protein and Carbon Nanotube Hybrids. *Acc. Chem. Res.* **2013**, *46* (11), 2454–2463. https://doi.org/10.1021/ar300347d.

(119) Boghossian, A. A.; Zhang, J.; Barone, P. W.; Reuel, N. F.; Kim, J.-H.; Heller, D. A.; Ahn, J.-H.; Hilmer, A. J.; Rwei, A.; Arkalgud, J. R.; Zhang, C. T.; Strano, M. S. Near-Infrared Fluorescent Sensors Based on Single-Walled Carbon Nanotubes for Life Sciences Applications. *ChemSusChem* **2011**, *4* (7), 848–863. https://doi.org/10.1002/cssc.201100070.

(120) López-Moreno, A.; Villalva, J.; Pérez, E. M. Mechanically Interlocked Derivatives of Carbon Nanotubes: Synthesis and Potential Applications. *Chem. Soc. Rev.* **2022**, *51* (23), 9433–9444. https://doi.org/10.1039/D2CS00510G.

(121) Pérez, E. M. Putting Rings around Carbon Nanotubes. *Chemistry – A European Journal* **2017**, *23* (52), 12681–12689. https://doi.org/10.1002/chem.201702992.

(122) López-Moreno, A.; Pérez, E. M. Pyrene-Based Mechanically Interlocked SWNTs. *Chem. Commun.* **2015**, *51* (25), 5421–5424. https://doi.org/10.1039/C4CC08970G.

(123) Li, J.; Lu, Y.; Ye, Q.; Cinke, M.; Han, J.; Meyyappan, M. Carbon Nanotube Sensors for Gas and Organic Vapor Detection. *Nano Lett.* **2003**, *3* (7), 929–933. https://doi.org/10.1021/nl034220x.

(124) Kong, J.; Franklin, N. R.; Zhou, C.; Chapline, M. G.; Peng, S.; Cho, K.; Dai, H. Nanotube Molecular Wires as Chemical Sensors. *Science* **2000**, *287* (5453), 622–625. https://doi.org/10.1126/science.287.5453.622.

(125) Vena, A.; Sydänheimo, L.; Tentzeris, M. M.; Ukkonen, L. A Fully Inkjet-Printed Wireless and Chipless Sensor for CO2 and Temperature Detection. *IEEE Sensors Journal* **2015**, *15* (1), 89–99. https://doi.org/10.1109/JSEN.2014.2336838.

(126) Rahm, C. E.; Torres-Canas, F.; Gupta, P.; Poulin, P.; Alvarez, N. T. Inkjet Printed Multi-Walled Carbon Nanotube Sensor for the Detection of Lead in Drinking Water. *Electroanalysis* **2020**, *32* (7), 1533–1545. https://doi.org/10.1002/elan.202000040.

(127) Fu, D.; Lim, H.; Shi, Y.; Dong, X.; Mhaisalkar, S. G.; Chen, Y.; Moochhala, S.; Li, L.-J. Differentiation of Gas Molecules Using Flexible and All-Carbon Nanotube Devices. *J. Phys. Chem. C* **2008**, *112* (3), 650–653. https://doi.org/10.1021/jp710362r.

(128) Trojanowicz, M. Analytical Applications of Carbon Nanotubes: A Review. *TrAC Trends in Analytical Chemistry* **2006**, *25* (5), 480–489. https://doi.org/10.1016/j.trac.2005.11.008.

(129) Norizan, M. N.; Moklis, M. H.; Demon, S. Z. N.; Halim, N. A.; Samsuri, A.; Mohamad, I. S.; Knight, V. F.; Abdullah, N. Carbon Nanotubes: Functionalisation and Their Application in Chemical Sensors. *RSC Adv.* **2020**, *10* (71), 43704–43732. https://doi.org/10.1039/D0RA09438B.

(130) Li, J.; Wang, Y.-B.; Qiu, J.-D.; Sun, D.; Xia, X.-H. Biocomposites of Covalently Linked Glucose Oxidase on Carbon Nanotubes for Glucose Biosensor. *Anal Bioanal Chem* **2005**, *383* (6), 918–922. https://doi.org/10.1007/s00216-005-0106-6.

(131) Zhan, K.; Liu, H.; Zhang, H.; Chen, Y.; Ni, H.; Wu, M.; Sun, D.; Chen, Y. A Facile Method for the Immobilization of Myoglobin on Multi-Walled Carbon Nanotubes: Poly(Methacrylic Acid-Co-Acrylamide) Nanocomposite and Its Application for Direct Bio-Detection of H2O2. *Journal of Electroanalytical Chemistry* **2014**, *724*, 80–86. https://doi.org/10.1016/j.jelechem.2014.04.012.

(132) Sulleiro, M. V.; Dominguez-Alfaro, A.; Alegret, N.; Silvestri, A.; Gómez, I. J. 2D Materials towards Sensing Technology: From Fundamentals to Applications. *Sensing and Bio-Sensing Research* **2022**, *38*, 100540. https://doi.org/10.1016/j.sbsr.2022.100540.

(133) Pandhi, T.; Chandnani, A.; Subbaraman, H.; Estrada, D. A Review of Inkjet Printed Graphene and Carbon Nanotubes Based Gas Sensors. *Sensors* **2020**, *20* (19), 5642. https://doi.org/10.3390/s20195642.

(134) Cambaz, Z. G.; Yushin, G.; Osswald, S.; Mochalin, V.; Gogotsi, Y. Noncatalytic Synthesis of Carbon Nanotubes, Graphene and Graphite on SiC. *Carbon* **2008**, *46* (6), 841–849. https://doi.org/10.1016/j.carbon.2008.02.013.

(135) Somani, P. R.; Somani, S. P.; Umeno, M. Planer Nano-Graphenes from Camphor by CVD. *Chemical Physics Letters* **2006**, *430* (1), 56–59. https://doi.org/10.1016/j.cplett.2006.06.081.

(136) Kim, K. S.; Zhao, Y.; Jang, H.; Lee, S. Y.; Kim, J. M.; Kim, K. S.; Ahn, J.-H.; Kim, P.; Choi, J.-Y.; Hong, B. H. Large-Scale Pattern Growth of Graphene Films for Stretchable Transparent Electrodes. *Nature* **2009**, *457* (7230), 706–710. https://doi.org/10.1038/nature07719.

(137) Hernandez, Y.; Nicolosi, V.; Lotya, M.; Blighe, F. M.; Sun, Z.; De, S.; McGovern, I. T.; Holland, B.; Byrne, M.; Gun'Ko, Y. K.; Boland, J. J.; Niraj, P.; Duesberg, G.; Krishnamurthy, S.; Goodhue, R.; Hutchison, J.; Scardaci, V.; Ferrari, A. C.; Coleman, J. N. High-Yield Production of Graphene by Liquid-Phase Exfoliation of Graphite. *Nature Nanotech* **2008**, *3* (9), 563–568. https://doi.org/10.1038/nnano.2008.215.

(138) Eda, G.; Fanchini, G.; Chhowalla, M. Large-Area Ultrathin Films of Reduced Graphene Oxide as a Transparent and Flexible Electronic Material. *Nature Nanotech* **2008**, *3* (5), 270–274. https://doi.org/10.1038/nnano.2008.83.

(139) Torrisi, F.; Hasan, T.; Wu, W.; Sun, Z.; Lombardo, A.; Kulmala, T. S.; Hsieh, G.-W.; Jung, S.; Bonaccorso, F.; Paul, P. J.; Chu, D.; Ferrari, A. C. Inkjet-Printed Graphene Electronics. *ACS Nano* **2012**, *6* (4), 2992–3006. https://doi.org/10.1021/nn2044609.

(140) Narayan, R.; Kim, S. O. Surfactant Mediated Liquid Phase Exfoliation of Graphene. *Nano Convergence* **2015**, *2* (1), 20. https://doi.org/10.1186/s40580-015-0050-x.

(141) Nicolosi, V.; Chhowalla, M.; Kanatzidis, M. G.; Strano, M. S.; Coleman, J. N. Liquid Exfoliation of Layered Materials. *Science* **2013**, *340* (6139), 1226419. https://doi.org/10.1126/science.1226419.

(142) Zhang, L.; Zhang, Z.; He, C.; Dai, L.; Liu, J.; Wang, L. Rationally Designed Surfactants for Few-Layered Graphene Exfoliation: Ionic Groups Attached to Electron-Deficient π-Conjugated Unit through Alkyl Spacers. *ACS Nano* **2014**, *8* (7), 6663–6670. https://doi.org/10.1021/nn502289w.

(143) Lotya, M.; Hernandez, Y.; King, P. J.; Smith, R. J.; Nicolosi, V.; Karlsson, L. S.; Blighe, F. M.; De, S.; Wang, Z.; McGovern, I. T.; Duesberg, G. S.; Coleman, J. N. Liquid Phase Production

of Graphene by Exfoliation of Graphite in Surfactant/Water Solutions. *J. Am. Chem. Soc.* **2009**, *131* (10), 3611–3620. https://doi.org/10.1021/ja807449u.

(144) Soldano, C.; Mahmood, A.; Dujardin, E. Production, Properties and Potential of Graphene. *Carbon* **2010**, *48* (8), 2127–2150. https://doi.org/10.1016/j.carbon.2010.01.058.

(145) Hao, Z.; Luo, Y.; Huang, C.; Wang, Z.; Song, G.; Pan, Y.; Zhao, X.; Liu, S. An Intelligent Graphene-Based Biosensing Device for Cytokine Storm Syndrome Biomarkers Detection in Human Biofluids. *Small* **2021**, *17* (29), 2101508. https://doi.org/10.1002/smll.202101508.

(146) Tkachev, S.; Monteiro, M.; Santos, J.; Placidi, E.; Hassine, M. B.; Marques, P.; Ferreira, P.; Alpuim, P.; Capasso, A. Environmentally Friendly Graphene Inks for Touch Screen Sensors. *Advanced Functional Materials* **2021**, *31* (33), 2103287. https://doi.org/10.1002/adfm.202103287.

(147) Quintana, M.; Spyrou, K.; Grzelczak, M.; Browne, W. R.; Rudolf, P.; Prato, M. Functionalization of Graphene via 1,3-Dipolar Cycloaddition. *ACS Nano* **2010**, *4* (6), 3527–3533. https://doi.org/10.1021/nn100883p.

(148) Maccaferri, G.; Zanardi, C.; Xia, Z. Y.; Kovtun, A.; Liscio, A.; Terzi, F.; Palermo, V.; Seeber, R. Systematic Study of the Correlation between Surface Chemistry, Conductivity and Electrocatalytic Properties of Graphene Oxide Nanosheets. *Carbon* **2017**, *120*, 165–175. https://doi.org/10.1016/j.carbon.2017.05.030.

(149) Denis, P. A. Organic Chemistry of Graphene: The Diels–Alder Reaction. *Chemistry – A European Journal* **2013**, *19* (46), 15719–15725. https://doi.org/10.1002/chem.201302622.

(150) Chen, X.; Assebban, M.; Kohring, M.; Bao, L.; Weber, H. B.; Knirsch, K. C.; Hirsch, A. Laser-Triggered Bottom-Up Transcription of Chemical Information: Toward Patterned Graphene/MoS2 Heterostructures. *J. Am. Chem. Soc.* **2022**, *144* (22), 9645–9650. https://doi.org/10.1021/jacs.2c00642.

(151) Labroo, P.; Cui, Y. Graphene Nano-Ink Biosensor Arrays on a Microfluidic Paper for Multiplexed Detection of Metabolites. *Analytica Chimica Acta* **2014**, *813*, 90–96. https://doi.org/10.1016/j.aca.2014.01.024.

(152) Silvestri, A.; Criado, A.; Poletti, F.; Wang, F.; Fanjul-Bolado, P.; González-García, M. B.; García-Astrain, C.; Liz-Marzán, L. M.; Feng, X.; Zanardi, C.; Prato, M. Bioresponsive, Electroactive, and Inkjet-Printable Graphene-Based Inks. *Advanced Functional Materials* **2022**, *32* (2), 2105028. https://doi.org/10.1002/adfm.202105028.

(153) Silvestri, A.; Vázquez-Díaz, S.; Misia, G.; Poletti, F.; López-Domene, R.; Pavlov, V.; Zanardi, C.; Cortajarena, A. L.; Prato, M. An Electroactive and Self-Assembling Bio-Ink, Based on Protein-Stabilized Nanoclusters and Graphene, for the Manufacture of Fully Inkjet-Printed Paper-Based Analytical Devices. *Small* **2023**, *19* (51), 2300163. https://doi.org/10.1002/smll.202300163.

(154) Hu, G.; Kang, J.; T. Ng, L. W.; Zhu, X.; T. Howe, R. C.; G. Jones, C.; C. Hersam, M.; Hasan, T. Functional Inks and Printing of Two-Dimensional Materials. *Chemical Society Reviews* **2018**, *47* (9), 3265–3300. https://doi.org/10.1039/C8CS00084K.

(155) Splendiani, A.; Sun, L.; Zhang, Y.; Li, T.; Kim, J.; Chim, C.-Y.; Galli, G.; Wang, F. Emerging Photoluminescence in Monolayer MoS2. *Nano Lett.* **2010**, *10* (4), 1271–1275. https://doi.org/10.1021/nl903868w.

(156) Joensen, P.; Frindt, R. F.; Morrison, S. R. Single-Layer MoS2. *Materials Research Bulletin* **1986**, *21* (4), 457–461. https://doi.org/10.1016/0025-5408(86)90011-5.

(157) Ho, W.; Yu, J. C.; Lin, J.; Yu, J.; Li, P. Preparation and Photocatalytic Behavior of MoS2 and WS2 Nanocluster Sensitized TiO2. *Langmuir* **2004**, *20* (14), 5865–5869. https://doi.org/10.1021/la049838g.

(158) Shi, S.; Sun, Z.; Hu, Y. H. Synthesis, Stabilization and Applications of 2-Dimensional 1T Metallic MoS2. *J. Mater. Chem. A* **2018**, *6* (47), 23932–23977. https://doi.org/10.1039/C8TA08152B.

(159) Gao, E.; Lin, S.-Z.; Qin, Z.; Buehler, M. J.; Feng, X.-Q.; Xu, Z. Mechanical Exfoliation of Two-Dimensional Materials. *Journal of the Mechanics and Physics of Solids* **2018**, *115*, 248–262. https://doi.org/10.1016/j.jmps.2018.03.014.

(160) Liu, H. F.; Wong, S. L.; Chi, D. Z. CVD Growth of MoS2-Based Two-Dimensional Materials. *Chemical Vapor Deposition* **2015**, *21* (10-11–12), 241–259. https://doi.org/10.1002/cvde.201500060.

(161) Li, F.; Sun, S.-K.; Chen, Y.; Naka, T.; Hashishin, T.; Maruyama, J.; Abe, H. Bottom-up Synthesis of 2D Layered High-Entropy Transition Metal Hydroxides. *Nanoscale Advances* **2022**, *4* (11), 2468–2478. https://doi.org/10.1039/D1NA00871D.

(162) Daukiya, L.; Teyssandier, J.; Eyley, S.; Kazzi, S. E.; González, M. C. R.; Pradhan, B.; Thielemans, W.; Hofkens, J.; Feyter, S. D. Covalent Functionalization of Molybdenum Disulfide by Chemically Activated Diazonium Salts. *Nanoscale* **2021**, *13* (5), 2972–2981. https://doi.org/10.1039/D0NR07310E.

(163) Chu, X. S.; Yousaf, A.; Li, D. O.; Tang, A. A.; Debnath, A.; Ma, D.; Green, A. A.; Santos, E. J. G.; Wang, Q. H. Direct Covalent Chemical Functionalization of Unmodified Two-

Dimensional Molybdenum Disulfide. *Chem. Mater.* **2018**, *30* (6), 2112–2128. https://doi.org/10.1021/acs.chemmater.8b00173.

(164) Chen, X.; Bartlam, C.; Lloret, V.; Moses Badlyan, N.; Wolff, S.; Gillen, R.; Stimpel-Lindner, T.; Maultzsch, J.; Duesberg, G. S.; Knirsch, K. C.; Hirsch, A. Covalent Bisfunctionalization of Two-Dimensional Molybdenum Disulfide. *Angewandte Chemie International Edition* **2021**, *60* (24), 13484–13492. https://doi.org/10.1002/anie.202103353.

(165) Presolski, S.; Pumera, M. Covalent Functionalization of MoS2. *Materials Today* **2016**, *19* (3), 140–145. https://doi.org/10.1016/j.mattod.2015.08.019.

(166) Chen, X.; Berner, N. C.; Backes, C.; Duesberg, G. S.; McDonald, A. R. Functionalization of Two-Dimensional MoS2: On the Reaction Between MoS2 and Organic Thiols. *Angewandte Chemie* **2016**, *128* (19), 5897–5902. https://doi.org/10.1002/ange.201510219.

(167) Vera-Hidalgo, M.; Giovanelli, E.; Navío, C.; Pérez, E. M. Mild Covalent Functionalization of Transition Metal Dichalcogenides with Maleimides: A "Click" Reaction for 2H-MoS2 and WS2. *J. Am. Chem. Soc.* **2019**, *141* (9), 3767–3771. https://doi.org/10.1021/jacs.8b10930.

(168) Iglesias, D.; Ippolito, S.; Ciesielski, A.; Samorì, P. Simultaneous Non-Covalent Bi-Functionalization of 1T-MoS2 Ruled by Electrostatic Interactions: Towards Multi-Responsive Materials. *Chem. Commun.* **2020**, *56* (50), 6878–6881. https://doi.org/10.1039/D0CC02371J.

(169) Garrido, M.; Criado, A.; Prato, M. Simultaneous Exfoliation and Functionalization of MoS 2 with Tetrapyridyl Porphyrin. *Nanoscale* **2024**, *16* (28), 13525–13533. https://doi.org/10.1039/D4NR01802H.

(170) Yue, Q.; Shao, Z.; Chang, S.; Li, J. Adsorption of Gas Molecules on Monolayer MoS2 and Effect of Applied Electric Field. *Nanoscale Res Lett* **2013**, *8* (1), 425. https://doi.org/10.1186/1556-276X-8-425.

(171) Yao, Y.; Tolentino, L.; Yang, Z.; Song, X.; Zhang, W.; Chen, Y.; Wong, C. High-Concentration Aqueous Dispersions of MoS2. *Advanced Functional Materials* **2013**, *23* (28), 3577–3583. https://doi.org/10.1002/adfm.201201843.

(172) Chen, W. Y.; Yen, C.-C.; Xue, S.; Wang, H.; Stanciu, L. A. Surface Functionalization of Layered Molybdenum Disulfide for the Selective Detection of Volatile Organic Compounds at Room Temperature. *ACS Appl. Mater. Interfaces* **2019**, *11* (37), 34135–34143. https://doi.org/10.1021/acsami.9b13827.

(173) Neethipathi, D. K.; Beniwal, A.; Bass, A. M.; Scott, M.; Dahiya, R. MoS_2 Modified Screen Printed Carbon Electrode Based Flexible Electrochemical Sensor for Detection of Copper Ions in Water. *IEEE Sensors Journal* **2023**, *23* (8), 8146–8153. https://doi.org/10.1109/JSEN.2023.3257188.

(174) Zhuravlova, A.; Ricciardulli, A. G.; Pakulski, D.; Gorczyński, A.; Kelly, A.; Coleman, J. N.; Ciesielski, A.; Samorì, P. High Selectivity and Sensitivity in Chemiresistive Sensing of Co(II) Ions with Liquid-Phase Exfoliated Functionalized MoS2: A Supramolecular Approach. *Small* **2023**, *19* (51), 2208100. https://doi.org/10.1002/smll.202208100.

(175) Huang, J.; He, Y.; Jin, J.; Li, Y.; Dong, Z.; Li, R. A Novel Glucose Sensor Based on MoS2 Nanosheet Functionalized with Ni Nanoparticles. *Electrochimica Acta* **2014**, *136*, 41–46. https://doi.org/10.1016/j.electacta.2014.05.070.

(176) Wang, T.; Zhu, H.; Zhuo, J.; Zhu, Z.; Papakonstantinou, P.; Lubarsky, G.; Lin, J.; Li, M. Biosensor Based on Ultrasmall MoS2 Nanoparticles for Electrochemical Detection of H2O2 Released by Cells at the Nanomolar Level. *Anal. Chem.* **2013**, *85* (21), 10289–10295. https://doi.org/10.1021/ac402114c.

(177) Chao, J.; Han, X.; Sun, H.; Su, S.; Weng, L.; Wang, L. Platinum Nanoparticles Supported MoS2 Nanosheet for Simultaneous Detection of Dopamine and Uric Acid. *Sci. China Chem.* **2016**, *59* (3), 332–337. https://doi.org/10.1007/s11426-015-5492-9.

(178) Lei, Y.; Butler, D.; Lucking, M. C.; Zhang, F.; Xia, T.; Fujisawa, K.; Granzier-Nakajima, T.; Cruz-Silva, R.; Endo, M.; Terrones, H.; Terrones, M.; Ebrahimi, A. Single-Atom Doping of MoS2 with Manganese Enables Ultrasensitive Detection of Dopamine: Experimental and Computational Approach. *Science Advances* **2020**, *6* (32), eabc4250. https://doi.org/10.1126/sciadv.abc4250.

(179) Savinova, E. R.; Oshchepkov, A. G. 7.16 - Benchmarking in Electrocatalysis. In *Comprehensive Inorganic Chemistry III (Third Edition)*; Reedijk, J., Poeppelmeier, K. R., Eds.; Elsevier: Oxford, 2023; pp 492–550. https://doi.org/10.1016/B978-0-12-823144-9.00093-5.

(180) Marković, N. M.; Ross, P. N. Surface Science Studies of Model Fuel Cell Electrocatalysts. *Surface Science Reports* **2002**, *45* (4), 117–229. https://doi.org/10.1016/S0167-5729(01)00022-X.

(181) Das, C.; Sinha, N.; Roy, P. Transition Metal Non-Oxides as Electrocatalysts: Advantages and Challenges. *Small* **2022**, *18* (28), 2202033. https://doi.org/10.1002/smll.202202033.

(182) O'Mullane, A. P.; Escudero-Escribano, M.; Stephens, I. E. L.; Krischer, K. The Role of Electrocatalysis in a Sustainable Future: From Renewable Energy Conversion and Storage to Emerging Reactions. *ChemPhysChem* **2019**, *20* (22), 2900–2903.

(183) Zhang, H.; Guo, H.; Ren, J.; Jin, X.; Li, X.; Song, R. Synergistic Engineering of Morphology and Electronic Structure in Constructing Metal-Organic Framework-Derived Ru Doped Cobalt-Nickel Oxide Heterostructure towards Efficient Alkaline Hydrogen Evolution Reaction. *Chemical Engineering Journal* **2021**, *426*, 131300. https://doi.org/10.1016/j.cej.2021.131300.

(184) Garcia-Segura, S.; Lanzarini-Lopes, M.; Hristovski, K.; Westerhoff, P. Electrocatalytic Reduction of Nitrate: Fundamentals to Full-Scale Water Treatment Applications. *Applied Catalysis B: Environmental* **2018**, *236*, 546–568. https://doi.org/10.1016/j.apcatb.2018.05.041.

(185) Khan, K.; Tareen, A. K.; Iqbal, M.; Zhang, Y.; Mahmood, A.; Mahmood, N.; Yin, J.; Khatoon, R.; Zhang, H. Recent Advance in MXenes: New Horizons in Electrocatalysis and Environmental Remediation Technologies. *Progress in Solid State Chemistry* **2022**, *68*, 100370. https://doi.org/10.1016/j.progsolidstchem.2022.100370.

(186) Solis, J. J. C.; Castillo, A.; Yin, S.; Sandoval-Pauker, C.; Ocuane, N.; Puerto-Diaz, D.; Jafari, N.; Villagrán, D. Molecular Inspired Electrocatalyst Materials for Environmental Remediation. *Inorg. Chem. Front.* **2023**, *10* (21), 6160–6175. https://doi.org/10.1039/D3QI01248D.

(187) Costentin, C.; Drouet, S.; Robert, M.; Savéant, J.-M. Turnover Numbers, Turnover Frequencies, and Overpotential in Molecular Catalysis of Electrochemical Reactions. Cyclic Voltammetry and Preparative-Scale Electrolysis. *J. Am. Chem. Soc.* **2012**, *134* (27), 11235–11242. https://doi.org/10.1021/ja303560c.

(188) Savéant, J.-M. Molecular Catalysis of Electrochemical Reactions. Mechanistic Aspects. *Chem. Rev.* **2008**, *108* (7), 2348–2378. https://doi.org/10.1021/cr068079z.

(189) Luo, Y.; Zhang, Z.; Chhowalla, M.; Liu, B. Recent Advances in Design of Electrocatalysts for High-Current-Density Water Splitting. *Advanced Materials* **2022**, *34* (16), 2108133. https://doi.org/10.1002/adma.202108133.

(190) Bard, A. J.; Faulkner, L. R.; White, H. S. *Electrochemical Methods: Fundamentals and Applications*; John Wiley & Sons, 2022.

(191) Wang, W.; Wei, X.; Choi, D.; Lu, X.; Yang, G.; Sun, C. Chapter 1 - Electrochemical Cells for Medium- and Large-Scale Energy Storage: Fundamentals. In *Advances in Batteries for Medium and Large-Scale Energy Storage*; Menictas, C., Skyllas-Kazacos, M., Lim, T. M.,

Eds.; Woodhead Publishing Series in Energy; Woodhead Publishing, 2015; pp 3–28. https://doi.org/10.1016/B978-1-78242-013-2.00001-7.

(192) Srinivasan, S.; Krishnan, L.; Marozzi, C. FUEL CELL PRINCIPLES. In *Fuel Cells: From Fundamentals to Applications*; Srinivasan, S., Ed.; Springer US: Boston, MA, 2006; pp 189–233. https://doi.org/10.1007/0-387-35402-6_4.

(193) Greeley, J.; Markovic, N. M. The Road from Animal Electricity to Green Energy: Combining Experiment and Theory in Electrocatalysis. *Energy Environ. Sci.* **2012**, *5* (11), 9246–9256. https://doi.org/10.1039/C2EE21754F.

(194) Elgrishi, N.; Rountree, K. J.; McCarthy, B. D.; Rountree, E. S.; Eisenhart, T. T.; Dempsey, J. L. A Practical Beginner's Guide to Cyclic Voltammetry. *J. Chem. Educ.* **2018**, *95* (2), 197–206. https://doi.org/10.1021/acs.jchemed.7b00361.

(195) Singh, H.; Wu, J.; Lagemann, K. A. L.; Nath, M. Highly Efficient Dopamine Sensing with a Carbon Nanotube-Encapsulated Metal Chalcogenide Nanostructure. *ACS Appl. Nano Mater.* **2024**, *7* (5), 4814–4823. https://doi.org/10.1021/acsanm.3c05422.

(196) Cui, M.; Xin, P.; Che, Z.; Zou, M.; Zhang, M.; Sun, X.; Yuan, Y.; Zou, Z.; Lv, G.; Wang, S.; Hu, W. Highly Anti-Interference Electrocatalytic Sensing for Dopamine with Nitrogen-Doped Graphdiyne Directly in Biofluids. *Chemical Engineering Journal* **2023**, *464*, 142629. https://doi.org/10.1016/j.cej.2023.142629.

(197) Wang, Y.-X.; Rinawati, M.; Zhan, J.-D.; Lin, K.-Y.; Huang, C.-J.; Chen, K.-J.; Mizuguchi, H.; Jiang, J.-C.; Hwang, B.-J.; Yeh, M.-H. Boron-Doped Graphene Quantum Dots Anchored to Carbon Nanotubes as Noble Metal-Free Electrocatalysts of Uric Acid for a Wearable Sweat Sensor. *ACS Appl. Nano Mater.* **2022**, *5* (8), 11100–11110. https://doi.org/10.1021/acsanm.2c02279.

(198) Liv, L.; Portakal, M.; Çukur, M. S.; Topaçlı, B.; Uzun, B. Electrocatalytic Determination of Uric Acid with the Poly(Tartrazine)-Modified Pencil Graphite Electrode in Human Serum and Artificial Urine. *ACS Omega* **2023**, *8* (38), 34420–34430. https://doi.org/10.1021/acsomega.3c02561.

(199) Navadeepthy, D.; Thangapandian, M.; Viswanathan, C.; Ponpandian, N. A Nanocomposite of NiFe 2 O 4 –PANI as a Duo Active Electrocatalyst toward the Sensitive Colorimetric and Electrochemical Sensing of Ascorbic Acid. *Nanoscale Advances* **2020**, *2* (8), 3481–3493. https://doi.org/10.1039/D0NA00283F.

(200) Zhang, Y.; Han, M.; Peng, D.; Qin, H.; Zheng, H.; Xiao, J.; Yang, N. MOF-Derived High-Density Carbon Nanotubes "Tentacle" with Boosting Electrocatalytic Activity for

Detecting Ascorbic Acid. *Talanta* **2024**, *279*, 126578. https://doi.org/10.1016/j.talanta.2024.126578.

(201) Mei, L.; Zhao, W.; Zhang, L.; Zhang, M.; Song, Y.; Liang, J.; Sun, Y.; Chen, S.; Li, H.; Hong, C. The Application of the Inexpensive and Synthetically Simple Electrocatalyst CuFe-MoC@NG in Immunosensors. *Analyst* **2021**, *146* (17), 5421–5428. https://doi.org/10.1039/D1AN00840D.

(202) Shea, J. J. Handbook of Instrumental Techniques for Analytical Chemistry. *IEEE Electrical Insulation Magazine* **1998**, *14* (6), 42–42. https://doi.org/10.1109/MEI.1998.730821.

(203) Beitollahi, H.; Khalilzadeh, M. A.; Tajik, S.; Safaei, M.; Zhang, K.; Jang, H. W.; Shokouhimehr, M. Recent Advances in Applications of Voltammetric Sensors Modified with Ferrocene and Its Derivatives. *ACS Omega* **2020**, *5* (5), 2049–2059. https://doi.org/10.1021/acsomega.9b03788.

(204) Sinha, A.; Dhanjai; Jain, R.; Zhao, H.; Karolia, P.; Jadon, N. Voltammetric Sensing Based on the Use of Advanced Carbonaceous Nanomaterials: A Review. *Microchim Acta* **2018**, *185* (2), 89. https://doi.org/10.1007/s00604-017-2626-0.

(205) Moro, G.; Silvestri, A.; Ulrici, A.; Conzuelo, F.; Zanardi, C. How to Optimize the Analytical Performance of Differential Pulse Voltammetry: One Variable at Time versus Design of Experiments. *J Solid State Electrochem* **2024**, *28* (3), 1403–1415. https://doi.org/10.1007/s10008-023-05753-x.

(206) Houssin, T.; Bridle, H.; Senez, V. Chapter 6 - Electrochemical Detection. In *Waterborne Pathogens (Second Edition)*; Bridle, H., Ed.; Academic Press, 2021; pp 147–187. https://doi.org/10.1016/B978-0-444-64319-3.00006-X.

(207) Karadas-Bakirhan, N.; Sarakbi, A.; Vandeput, M.; Ozkan, S. A.; Kauffmann, J.-M. Liquid Chromatography with Amperometric Detection at a Silver Based Detector for the Determination of Thiocompounds: Application to the Assay of Thiopurine Antimetabolites in Urine. *Anal. Chem.* **2015**, *87* (13), 6730–6735. https://doi.org/10.1021/acs.analchem.5b00879.

(208) Lazanas, A. Ch.; Prodromidis, M. I. Electrochemical Impedance Spectroscopy—A Tutorial. *ACS Meas. Sci. Au* **2023**, *3* (3), 162–193. https://doi.org/10.1021/acsmeasuresciau.2c00070.

(209) Wörner, H. J.; Arrell, C. A.; Banerji, N.; Cannizzo, A.; Chergui, M.; Das, A. K.; Hamm, P.; Keller, U.; Kraus, P. M.; Liberatore, E.; Lopez-Tarifa, P.; Lucchini, M.; Meuwly, M.; Milne, C.; Moser, J.-E.; Rothlisberger, U.; Smolentsev, G.; Teuscher, J.; van Bokhoven, J. A.;

Wenger, O. Charge Migration and Charge Transfer in Molecular Systems. *Structural Dynamics* **2017**, *4* (6), 061508. https://doi.org/10.1063/1.4996505.

(210) Randles, J. E. B. Kinetics of Rapid Electrode Reactions. *Discuss. Faraday Soc.* **1947**, *1*, 11–19. https://doi.org/10.1039/DF9470100011.

(211) Swamy, T.; Chiang, Y.-M. Electrochemical Charge Transfer Reaction Kinetics at the Silicon-Liquid Electrolyte Interface. *J. Electrochem. Soc.* **2015**, *162* (13), A7129. https://doi.org/10.1149/2.0181513jes.

Chapter II

Nanocomposite based on Multiwalled Carbon Nanotubes and Gold Nanoparticles from Metal Vapor Synthesis for Voltammetric detection of Monoamine Neurotransmitters in Complex Biological Systems

Abstract

Monoamine neurotransmitters are involved in a plethora of biological processes, in the central and peripheral nervous system. Rapid and robust electrochemical sensors for real-time monitoring of their concentration can be a valuable tool to study these processes, both for prompt diagnosis or correlated diseases and for a deeper understanding of their physiological pathways. However, biological matrices pose a challenging environment for these devices, as biogenic interfering agents can compete with the analyte and adsorb on the surface of electrodes, leading to the fouling of the electroactive area. In this chapter, a new nanocomposite based on multi-walled carbon nanotubes and gold nanoparticles is presented as electrocatalyst for various substrates. The nanocomposite is implemented in the design of two voltammetric sensors for monoamine neurotransmitters, serotonin and dopamine, in complex biological matrices.

2.1 Introduction

2.1.1 Monoamine Neurotransmitters as Analytes

Monoamine neurotransmitters are a class of small biomolecules that share similar structural features: they contain one amino group that is connected to an aromatic ring by a two-carbon alkyl chain. Monoamines are synthesized in different areas of the upper part of brainstem by decarboxylation of the respective precursor aromatic amino acids (L-phenylalanine, L-tyrosine, L-tryptophan, L-DOPA) catalyzed by L-amino decarboxylase.[1,2] Dopamine, serotonin and noradrenaline are the most important representatives of this class of molecules.

As neurotransmitters, these molecules are used as signaling tools by neurons at the level of synapses, and specifically to regulate behavioral and emotional information.[1] Presynaptic

neurons synthesize monoamines and release them into vesicles into the synaptic gap between two neurons. Monoamines subsequently bind to specific receptors and neurotransmission is finalized by degradation or reuptake of the neurotransmitter. Moreover, it has been proved that monoamines influence the expression of neurotrophin-3, which is a neurotrophic factor.[3] Neurotrophins are a family of proteins involved in the regulation of growth and survival of neurons,[4] and by modulating their expression, monoamine play a pivotal role in maintaining integrity and functionality of the neuronal network. At the level of peripheral nervous system, monoamines are involved in the regulation of several processes, like movement, vasodilation and vasoconstriction, thermoregulation and pain modulation.[5,6]

Numerous neurological symptoms can arise from an imbalance in the metabolism of monoamines. The problems might appear as motor and cognitive delays, seizures, autonomic dysfunction (sweating, dysregulation of body temperature, hypersalivation, congestion of the nose), and neuropsychiatric symptoms including autism spectrum disorder or anxiety.[7] Abnormal variations of concentration of monoamine neurotransmitters are correlated with insurgence of neurodegenerative diseases and chronic mental disorders, like Parkinson's disease[8–10] and schizophrenia.[11]

Specifically, serotonin, also known as 5-hydroxytryptamine (5-HT), is involved in diverse physiological functions such as sleep, cognition, memory, aggressiveness, appetite and stress management. In the periphery of human body, 5-HT functions as well as a hormone, regulating non-neuronal processes like cardiovascular activity, metabolism and glucose homeostasis.[12,13] Studies on the role of 5-HT in pathological conditions demonstrated that elevated levels of 5-HT may be associated with neuropsychiatric symptoms of autism spectrum disorder[14] and attention deficit hyperactivity disorder[15,16] as well as non-neuropathological conditions like diabetes[17] or coronary artery disease.[18] Over the past 100 years, since its discovery, research on the physiological roles of 5-HT has unveiled the importance of this molecule in several physiological pathways and yet a comprehensive understanding of its effect over many pathological conditions such as mental depression[19,20] and communicative diseases[21] remains challenging.

The development of sensing systems for real-time detection and quantification of 5-HT in peripheral systems could foster greatly neuroscience and general physiology, solving finally several queries around this molecule. Moreover, rapid, portable, and dependable technology for serotonin detection may potentially be able to assist emergency physicians in the prompt

diagnosis and treatment of pathological conditions like serotonin lethal syndrome,[22] a rare drug-induced clinical disease that has a 50% death rate within 24 hours of symptom onset.[23]

Dopamine (DA) is involved in the regulation of motor control and motor planning. Low expression of DA in this pathway is correlated with appearance of issues in motor control after neurodegenerative diseases, like Parkinson's disease[9,24] and Tourette's syndrome.[25] Other functions of DA are related to reward and motivation pathway in the limbic system[26] and cognition and attention capability in the frontal and prefrontal cortex.[27] Disturbances of these pathways lead to insurgence of psychiatric conditions of psychosis and schizophrenia.[28] Finally, DA is involved in regulation of sleep at the level of the hypothalamus and pituitary.[29]

The ability to study variation of concentration of DA directly at the level of synapses could shed light on causal relations and provide insight on the response of dopaminergic pathways to external stimuli, allowing deeper understanding of degenerative processes that determine pathological conditions.

Of various instrumental approaches for the detection of monoamine neurotransmitters, high-performance liquid chromatography (HPLC), often coupled with mass spectrometry (MS), is the most used technique.[30–32] HPLC-MS ensures high selectivity and sensitivity; however, it requires expensive analytical equipment and trained personnel, making it unsuitable for rapid *in situ* analysis and monitoring.

On the other hand, electrochemical sensors can be easily miniaturized and integrated in portable designs, for rapid detection of electroactive molecules, like 5-HT and DA. One main challenge for electrochemical detection of monoamines is the complexity of biological fluids. Both 5-HT and DA are present at nanomolar concentration in the central nervous system[33,34] and at micromolar concentration in the peripheral biological fluids like blood serum,[30,35] urine[36] and saliva.[37] Selective detection of monoamines in these complex matrices is hampered by the presence of a plethora of interfering species affecting the response of the sensor and by fouling processes due to adsorption of macromolecules on the surface of electrodes.

Consequently, the design of selective electrochemical sensors for rapid detection of neurotransmitters in complex biological matrices remains a lively and timely research field in the world of biosensing.

2.1.2 Carbon Nanotubes as Transducers for Neurotransmitters

As demonstrated by Schmidt et al.,[38] multiwalled carbon nanotubes (MWCNTs) constitute an optimal material for transduction in electrochemical sensors for neurotransmitters, thanks to their superior electron transfer and mass transfer kinetics. By comparing electrodes fabricated with MWCNTs to carbon-fiber microelectrodes, they demonstrated that MWCNTs improve sensitivity and selectivity for voltammetric detection of electroactive neurotransmitters. Their intrinsic electrocatalytic activity,[39] due to the arrangement of sp^2 carbon atoms on their surface, allows for sharper voltammetric peaks, facilitating discrimination between different electroactive species.

Furthermore, the possibility of functionalizing their surface to modulate their properties opens to almost infinite possibilities for sensor manufacture. For instance, it is possible to decorate the surface of CNTs with metal nanoparticles to enhance their electrocatalytic performance. Yang et al. used Fe/Fe_3C to decorate MWCNTs, with an ultrafast microwave-assisted method, to design a voltammetric sensor for DA in the micromolar range in human serum.[40] Wu et al. instead developed a sensitive electrochemical sensor for 5-HT in urines, using ferrocene covalently linked AuNPs on MWCNTs.[41]

Finally, their compatibility with neurons and the ability of promoting growth and organization of neural networks make CNTs a promising material for bioelectronics based on neuronal interfaces.[42,43] CNTs can promote neuron attachment, growth and differentiation on planar surfaces by favoring propagation of electrical signals at level of axons.[44] Neurons grow in close contact with the surface of CNTs and synaptic that happen at the cell-material interface can be electrochemically studied.[43]

2.1.3 Gold Nanoparticles from Metal Vapor Synthesis for Heterogeneous Catalysis

AuNPs, thanks to their chemical inertia, high surface area, and electronic properties, constitute and ideal electrocatalytic material for manufacture of biosensors for neurotransmitters.[45] Currently in literature, it is possible to find a plethora of examples of AuNPs-modified electrodes for electrochemical detection of monoamine neurotransmitters, specifically dopamine and serotonin.[41,46]

MVS is a well-known synthetic approach for metal nanoparticles, which has been deeply studied since the early eighties.[47] This technique allows to obtain highly catalytic metal

nanoparticles with narrow size distribution, both homometallic and heterometallic, of different transition metals.[48]

AuNPs from MVS can be prepared from Au-acetone solvated metal atoms (SMA) and are highly catalytically active in heterogeneous catalysis.[48] The high activity derives from the weak interactions between the AuNPs and the stabilizing acetone molecules that coordinate their surface: these interactions are so weak that the AuNPs can be regarded as naked.[49]

2.1.4 Molecularly Imprinted Polymers as Artificial Receptors

Molecularly imprinted polymers (MIPs) are synthetic recognition materials that are obtained by polymerization of monomers, crosslinkers and eventual other essential components in presence of a large excess of the target analyte, which serves as a template.[50] During this process, the highly cross-linked polymeric network grows around the molecular template. After polymerization, the template is removed, leaving behind high-affinity binding sites.[51–53]

MIPs can be generated either by chemical polymerization,[54] enzymatic production[55] or electropolymerization.[56] This last method in particular offers several advantages for manufacture of electrochemical devices: for instance, it allows for precise control over polymer morphology and site-specific functionalization, which is crucial for optimal recognition capabilities. Furthermore, the fast polymerization kinetics and efficient template removal, contribute to the simplification of the synthetic process, while maintaining high reproducibility, and the possibility of reducing the use of hazardous chemicals make this technique extremely valuable.

Conductive polymers such as polypyrrole (PPy), poly(3,4-ehtylenedioxythiophene) (PEDOT) and polyaniline (PANI) are ideal candidates for electropolymerization, thanks to their electrical properties.[50,54]

Integration of conductive MIPs and electroactive nanomaterials has been highly advantageous for design of sensitive electrochemical sensing platforms. Specifically, CNTs have been used for over a decade together with MIPs, to boost sensitivity of electrochemical sensors. Shen et al. used molecularly imprinted PPy to decorate CNTs, designing an ultrasensitive voltammetric sensor for dopamine detection.[57] Later, in 2017, Zhang et al. developed a sensor based on molecularly imprinted poly(3-aminophenylboronic acid)/MWCNTs nanocomposite for voltammetric detection of epinephine.[58]

2.1.5 Aim of the Project

In this work, a nanocomposite (MWCNT-S-Au) based on multiwalled carbon nanotubes (MWCNTs) and gold nanoparticles from metal vapor synthesis (MVS AuNPs) is presented and applied for electrochemical detection of monoamine neurotransmitters serotonin and dopamine, in two different sensor designs. The nanocomposite was designed under the supervision of Prof. Maurizio Prato and Dr. Alessandro Silvestri, in collaboration with Dr. Claudio Evangelisti and Dr. Emanuela Pitzalis from CNR-ICCOM, Pisa, who synthesized the MVS AuNPs.

In the first sensor design, a screen-printed electrode was modified with MWCNT-S-Au, and the a MIP selective for serotonin was synthesized *in situ*, by electropolymerization. The final sensor is capable of detecting serotonin at micromolar scale in plasma, with excellent reproducibility, thanks to the presence of the polymer that prevents fouling of the electrode, while providing selectivity for serotonin. This sensor was developed under the supervision of Prof. Maurizio Prato and Dr. Alessandro Silvestri, in collaboration with Dr. Juan Pedro Merino, Adrián M Abelairas, Dr. Jesús Mosquera and Dr. Alejandro Criado from University of Coruña, who developed the MIP.

The second sensor is based on ITO-coated glass slides modified with MWCNTs and MWCNT-S-Au for detection of dopamine at cellular level. In this case, neurons are directly grown and diversified on the nanostructured electrode active surface, and subsequently the production of dopamine upon chemical stimulation is monitored by voltammetric and amperometric measurement. This sensor was developed under the supervision of Prof. Maurizio Prato and Dr. Alessandro Silvestri, in collaboration with Nerea Pascual Frías, Dr. Nuria Alegret and Dr. Francisco Gil Bea, from Biogipuzkoa, who developed the protocol for neurons differentiation, assembled the sensor and studied the response of cells upon chemical stimulation.

2.2 Results and Discussions

2.2.1 Functionalization of MWCNTs

First, MWCNTs were functionalized with thiol groups to subsequently use them as anchoring moieties for stable immobilization of AuNPs on their surface. To achieve this, the chosen strategy was based on a two-step controlled functionalization, which ensured at once protection of thiols during the functionalization and control over the length of linkers on the surface of MWCNTs. (**Figure 18**)

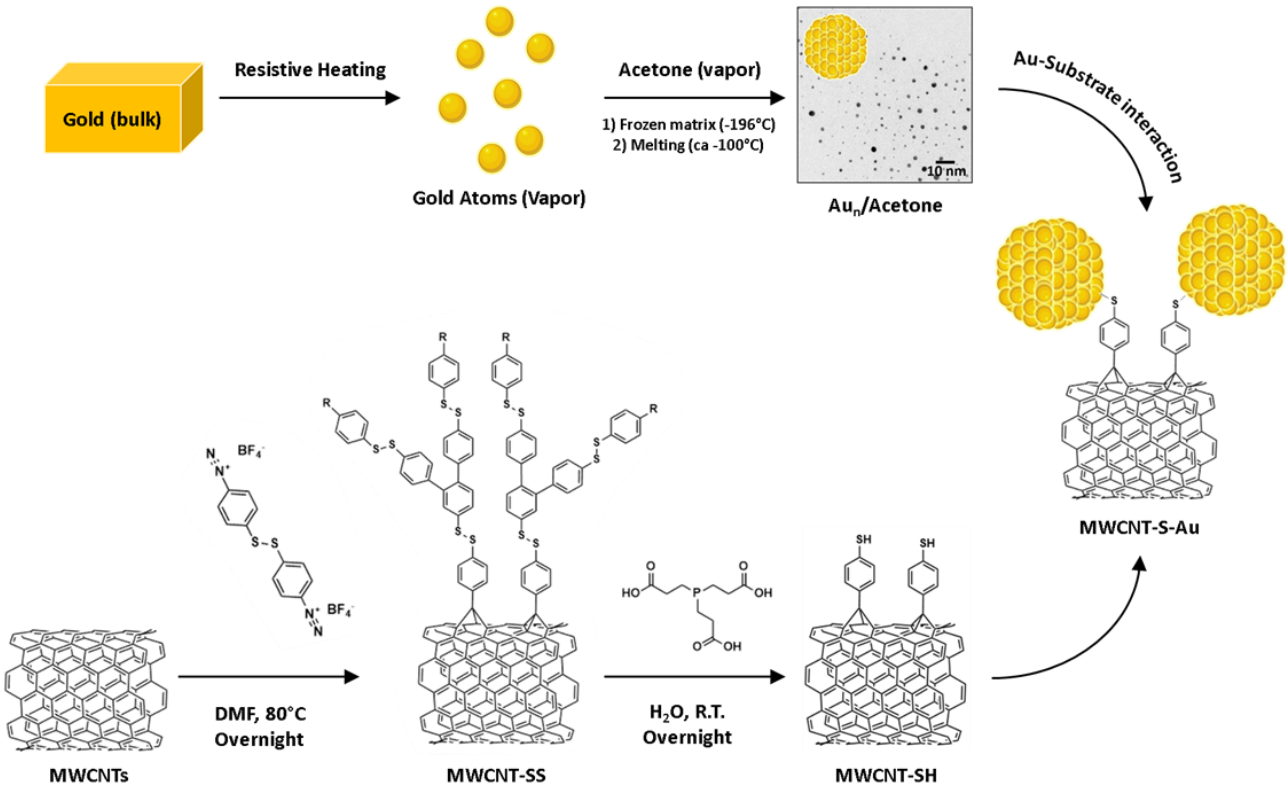

Figure 18 *Synthetic scheme of MWCNT-S-Au, illustrating the functionalization strategy based on SET reaction and disulfide cleavage to obtain MWCNT-SH and the synthesis of AuNPs by MVS approach and their grafting on MWCNT-SH.*

In light of these requirements, MWCNTs were functionalized using reactive radicals from decomposition of a symmetric disulfide-bearing aryl diazonium salt.[59,60] The high reactivity of radicals from diazonium salts leads to high degree of functionalization, but at the same time the radicalic process is poorly controllable and often leads to the formation of oligomeric chains on the surface of the material, which passivate its surface and hinder electron transfer. The strategy herein presented addresses this issue, achieving control over uncontrolled oligomerization: indeed, cleavage of the disulfide bond in the second step of

the synthesis allows simultaneously eliminating the oligomeric chains formed during the radicalic reaction and deprotects the thiol moieties for anchoring of AuNPs.[61]

Instead of being generated *in situ*, the diazonium salt was isolated as tetrafluoroborate salt, starting from 4-aminothiophenol.[62] This allowed proper characterization by ^{1}H-NMR and ATR-FTIR and to assess its thermal stability by Differential scanning calorimetry (DSC). Moreover, carrying out the functionalization of MWCNTs in DMF allowed increasing dispersibility of the nanomaterial, thus the surface area exposed to radical addition, resulting in a more homogeneous and efficient coverage of the surface.[63]

X-ray photoelectron spectroscopy (XPS) and thermogravimetric analysis (TGA) were the techniques of choice to characterize all steps of the functionalization. XPS spectra of pristine MWCNTs show that the material is mainly composed of C atoms, with only 3.2% of O atoms. Both survey and high-resolution spectra demonstrate the absence of Fe atoms and other metal contaminations (**Figure 19**).

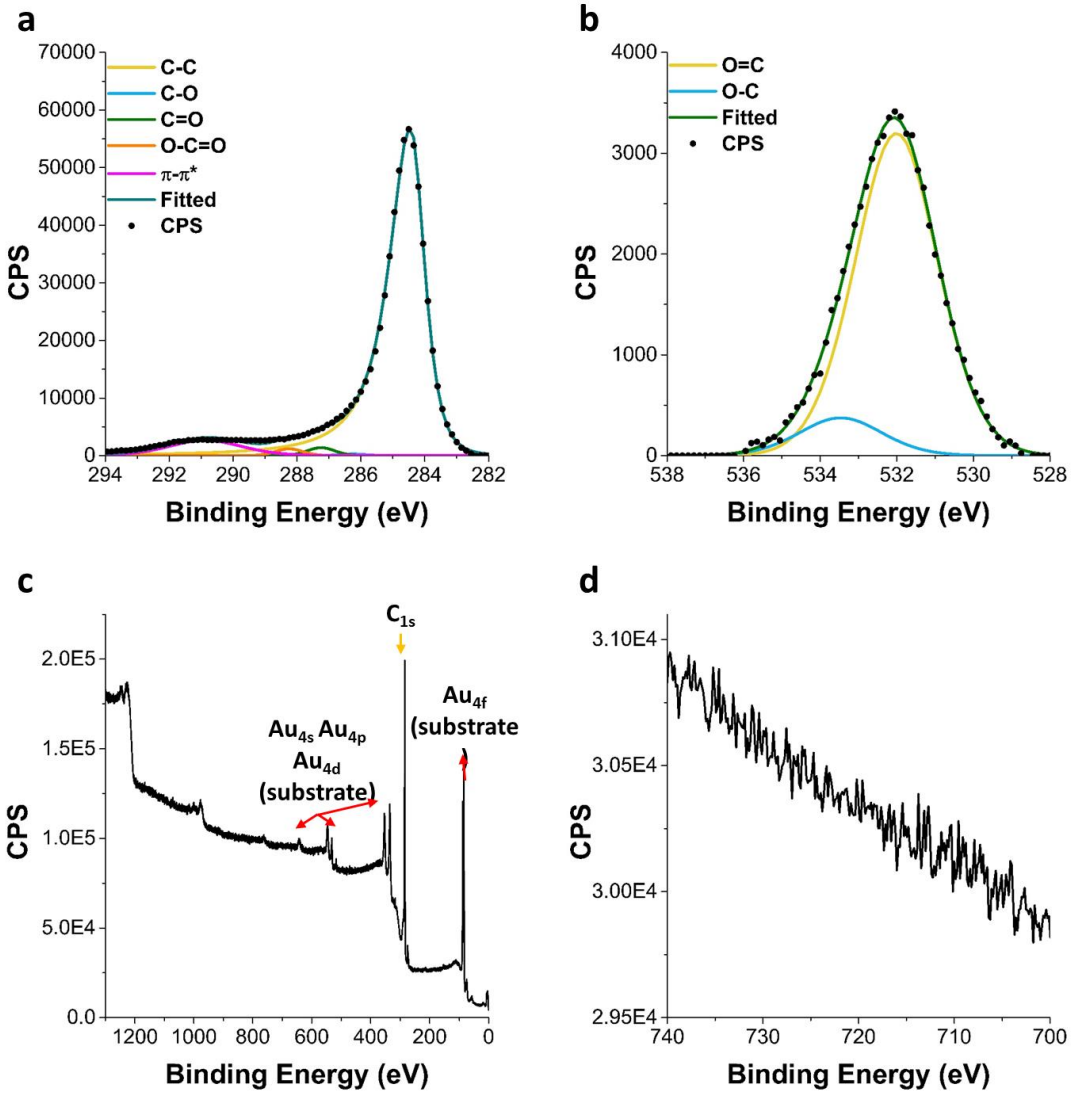

Figure 19 *High-resolution XPS spectra of a) C_{1s} and b) O_{1s} of MWCNTs; c) Survey and d) high-resolution Fe_{2p} XPS spectra of MWCNTs, highlighting the absence of Fe or other metal impurities after the purification.*

After the first step of the synthesis, the increase in the overall content of Sulfur was observed in the XPS survey spectrum, from an undetectable amount to 3.81 % of the atoms composing the surface of the material (**Table 2**, **Figure 20**). This evidence can be correlated with the grafting of disulfide-bearing aryl radicals on the surface of MWCNTs (Beamson, G.; Briggs, D., 1993).

Moreover, high-resolution spectrum of 2p orbitals (**Figure 20d**) of S provides insight on the type of S atoms on the surface of the material, demonstrating that they are mainly involved in S-S/S-H bonds (3.05 % in atomic percentage). Indeed, disulfides and thiols cannot be

easily distinguished with laboratory XPS, as both components fall at a binding energy of around 164 eV, but they can be discerned from other type of S atoms, like sulfite and sulfate.

Table 2 *Elemental composition of MWCNTs in the steps of functionalization, determined by XPS.*

Sample	%C	%O	%N	%S	%Fe
MWCNTs	96.80	3.20	-	-	-
MWCNT-SS	89.06	6.09	1.04	3.81	-
MWCNT-SH	89.58	5.85	2.01	2.55	-

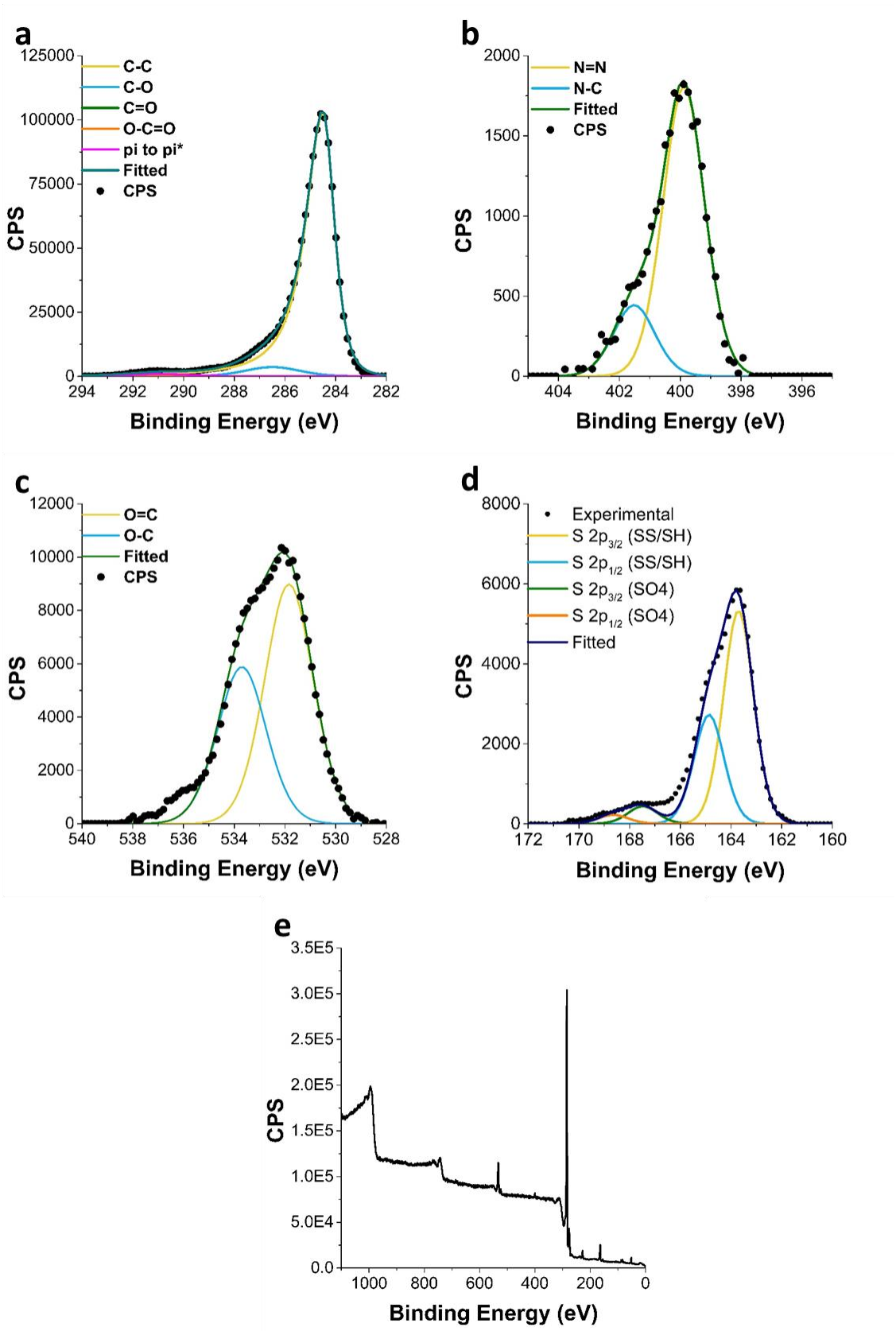

Figure 20 *High-resolution XPS spectra of a) C_{1s}, b) N_{1s}, c) O_{1s} and d) S_{2p} and e) Survey spectrum of MWCNT-SS.*

Additionally, it was possible to assess the successful functionalization by TGA, by the weight loss showed by the material at 500°C (**Figure 21**). At this temperature, complete degradation of organic functionalization takes place, while the graphitic structure of MWCNTs is still maintained.[64,65] From the difference of weight loss at 500° C between MWCNT-SS and pristine MWCNTs, it was possible to calculate a degree of functionalization of 119 μmol/mg of MWCNTs.

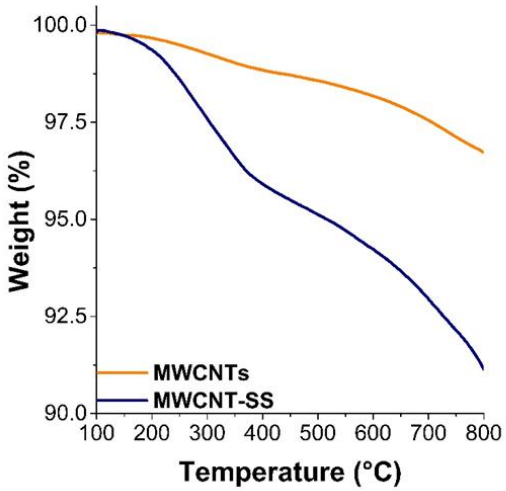

Figure 21 *TGA of MWCNTs (orange) and MWCNT-SS (blue).*

During the second step of the functionalization, upon cleavage of disulfide bonds, the total S atomic percentage decreased to 2.5%, of which 2% related to SS/SH component (**Figure 22**).

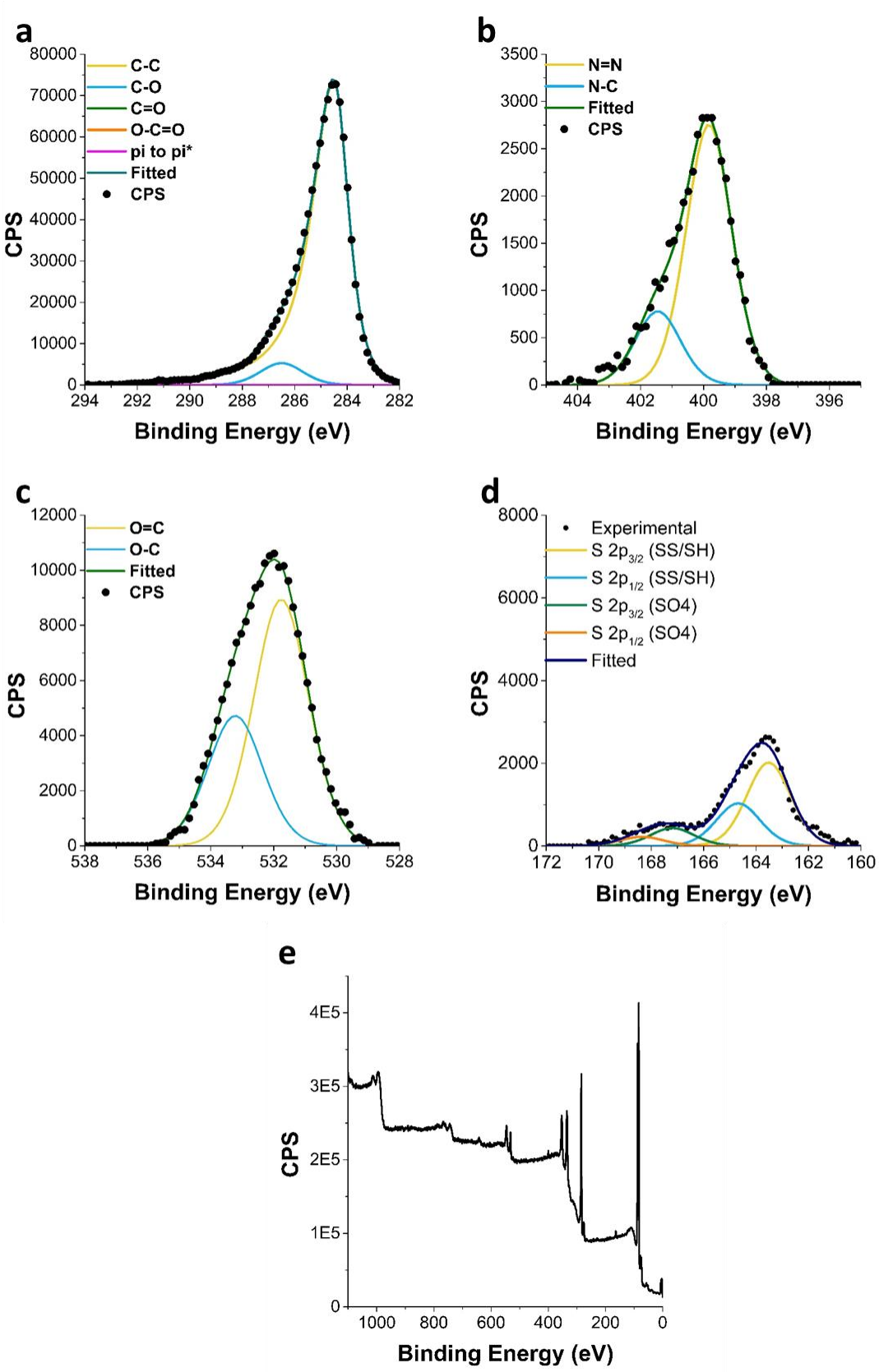

Figure 22 *High-resolution XPS spectra of a) C_{1s}, b) N_{1s}, c) O_{1s} and d) S_{2p} and e) Survey spectrum of MWCNT-SH.*

The decrease of the S atomic percentage from MWCNT-SS to MWCNT-SH is consistent with the elimination of oligomeric excess on the surface of the material, upon cleavage of disulfide bonds. By comparing these results with similar functionalization strategies that have been previously reported in literature,[61] it emerges that isolating the diazonium salt and carrying out the reaction in DMF allows for a better control over the functionalization. In fact, even if TGA measurements show lower degree of functionalization if compared with previous reports,[61] XPS spectra show a S atomic percentage that is 5 times higher. Consequently, this strategy allowed drastically reducing the amount of oligomers formed during the radical reaction and subsequently removed during the cleavage, improving the total mass balance of the process.

To enhance their intrinsic electrocatalytic activity, MWCNT-SH were decorated with AuNPs derived from MVS approach. Thanks to their high surface area and weakly coordinated metallic surface, these NPs present extremely high catalytic activity,[66–68] which is herein exploited for the first time to design electrochemical sensing platforms.

In a MVS reactor, upon resistive heating of bulk gold under high vacuum, a vapor of Au atoms was produced. Subsequently, Au atoms were co-condensed at liquid nitrogen temperature (-196 °C), with acetone vapors. The solid matrix was then melted at -95 °C, obtaining a deep-purple solution containing small AuNPs (2-4 nm), stabilized by the excess of organic solvents that serve as weakly coordinating ligands on the surface. Subsequently, the small AuNPs were immobilized on the surface of MWCNT-SH by simple impregnation at 25 °C, and the excess was removed by accurately washing the resulting material (MWCNT-S-Au).

2.2.2 Characterization of MWCNT-S-Au

To determine the amount of Au grafted on the MWCNTs, ICP-MS and TGA were used. For ICP-MS, MWCNT-S-Au were first digested in microwave digester to remove the carbonaceous matrix, and the final amount of Au was determined to be 11.55%. TGA was performed in oxidative environment, to favor the thermal degradation of the carbonaceous matrix, and Au percentage was determined from the residue at 800 °C (**Figure 23a**). By TGA, the amount of Au was determined to be 12.4%, which is in agreement with ICP-MS data.

XPS was used to investigate the oxidation state of AuNPs in MWCNT-S-Au. In the high-resolution spectrum of Au (**Figure 23b**), the main component of Au $4f_{7/2}$ core was centered at the binding energy of 84.08 eV, which is in accordance with oxidation state of Au^0.[69,70] This component makes up to 96.3% of the total Au region, demonstrating that the majority of gold atoms composing the NPs are indeed metallic, in agreement with what was previously observed for MVS AuNPs deposited onto different substrates.[67,71,72]

Topological characterization of MWCNT-S-Au by TEM (**Figure 23c**) revealed the presence of well-distributed spherical AuNPs on the surface of MWCNTs, with an average diameter of 2.9 ± 1.2 nm that is optimal for electrocatalytic applications.[73,74] By cyclic voltammetry (CV), it was possible to further assess the presence of gold in the nanocomposite, comparing the voltammetric response of MWCNT-S-Au with MWCNT-SH in 0.1 M PBS + 0.1 M KCl as a supporting electrolyte. The presence of a peak at 0.9 V can be associated with the oxidation of Au^0 to Au^+, as already reported in the literature for AuNPs (**Figure 23d**).[75,76]

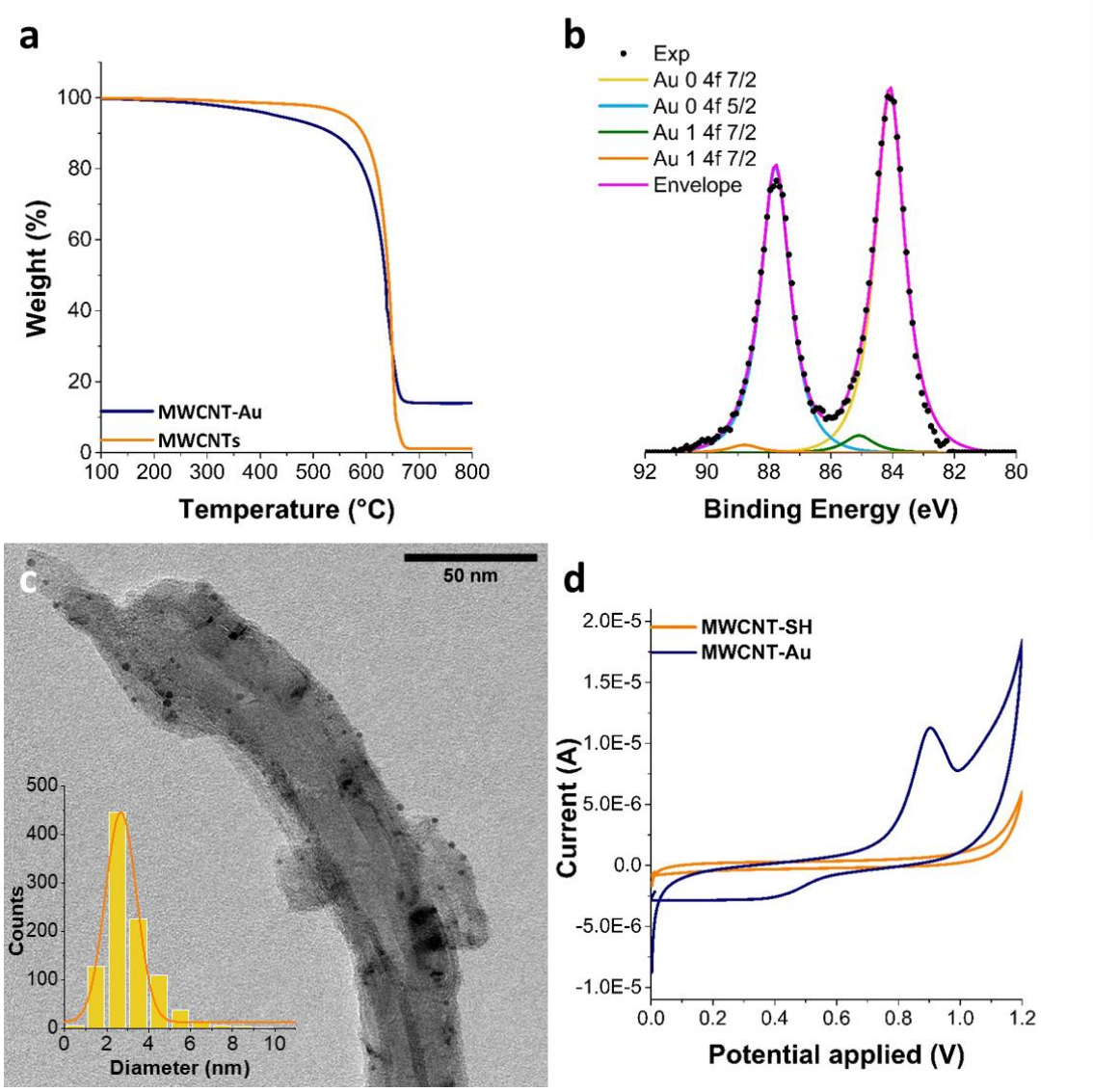

Figure 23 *Characterization of MWCNT-S-Au. a) TGA of MWCNTs (orange) and MWCNT-S-Au (blue) in the air; b) High-resolution XPS spectrum of Au4f orbitals of MWCNT-S-Au; c) TEM image of MWCNT-S-Au with size distribution analysis of Au NPs on the surface of the material; d) Cyclic voltammogram of MWCNT-S-Au (blue) registered at a scan rate of 20 mV/s, showing an oxidation peak at 0.9 V which can be related to the oxidation of* Au^0 *to* Au^+

2.2.3 Electrocatalytic Activity

Electrocatalytic activity of MWCNT-S-Au for different target analytes was investigated by linear sweep voltammetry (LSV). By modifying the surface of either glassy carbon electrodes (GCE) or screen-printed carbon electrodes (SPCE) and comparing the performances of the modified electrodes with the bare electrodes, we evaluated the activity of MWCNT-S-Au for oxidation and reduction reactions.[76] The electrocatalytic activity of a material causes a shift of the onset potential (*i.e.* the potential at which the reaction starts to take place) to values closer to 0V, and an increase of the faradaic current. (**Figure 24**).

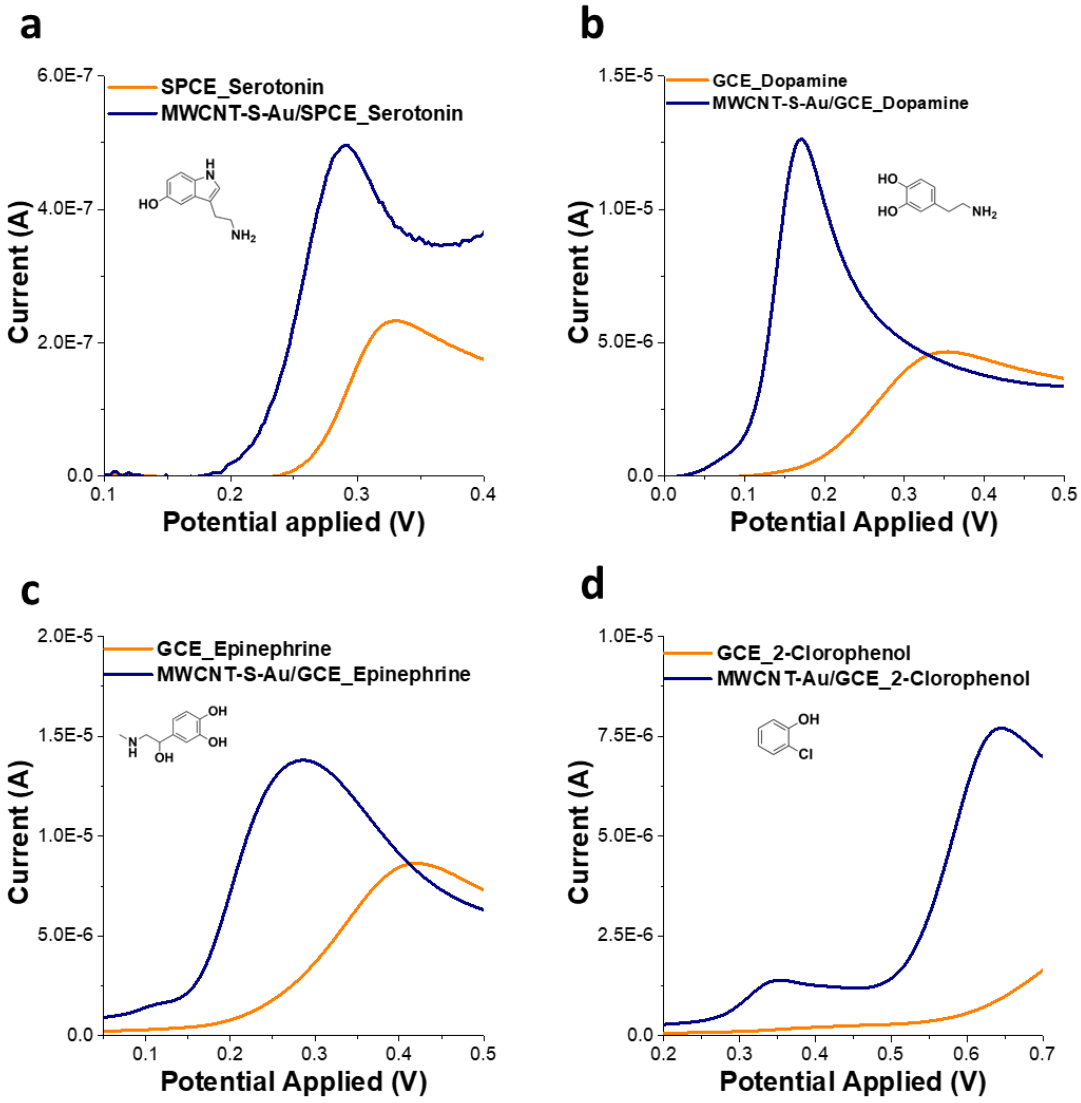

Figure 24 *LSV voltammograms for a) serotonin on bare and modified SPCEs; b) Dopamine on bare and modified GCEs; c) Epinephrine on bare and modified GCEs; d) 2-Chlorophenol on bare and modified GCEs. The voltammograms were baseline-subtracted.*

The nanocomposite proved to be electrocatalytic for eight different reactions of choice. **Table 3** summarizes the electrocatalytic activity of MWCNT-S-Au for the different substrates, in terms of peak potential anticipation (**ΔV**) and ratio between catalytic and non-catalytic current ($\mathbf{i_{cat}/i}$).

Table 3 *Electrocatalytic activity of MWCNT-S-Au for different substrates.*

Electrode	Substrate	Reaction	ΔV (mV)	i_{cat}/i
SPCE	Serotonin 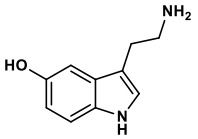	Oxidation	49.8	2.13
GCE	Dopamine 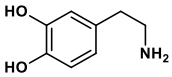	Oxidation	82.2	2.73
GCE	Epinephrine 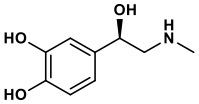	Oxidation	77.2	1.60
GCE	2-Chlorophenol 	Oxidation	65.2	5.31
GCE	Gallic Acid 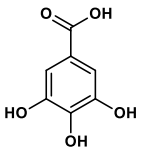	Oxidation	121.1	1.27
GCE	Hydroquinone 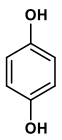	Oxidation	105.6	0.86
GCE	Hydrogen Peroxide	Reduction	-125.0	5.97
GCE	Oxygen	Reduction	-162.0	1.28

As demonstrated by these results, the electrocatalyst proves very efficient for the oxidation of phenols and catechols, as well as for the reduction of oxygen and hydrogen peroxide. The following paragraphs focus on the detection of serotonin and dopamine, which are particularly interesting for the reasons mentioned in the introduction to this chapter.

2.2.4 Design of Electrochemical Sensor for Serotonin in Human Serum

The design for the electrochemical sensor for serotonin in human serum is based on a commercial SPCE modified with MWCNT-S-Au on the working electrode. To provide the sensor with selectivity and antifouling properties, which allow application in complex media such as human serum, a MIP was implemented in the final design. The technique of choice was DPV, to minimize contribution of capacitive current coming from the polymeric coverage (**Figure 25**).[77–79]

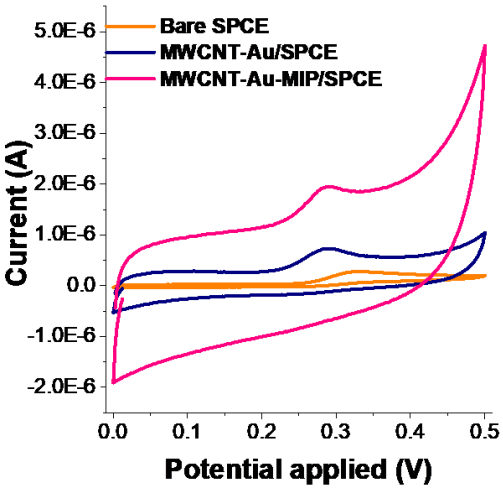

Figure 25 *Cyclic voltammograms of 12 µmol L^{-1} serotonin solution with SPCE, MWCNT-S-Au/SPCE, and MWCNT-S-Au-MIP/SPCE. The modification of the SPCE with MWCNTs and PPy induced an increase in the capacitive current as a consequence of the high specific capacitance.*[80]

2.2.4.1 Optimization of Sensing Performance of SPCE/MWCNT-S-Au for Detection of Serotonin

In DPV, the optimization of experimental conditions is pivotal for the final performance of the analysis. To determine the best operational parameters, a SPCE was modified with MWCNT-S-Au (SPCE/MWCNT-S-Au) and used to carry out a design of experiment (DoE).[81] Two main parameters were investigated: the modulation amplitude (*i.e.* the intensity of the potential pulses) and the modulation time (*i.e.* the duration of each pulse).[82]

The DoE was set as a factorial design, in which three equally spaced levels were chosen for each parameter. Considering all the possible combinations of levels and factors, a set of 9 experiments is needed to optimize the performance of the system (**Table 4**).

Table 4 *Factors (MA and MT) and levels chosen for DoE.*

	MA (V)	MT (s)
Low	0.01	0.01
Medium	0.055	0.055
High	0.1	0.1

All 9 experiments were carried out in triplicate using the same electrode (SPCE/MWCNT-S-Au), and in random order so that influence of memory effects related with the specific order of the measurements could be avoided (

Table 5).

Table 5 *Sets of experiments for DoE.*

SET 1			SET 2			SET 3		
exp n.	MA (V)	MT (s)	exp n.	MA (V)	MT (s)	exp n.	MA (V)	MT (s)
1	0	0	1	-1	0	1	-1	1
2	1	1	2	0	-1	2	0	0
3	1	-1	3	0	1	3	0	1
4	-1	0	4	1	1	4	1	0
5	0	-1	5	0	0	5	-1	0
6	-1	1	6	-1	-1	6	1	-1
7	0	1	7	1	0	7	1	1
8	1	0	8	-1	1	8	-1	-1
9	-1	-1	9	1	-1	9	0	-1

The aim of this DoE was to maximize the peak resolution, the intensity of faradaic current, and the signal-to-noise ratio.

Peak resolution and current intensity were described through a first figure of merit ($FoM1$), which is obtained as the ratio between the faradaic current (i_F) and the width of the peak at medium height ($\Delta E_{1/2}$):

Equation 1 $$FoM1 = \frac{i_F}{\Delta E_{1/2}}$$

When this $FoM1$ is maximized, the voltammogram results in sharp peaks, and sensitivity and resolution are optimized.

Next, it is possible to optimize the signal-to-noise ratio by maximizing the ratio between the faradaic current (i_F) and the baseline current measured right before the start of the oxidation peak (i_b), which corresponds to the second figure of merit ($FoM2$):

Equation 2 $$FoM2 = \frac{i_F}{i_b}$$

The maximization of *FoM*2 allows for lower limit of detection (LOD).

After performing all experiments, average values of both *FoM*1 and *FoM*2 were calculated for each factor-level combination, as reported in **Figure 26**.

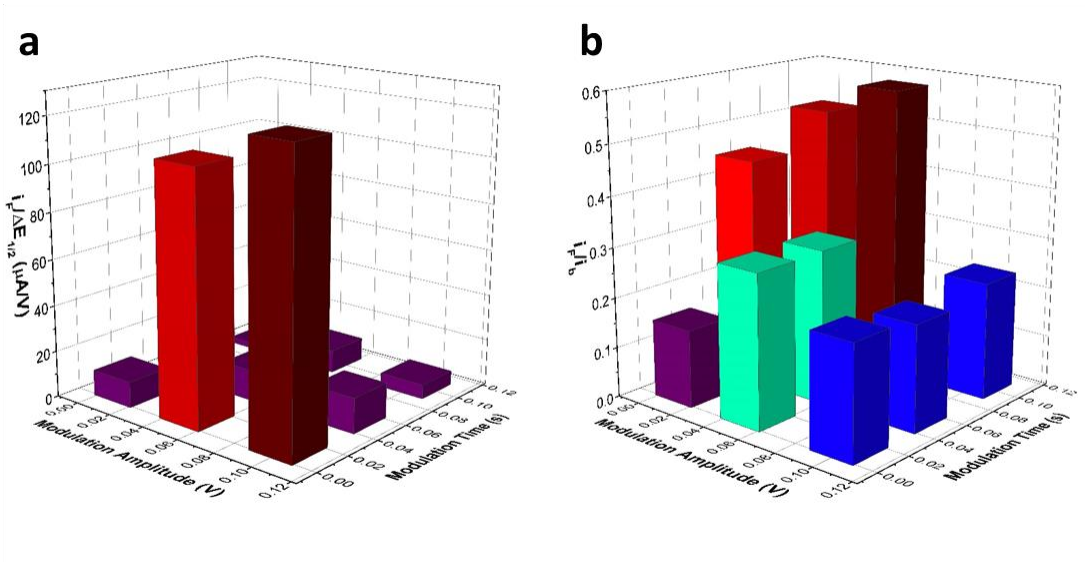

Figure 26 *Average values of a) FoM1 and b) FoM2.*

The following model was used to fit experimental data as a paraboloid, by multiple regression analysis:

$$FoM = b_0 + b_1\,MA - b_2\,MT - b_3\,MA\,MT - b_4\,MA^2 + b_5\,MT^2 + b_6 MA^2 MT + b_7 MAMT^2 + b_8 MA^2 MT^2$$

The calculated coefficients for FoM1 and FoM2 are listed in **Table 6** and **Table 7**, respectively.

Table 6 *Coefficient values from multiple regression of FoM1.*

Regression coefficient	***Corresponding term***	***Regression coefficient value***
b_0	*Intercept*	-0.076
b_1	*MA (V)*	13.280
b_2	*MT (s)*	17.570
b_3	*MA MT*	-660.019
b_4	MA^2	-101.758
b_5	MT^2	-122.732
b_6	MA^2MT	4749.985
b_7	$MAMT^2$	5990.258
b_8	MA^2MT^2	-46711.216

Table 7 *Coefficient values from multiple regression for FoM2.*

Regression coefficient	***Corresponding term***	***Regression coefficient value***
b_0	*Intercept*	-0.190
b_1	*MA (V)*	22.981
b_2	*MT (s)*	5.863
b_3	*MA MT*	-628.683
b_4	MA^2	-158.765
b_5	MT^2	-40.664
b_6	MA^2MT	4314.788
b_7	$MAMT^2$	4314.872
b_8	MA^2MT^2	-30199.261

The derived functions were graphed as 3D colormap surfaces, as reported in **Figure 27**, where the minimum value of each function is represented in purple, while the maximum is reported in red.

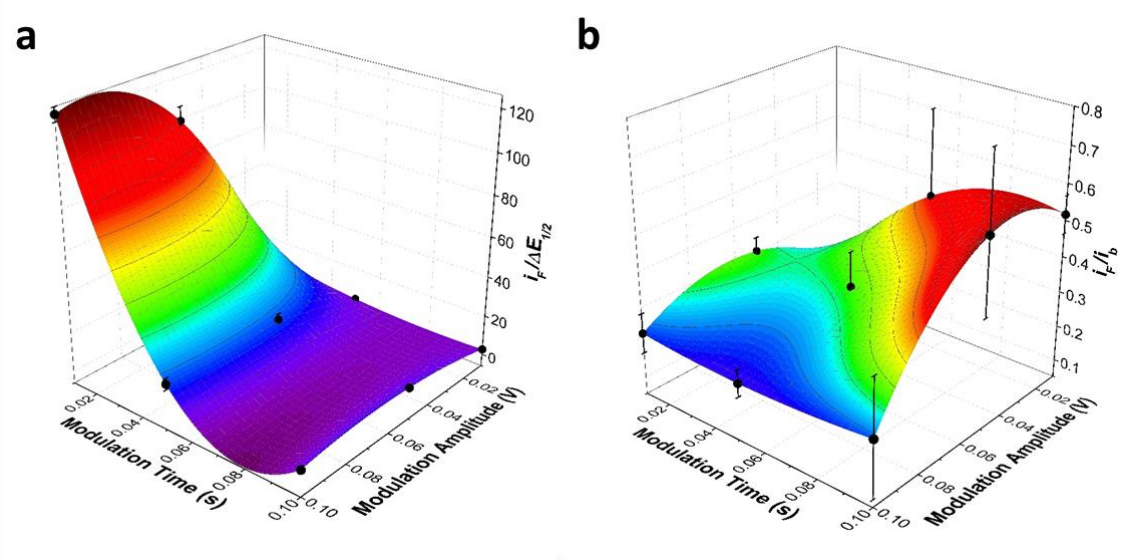

Figure 27 *3D colormaps for functions derived from multiple regression of a) FoM1 and b) FoM2.*

The DoE demonstrates that to maximize *FoM*1 low MT and high MA are required (**Figure 27a**). However, under these conditions the background cannot decay efficiently, resulting in low signal-to-noise ratio and affecting the LOD. Conversely, high MT and low MA promote higher values of *FoM*2 (**Figure 27b**), but generate low peak currents. Consequently, there is no univocal solution for concurrent maximization of *FoM*1 and *FoM*2.

To achieve an acceptable compromise between high sensitivity, peak resolution and low LOD, a third *FoM* was formulated (**Equation 3**), as the product between normalized *FoM*1 and *FoM*2.

Equation 3

$$FoM3 = \frac{i_F^2}{\Delta E_{1/2} i_b}$$

The calculated values for FoM3 are shown in **Figure 28**.

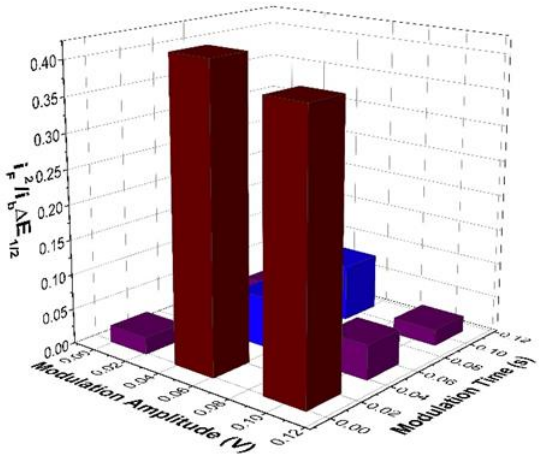

Figure 28 *Calculated values of FoM3.*

By applying the same polynomial model, a polynomial function was derived for *FoM*3 by multiple regression analysis. The calculated values for the coefficients are reported in **Table 8**.

Table 8 *Coefficient values from multiple regression of FoM3.*

Regression coefficient	***Corresponding term***	***Regression coefficient value***
b_0	*Intercept*	-0.190
b_1	*MA (V)*	22.981
b_2	*MT (s)*	5.863
b_3	*MA MT*	-628.683
b_4	MA^2	-158.765
b_5	MT^2	-40.664
b_6	MA^2MT	4314.788
b_7	$MAMT^2$	4314.872
b_8	MA^2MT^2	-30199.261

The derived function for *FoM*3 is graphed as a 3D colormap in **Figure 29**. From this surface of response it was possible to interpolate the optimal values of MT (0.01 s) and MA (0.075 V) to perform all following sensing experiments.

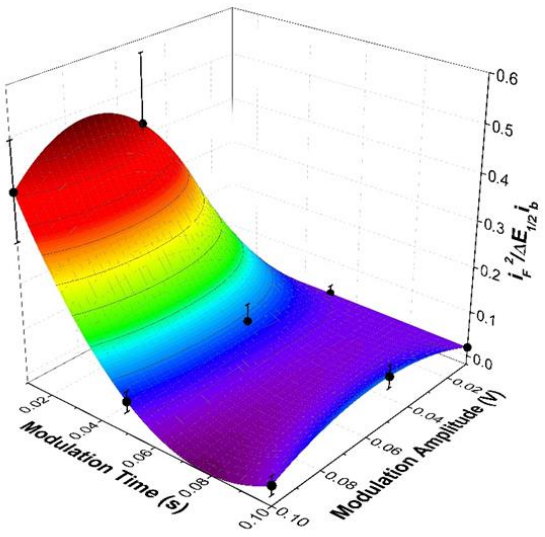

Figure 29 *3D colormap for the function derived from multiple regression of FoM3.*

2.2.4.2 Evaluation of Sensing Performance of SPCE/MWCNT-S-Au

The optimized conditions for sensing by performing DPV of eleven solutions of serotonin at different concentration (from 0.5 to 50 μmol L^{-1}) with SPCE/MWCNT-S-Au (**Figure 30a, 13b**).

The response of the modified SPCE was linear in the concentration range of 1-12 μmol L^{-1} (**Figure 30c**), with a calculated R^2 = 0.98934, sensitivity 17.4 μA L μmol^{-1} cm^{-2} and LOD of 1.9 μmol L^{-1}.

The repeatability of measurements was studied by comparing the linear response over three measurements with the same electrode (**Figure 30d**) and measuring the standard deviation of slope of registered calibration line (20.8%). The reproducibility standard deviation (9.8%) was determined over three calibration lines performed with three different modified electrodes (**Figure 30e**). The high repeatability standard deviation could be caused by adsorption phenomena and consequent partial passivation of the electroactive material in consecutive measurements.

Lastly, the influence of common interfering agents for detection of serotonin (ascorbic acid, AA, dopamine, DA, tryptophan, TRP, and uric acid, UA) was investigated, using DPV of 50 μmol L^{-1} solutions of each species in PBS/KCl 0.1 mol L^{-1} throughout a scan range of -0.20 to 0.50 V. As demonstrated by **Figure 30f**, ascorbic acid and tryptophan do not determine any response in the studied potential range, while an intense faradaic peak for the oxidation of dopamine can be observed at 0.10 V. In the optimized operational conditions, the peaks of dopamine and serotonin are well resolved, so that not only it is possible to neglect mutual interferences, but also to simultaneously detect the two neurotransmitters, expanding the potential applications of the electrocatalytic material for sensing. The only species affecting the detection of serotonin is uric acid, as the ΔV between the respective oxidation peaks is only 23 mV. However, the sensitivity for uric acid is significantly lower than that for serotonin, as the faradaic current associated with oxidation of uric acid is 8.8 times lower than the current generated by serotonin oxidation.

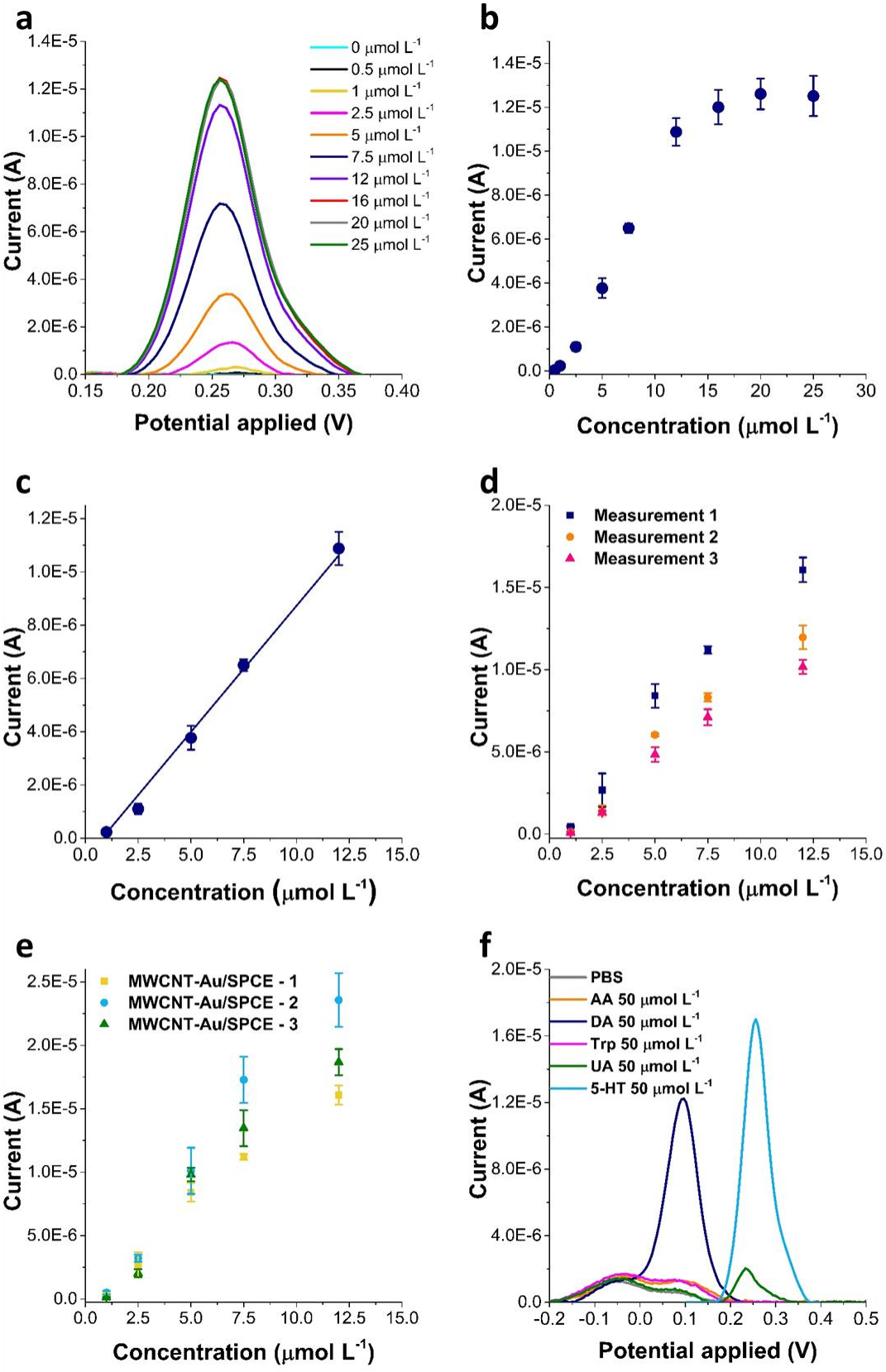

Figure 30 *a) DPV response of SPCE/MWCNT-S-Au to 0.5, 1.0, 2.5 , 5.0, 7.5, 12.0, 16.0, 20.0, 25.0 µmol L-1 solutions of serotonin (5-HT) in optimized conditions; b) Calibration curve in the range from 0.5 to 25.0 µmol L-1; c) Linear regression in the range from 2.5 to 12.0 µmol L-1; d)*

Repeatability for detection of serotonin (5-HT) with SPCE/MWCNT-S-Au; e) Reproducibility for detection of serotonin (5-HT) with SPCE/MWCNT-S-Au; f) DPV of different interfering agents (AA, DA, TRP, UA) at the concentration of 50 mmol L^{-1} in PBS buffer. DPV were recorded in a potential window comprised between -0.2 and 0.5 V, with the optimized parameters from DoE.

2.2.4.3 Manufacture of SPCE/MWCNT-S-Au/MIP

To enhance selectivity of the electrochemical sensor for serotonin, providing at the same time its surface with antifouling properties, a MIP was implemented in its design. Specifically, PPy was electropolymerized in situ on SPCE/MWCNT-S-Au. The MIP acts as an artificial receptor selective for serotonin and is prepared by polymerization of the monomer in the presence of the analyte that serves as a template.[50] The result is a highly cross-linked three-dimensional polymeric matrix.[53]

The synthesis of the MIP on the surface of the working electrode is schematized in **Figure 31**. First, SPCE/MWCNT-S-Au was incubated with a solution of pyrrole in presence of an excess of serotonin. Then, electropolymerization was performed *in situ*, by CV (5 consecutive scans from 0.0 to 1.0 V). Finally, serotonin is removed by electrochemical overoxidation, and the final sensor (SPCE/MWCNT-S-Au/MIP) is obtained.

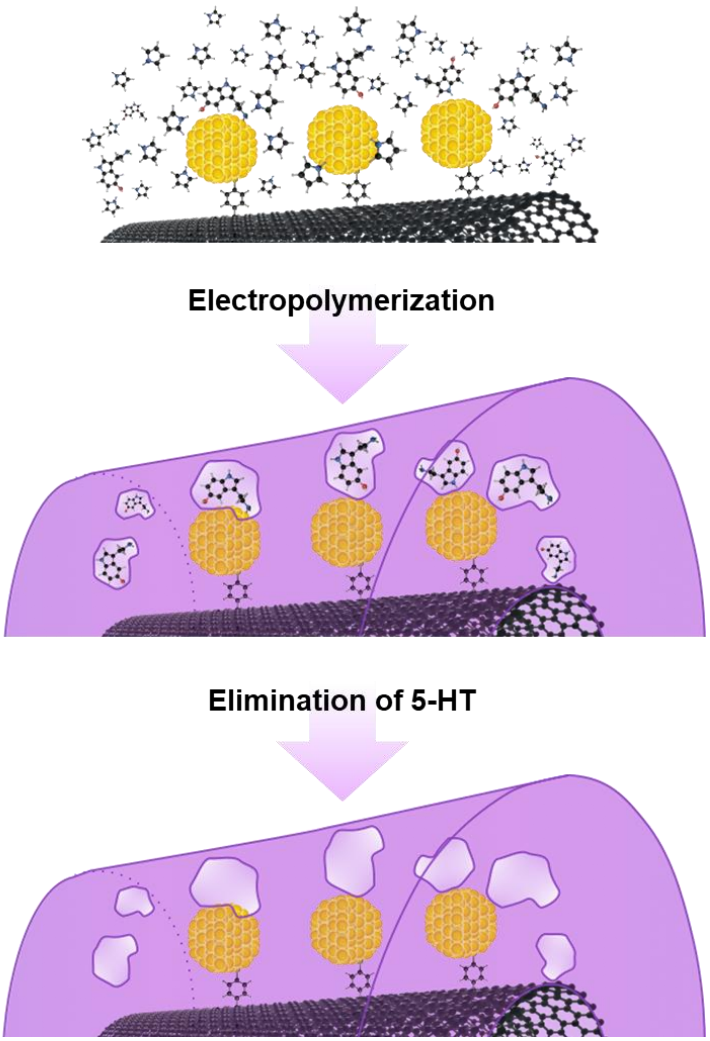

Figure 31 *Scheme for in situ synthesis of MIP on SPCE/MWCNT-S-Au.*

The surface of the modified SPCEs was characterized by scanning electron microscopy (SEM). **Figure 32a** shows the surface of SPCE/MWCNT-S-Au before the polymerization. It is possible to appreciate how MWCNT-S-Au are distributed to create a 3D network structure, which significantly enhances the total surface area of the working electrode. **Figure 32b** shows the surface of SPCE/MWCNT-S-Au/MIP, where the overall morphology of the 3D network is maintained after polymerization of PPy. From the statistical analysis of SEM micrographs, it was possible to determine the average diameter of MWCNTs before and after polymerization (30 ± 8 nm and 45 ± 10 nm respectively, **Figure 32c**). Consequently, it can be affirmed that the MIP layer covering the 3D network has an average thickness of 7.5 nm.

A non-molecularly imprinted polymer (NIP) was deposited on a modified electrode in place of the MIP, as a control (SPCE/MWCN-S-Au/NIP), using the same electropolymerization

process but in absence of serotonin. As shown in **Figure 32d**, the efficiency of the electrochemical response between SPCE/MWCNT-S-Au and the NIP control demonstrates the contribution of molecular imprinting to the performance of the sensor.

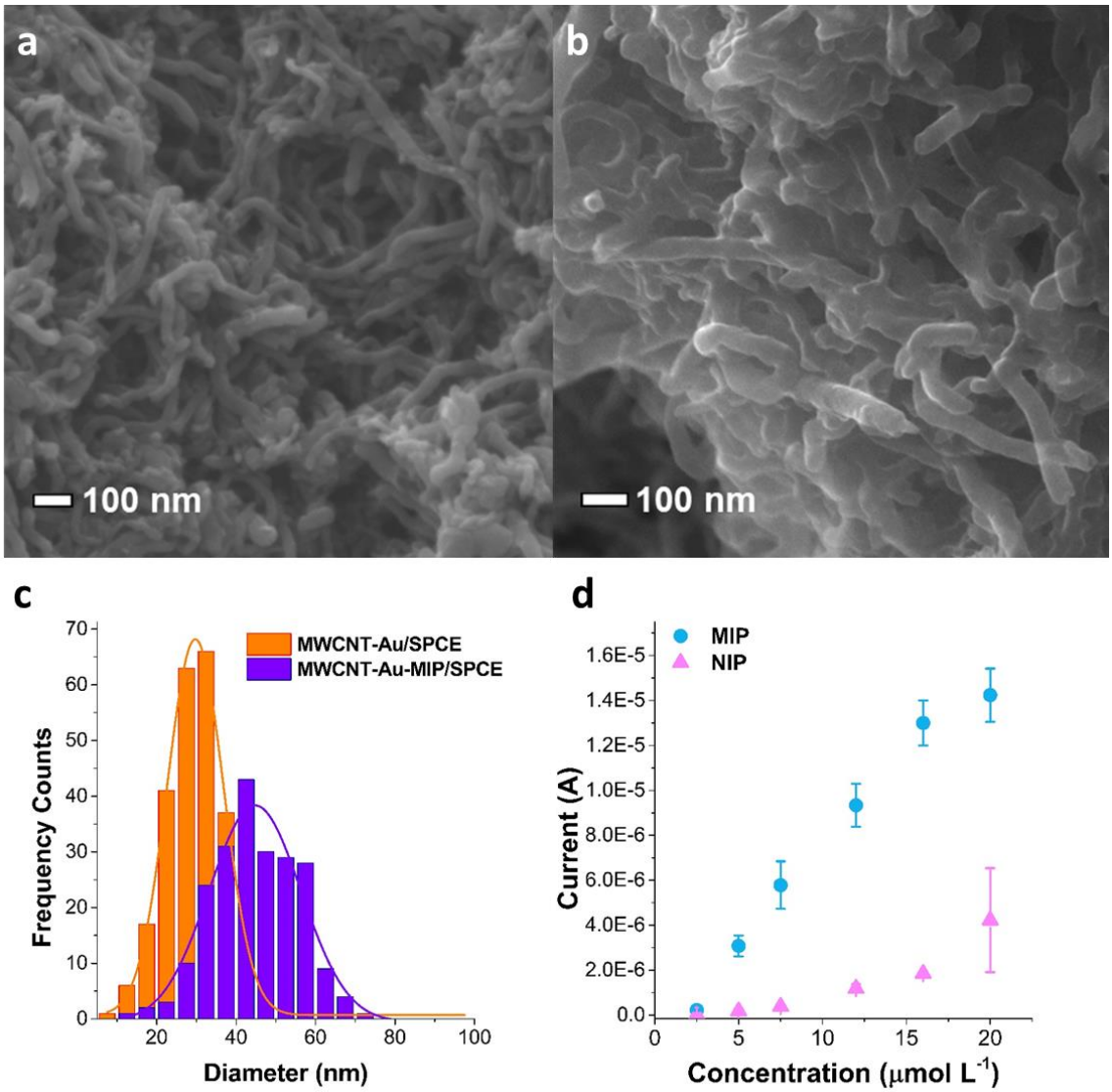

Figure 32 *a) SEM image of the working electrode of SPCE/MWCNT-S-Au; b) SEM image of the working electrode SPCE/MWCNT-S-Au/MIP; c) Statistical dimensional analysis of the diameter of MWCNTs in the modified SPCE; d) DPV response of SPCE/MWCNT-S-Au/MIP and SPCE/MWCNT-S-Au/NIP to 2.5, 5.0, 7.5, 12.0, 16.0, 20.0 μmol L^{-1} solutions of 5-HT. DPV were recorded in a potential window comprised between -0.2 and 0.5 V, with the optimized parameters from DoE.*

2.2.4.4 Evaluation of Sensing Performance of SPCE/MWCNT-S-Au/MIP in different matrices

The final sensor (SPCE/MWCNT-S-Au/MIP) was tested to evaluate its performance both in PBS and in a more complex biological matrix that is fetal bovine serum (FBS).

First, the response in PBS was studied by performing DPV measurements of 8 solutions of serotonin (from 1µmol L^{-1} to 25 µmol L^{-1}), using the optimized conditions derived from DoE. The addition of the MIP to the design of the sensor led to a decrease of the sensitivity and higher LOD with respect to SPCE/MWCNT-S-Au. Moreover, the linear range of concentration shifted from 1 - 16 µmol L^{-1} to 7.5-25 µmol L^{-1}. The worsening of the performance was imputed to the MIP covering the electroactive material surface and slowing down the diffusion of the analyte towards the catalytic sites.

To favor the diffusion of serotonin through the polymeric network and enhance sensitivity, adsorptive stripping was applied to pre-concentrate serotonin on the surface of the working electrode and in the polymeric network, before sweeping the potential.[83] This way, it was possible to fully exploit two characteristic properties of the MIP that are its high capacitance[80] and the selective supramolecular interactions.

As serotonin is positively charged at neutral pH, the application of negative potentials was investigated to foster the migration of serotonin molecules towards the electrode surface. The application of a potential of -300 mV for 10 s before each measurement was found out to be effective in increasing the response of the sensor (**Figure 33**). Moreover, the use of negative polarization can be beneficial by repelling negatively charged species, like uric acid, which was previously identified as the major interfering agent for this system.

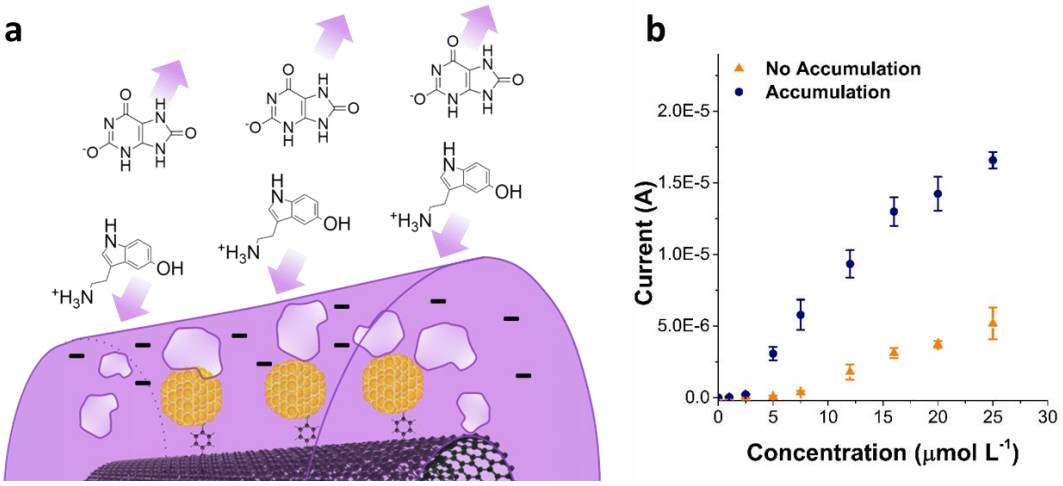

Figure 33 *a) Pre-accumulation of 5-HT on the surface of the electrode; b) calibration curves for 5-HT with SPCE/MWCNT-S-Au/MIP with and without adsorptive stripping. Calibration curves were obtained from DPV measurements in a potential window comprised between 0.1 and 0.4 V, with the optimized parameters from DoE.*

In the final conditions, by implementing the pre-accumulation step, the sensor exhibits a broader linear range, from 2.5 to 20 μmol L^{-1}, with excellent linearity (R^2 = 0.99901), sensitivity of 8.0 μA L μmol^{-1} cm^{-2} and a LOD of 1.7 μmol L^{-1} (**Figure 34a, b**). Furthermore, the presence of the MIP enhances repeatability and reproducibility, with SD of 4.4% and 1.1% respectively (**Figure 34c, d**), solving the problems of adsorption and passivation shown with SPCE/MWCNT-S-Au. This level of reproducibility is better than most sensors previously reported in literature (

Table 9).

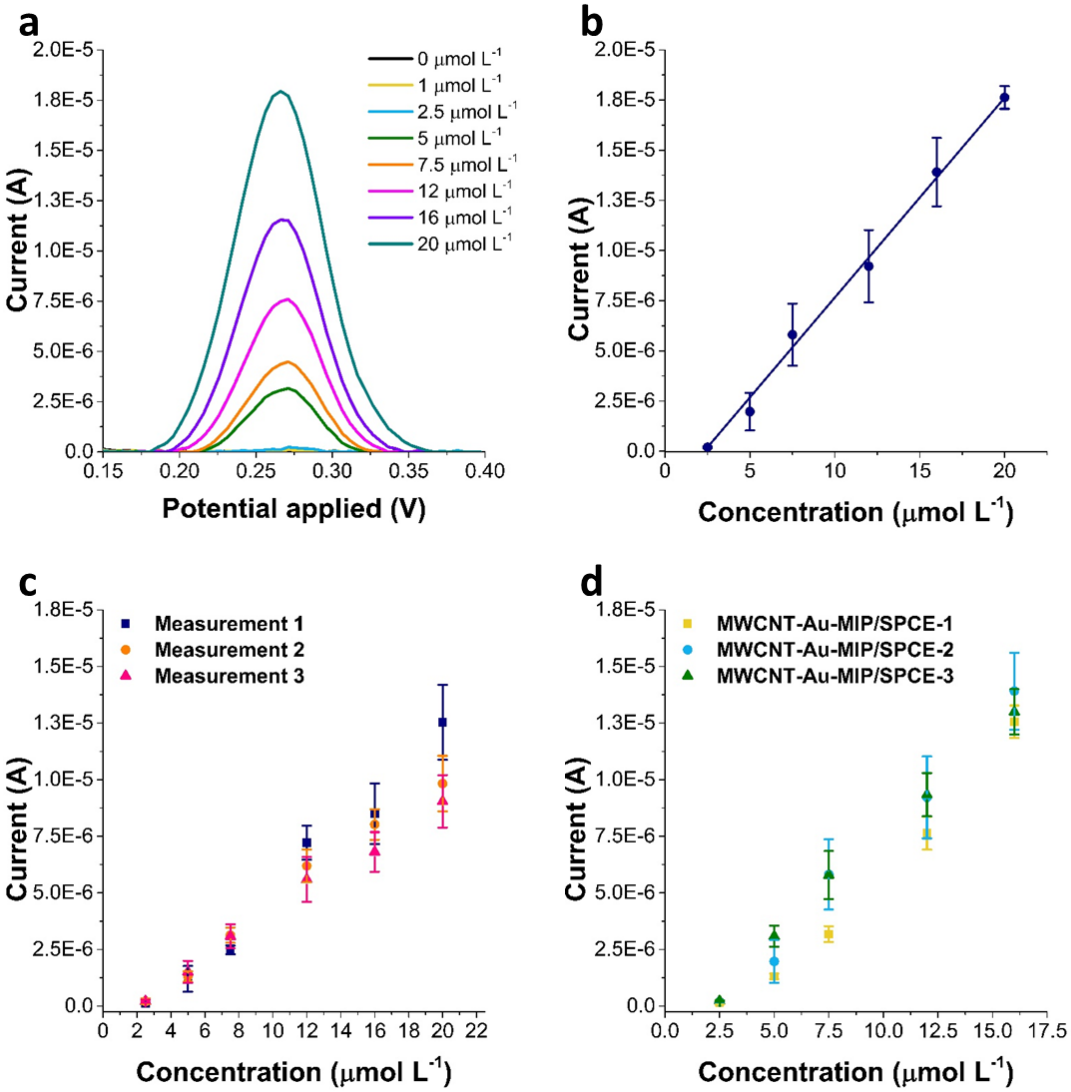

Figure 34 *a) DPV response of SPCE/MWCNT-S-Au/MIP to different concentrations of 5-HT in PBS; B) calibration curve for SPCE/MWCNT-S-Au/MIP in PBS; c) repeatability data for detection of 5-HT with MWCNT-Au/SPCE; d) reproducibility data for detection of 5-HT with MWCNT-Au/SPCE.*

Table 9 Comparison of different electrochemical sensors from literature, for detection of 5-HT, in differential pulse voltammetry.

Electrode	LOD	Linear range	Repeatability (RSD %)	Reproducibility (RSD %)	Ref.
GCE-MWCNT-Nafion/Ni(OH)$_2$NPs	15 nmol L^{-1}(1)	0.05 - 25 µmol L^{-1}	2.20%	-	[5]
GCE-MWCNT-Chit	50 nmol L^{-1}	0.05 - 16 µmol L^{-1}	-	2.6 %	[6]
GCE-GO-MIP(Chit)	1.6 nmol L^{-1} (2)	0.005 - 10 µmol L^{-1}	8.7 %	4.9 %	[7]
GCE-WO$_3$NPs	1.42 nmol L^{-1} (1)	0.01 - 10 µmol L^{-1}	4.1-3.8%	3.5- 3.9%.	[8]
SPCE-FeC-AuNPs	17 nmol L^{-1} (2)	0.05 - 20 µmol L^{-1}	-	4.40%	[9]
B,N-doped graphene	9-266 nmol L^{-1} (1)	0.10 - 224 µmol L^{-1}	3.05%	2.08% -3.16%	[10]
TiO$_2$/AuNPs-PNB (in deep eutectic solvent)	2.47 nmol L^{-1} (1)	0.5 - 10 µmol L^{-1}	3.44%	4.88%	[11]
SPCE-ZnONR-PMB	1.91 nmol L^{-1} (1)	0.1 - 25 µmol L^{-1}	4.84%	5.91%	[12]
SPCE-MWCNT-AuNPs-MIP	1.7 µmol L^{-1} (3)	2.5 - 20 µmol L^{-1}	4.40%	1.10%	This work

(1) It is not reported how σ is calculated. (2) σ is calculated as the standard deviation among blank measurements. (3) σ is calculated as the standard error on the linear regression.

At concentrations higher than 20 μmol L^{-1}, a limit current and plateau are reached. By CV, it was possible to understand the cause of the observed behavior, studying the correlation between the scan rate and the current intensity. The scan rate influences the peak current, since usually faster scan rates produce higher currents.[84] The correlation between the peak current and the scan rate, for electrochemically reversible processes involving redox species that are freely diffusing from bulk solution to the surface of the electrode, is expressed by the Randles-Sevcik equation (**Equation 4**).

Equation 4 $$i_p = 0.446\, nFAC^0 \left(\frac{nFvD}{RT}\right)^{\frac{1}{2}}$$

Where:

- i_p (A) is the peak current;
- n is the number of electrons involved in the redox process;
- F is the Faraday constant (=96 485.3321 s A mol^{-1});
- A is the area of the electrode (cm^2);
- C^0 is the concentration of the analyte (mol cm^{-3});
- D is the diffusion coefficient of the analyte (cm^2 s^{-1});
- R is the ideal gas constant (=8,314472 J K^{-1} mol^{-1});
- T (K) is the absolute temperature;
- v is the scan rate (V s^{-1}).

On the other hand, when adsorption of the analyte onto the surface of the electrode is involved in the reaction mechanism, the system does not follow the Randles-Sevcik equation, but **Equation 5**.

Equation 5 $$i_p = \frac{n^2F^2}{4RT}\, vA\Gamma^*$$

Where Γ^* (mol cm-2) is the coverage factor.[84] Therefore, it is possible to understand if an electrochemical process is diffusion-dependent or adsorption-dependent, by performing CVs at different scan rates and studying the evolution of i_p. If i_p is linearly dependent on $v^{1/2}$, the process is diffusion-dependent, while on the contrary, if i_p is linearly dependent on v, the process is governed by adsorption.

As shown in **Figure 35**, for oxidation of serotonin at the interface of SPCE/MWCNT-S-Au, electron transfer takes place via a surface-adsorbed species, since i_p increases linearly with v (R^2 = 0.9982).

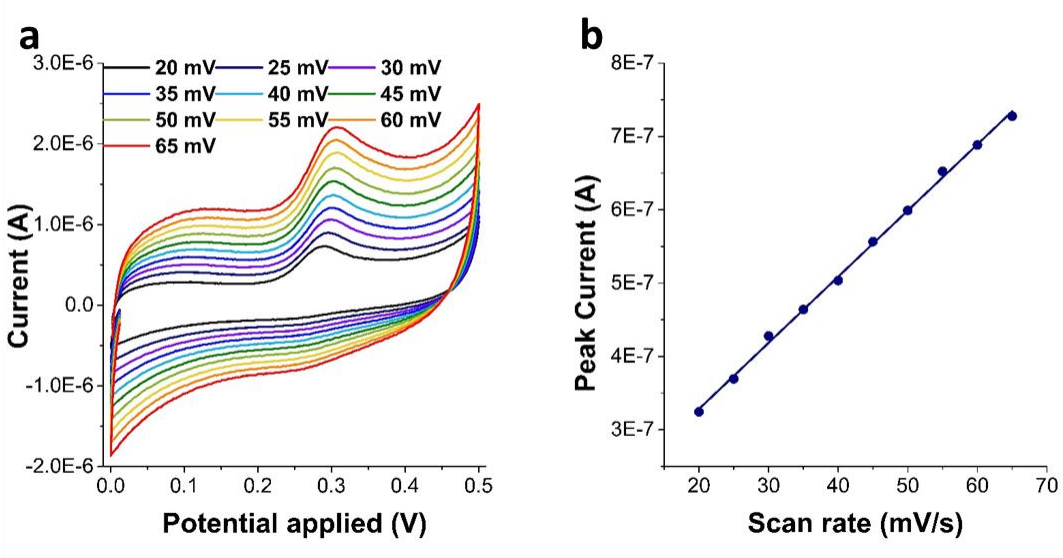

Figure 35 *a) Cyclic voltammograms of 12 µmol L^{-1} solution of serotonin at different scan rates with MWCNT-S-Au/SPCE; b) Linear dependence of peak current vs scan rate.*

From these data, it is possible to affirm that at concentrations higher than 20 µmol L^{-1} the catalytic sites of the electroactive material are saturated, consequently to serotonin adsorption.

Finally, we demonstrated that the sensor functions in complex matrix, by performing sensing of serotonin in spiked solutions of FBS. This medium provides a challenging proving ground for the proposed sensor, since it contains more than 1,000 different components, including small molecules such as hormones and lipids, and bigger species like proteins. The test in FBS demonstrates the importance of the MIP for the design of this sensor, as in absence of the MIP, the exposed surface of the electrocatalytic material is easily attacked by biomolecules, which adsorb irreversibly on the surface of the electrode and passivate it. As a result of the adsorption, a severe shift of the oxidation potential and loss of sensitivity affect the sensor (**Figure 36a**).

The introduction of the MIP prevents the fouling of the electrode surface, blocking most biomolecules far from the catalytic surface. As a result, the response of SPCE/MWCNT-S-Au/MIP is maintained in FBS, with no significant potential shift (**Figure 36b**), and is linear in the concentration range of 1-12 µmol L^{-1} (**Figure 36c**), with R^2 = 0.9922. The sensitivity (6.7 µA L µmol^{-1} cm^{-2}) and LOD (1.0 µmol L^{-1}) are comparable to data retrieved in PBS. The

oxidation current registered when no serotonin is spiked can be attributed to serotonin and uric acid that are naturally occurring in FBS.

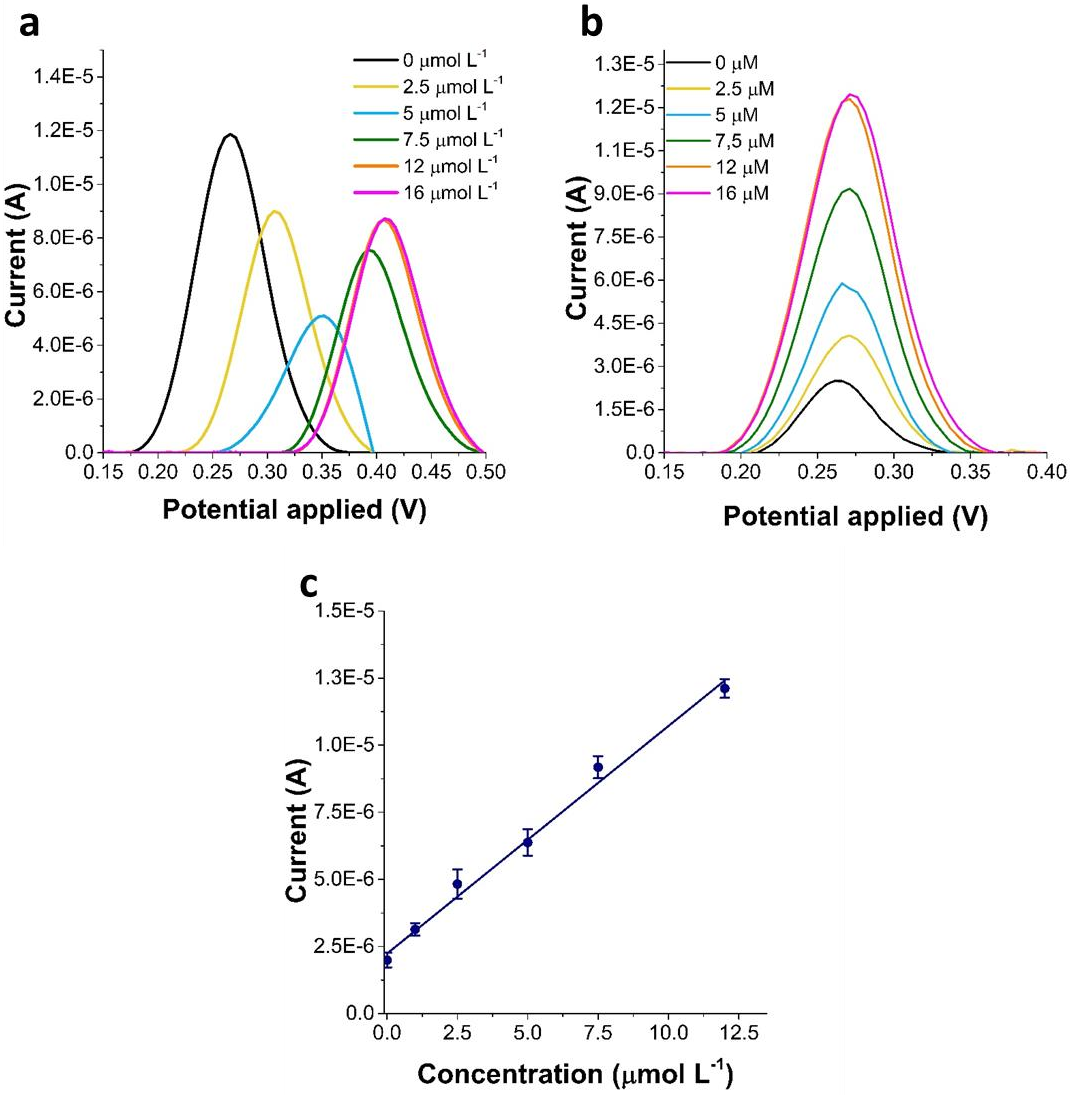

Figure 36 *a) DPV response of SPCE/MWCNT-S-Au to different solutions of 5-HT in FBS/PBS 1:4; b) DPV response of SPCE/MWCNT-S-Au/MIP to different concentrations of 5-HT in FBS/PBS 1:4; c) calibration curve for SPCE/MWCNT-S-Au/MIP in FBS/PBS 1:4.*

2.2.5 Design of Electrochemical Sensor for Dopamine at Cellular Level

MWCNT-S-Au were implemented in a voltammetric and amperometric electrochemical biosensor for detection of dopamine at cellular level. The sensor design is based on a modified indium tin oxide (ITO) coated glass that serves as working electrode, in a three-electrode setup with a Ag/AgCl microelectrode as reference and a platinum wire as counter electrode. The final sensor is meant to detect real-time variations of dopamine concentration in neuronal cell cultures, directly grown on the surface of the modified working electrode. This function may be extremely useful for *in vitro* screening of drugs for neurodegenerative diseases targeting directly the activity of dopaminergic neurons.

The first step for the manufacture of the sensor was the fabrication of squared wells by 3D-printing, which were attached on the surface of the pristine ITO coated glass. These wells are used for the incubation and growth of neuronal cells in cell culture media. The inside of the wells and the surface of the ITO coated glass were subsequently covered with a layer of pristine MWCNTs, by dropcasting. The pristine MWCNTs greatly enhance the active surface of the electrode, favoring the charge transfer from the catalytic sites to the ITO surface. Finally, MWCNT-S-Au are deposited by dropcasting on top of the MWCNTs, to serve as electrocatalytic sites for dopamine oxidation. **Figure 37** illustrates the design of the final sensor.

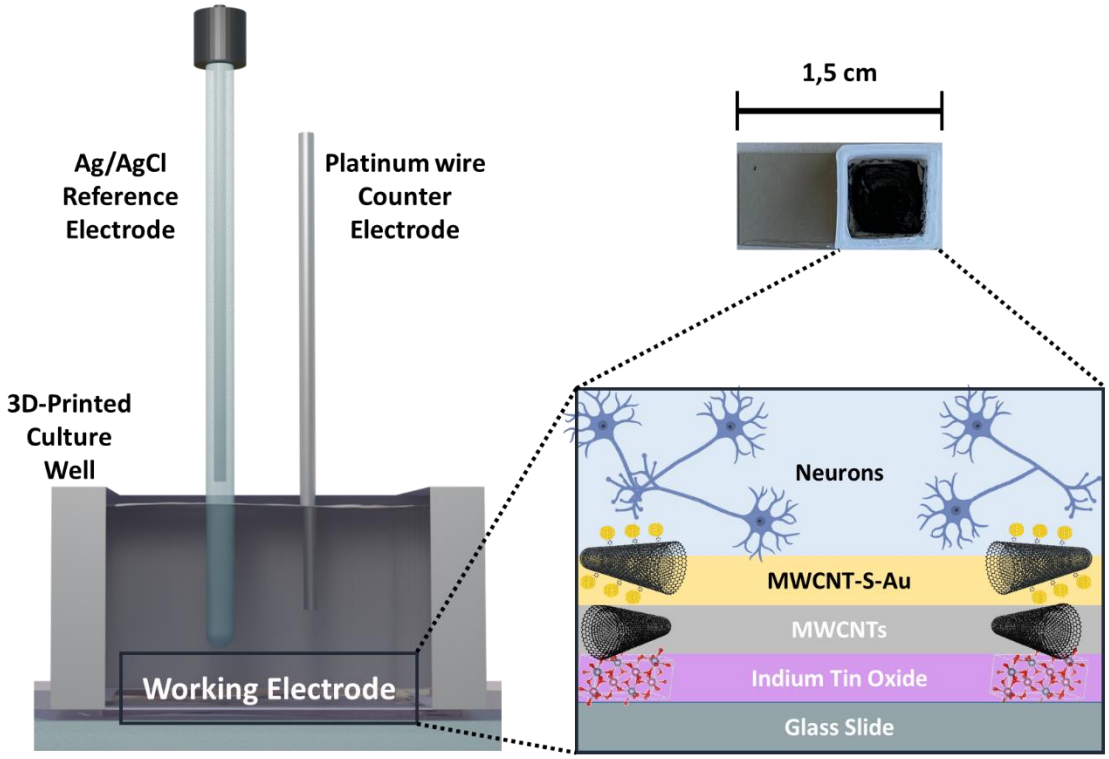

Figure 37 *Schematic representation of the sensor setup for dopamine detection at cellular level.*

2.2.5.1 Neuron Differentiation from Induced Pluripotent Stem Cells

To test the performances of the obtained sensor for *in vitro* detection of dopamine, a positive and a negative control were necessary. The positive control consisted of dopaminergic neurons, *i.e.* neurons that produce dopamine through tyrosine hydroxylase (TH).[85] The negative control consisted of glutamatergic neurons that do not express TH, and use glutamate as main transmitter.[86] The different types of neurons were all grown from human induced pluripotent stem cells (iPSC), by a chemical and genetical induction, via two neurogenic factors from viral vector transfection.

First, a protocol for the differentiation of neuronal cells on MWCNTs was established, monitoring the growth of neurons *in vitro*. Bright field optical microscopy, fluorescence microscopy with immunostaining and quantitative PCR were used to follow their maturation and to assess their degree of differentiation.

Bright field images show how iPSCs diversify in 25-30 days, going from the almost spheroidal shape typical of undifferentiated stem cells of **Figure 38a**, to the branched neuronal network with well-formed axons of **Figure 38b**.

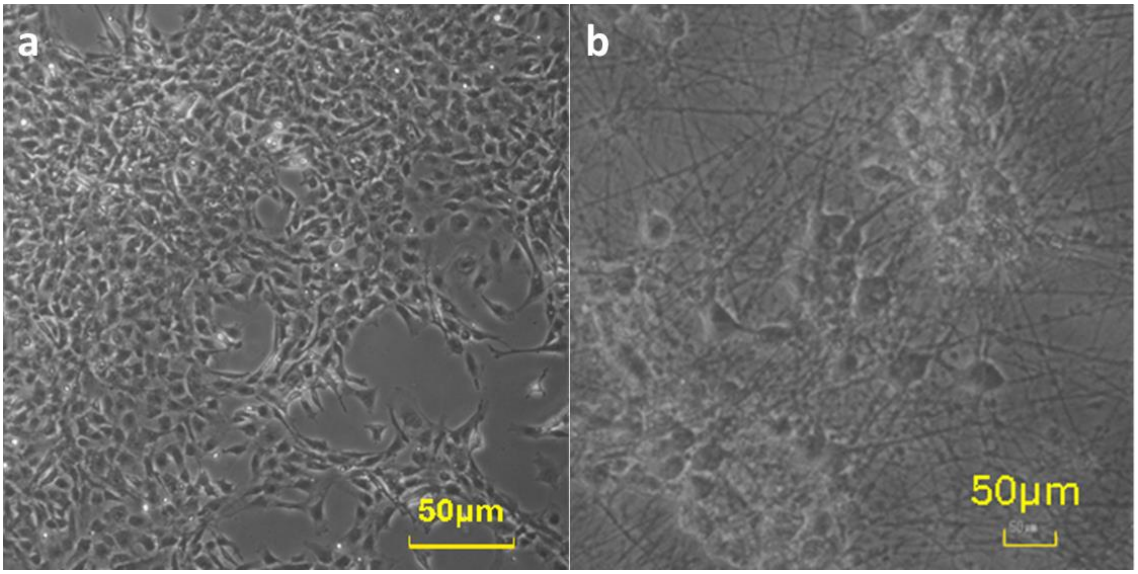

Figure 38 *a) iPSCs at day 0 after viral transfection; b) fully differentiated dopaminergic neurons from iPS cells, at day 25.*

Immunostaining of dopaminergic neurons was performed with neurofilament H antibody and TH antibody assays. Neurofilament H antibody staining (**Figure 39a**) highlights the formation of mature axons constituting the neuronal network. TH antibody staining (**Figure 39b**) assesses the presence of TH in neurons, which is fundamental requirement to define neuronal subtype and neuronal phenotype confirmation.

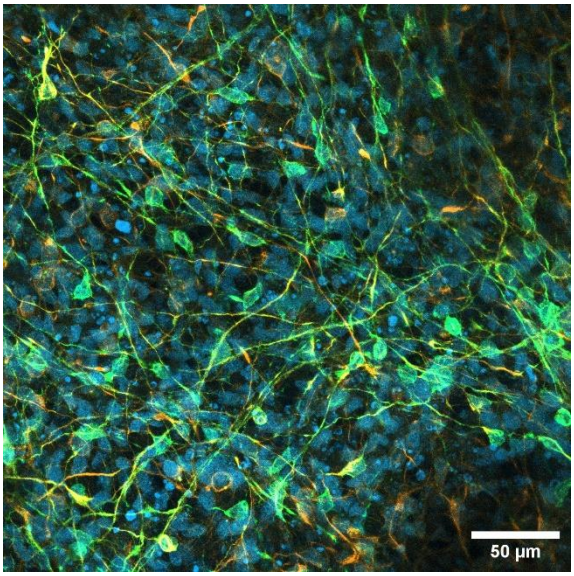

Figure 39 *Merged confocal image of iPSC-derived dopaminergic neurons grown on MWCNT-S-Au, with Neurofilament H antibody staining (yellow channel), TH antibody staining (green channel) and DAPI highlighting the nuclei (blue channel).*

The gene expression of TH was monitored also by quantitative PCR, by amplifying the corresponding mRNA strand. As shown in **Figure 40**, the expression for the mRNA coding

the synthesis of TH increases sensitively going from the undifferentiated cells (PUNA) to the mature dopaminergic neurons (DOP), but does not change when compared to glutamatergic neurons (GLUT). Moreover, it is interesting to see how, for the same PCR, the presence of MWCNTs fosters the growth and differentiation of neurons (DOP/MWCNTs), leading to huge enhancement of the TH gene expression.

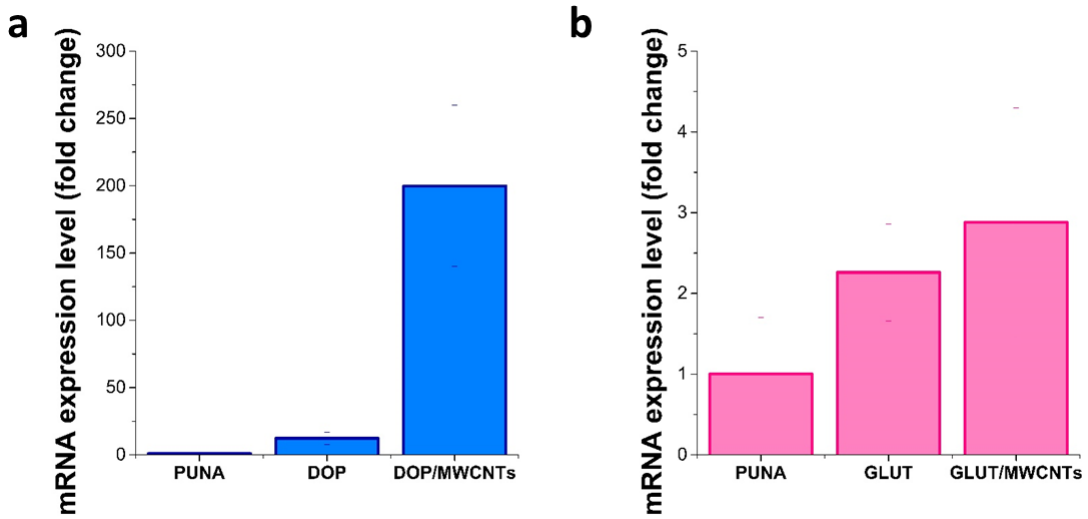

Figure 40 *Data for TH gene expression from PCR performed on a) dopaminergic neurons from iPS cells and b) glutamatergic neurons from iPS cells.*

2.2.5.2 Optimization of Electrocatalytic Performance of MWCNT-S-Au for Dopamine

Once the protocol for the cell differentiation on MWCNTs was established, it was necessary to optimize the electrochemical response of the sensor. Once again, the technique of choice is DPV, for its superior sensitivity and the possibility of eliminating background interferences. Using the same factorial design presented for serotonin detection, DoE was performed to optimize the experimental conditions for electrocatalytic oxidation of dopamine with MWCNT-S-Au as electrocatalyst. Using the same equations (**Equation 1**, **2** and **3**), we defined the figures of merit for dopamine oxidation, which are reported in **Figure 41**. The optimal values of MA and MT to optimize *FoM*3 were interpolated from **Figure 41c** and are 0.057 V and 0.062 s respectively.

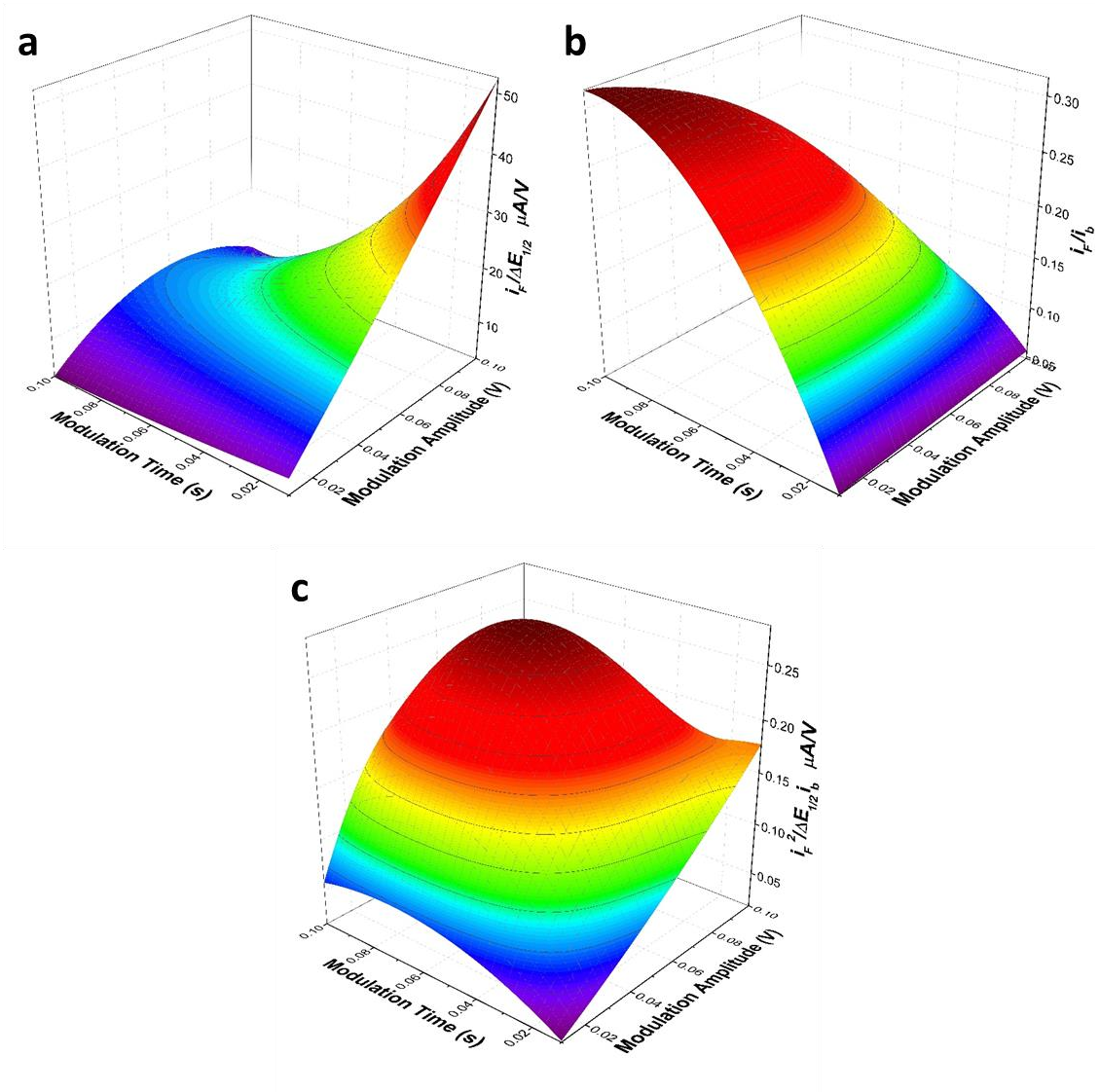

Figure 41 *3D colormaps for the function derived from multiple regression of a) FoM1, b) FoM2 and 3) FoM3 for dopamine oxidation.*

2.2.5.3 Evaluation of Sensing Performance of ITO/MWCNT-S-Au

Sensing of dopamine was performed in Krebs-Ringer buffer. This is a bicarbonate buffer that provides neurons with an isotonic environment, ensuring homeostasis, but at the same time it is free of growth factors and hormones used during the differentiation phase, which could interfere with the measurement.

First, to test the optimized conditions from DoE, a modified ITO coated glass with MWCNT-S-Au (ITO/MWCNT-S-Au) was used to perform a calibration of the sensor in absence of cells. In Krebs-Ringer buffer, the voltammogram presents an intense peak centered at 0.166 V

(**Figure 42a**). The LOD was calculated to be 62.2 nmol L^{-1} and the response is linear in the concentration range going from 0.062 to 10 µmol L^{-1} (**Figure 42b**).

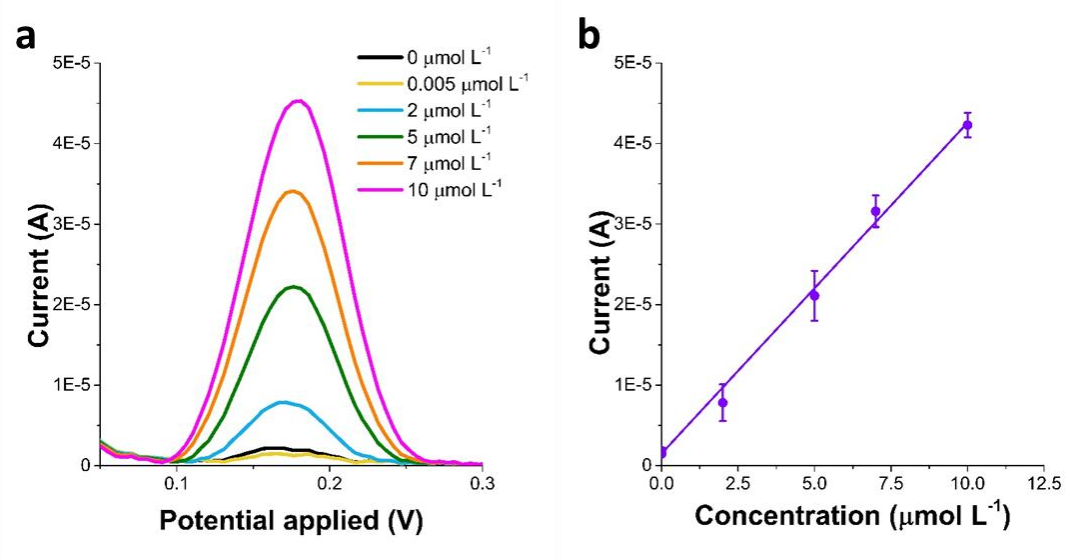

Figure 42 *a) DPV response of different concentrations of dopamine in Krebs-Ringer buffer; b) calibration curve in the concentration range from 0.005 to 10 µmol* L^{-1}.

2.2.5.4 Detection of Dopamine at Cellular Level

The final step was to carry out detection of dopamine in presence of the neuron culture. In the optimized experimental conditions from DoE, it was possible to detect dopamine produced by dopaminergic neurons upon application of two different stimuli: KCl was added to increase the concentration of K^+ ions in the medium, causing depolarization of the cellular membrane and inducing the release of more dopamine at the level of synapses.[87] On the other hand, benztropine, which is a common drug used for treatment of depression, was used to observe the effect of the inhibition of dopamine reuptake.[88,89] In both cases, the modified electrode with dopaminergic neurons (ITO/MWCNT-S-Au/DOP) showed an increase of the signal correlated with dopamine oxidation (**Figure 43a**).

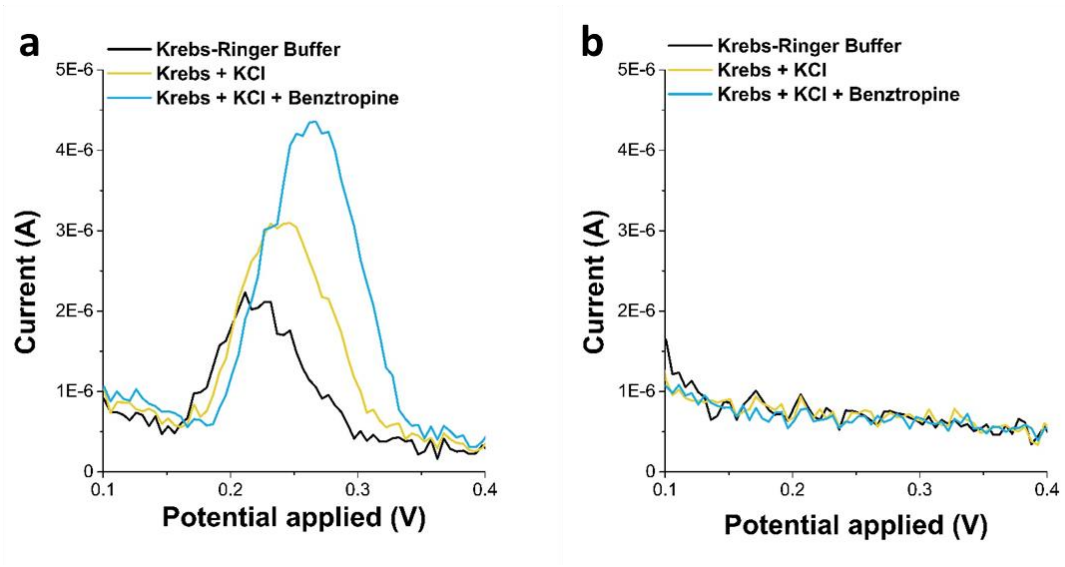

Figure 43 *DPV of dopamine produced in vitro with a) ITO/MWCNT-S-Au/DOP and b) ITO/MWCNT-S-Au/GLUT.*

When the same experiment was carried out with the modified electrode with glutamatergic neurons (ITO/MWCNT-S-Au/GLUT), no peak was recorded for dopamine oxidation, either before or after the external stimulation (**Figure 43b**).

The peak recorded before addition of KCl and benztropine in DOP neurons can be related to the basal production of dopamine by the DOP neurons. However, the signal could be induced by the application of the potential pulses in DPV, which could stimulate the DOP neurons' activity.

To rule out the effect of the potential variation, the release of dopamine was studied also in chronoamperometry (CA). As for CA the potential applied is constant, any variation of current is caused only by the specific response of the neurons to chemical stimuli. As shown in **Figure 44**, the faradaic current registered increases by 85 nA upon addition of KCl and again by 73 nA upon addition of benztropine.

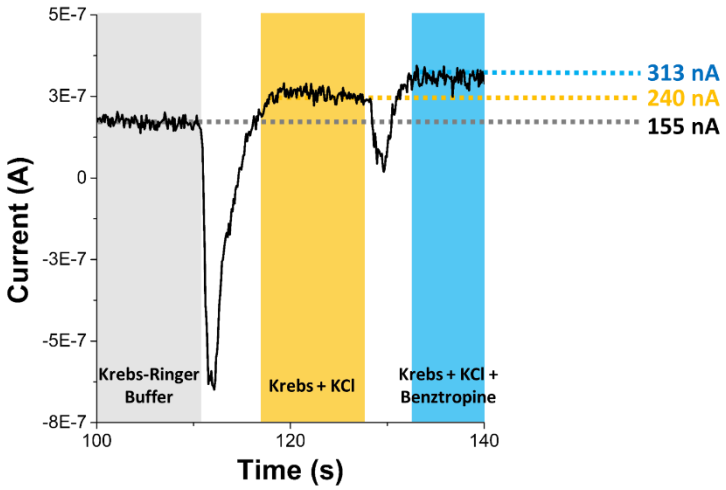

Figure 44 *Chronoamperogram of ITO/MWCNT-S-Au/DOP with addition of KCl (yellow) and benztropine (light blue).*

These data from CA are interesting not only because they demonstrate that the DPV response is chemically induced and does not depend on the application of consecutive potential sweeps, but also because it shows that the sensor can be used for real-time monitoring of cell activity.

2.3 Conclusions

In conclusion, a new nanocomposite, based on MWCNTs functionalized with MVS AuNPs, was synthesized and successfully applied for voltammetric sensing of two monoamine neurotransmitters, serotonin and dopamine, in complex biological matrices.

To anchor the MVS AuNPs, MWCNTs were functionalized with thiol groups. The functionalization was carried out with an addition-cleavage approach that allowed protecting SH moieties before the anchoring of the AuNPs, and at the same time controlling the length of the linkers, minimizing the distance between the catalytically active sites of AuNPs and the conductive transducing material. This resulted in improved electron transfer, which in turn enhanced the sensitivity of the final sensors. The material proved electrocatalytic for not only serotonin and dopamine, but also for the oxidation of other phenolic compounds such as epinephrine, gallic acid and 2-chlorophenol, and for reduction of hydrogen peroxide and oxygen.

The nanocomposite was used to design a voltammetric sensor for serotonin. First, MWCNT-S-Au were deposited on the working electrode of commercial screen-printed carbon electrodes. Then, a molecularly imprinted polymer selective for serotonin was used to complete the sensor design, providing antifouling properties and enhancing selectivity of the sensor. The polymer was electropolymerized *in situ*, growing as a thin layer (7.5 nm) on the surface of MWCNT-S-Au. The polymer is characterized by high capacitance, which was exploited to pre-accumulate the analyte in its cavities, by applying negative polarization before each measurement. The performances of the sensor for serotonin sensing were optimized by application of DoE, reaching optimal conditions in terms of sensitivity, LOD and resolution. The final sensor was able to detect serotonin in few seconds in a range of concentration comprised between 1.6 and 20 μmol L^{-1}, demonstrating its potential in monitoring of diseases correlated with high blood concentration of serotonin, such as serotonin fatal syndrome, carcinoid syndrome or coronary artery disease.

MWCNT-S-Au were implemented also in the design of a voltammetric and amperometric sensor for detection of dopamine at cellular level. In this case, MWCNTs and MWCNT-S-Au were deposited on ITO-coated glass slides that functioned as working electrodes, inside a PLA cubic cell. Then, neurons were grown and differentiated from iPS cells directly on MWCNT-S-Au: dopaminergic neurons, which produce dopamine as main transmitter, were used as positive control, while glutamatergic neurons that use glutamate as transmitter served as negative control. The final sensor was able to detect dopamine at cellular level, and to monitor fluctuation of dopamine concentration upon chemical stimulation of the cells, by addition of KCl and benztropines. This technology could prove extremely helpful for screening of drugs and treatments for neurodegenerative disease, as a responsive platform for *in vitro* studies.

2.4 Experimental Section

2.4.1 Materials and Instruments

MWCNTs were purchased from Nanostructured & Amorphous Materials Inc. and purified as described in section 2.4.4. 4-aminothiophenol was purchased from TCI chemicals and used without further purification. All other reagents and analytes were purchased from Sigma Aldrich and used without further purification.

^{1}H-NMR spectra were registered with a Varian 400 MHz spectrometer (^{1}H: 400 MHz, ^{19}F: 376 MHz, ^{13}C: 101 MHz). Fourier transform infrared spectroscopy (FTIR) spectra were registered using a FT-IR Bruker Invenio-X in attenuated total reflectance (ATR) mode with diamond crystal.

Differential Scanning Calorimetry (DSC) measurements were performed on Discovery DSC 250 (TA Instruments), where 2.6 mg of $DTDBBF_4$ were weighed in a Tzero Aluminium Hermetic pan and were heated from 25°C to 250°C, with a ramp of 5°C/min.

Thermogravimetric analysis (TGA) measurements were carried out with a TGA Discovery (TA Instruments), where 0.5 mg of material were weighed in a Platinum HT pan and were heated in N_2 atmosphere (for MWCNTs, disulfide-functionalized MWCNTs, MWCNT-SS, and thiol-functionalized MWCNTs, MWCNT-SH) or air (for MWCNTs and gold-nanoparticles-functionalized MWCNTs, MWCNT-S-Au). First, an isotherm at 100°C was applied 20 min, subsequently the samples were heated to 800°C with a ramp of 10°C/min.

X-ray Photoelectron Spectroscopy (XPS) spectra were registered with an XPS/UPS – SPECS SAGE HR-100 equipped with a 100 mm radius PHOIBOS analyzer, where 421 Mg Kα X-ray source was used. The samples were prepared by drop-casting 80 µL of a 0.5 mg/mL suspension of material in Milli-Q water, on a gold-coated substrate (for MWCNTs, MWCNT-SS, MWCNT-SH) or silicon oxide substrate (for MWCNT-S-Au). The samples were then let dry under vacuum. The spectra were fitted using CasaXPS and calibration was performed using the major component of the C high-resolution spectrum as a reference at 284.5 eV, which is the value reported for sp^2 carbon for CNTs.[90]

For inductively coupled plasma optical emission spectrometry (ICP-OES, PerkinElmer Optima 8000), the metal-containing acetone solution (0.5 mL) was heated over a heating plate in a porcelain crucible, in the presence of *aqua regia* (2 mL), four times and the solid residue was dissolved in 0.5 M aqueous HCl and diluted with de-ionized water to a final volume of 50 mL.

For inductively coupled plasma mass spectrometry (ICP-MS) analysis, Thermo Fisher iCap-Q, equipped with a He gas kinetic energy discrimination (KED) collision/reaction cell, was used. MWCNT-S-Au were digested in 2 mL of a HCl/HNO_3 (1:3) mixture, in a microwave digester, applying a ramp of temperature of 10 °C/min from 25 °C to 200 °C. The obtained solution was diluted to 10 mL with milliQ water, prior to the analysis.

Transmission electron microscopy (TEM) micrographs were obtained with a JEOL JEM-1400 PLUS transmission electron microscope equipped with a GATAN US1000 CCD camera, operating at an acceleration voltage of 120 kV. The samples were prepared by drop-casting 5 μL a 0.1 mg/mL suspension of material on carbon film 300 mesh copper grids, purchased from Electron Microscopy Sciences. The statistical dimensional analysis of gold nanoparticles was executed with Fiji software.

All electrochemical measurements were carried out using an electrochemical workstation Autolab MSTAT204 potentiostat/galvanostat (Metrohm Autolab) interfaced to a PC with Nova 2.1.6 software, at laboratory room temperature (25°C). Commercially available SPCE (DRP 110, provided by Metrohm Dropsens) were used to study the electrocatalytic activity of MWCNT-S-Au and to manufacture the final sensor, SPCE/MWCNT-S-Au/MIP. GCE (Ref. 609395014, provided by Metrohm) was used to study electrocatalytic activity of MWCNT-S-Au for all other analytes. ITO-coated glass slides for manufacture of the sensor for dopamine at cellular level were purchased from SPI Supplies (Ref. #06485-AB).

Scanning electron microscopy (SEM) images were obtained using JSM7200F JEOL at 3 to 10 kV. For the characterization of AuNPs, a lower electron detector (LED) was used instead of the upper secondary electron detector (USD).

Fluorescence micrograph of neurons with immunostaining were obtained using a Zeiss LSM 900 with Airyscan 2, equipped with three Ar laser excitation sources (458, 488 and 514 nm), DPSS (561 and 590 nm) and HeNe (633 nm), coupled to a MaiTai DeepSee multiphoton laser with variable excitation range (690 to 1040 nm). Cells were stained with, Purified anti-Neurofilament H (NF-H), Nonphosphorylated Antibody (#SMI-32P, purchased from BioLegend), Anti-TH Antibody (AB152, purchased from Sigma-Aldrich) and DAPI staining (purchased from Sigma-Aldrich).

2.4.2 Synthesis of 4,4'-dithiodibenzenediazonium tetrafluoroborate

To synthesize 4,4'-dithiodibenzenediazonium tetrafluoroborate ($DTDBBF_4$), first 4-aminothiophenol (ATP) was oxidized to dithiodianiline (DTDA). 2 g of ATP were dissolved in 300 mL of H_2O/EtOH (1:1) mixture, then 1.25 eq of H_2O_2 and 0.15 eq of NH_3 were added to the solution, which was left stirring at room temperature for 2 hours. DTDA was extracted with DCM, washing twice with H_2O and finally the organic phase was dried over Na_2SO_4 and the solvent was evaporated to isolate the product. DTDA was obtained with a quantitative yield and characterized by ^{1}H-NMR. (DMSO-d6, δ = 7.06 (m, 4H), 6.56 (m, 4H), 5.49 (s, 4H), **Figure 45** $^{1H\text{-}NMR}$ spectrum of DTDA in DMSO-d6.)

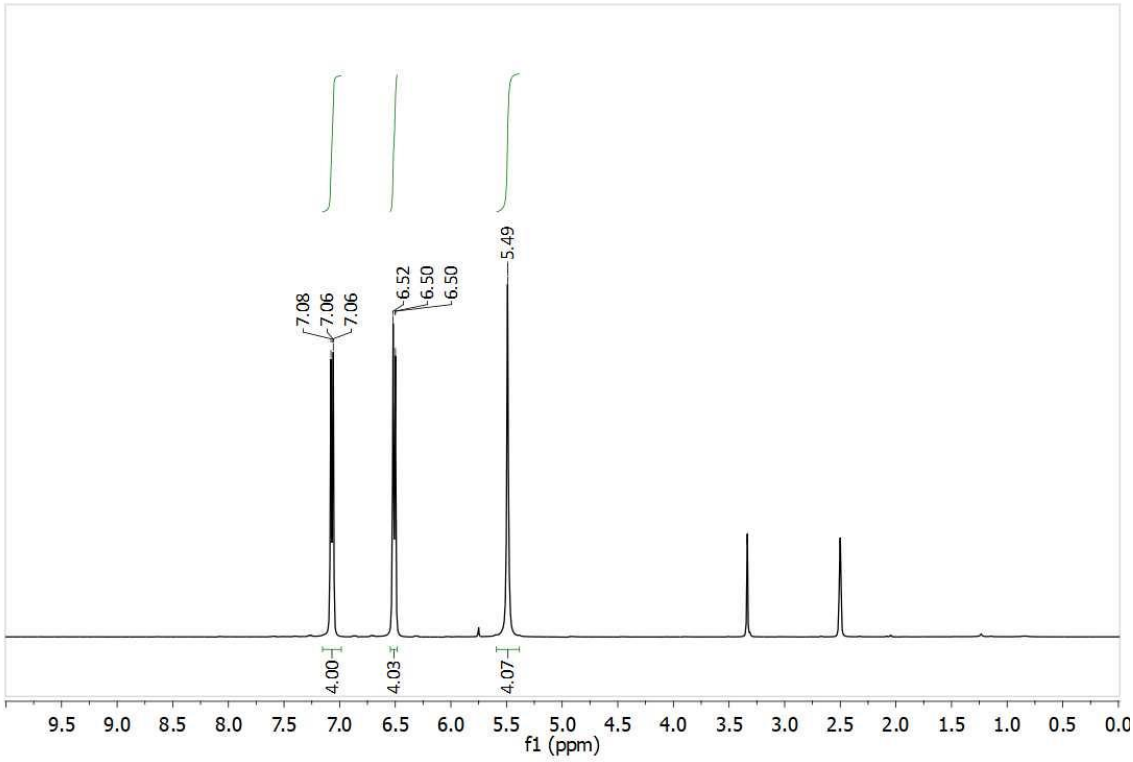

***Figure 45** ^{1}H-NMR spectrum of DTDA in DMSO-d_6.*

Subsequently, the obtained DTDA was dissolved in 60 mL of glacial acetic acid and 12 mL of HBF_4 were added. While stirring, 6 mL of isopentyl nitrite were added dropwise. The mixture was left stirring for 45 minutes and then 100 mL of Et_2O were poured into the reaction mixture and the flask was stored at -20°C overnight. Finally, $DTDBBF_4$ was isolated by filtration and characterized by ^{1}H-NMR (DMSO-d6, δ = 8.61 (m, 4H), 8.14 (m, 4H), **Figure 46**) and ATR-FTIR (2264 cm^{-1}(N≡N), 1552 cm^{-1}(Aromatic C=C), 1054 cm^{-1}(BF_4^-), 521 cm^{-1}(S-S), **Figure 47**).[62]

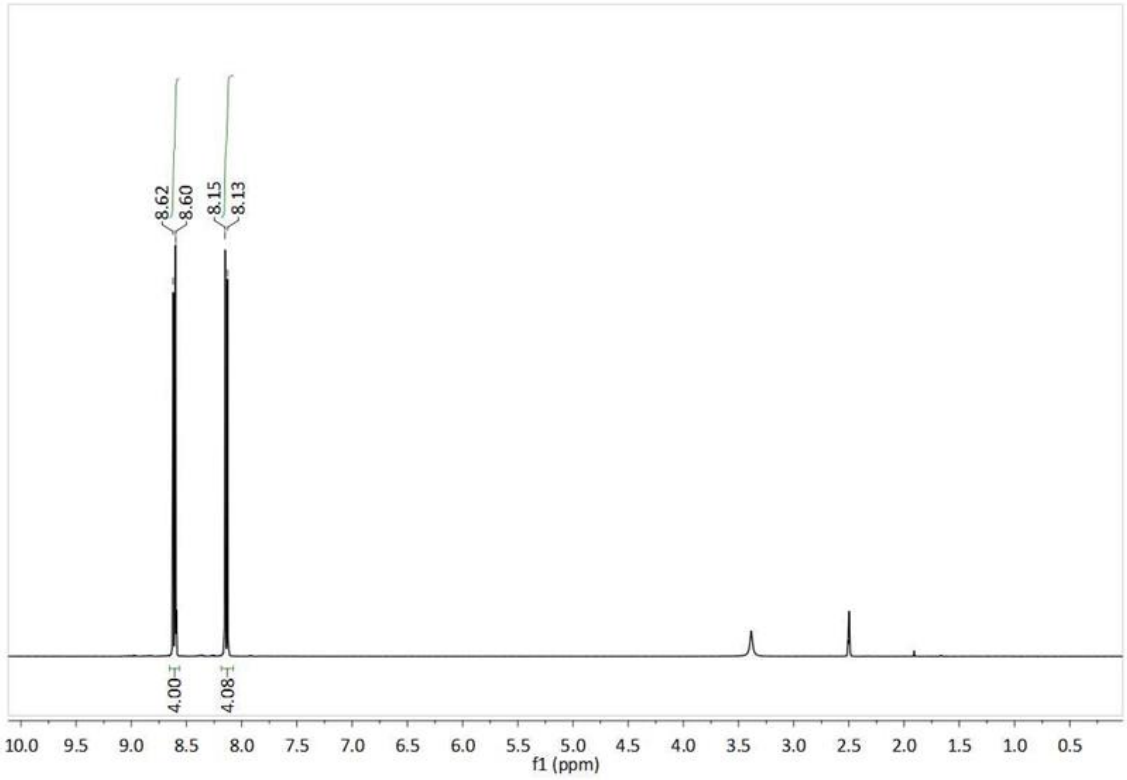

Figure 46 *^{1}H-NMR spectrum of DTDBBF$_4$ in DMSO-d6. The formation of the diazonium salt is followed by a shift in the chemical shift of the aromatic protons and the loss of the peak related to the amine.*[62]

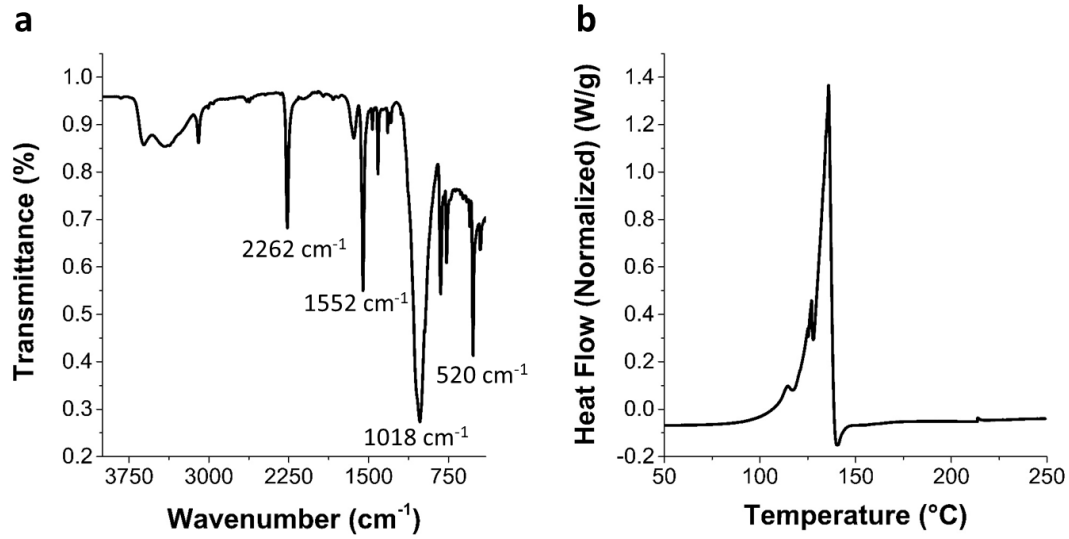

Figure 47 *a) FT-IR spectrum of DTDBBF$_4$ registered in the solid phase in ATR mode. The characteristic peaks at 2264 cm^{-1} (R-N+≡N), 1552 cm^{-1} (Aromatic C=C), 1054 cm^{-1} (BF4-), and 521 cm^{-1} (S-S) are highlighted;*[62] *b) DSC analysis of DTDBBF$_4$, highlighting the stability of the diazonium salt until 100 °C, and an exothermic decomposition peak at 136 °C.*[91]

2.4.3 Metal Vapor Synthesis of AuNPs

In a typical experiment, Au vapors, generated at 10^{-5} mBar by resistive heating of the metal (100 mg of Au chips) in an alumina-coated tungsten crucible, were co-condensed at liquid nitrogen temperature (– 196 °C) with acetone (100 mL) in the glass reactor chamber of a previously described MVS reactor [34] for 1 h. The reactor chamber was then heated to the melting point of the solid matrix (ca. – 95 °C), and the resulting deep purple solution (95 mL) was siphoned and handled at low temperature (– 20 °C) with the Schlenk tube technique. The gold content of the acetone solution was calculated from ICP-OES, and resulted in 0.57 mg mL^{-1}.

2.4.4 Synthesis of MWCNT-S-Au

MWCNTs were first purified, by sonication in 6M HCl for 6h in a sonicating bath, then recovered by filtration and washed with Milli-Q water until neutral pH was reached. The XPS confirmed that they are mainly composed of C (96.80%) with a low degree of O (3.20%). The survey and high-resolution spectra of the purified MWCNTs confirmed the absence of contaminations by Fe and other metals.

MWCNTs were functionalized by a SET reaction with the previously synthesized $DTDBBF_4$. 60 mg of MWCNTs were suspended in 60 mL of dimethylformamide (DMF), by sonicating for 5 minutes in a sonicating bath. The suspension was heated at 80°C and 1.114 g (0.5 eq for each carbon atom) of $DTDBBF_4$ were added. The mixture was left stirring overnight and the product, MWCNT-SS, was isolated by filtration, washing twice with DMF and EtOAc.

To obtain the final MWCNT-SH, MWCNT-SS were reduced with tris(2-carboxyethyl)phosphine (TCEP). A solution was prepared by dissolving 250 mg of TCEP in 50 mL of phosphate buffer solution at pH= 7. 50 mg of MWCNT-SS were then dispersed in 50 mL of Milli-Q water by sonicating for 5 minutes and the TCEP was added. The mixture was left stirring overnight and finally, the product was isolated by filtration washing with 1 L of Milli-Q water.

Au NPs-acetone solution (was then added to a suspension containing the MWCNT-SH (or MWCNT-SS) (50 mg) in acetone (5 mL). The mixture was stirred over night at 25 °C. The Au NPs solution was removed and the solid was washed with *n*-pentane (3 × 10 mL) and dried under reduced pressure.

2.4.5 Electrochemical Characterization of MWCNT-S-Au

The electrocatalytic activity of MWCNT-S-Au was evaluated by Linear Sweep Voltammetry (LSV). In the case of serotonin, 10 µL of a 0.5 mg/mL suspension of MWCNT-S-Au were drop-casted on the surface of the working electrode of an SPCE; for all other molecules, the electrocatalytic activity was assessed with a GCE, dropcasting 5 µL of a 0.5 mg/mL suspension of MWCNT-S-Au.

For serotonin, upon drying, 60 µL of a 12 µmol L^{-1} solution of 5-HT in phosphate buffer (PBS) 0.1 mol L^{-1} and KCl 0.1 mol L^{-1} (pH= 7.0) were cast on the surface of the SPCE/MWCNT-S-Au and LSV was carried out by scanning applied potential from 0.1 to 0.4 V, with a scan rate of 20 mV/s.

For all other analytes, the modified GCE was immersed in 20 mL of 5 mmol L^{-1} analyte solution in PBS 0.1 mol L^{-1} KCl 0.1 mol L^{-1}. LSV was carried out in different potential ranges (depending on the analyte), with a scan rate of 20 mV/s.

Cyclic Voltammetry (CV) was used to study the mechanism of oxidation of 5-HT at the interface. The applied potential was scanned from 0 to 0.5 V, at different scan rates, ranging from 20 to 65 mV/s.

2.4.6 Design of Experiment for Sensing of Serotonin

DPV was used to perform sensing of 5-HT. The applied potential was scanned from 0.1 to 0.4 V, with a step potential of 5 mV and an interval time of 250 ms. The baseline was subtracted from the obtained voltammograms with a moving average baseline model. Modulation time (MT) and modulation amplitude (MA) were optimized by DoE.[82]

2.4.7 Manufacture of the Electrochemical Sensor for Serotonin

15 µL of MWCNT-S-Au dispersion (1mg/mL) in Milli-Q water was drop-casted onto the SPCE surface. Then, 70 µL of a 1.15 mmol L^{-1} solution of pyrrole, in the presence of 5-HT (200 mmol L^{-1}), were deposited onto the resulting SPCE/MWCNT-S-Au. MIP-modified SPCE/MWCNT-S-Au was obtained by performing 5 cycles of CV (0 V to +1.00 V, 100 mV/s) using 0.1mol L^{-1} PBS enriched with 0.1 mol L^{-1} of KCl (pH7) as an electrolyte (**Figure 48a**). Subsequently, the embedded 5-HT was eliminated by scanning between - 0.6 and +1.00 V in

0.1 mol L^{-1} phosphate buffer solution (pH 7.4) for several cycles until no oxidation peak for 5-HT was observed (**Figure 48b**).

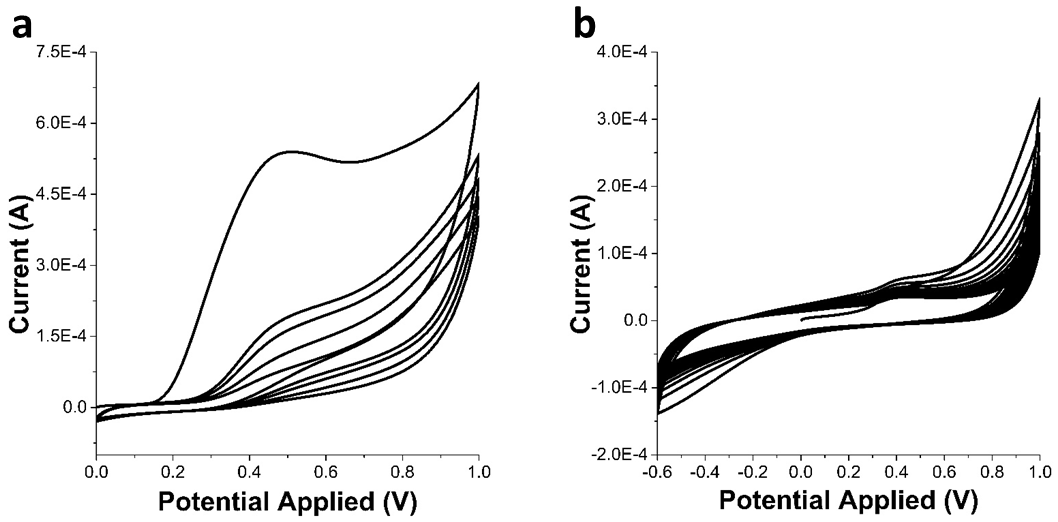

Figure 48 *Cyclic voltammograms registered during a) the MIP electro-polymerization and b) the cleaning process of the SPCE/MWCNT-S-Au/MIP (scan rate of 100 mV/s, PBS 0.1M KCl 0.1M).*

Different concentrations of pyrrole were tested. The use of concentration higher than 1.15 mmol L^{-1} led to the overgrowth of polymer on the surface of the electrode (**Figure 49**), causing higher passivation and negatively influencing the performance of the sensor.

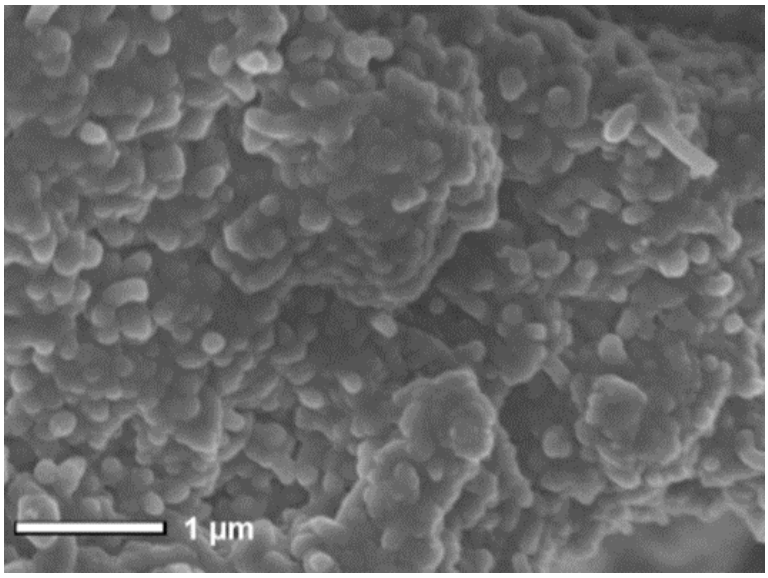

Figure 49 *SEM image of MWCNT-Au-MIP/SPCE polymerizing with 26 mmol L^{-1} pyrrole.*

As a control, a non-molecularly imprinted polymer (NIP) modified SPCE/MWCNT-S-Au (SPCE/MWCNT-S-Au/NIP) was also prepared and treated in the same way, except for the omission of 5-HT in the electro-polymerization process (**Figure 50**).

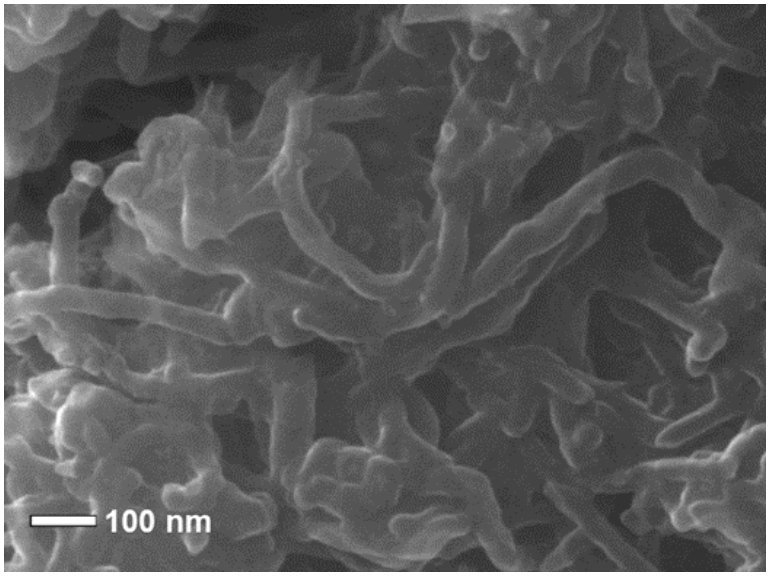

Figure 50 *SEM image of MWCNT-Au-NIP/SPCE.*

In addition, a lower electron detector (LED) was used instead of the upper secondary electron detector (USD) to prove that the AuNPs were not affected after the polymerization (**Figure 51**). Brighter spheres can be observed, confirming the presence of the metallic particles below the MIP layer.

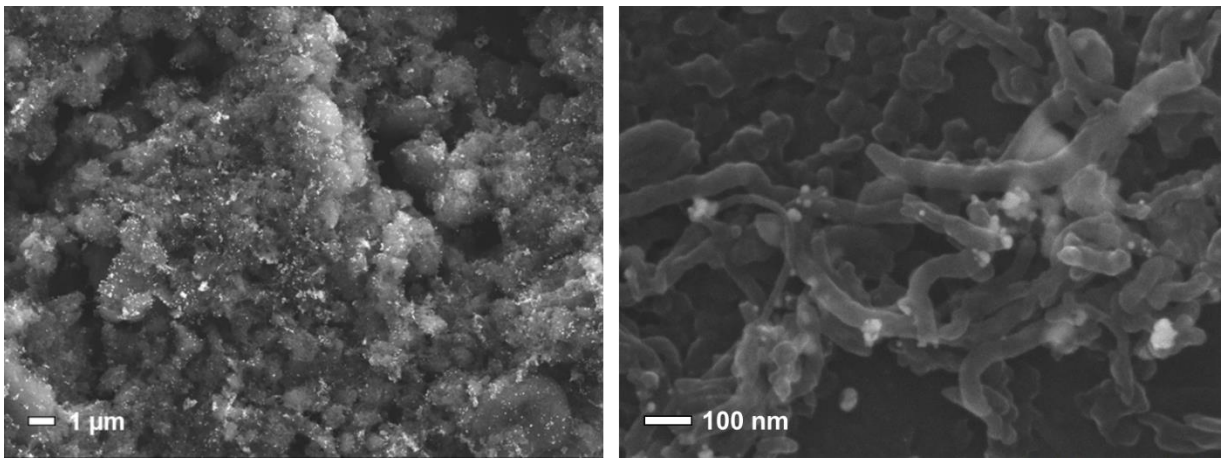

Figure 51 *SEM images of MWCNT-Au-MIP/SPCE using a Low Energy Detector (LED) at different magnifications.*

2.4.8 Detection of Serotonin and Evaluation of Sensing Performances

The dose-dependent responses of SPCE/MWCNT-S-Au and SPCE/MWCNT-S-Au/MIP were evaluated. In the optimized conditions obtained from the DoE, analyzing 11 solutions spiked with different concentrations of 5-HT (0.5 μmol L^{-1}, 1 μmol L^{-1}, 2.5 μmol L^{-1}, 5 μmol L^{-1}, 7.5 μmol L^{-1}, 12 μmol L^{-1}, 16 μmol L^{-1}, 20 μmol L^{-1}, 25 μmol L^{-1}, 40 μmol L^{-1}, 50 μmol L^{-1}). 0.1 M of PBS enriched with 0.1 M of KCl was used as a supporting electrolyte. For SPCE/MWCNT-S-Au/MIP, a potential of -300 mV was applied for 10 s before each measurement to favor the accumulation of the analyte in the MIP.

The LOD was determined as 3 times the standard error from the linear regression on the calibration curve. Sensitivity was calculated as the ratio between the slope of the calibration curve (μA L μmol^{-1}) and the geometric surface area of the Dropsens electrode (~0.126 cm^2). Repeatability was determined by recording 3 consecutive calibration curves with the same sensor and by determining the standard deviation of the obtained slopes. Reproducibility was determined by recording 3 calibration curves with 3 different sensors and by determining the standard deviation of the obtained slopes.

To evaluate the influence of interfering agents, solutions of DA, tryptophan (TRP), uric acid (UA), and ascorbic acid (AA), at the concentrations of 50 mmol L^{-1} in PBS/KCl 0.1 mol L^{-1}, were prepared and measured, in a potential window comprised between -0.2 and 0.5 V.

2.4.9 Manufacture of the Electrochemical Sensor for Dopamine

ITO-coated glass slides were cut with diamond-tip cutter to obtain 0.75 × 1.5 cm slides. Subsequently, poly(lactic acid) (PLA) 3D-printed squared wells, 0.75 × 0.75 cm, were attached on the electroactive surface of one end of the rectangular slide, using a 1:10 solution of poly(dimethylsiloxane) (PDMS). Upon drying, the electroactive surfaces inside the PLA wells are functionalized with 60 μL of MWCNTs aqueous suspension (1 mg/mL) and let dry. Then 120 μL of MWCNT-S-Au suspension (0.5 mg/mL) are dropcasted on top of the MWCNT layer. Finally, the electrodes are dried on a heating plate at 50 °C.

Before proceeding with seeding and culture of neuronal cells, the sensors are exposed to UV lights for 30 minutes and then the interior part of the 3D-printed wells is rinsed with PBS.

2.5 References

(1) Lövheim, H. A New Three-Dimensional Model for Emotions and Monoamine Neurotransmitters. *Medical Hypotheses* **2012**, *78* (2), 341–348. https://doi.org/10.1016/j.mehy.2011.11.016.

(2) Broadley, K. J. The Vascular Effects of Trace Amines and Amphetamines. *Pharmacology & Therapeutics* **2010**, *125* (3), 363–375. https://doi.org/10.1016/j.pharmthera.2009.11.005.

(3) Mele, T.; Čarman-Kržan, M.; Jurič, D. M. Regulatory Role of Monoamine Neurotransmitters in Astrocytic NT-3 Synthesis. *International Journal of Developmental Neuroscience* **2010**, *28* (1), 13–19. https://doi.org/10.1016/j.ijdevneu.2009.10.003.

(4) *Neurotrophin-regulated signalling pathways | Philosophical Transactions of the Royal Society B: Biological Sciences*. https://royalsocietypublishing.org/doi/abs/10.1098/rstb.2006.1894 (accessed 2024-10-17).

(5) Ng, J.; Papandreou, A.; Heales, S. J.; Kurian, M. A. Monoamine Neurotransmitter Disorders—Clinical Advances and Future Perspectives. *Nat Rev Neurol* **2015**, *11* (10), 567–584. https://doi.org/10.1038/nrneurol.2015.172.

(6) Goldstein, D. S. Catecholamines in the Periphery. In *Advances in Pharmacology*; Goldstein, D. S., Eisenhofer, G., McCarty, R., Eds.; Academic Press, 1997; Vol. 42, pp 529–539. https://doi.org/10.1016/S1054-3589(08)60806-6.

(7) Pearl, P. L.; Capp, P. K.; Novotny, E. J.; Gibson, K. M. Inherited Disorders of Neurotransmitters in Children and Adults. *Clinical Biochemistry* **2005**, *38* (12), 1051–1058. https://doi.org/10.1016/j.clinbiochem.2005.09.012.

(8) Nagatsu, T.; Mogi, M.; Ichinose, H.; Togari, A. Changes in Cytokines and Neurotrophins in Parkinson's Disease. In *Advances in Research on Neurodegeneration*; Riederer, P., Calne, D. B., Horowski, R., Mizuno, Y., Olanow, C. W., Poewe, W., Youdim, M. B. H., Eds.; Springer: Vienna, 2000; pp 277–290. https://doi.org/10.1007/978-3-7091-6301-6_19.

(9) Latif, S.; Jahangeer, M.; Maknoon Razia, D.; Ashiq, M.; Ghaffar, A.; Akram, M.; El Allam, A.; Bouyahya, A.; Garipova, L.; Ali Shariati, M.; Thiruvengadam, M.; Azam Ansari, M. Dopamine in Parkinson's Disease. *Clinica Chimica Acta* **2021**, *522*, 114–126. https://doi.org/10.1016/j.cca.2021.08.009.

(10) Politis, M.; Niccolini, F. Serotonin in Parkinson's Disease. *Behavioural Brain Research* **2015**, *277*, 136–145. https://doi.org/10.1016/j.bbr.2014.07.037.

(11) Eggers, A. E. A Serotonin Hypothesis of Schizophrenia. *Medical Hypotheses* **2013**, *80* (6), 791–794. https://doi.org/10.1016/j.mehy.2013.03.013.

(12) Jonnakuty, C.; Gragnoli, C. What Do We Know about Serotonin? *Journal of Cellular Physiology* **2008**, *217* (2), 301–306. https://doi.org/10.1002/jcp.21533.

(13) Jones, L. A.; Sun, E. W.; Martin, A. M.; Keating, D. J. The Ever-Changing Roles of Serotonin. *The International Journal of Biochemistry & Cell Biology* **2020**, *125*, 105776. https://doi.org/10.1016/j.biocel.2020.105776.

(14) Pagan, C.; Delorme, R.; Callebert, J.; Goubran-Botros, H.; Amsellem, F.; Drouot, X.; Boudebesse, C.; Le Dudal, K.; Ngo-Nguyen, N.; Laouamri, H.; Gillberg, C.; Leboyer, M.; Bourgeron, T.; Launay, J.-M. The Serotonin-N-Acetylserotonin–Melatonin Pathway as a Biomarker for Autism Spectrum Disorders. *Transl Psychiatry* **2014**, *4* (11), e479–e479. https://doi.org/10.1038/tp.2014.120.

(15) Spivak, B.; Vered, Y.; Yoran-Hegesh, R.; Averbuch, E.; Mester, R.; Graf, E.; Weizman, A. Circulatory Levels of Catecholamines, Serotonin and Lipids in Attention Deficit Hyperactivity Diiorder. *Acta Psychiatrica Scandinavica* **1999**, *99* (4), 300–304. https://doi.org/10.1111/j.1600-0447.1999.tb07229.x.

(16) Moriarty, M.; Lee, A.; O'Connell, B.; Kelleher, A.; Keeley, H.; Furey, A. Development of an LC-MS/MS Method for the Analysis of Serotonin and Related Compounds in Urine and the Identification of a Potential Biomarker for Attention Deficit Hyperactivity/Hyperkinetic Disorder. *Anal Bioanal Chem* **2011**, *401* (8), 2481–2493. https://doi.org/10.1007/s00216-011-5322-7.

(17) Hara, K.; Hirowatari, Y.; Shimura, Y.; Takahashi, H. Serotonin Levels in Platelet-Poor Plasma and Whole Blood in People with Type 2 Diabetes with Chronic Kidney Disease. *Diabetes Research and Clinical Practice* **2011**, *94* (2), 167–171. https://doi.org/10.1016/j.diabres.2011.06.020.

(18) Fanciulli, G.; Ruggeri, R. M.; Grossrubatscher, E.; Calzo, F. L.; Wood, T. D.; Faggiano, A.; Isidori, A.; Colao, A.; on behalf of NIKE. Serotonin Pathway in Carcinoid Syndrome: Clinical, Diagnostic, Prognostic and Therapeutic Implications. *Rev Endocr Metab Disord* **2020**, *21* (4), 599–612. https://doi.org/10.1007/s11154-020-09547-8.

(19) Moncrieff, J.; Cooper, R. E.; Stockmann, T.; Amendola, S.; Hengartner, M. P.; Horowitz, M. A. The Serotonin Theory of Depression: A Systematic Umbrella Review of

the Evidence. *Mol Psychiatry* **2023**, *28* (8), 3243–3256. https://doi.org/10.1038/s41380-022-01661-0.

(20) Jauhar, S.; Arnone, D.; Baldwin, D. S.; Bloomfield, M.; Browning, M.; Cleare, A. J.; Corlett, P.; Deakin, J. F. W.; Erritzoe, D.; Fu, C.; Fusar-Poli, P.; Goodwin, G. M.; Hayes, J.; Howard, R.; Howes, O. D.; Juruena, M. F.; Lam, R. W.; Lawrie, S. M.; McAllister-Williams, H.; Marwaha, S.; Matuskey, D.; McCutcheon, R. A.; Nutt, D. J.; Pariante, C.; Pillinger, T.; Radhakrishnan, R.; Rucker, J.; Selvaraj, S.; Stokes, P.; Upthegrove, R.; Yalin, N.; Yatham, L.; Young, A. H.; Zahn, R.; Cowen, P. J. A Leaky Umbrella Has Little Value: Evidence Clearly Indicates the Serotonin System Is Implicated in Depression. *Mol Psychiatry* **2023**, *28* (8), 3149–3152. https://doi.org/10.1038/s41380-023-02095-y.

(21) Kumar, A.; Russell, R. M.; Pifer, R.; Menezes-Garcia, Z.; Cuesta, S.; Narayanan, S.; MacMillan, J. B.; Sperandio, V. The Serotonin Neurotransmitter Modulates Virulence of Enteric Pathogens. *Cell Host & Microbe* **2020**, *28* (1), 41-53.e8. https://doi.org/10.1016/j.chom.2020.05.004.

(22) Spadaro, A.; Scott, K. R.; Koyfman, A.; Long, B. High Risk and Low Prevalence Diseases: Serotonin Syndrome. *The American Journal of Emergency Medicine* **2022**, *61*, 90–97. https://doi.org/10.1016/j.ajem.2022.08.030.

(23) Prakash, S.; Rathore, C.; Rana, K.; Prakash, A. Fatal Serotonin Syndrome: A Systematic Review of 56 Cases in the Literature. *Clinical Toxicology* **2021**, *59* (2), 89–100. https://doi.org/10.1080/15563650.2020.1839662.

(24) Zhai, S.; Cui, Q.; Simmons, D. V.; Surmeier, D. J. Distributed Dopaminergic Signaling in the Basal Ganglia and Its Relationship to Motor Disability in Parkinson's Disease. *Current Opinion in Neurobiology* **2023**, *83*, 102798. https://doi.org/10.1016/j.conb.2023.102798.

(25) Singer, H. S.; Butler, I. J.; Tune, L. E.; Seifert Jr, W. E.; Coyle, J. T. Dopaminergic Dysfunction in Tourette Syndrome. *Annals of Neurology* **1982**, *12* (4), 361–366. https://doi.org/10.1002/ana.410120408.

(26) Koob, G. F. Dopamine, Addiction and Reward. *Seminars in Neuroscience* **1992**, *4* (2), 139–148. https://doi.org/10.1016/1044-5765(92)90012-Q.

(27) Nieoullon, A. Dopamine and the Regulation of Cognition and Attention. *Progress in Neurobiology* **2002**, *67* (1), 53–83. https://doi.org/10.1016/S0301-0082(02)00011-4.

(28) Kesby, J. P.; Eyles, D. W.; McGrath, J. J.; Scott, J. G. Dopamine, Psychosis and Schizophrenia: The Widening Gap between Basic and Clinical Neuroscience. *Transl Psychiatry* **2018**, *8* (1), 1–12. https://doi.org/10.1038/s41398-017-0071-9.

(29) Monti, J. M.; Monti, D. The Involvement of Dopamine in the Modulation of Sleep and Waking. *Sleep Medicine Reviews* **2007**, *11* (2), 113–133. https://doi.org/10.1016/j.smrv.2006.08.003.

(30) Ma, L.; Zhao, T.; Zhang, P.; Liu, M.; Shi, H.; Kang, W. Determination of Monoamine Neurotransmitters and Metabolites by High-Performance Liquid Chromatography Based on Ag(III) Complex Chemiluminescence Detection. *Analytical Biochemistry* **2020**, *593*, 113594. https://doi.org/10.1016/j.ab.2020.113594.

(31) Lindström, M.; Tohmola, N.; Renkonen, R.; Hämäläinen, E.; Schalin-Jäntti, C.; Itkonen, O. Comparison of Serum Serotonin and Serum 5-HIAA LC-MS/MS Assays in the Diagnosis of Serotonin Producing Neuroendocrine Neoplasms: A Pilot Study. *Clinica Chimica Acta* **2018**, *482*, 78–83. https://doi.org/10.1016/j.cca.2018.03.030.

(32) He, Q.; Li, M.; Wang, X.; Xia, Z.; Du, Y.; Li, Y.; Wei, L.; Shang, J. A Simple, Efficient and Rapid HPLC–UV Method for the Detection of 5-HT in RIN-14B Cell Extract and Cell Culture Medium. *BMC Chemistry* **2019**, *13* (1), 76. https://doi.org/10.1186/s13065-019-0591-x.

(33) Slaney, T. R.; Mabrouk, O. S.; Porter-Stransky, K. A.; Aragona, B. J.; Kennedy, R. T. Chemical Gradients within Brain Extracellular Space Measured Using Low Flow Push–Pull Perfusion Sampling in Vivo. *ACS Chem. Neurosci.* **2013**, *4* (2), 321–329. https://doi.org/10.1021/cn300158p.

(34) Pazos, A.; Probst, A.; Palacios, J. M. Serotonin Receptors in the Human Brain—III. Autoradiographic Mapping of Serotonin-1 Receptors. *Neuroscience* **1987**, *21* (1), 97–122. https://doi.org/10.1016/0306-4522(87)90326-5.

(35) Steckl, A. J.; Ray, P. Stress Biomarkers in Biological Fluids and Their Point-of-Use Detection. *ACS Sens.* **2018**, *3* (10), 2025–2044. https://doi.org/10.1021/acssensors.8b00726.

(36) Feldman, J. M. Urinary Serotonin in the Diagnosis of Carcinoid Tumors. *Clinical Chemistry* **1986**, *32* (5), 840–844. https://doi.org/10.1093/clinchem/32.5.840.

(37) Karbownik, M. S.; Hicks, S. D. The Association of Salivary Serotonin With Mood and Cardio-Autonomic Function: A Preliminary Report. *Front. Psychiatry* **2022**, *13*. https://doi.org/10.3389/fpsyt.2022.788153.

(38) Schmidt, A. C.; Wang, X.; Zhu, Y.; Sombers, L. A. Carbon Nanotube Yarn Electrodes for Enhanced Detection of Neurotransmitter Dynamics in Live Brain Tissue. *ACS Nano* **2013**, *7* (9), 7864–7873. https://doi.org/10.1021/nn402857u.

(39) Li, Y.; Du, J.; Yang, J.; Liu, D.; Lu, X. Electrocatalytic Detection of Dopamine in the Presence of Ascorbic Acid and Uric Acid Using Single-Walled Carbon Nanotubes Modified Electrode. *Colloids and Surfaces B: Biointerfaces* **2012**, *97*, 32–36. https://doi.org/10.1016/j.colsurfb.2012.03.029.

(40) Yang, H.; Zhou, C.; An, J.; Yang, L.; Yang, Y.; Liu, X. Ultra-Fast Synthesis of Iron Decorated Multiwalled Carbon Nanotube Composite Materials: A Sensitive Electrochemical Sensor for Determining Dopamine. *Journal of Alloys and Compounds* **2022**, *897*, 163257. https://doi.org/10.1016/j.jallcom.2021.163257.

(41) Wu, B.; Yeasmin, S.; Liu, Y.; Cheng, L.-J. Sensitive and Selective Electrochemical Sensor for Serotonin Detection Based on Ferrocene-Gold Nanoparticles Decorated Multiwall Carbon Nanotubes. *Sensors and Actuators B: Chemical* **2022**, *354*, 131216. https://doi.org/10.1016/j.snb.2021.131216.

(42) Cellot, G.; Cilia, E.; Cipollone, S.; Rancic, V.; Sucapane, A.; Giordani, S.; Gambazzi, L.; Markram, H.; Grandolfo, M.; Scaini, D.; Gelain, F.; Casalis, L.; Prato, M.; Giugliano, M.; Ballerini, L. Carbon Nanotubes Might Improve Neuronal Performance by Favouring Electrical Shortcuts. *Nature Nanotech* **2009**, *4* (2), 126–133. https://doi.org/10.1038/nnano.2008.374.

(43) Fabbro, A.; Bosi, S.; Ballerini, L.; Prato, M. Carbon Nanotubes: Artificial Nanomaterials to Engineer Single Neurons and Neuronal Networks. *ACS Chem. Neurosci.* **2012**, *3* (8), 611–618. https://doi.org/10.1021/cn300048q.

(44) Mazzatenta, A.; Giugliano, M.; Campidelli, S.; Gambazzi, L.; Businaro, L.; Markram, H.; Prato, M.; Ballerini, L. Interfacing Neurons with Carbon Nanotubes: Electrical Signal Transfer and Synaptic Stimulation in Cultured Brain Circuits. *J. Neurosci.* **2007**, *27* (26), 6931–6936. https://doi.org/10.1523/JNEUROSCI.1051-07.2007.

(45) Yusoff, N.; Pandikumar, A.; Ramaraj, R.; Lim, H. N.; Huang, N. M. Gold Nanoparticle Based Optical and Electrochemical Sensing of Dopamine. *Microchim Acta* **2015**, *182* (13), 2091–2114. https://doi.org/10.1007/s00604-015-1609-2.

(46) Goyal, R. N.; Gupta, V. K.; Oyama, M.; Bachheti, N. Gold Nanoparticles Modified Indium Tin Oxide Electrode for the Simultaneous Determination of Dopamine and

Serotonin: Application in Pharmaceutical Formulations and Biological Fluids. *Talanta* **2007**, *72* (3), 976–983. https://doi.org/10.1016/j.talanta.2006.12.029.

(47) Klabunde, K. *Chemistry of Free Atoms and Particles*; Elsevier, 2012.

(48) Pitzalis, E.; Psaro, R.; Evangelisti, C. From Metal Vapor to Supported Single Atoms, Clusters and Nanoparticles: Recent Advances to Heterogeneous Catalysts. *Inorganica Chimica Acta* **2022**, *533*, 120782. https://doi.org/10.1016/j.ica.2021.120782.

(49) Klabunde, K. J. *Free Atoms, Clusters, and Nanoscale Particles*; Elsevier, 2012.

(50) Eersels, K.; Lieberzeit, P.; Wagner, P. A Review on Synthetic Receptors for Bioparticle Detection Created by Surface-Imprinting Techniques—From Principles to Applications. *ACS Sens.* **2016**, *1* (10), 1171–1187. https://doi.org/10.1021/acssensors.6b00572.

(51) Ertürk, G.; Mattiasson, B. Molecular Imprinting Techniques Used for the Preparation of Biosensors. *Sensors* **2017**, *17* (2), 288. https://doi.org/10.3390/s17020288.

(52) Ramanavičius, S.; Morkvėnaitė-Vilkončienė, I.; Samukaitė-Bubnienė, U.; Ratautaitė, V.; Plikusienė, I.; Viter, R.; Ramanavičius, A. Electrochemically Deposited Molecularly Imprinted Polymer-Based Sensors. *Sensors* **2022**, *22* (3), 1282. https://doi.org/10.3390/s22031282.

(53) Berni, A.; Ait Lahcen, A.; Salama, K. N.; Amine, A. 3D-Porous Laser-Scribed Graphene Decorated with Overoxidized Polypyrrole as an Electrochemical Sensing Platform for Dopamine. *Journal of Electroanalytical Chemistry* **2022**, *919*, 116529. https://doi.org/10.1016/j.jelechem.2022.116529.

(54) Leonavicius, K.; Ramanaviciene, A.; Ramanavicius, A. Polymerization Model for Hydrogen Peroxide Initiated Synthesis of Polypyrrole Nanoparticles. *Langmuir* **2011**, *27* (17), 10970–10976. https://doi.org/10.1021/la201962a.

(55) Felix, F. S.; Angnes, L. Electrochemical Immunosensors – A Powerful Tool for Analytical Applications. *Biosensors and Bioelectronics* **2018**, *102*, 470–478. https://doi.org/10.1016/j.bios.2017.11.029.

(56) Samukaite-Bubniene, U.; Valiūnienė, A.; Bucinskas, V.; Genys, P.; Ratautaite, V.; Ramanaviciene, A.; Aksun, E.; Tereshchenko, A.; Zeybek, B.; Ramanavicius, A. Towards Supercapacitors: Cyclic Voltammetry and Fast Fourier Transform Electrochemical Impedance Spectroscopy Based Evaluation of Polypyrrole Electrochemically Deposited on the Pencil Graphite Electrode. *Colloids and Surfaces A: Physicochemical and*

Engineering Aspects **2021**, *610*, 125750. https://doi.org/10.1016/j.colsurfa.2020.125750.

(57) Qian, T.; Yu, C.; Zhou, X.; Ma, P.; Wu, S.; Xu, L.; Shen, J. Ultrasensitive Dopamine Sensor Based on Novel Molecularly Imprinted Polypyrrole Coated Carbon Nanotubes. *Biosensors and Bioelectronics* **2014**, *58*, 237–241. https://doi.org/10.1016/j.bios.2014.02.081.

(58) Zhang, J.; Guo, X.-T.; Zhou, J.-P.; Liu, G.-Z.; Zhang, S.-Y. Electrochemical Preparation of Surface Molecularly Imprinted Poly(3-Aminophenylboronic Acid)/MWCNTs Nanocomposite for Sensitive Sensing of Epinephrine. *Materials Science and Engineering: C* **2018**, *91*, 696–704. https://doi.org/10.1016/j.msec.2018.06.011.

(59) Bahr, J. L.; Tour, J. M. Covalent Chemistry of Single-Wall Carbon Nanotubes. *J. Mater. Chem.* **2002**, *12* (7), 1952–1958. https://doi.org/10.1039/B201013P.

(60) Wetzl, C.; Silvestri, A.; Garrido, M.; Hou, H.-L.; Criado, A.; Prato, M. The Covalent Functionalization of Surface-Supported Graphene: An Update. *Angewandte Chemie* **2023**, *135* (6), e202212857. https://doi.org/10.1002/ange.202212857.

(61) Peng, Z.; Holm, A. H.; Nielsen, L. T.; Pedersen, S. U.; Daasbjerg, K. Covalent Sidewall Functionalization of Carbon Nanotubes by a "Formation−Degradation" Approach. *Chem. Mater.* **2008**, *20* (19), 6068–6075. https://doi.org/10.1021/cm800954t.

(62) Shahar, T.; Tal, N.; Mandler, D. The Synthesis and Characterization of Thiol-Based Aryl Diazonium Modified Glassy Carbon Electrode for the Voltammetric Determination of Low Levels of Hg(II). *J Solid State Electrochem* **2013**, *17* (6), 1543–1552. https://doi.org/10.1007/s10008-013-2009-3.

(63) J. Salavagione, H.; Sherwood, J.; Bruyn, M. D.; L. Budarin, V.; J. Ellis, G.; H. Clark, J.; S. Shuttleworth, P. Identification of High Performance Solvents for the Sustainable Processing of Graphene. *Green Chemistry* **2017**, *19* (11), 2550–2560. https://doi.org/10.1039/C7GC00112F.

(64) Silvestri, A.; Criado, A.; Poletti, F.; Wang, F.; Fanjul-Bolado, P.; González-García, M. B.; García-Astrain, C.; Liz-Marzán, L. M.; Feng, X.; Zanardi, C.; Prato, M. Bioresponsive, Electroactive, and Inkjet-Printable Graphene-Based Inks. *Advanced Functional Materials* **2022**, *32* (2), 2105028. https://doi.org/10.1002/adfm.202105028.

(65) Daou, B.; Silvestri, A.; Lasa, H.; Mancino, D.; Prato, M.; Alegret, N. Organic Functional Group on Carbon Nanotube Modulates the Maturation of SH-SY5Y Neuronal

Models. *Macromolecular Bioscience* **2023**, *23* (11), 2300173. https://doi.org/10.1002/mabi.202300173.

(66) Marelli, M.; Jouve, A.; Villa, A.; Psaro, R.; Balerna, A.; Prati, L.; Evangelisti, C. Hybrid Au/CuO Nanoparticles: Effect of Structural Features for Selective Benzyl Alcohol Oxidation. *J. Phys. Chem. C* **2019**, *123* (5), 2864–2871. https://doi.org/10.1021/acs.jpcc.8b09449.

(67) Oberhauser, W.; Evangelisti, C.; Marelli, M.; Santo, V. D.; Cepek, C.; Bellini, M. Gold Nanoparticles onto Cerium Oxycarbonate as Highly Efficient Catalyst for Aerobic Allyl Alcohol Oxidation. *Catalysis Communications* **2020**, *140*, 105989. https://doi.org/10.1016/j.catcom.2020.105989.

(68) Evangelisti, C.; Schiavi, E.; Aronica, L. A.; Psaro, R.; Balerna, A.; Martra, G. Solvated Metal Atoms in the Preparation of Supported Gold Catalysts. In *Gold Catalysis*; Jenny Stanford Publishing, 2015.

(69) Casaletto, M. P.; Longo, A.; Martorana, A.; Prestianni, A.; Venezia, A. M. XPS Study of Supported Gold Catalysts: The Role of Au0 and Au+δ Species as Active Sites. *Surface and Interface Analysis* **2006**, *38* (4), 215–218. https://doi.org/10.1002/sia.2180.

(70) Silvestri, A.; Vázquez-Díaz, S.; Misia, G.; Poletti, F.; López-Domene, R.; Pavlov, V.; Zanardi, C.; Cortajarena, A. L.; Prato, M. An Electroactive and Self-Assembling Bio-Ink, Based on Protein-Stabilized Nanoclusters and Graphene, for the Manufacture of Fully Inkjet-Printed Paper-Based Analytical Devices. *Small* **2023**, *19* (51), 2300163. https://doi.org/10.1002/smll.202300163.

(71) Vasil'kov, A. Yu.; Naumkin, A. V.; Volkov, I. O.; Podshibikhin, V. L.; Lisichkin, G. V.; Khokhlov, A. R. XPS/TEM Characterisation of Pt□Au/C Cathode Electrocatalysts Prepared by Metal Vapour Synthesis. *Surface and Interface Analysis* **2010**, *42* (6–7), 559–563. https://doi.org/10.1002/sia.3269.

(72) Jouve, A.; Nagy, G.; Somodi, F.; Tiozzo, C.; Villa, A.; Balerna, A.; Beck, A.; Evangelisti, C.; Prati, L. Gold-Silver Catalysts: Effect of Catalyst Structure on the Selectivity of Glycerol Oxidation. *Journal of Catalysis* **2018**, *368*, 324–335. https://doi.org/10.1016/j.jcat.2018.10.019.

(73) Suchomel, P.; Kvitek, L.; Prucek, R.; Panacek, A.; Halder, A.; Vajda, S.; Zboril, R. Simple Size-Controlled Synthesis of Au Nanoparticles and Their Size-Dependent Catalytic Activity. *Sci Rep* **2018**, *8* (1), 4589. https://doi.org/10.1038/s41598-018-22976-5.

(74) Hayden, B. E. Particle Size and Support Effects in Electrocatalysis. *Acc. Chem. Res.* **2013**, *46* (8), 1858–1866. https://doi.org/10.1021/ar400001n.

(75) Masitas, R. A.; Zamborini, F. P. Oxidation of Highly Unstable <4 Nm Diameter Gold Nanoparticles 850 mV Negative of the Bulk Oxidation Potential. *J. Am. Chem. Soc.* **2012**, *134* (11), 5014–5017. https://doi.org/10.1021/ja2108933.

(76) Lee, K. J.; Elgrishi, N.; Kandemir, B.; Dempsey, J. L. Electrochemical and Spectroscopic Methods for Evaluating Molecular Electrocatalysts. *Nat Rev Chem* **2017**, *1* (5), 1–14. https://doi.org/10.1038/s41570-017-0039.

(77) Khoshnevisan, K.; Maleki, H.; Honarvarfard, E.; Baharifar, H.; Gholami, M.; Faridbod, F.; Larijani, B.; Faridi Majidi, R.; Khorramizadeh, M. R. Nanomaterial Based Electrochemical Sensing of the Biomarker Serotonin: A Comprehensive Review. *Microchim Acta* **2019**, *186* (1), 49. https://doi.org/10.1007/s00604-018-3069-y.

(78) Shahrokhian, S.; Fotouhi, L. Carbon Paste Electrode Incorporating Multi-Walled Carbon Nanotube/Cobalt Salophen for Sensitive Voltammetric Determination of Tryptophan. *Sensors and Actuators B: Chemical* **2007**, *123* (2), 942–949. https://doi.org/10.1016/j.snb.2006.10.053.

(79) Simões, F. R.; Xavier, M. G. 6 - Electrochemical Sensors. In *Nanoscience and its Applications*; Da Róz, A. L., Ferreira, M., de Lima Leite, F., Oliveira, O. N., Eds.; Micro and Nano Technologies; William Andrew Publishing, 2017; pp 155–178. https://doi.org/10.1016/B978-0-323-49780-0.00006-5.

(80) Chen, S.; Zhitomirsky, I. Capacitive Behaviour of Polypyrrole, Prepared by Electrochemical and Chemical Methods. *Materials Letters* **2014**, *125*, 92–95. https://doi.org/10.1016/j.matlet.2014.03.124.

(81) Ensafi, A. A.; Zarei, K.; Khayamian, T. Determination of Ultratrace Amounts of Ruthenium by Differential Pulse Voltammetry Using Factorial Design for Optimization. *Microchemical Journal* **1999**, *63* (2), 235–242. https://doi.org/10.1006/mchj.1999.1786.

(82) Moro, G.; Silvestri, A.; Ulrici, A.; Conzuelo, F.; Zanardi, C. How to Optimize the Analytical Performance of Differential Pulse Voltammetry: One Variable at Time versus Design of Experiments. *J Solid State Electrochem* **2024**, *28* (3), 1403–1415. https://doi.org/10.1007/s10008-023-05753-x.

(83) Costa-Rama, E.; Fernández Abedul, M. T. Chapter 5 - Adsorptive Stripping Voltammetry of Indigo Blue in a Flow System. In *Laboratory Methods in Dynamic*

Electroanalysis; Fernandez Abedul, M. T., Ed.; Elsevier, 2020; pp 47–56. https://doi.org/10.1016/B978-0-12-815932-3.00005-X.

(84) Elgrishi, N.; Rountree, K. J.; McCarthy, B. D.; Rountree, E. S.; Eisenhart, T. T.; Dempsey, J. L. A Practical Beginner's Guide to Cyclic Voltammetry. *J. Chem. Educ.* **2018**, *95* (2), 197–206. https://doi.org/10.1021/acs.jchemed.7b00361.

(85) Hof, P. R.; Kidd, G.; DeFelipe, J.; de Vellis, J.; Sosa, M. A. G.; Elder, G. A.; Trapp, B. D. Chapter 1 - Cellular Components of Nervous Tissue. In *From Molecules to Networks (Third Edition)*; Byrne, J. H., Heidelberger, R., Waxham, M. N., Eds.; Academic Press: Boston, 2014; pp 3–21. https://doi.org/10.1016/B978-0-12-397179-1.00001-4.

(86) Chakraborty, P.; Dey, A.; Gopalakrishnan, A. V.; Swati, K.; Ojha, S.; Prakash, A.; Kumar, D.; Ambasta, R. K.; Jha, N. K.; Jha, S. K.; Dewanjee, S. Glutamatergic Neurotransmission: A Potential Pharmacotherapeutic Target for the Treatment of Cognitive Disorders. *Ageing Research Reviews* **2023**, *85*, 101838. https://doi.org/10.1016/j.arr.2022.101838.

(87) Rienecker, K. D. A.; Poston, R. G.; Segales, J. S.; Finholm, I. W.; Sono, M. H.; Munteanu, S. J.; Ghaninejad-Esfahani, M.; Rejepova, A.; Tejeda-Garibay, S.; Wickman, K.; Marron Fernandez de Velasco, E.; Thayer, S. A.; Saha, R. N. Mild Membrane Depolarization in Neurons Induces Immediate Early Gene Transcription and Acutely Subdues Responses to a Successive Stimulus. *Journal of Biological Chemistry* **2022**, *298* (9), 102278. https://doi.org/10.1016/j.jbc.2022.102278.

(88) Goodale, D. B.; Moore, K. E. Benztropine-Induced Release of Dopamine from Brain *in Vivo*. *Neuropharmacology* **1975**, *14* (8), 585–589. https://doi.org/10.1016/0028-3908(75)90125-2.

(89) Reith, M. E. A.; Berfield, J. L.; Wang, L. C.; Ferrer, J. V.; Javitch, J. A. The Uptake Inhibitors Cocaine and Benztropine Differentially Alter the Conformation of the Human Dopamine Transporter *. *Journal of Biological Chemistry* **2001**, *276* (31), 29012–29018. https://doi.org/10.1074/jbc.M011785200.

(90) Biesinger, M. C. Accessing the Robustness of Adventitious Carbon for Charge Referencing (Correction) Purposes in XPS Analysis: Insights from a Multi-User Facility Data Review. *Applied Surface Science* **2022**, *597*, 153681. https://doi.org/10.1016/j.apsusc.2022.153681.

(91) Souza, E. L. S. de; Chorro, T. H. D.; Correia, C. R. D. Thermal Analysis of Arenediazonium Tetrafluoroborate Salts: Stability and Hazardous Evaluation. *Process*

Safety and Environmental Protection **2023**, *177*, 69–81.
https://doi.org/10.1016/j.psep.2023.06.082.

Chapter III

Electrocatalytic Properties of Crystalline Phases of Molybdenum Disulfide for Hydrogen Peroxide Reduction and Non-Covalent Functionalization of 1T Nanosheets

Abstract

One of the key characteristics that determines the chemical and physical characteristics of two-dimensional molybdenum disulfide (2D MoS_2) is its crystalline phase. However, this parameter is not taken into account in 80% of the research examining the electrocatalytic characteristics of 2D MoS_2. In this chapter, a thorough electrochemical and colorimetric study is carried out to shed light on the influence of the crystalline phase and morphology of 2D MoS_2 in the electrocatalysis of the H_2O_2 reduction reaction (HPRR). The results highlight the superior catalytic activity of 1T phase and the difference in catalytic performances between 1T-MoS_2 nanosheets and nanoflowers.

The second part of the chapter focus on the development of a non-covalent functionalization approach to introduce primary amines on 1T-MoS_2 nanosheets, which could be exploited for further derivatizations of the materials for sensing applications.

3.1 Introduction

3.1.1 Molybdenum Disulfide as Sustainable Electrocatalyst

Two-dimensional molybdenum disulfide (MoS_2) is one of the most studied members of the large family of graphene-like materials known as transition metal dichalcogenides (TMDs). One of the most important properties of MoS_2 and other TMDs is the dependence of their band gap on the number of layers[1] and crystalline phase.[2]

In particular, 2D MoS_2 can exist mainly in two distinct phases: the metastable 1T phase has an octahedral structure and is metallic, while the thermodynamically stable 2H phase has a hexagonal lattice, operates as a semiconductor, and has a direct band gap of 1.8 eV.[3]

From optoelectronics[4] to memory storage,[5,6] from solar cells[7] to biomedical applications,[8] MoS_2 has emerged as an incredibly promising material.[9] Its outstanding mechanical

qualities, broad surface area, affordability, and tunability of electronic properties all contribute to its enormous success.

MoS_2 is considered a promising material for electrocatalysis, as it could represent a viable solution for some of the major issues that modern society is currently facing, in the fields of environmental remediation and energy conversion and storage. A noteworthy example is the electrocatalytic synthesis of green hydrogen, in which MoS2 stands out as sustainable alternative to the expensive catalysts based on noble metals like platinum.[10,11]

MoS_2 has been studied as well as electrocatalyst for nitrogen reduction reaction (NRR) as alternative to the Haber-Bosch process, the most used industrial process for the production of ammonia,[12] and for oxygen reduction reaction (ORR), necessary for fuel cell technology.[13]

The design of electrochemical sensors and biosensors can benefit greatly from electrocatalytic activity of MoS_2. In particular, its reported peroxidase-like activity makes it a potential tool for detection of hydrogen peroxide (H_2O_2).

3.1.2 The Role of Hydrogen Peroxide in the Human Body

H_2O_2 is the most important redox metabolite of human body, involved in redox sensing, signaling and redox regulation within many physiological processes.[14] At intracellular level, it is mostly produced in the mitochondria and by monoamine oxidases,[15] while at extracellular level the concerted activity of phagocyte NADPH oxidase and superoxide reductase/dismutase is its main source.[16–18]

At physiological concentrations (1-100 nmol L^{-1} at intracellular level, 1-5 μmol L^{-1} in plasma)[14,17] H_2O_2 plays the role of redox mediator, regulating the function of peroxidase enzymes like thiol peroxidases for reversible oxidation of cysteine in proteins,[19] as well as transcription factors.[20] The occurrence of pathological conditions determines variations of H_2O_2 concentration, leading to inflammation and oxidative stress.

Increased levels of H_2O_2 in biofluids (blood, lymph, bile) are associated with the progression of tumor metastasis[21] Alzheimer's disease,[22,23] Parkinson's disease[24–26] and dermatologic diseases like atopic dermatitis.[27,28]

As a consequence of its role in several physiological and pathological processes, the design and improvement of sensing device for H_2O_2 is an ever-growing field of research. Moreover, H_2O_2 is a useful mediator for enzymatic electrochemical sensors. Since many oxidoreductases, such as lactate oxidase and glucose oxidase, produce H_2O_2 as a byproduct,

it is possible to design composite electrochemical sensors that combine an electrocatalyst for H_2O_2 as a transducer and an oxidoreductase enzyme as a bioreceptor.[29–31]

3.1.3 Molybdenum Disulfide as Peroxidase Mimic

The catalytic activity of MoS_2 for electrochemical reduction of H2O2 was first reported by T. Wang et al., back in 2013.[32] In their work, a top-down approach, based on exfoliation in NMP, was used to obtain ultrasmall MoS_2 nanoparticles that were immobilized on a glassy carbon electrode (GCE). The modified GCE catalyzed the reduction of H_2O_2, anticipating the reduction peak at -0.5 V. Moreover, they demonstrated that the response was dependent on the size of nanoparticles, as smaller nanoparticles gave higher electrocatalytic effect.

Later, in 2015, X. Guo et al.[33] used the catalytic activity of MoS_2 for a colorimetric assay of H_2O_2 based on 3,3',5,5'-tetramethylbenzidine (TMB). To synthesize MoS_2, they used a hydrothermal synthesis, starting from Na_2MoO_4 and L-cysteine, obtaining layered MoS_2. Then they performed the colorimetric assay in acidic pH to demonstrate that the material behaved as a peroxidase-mimic nanozyme.

Lastly, in 2021 P. Cao et al. used a composite of MoS_2 with MoO_3 and polypyrrole to design a flexible sensor for H_2O_2 detection in living cells.[34] In their work, once again a bottom-up hydrothermal approach was used to synthesize the material, using polypyrrole as nucleation center for the growth of MoS_2 and MoO_3. The final sensor could detect H_2O_2 with a LOD of 0.18 μmol L^{-1}.

All these works share the fact of never specifically mentioning the crystalline phase of the synthesized MoS_2. To the best of our knowledge, not many studies have examined MoS_2 phase for its peroxidase-mimic activity. Y. Shu et al. did it in their work, where they synthesized MoS_2 nanoflowers enriched in 1T phase, using a hydrothermal approach with $(NH_4)_6Mo_7O_{24}$ and thiourea as precursors.[35] The obtained material was characterized by an interlayer-expanded structure and was applied in the design of a chronoamperometric with a LOD of 0.2 μmol L^{-1}. The crystalline phase is completely ignored in the remaining articles. In general, expanding the survey to more investigated electrocatalytic reactions (e.g., HER, OER, NRR, and ORR), it is possible to notice that, also in those fields, up to 80% of research articles still do not consider this fundamental parameter (**Figure 52**).

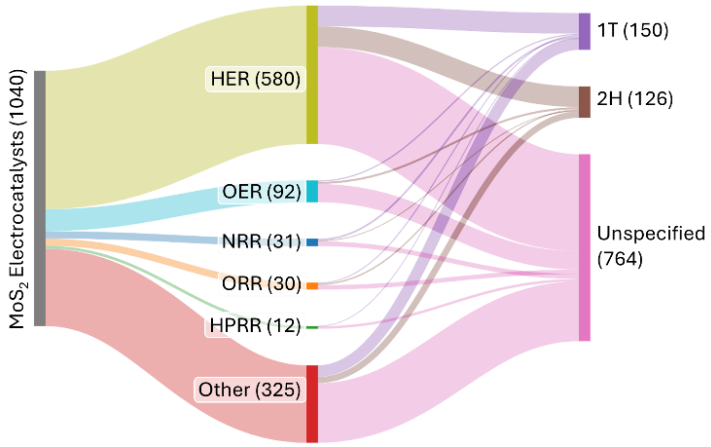

Figure 52 *Sankey diagram correlating the number of publications in the field of MoS_2 Electrocatalyst with the specific application (middle) and the phase of the material mentioned in the papers (right). Data: Scopus*

3.1.4 Aim of the Project

The aim of the project herein presented is to investigate the electrocatalytic activity of MoS2 for hydrogen peroxide reduction reaction (HPRR), to finally implement this material into enzymatic electrochemical sensors based on oxidoreductase enzymes.

In the first part of the project, different phases (1T and 2H) and morphologies (1T nanosheets and 1T nanoflowers) are synthesized, using top-down and bottom-up methods. The activities of the different materials for HPRR were compared using cyclic voltammetry (CV), Tafel analysis, and electrochemical impedance spectroscopy (EIS). Furthermore, the peroxidase-mimic activity of the different phases of MoS2 was investigated by colorimetric assay based on 3,3',5,5'-tetramethylbenzidine (TMB) and compared with Pt-based catalysts. The electrochemical study was performed under the supervision of Dr. Alessandro Silvestri and Prof. Maurizio Prato.

In the second part, a protocol was developed for non-covalent functionalization of 1T-MoS2 nanosheets with amine-bearing alkylammonium salts. The functionalization is meant to introduce available amine on the surface of MoS_2, for further derivatization and immobilization of enzymes on the surface of the material. The protocol was developed under the supervision of Dr. Alessandro Silvestri and Prof. Maurizio Prato, in collaboration with Dr. Michele Cesco from CICbiomaGUNE, Donosti-San Sebastian, Spain, who carried out part of the characterization of the functionalized materials (TGA, XPS, STEM-EDX).

3.2 Results and Discussion

3.2.1 Synthesis and Characterization of Molybdenum Disulfide

In order to carry out a comparative investigation of electrocatalytic activity of different MoS2 crystalline phases for H_2O_2 reduction, both 1T and 2H phases were synthesized, by top-down approach. In particular, 2D 2H-MoS_2 was obtained by ultrasound-aided physical exfoliation of bulk MoS_2 in NMP.[36] On the other hand, MoS2 enriched in 1T phase was achieved by chemical exfoliation, which involves intercalation of lithium ions between layers of bulk MoS_2 and consequent reduction of the 2H phase to 1T phase. The so obtained 1T-MoS_2 will be indicated as E1T-MoS_2.[37] To evaluate the effect of the synthetic pathway on the electrocatalytic performance of MoS_2, another batch of low-dimensional MoS_2 enriched in 1T-MoS_2 was synthesized by bottom-up approach. Specifically, a hydrothermal synthesis involving MoO_3 and C_2H_5NS as precursors was used.[38] The so-obtained MoS_2 will be referred to as H1T-MoS_2. The three synthetic approaches are resumed in **Figure 53**.

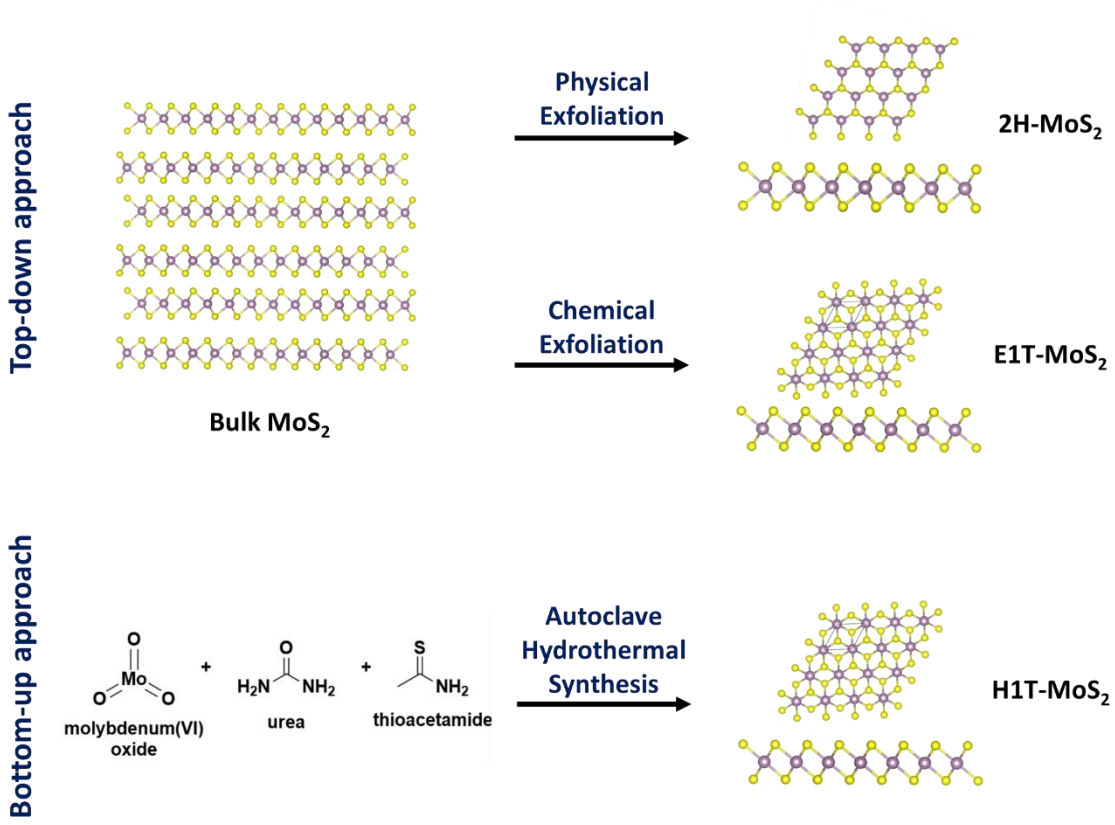

Figure 53 *Synthetic approaches for 2D 2H-MoS_2, E1T-MoS_2 and H1T-MoS_2.*

After synthesis, the three materials were characterized thoroughly. UV-Vis and Raman spectroscopy are techniques commonly used in literature to discern 2H and 1T phases of

MoS_2 (**Figure 54**). As for 2H-MoS_2, in UV-Vis spectrum the material presents typical bands at ca. 630 nm and 690 nm, which can be ascribed to A and B excitonic absorption.[39,40] The Raman spectrum of 2H phase exhibits one peak at 377.4 cm^{-1} (E_{2g}, in-plane vibration) and one peak at 404.2 cm^{-1} (A_{1g}, out-of-plane vibration), in agreement with literature.[41]

Both E1T-MoS_2 and H1T-MoS_2 show two absorption peaks in the UV-Vis spectrum, at 255 nm and 305 nm. In the Raman spectrum, typical vibrational modes associated with 1T phase are J_1 (154.6 cm^{-1} for E1T-MoS_2 and 152.4 cm^{-1} for H1T-MoS_2), J_2 (229.7 for E1T-MoS_2 and 225.3 cm^{-1} for H1T-MoS_2) and J_3 (327.8 cm^{-1} for E1T-MoS_2 and 324.6 cm^{-1} for H1T-MoS_2), associated with vibrations of the zigzag edges of the octahedral structure.[42]

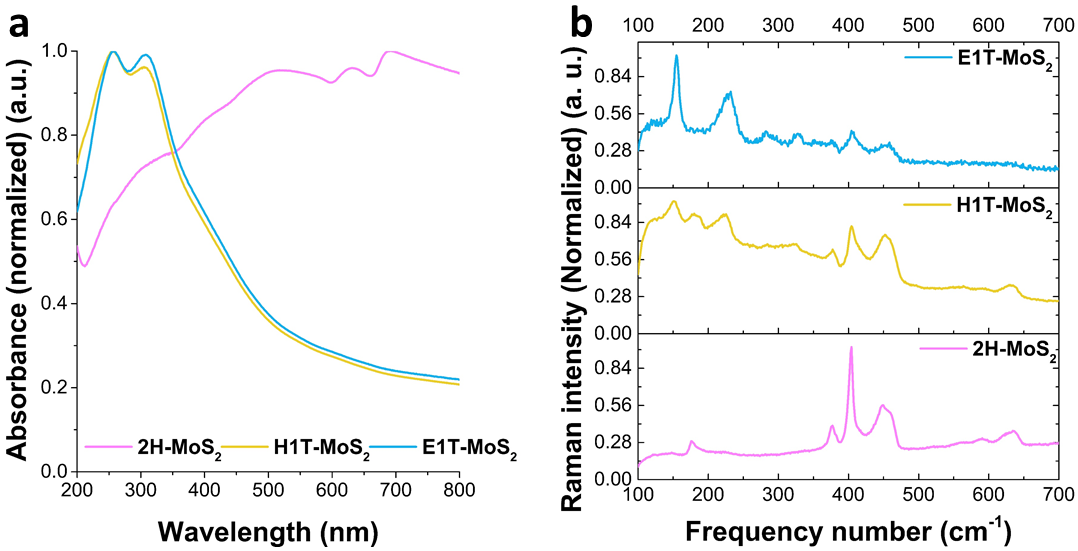

Figure 54 *a) UV-Vis spectra and b) Raman spectra of 2H-MoS_2, H1T-MoS_2 and E1T-MoS_2.*

The topology of the materials was investigated by TEM and AFM. Micrographs from TEM highlighted important differences between the three materials. 2H-MoS2 is characterized by large nanoplatelets with lateral size ranging from 0.2 to 2 μm, with an average size of 616 ± 285 nm (**Figure 55a**, statistical analysis performed on 96 nanoplatelets). H1T-MoS_2 (**Figure 55b**) presented peculiar nanoflower structures, a feature already known from literature for this hydrothermal synthesis.[35] The average size of the nanoflowers was determined to be 235 ± 53 nm (statistical analysis performed on 55 nanoflowers). Finally, E1T-MoS_2 exhibited large nanosheets with average lateral size of 874 ± 121 nm (**Figure 55c**, statistical analysis performed on 43 sheets), characterized by gaps and edges that result in defect-rich surface.

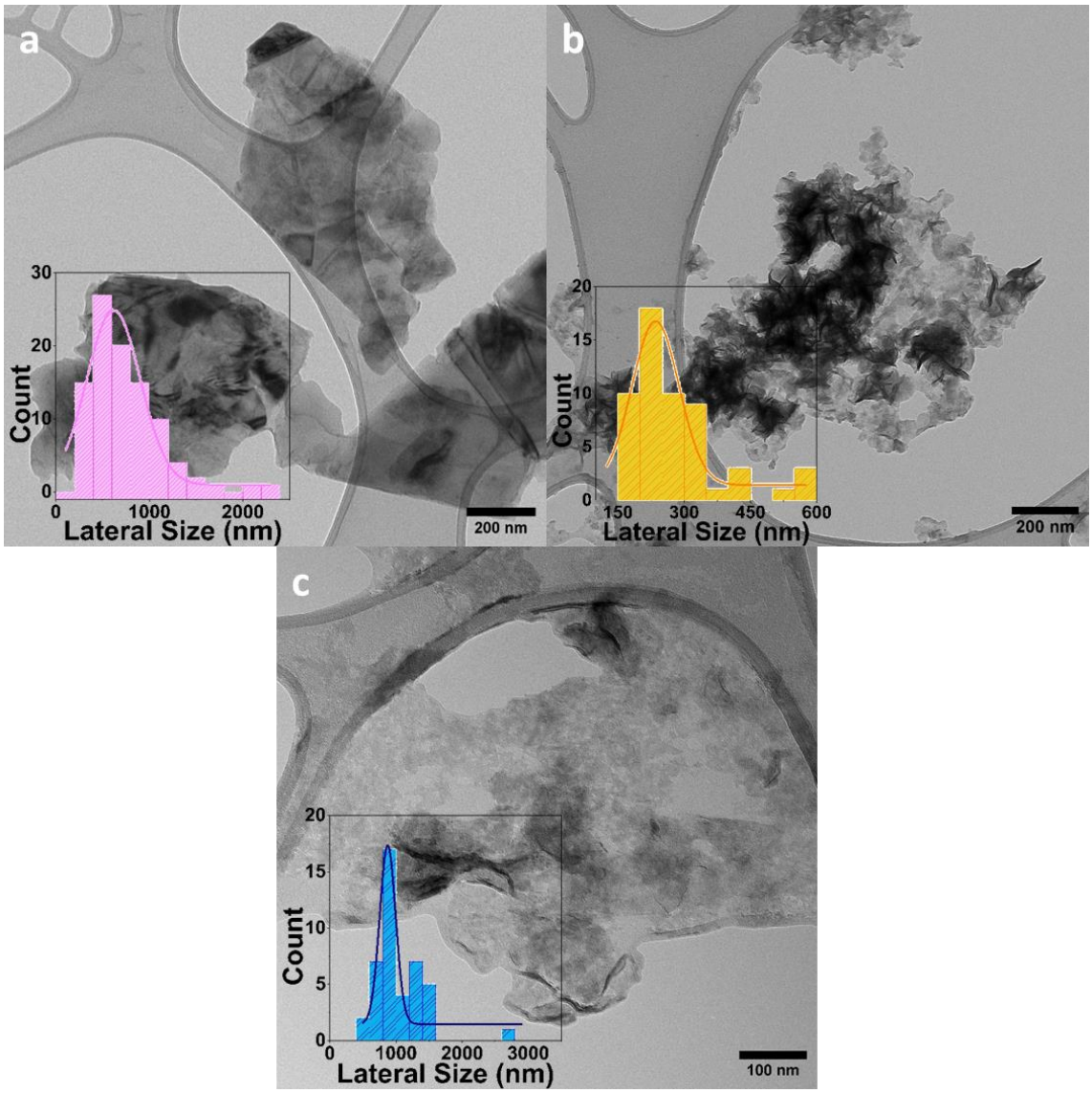

Figure 55 *TEM micrographs of a) 2H-MoS_2, b) H1T-MoS_2 and c) E1T-MoS_2. Statistical analysis is included as inset for each micrograph.*

By AFM, it was possible to determine the average thickness of the three materials. For 2H-MoS_2 (**Figure 56a**), the average thickness was found to be 1.31 ± 0.31 nm, which is consistent with 2-layer MoS_2.[43] A similar height profile was determined for E1T-MoS_2, with average height of 1.34 ± 0.28 nm (**Figure 56b**). On the other hand, H1T-MoS_2 presented high surface roughness, with height maxima of 5 nm and valleys of 4 nm deep (**Figure 56c**).

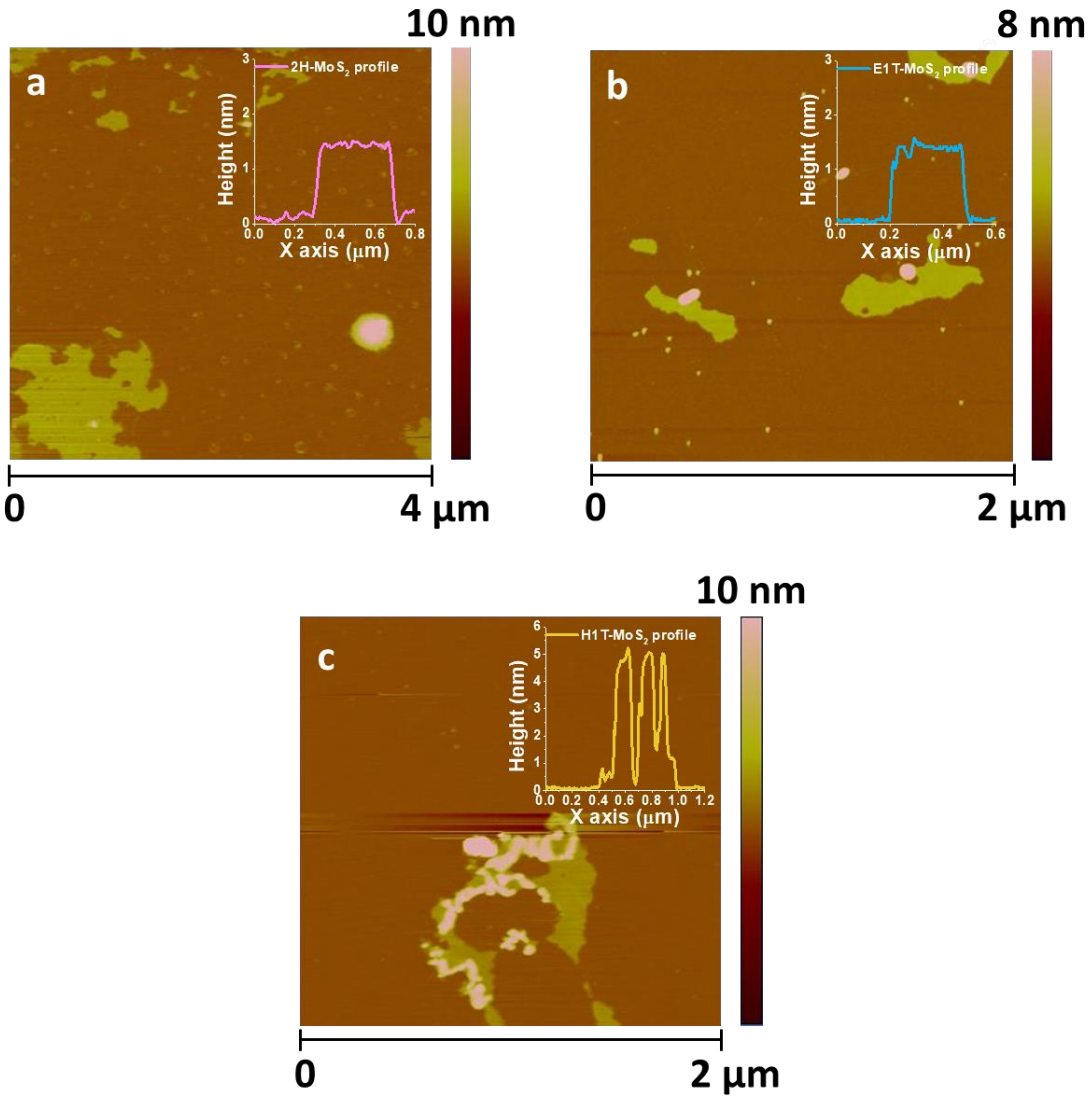

Figure 56 *AFM images of a) 2H-MoS_2, b) E1T-MoS_2 and c) H1T-MoS_2. The height profile is included as inset for each micrograph.*

3.2.2 Evaluation of Electrocatalytic Activity of Different Crystalline Phases

To assess the electrocatalytic activity of different crystalline phases, in first instance cyclic voltammetry was used to define the electrochemical system, the redox processes occurring and the relative onset potentials. The measurements were carried out with modified GCEs in oxygen-free solutions of H_2O_2 (8mmol L^{-1}), in PBS/KCl buffer. The potential was scanned in a range between 0.2 and -0.8 V, with scan rate of 10 mV/s, and the resultant voltammograms are reported in **Figure 57**.

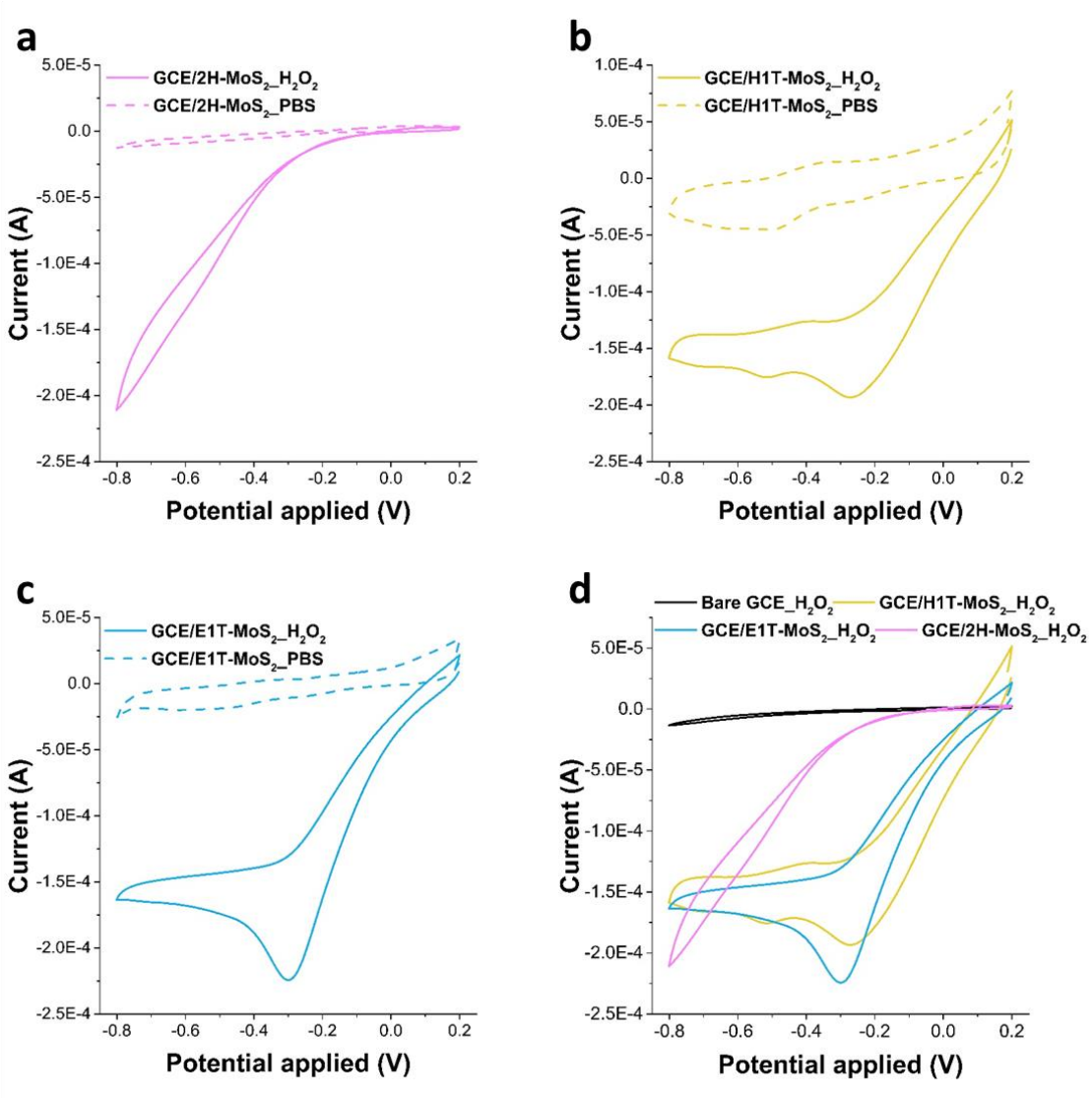

Figure 57 *Cyclic voltammograms of PBS and of solutions of H_2O_2 8mmol L^{-1}, with a) 2H-MoS_2-modified GCE; b) H1T-MoS_2-modified GCE; c) E1T-MoS_2-modified GCE. D) Overlay of voltammograms registered in the presence of H_2O_2 8mmol L^{-1} with modified GCE and Bare unmodified GCE.*

With all three materials, a cathodic faradaic current can be observed in the presence of H_2O_2. In particular, the overlay of the voltammograms (**Figure 57d**) shows how the materials enriched in 1T phase emerge for their superior activity compared to 2H-MoS_2, as they anticipate the reduction peak closer to 0 V, with a maximum at around -0.3 V. Furthermore, when the GCE is modified with E1T-MoS_2, the cathodic current is apparently higher (-224 µA) than what is observed with H1T-MoS_2 (-193 µA), and this could be related to a faster electron transfer.

For both E1T-MoS_2 and H1T-MoS_2, chronoamperometric studies recorded at -0.3 V showed that the faradaic current is linearly dependent on H_2O_2 concentrations in the range of 0.5 – 8 mmol L^{-1}, with R^2 = 0.9999 and 0.9877, respectively (**Figure 58**).

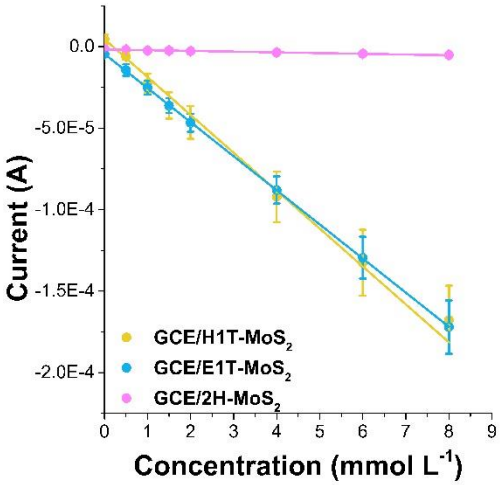

Figure 58 *Chronoamperograms registered at -0.3 V H_2O_2 solutions at 0.5, 1, 1.5, 2, 4, 6 and 8 µmol L^{-1} in PBS 0.1 mol L^{-1} KCl 0.1 mol L^{-1}, with GCE/2H-MoS_2 (pink), GCE/E1T-MoS_2 (light blue) and GCE/H1T-MoS_2 (yellow).*

To get a better understanding of the kinetics of the reaction and compare quantitatively the performance of the different materials, Tafel analysis was applied to the electrochemical system under study. First, linear polarization experiments were carried out with each modified electrode. The polarization curves were obtained by plotting the logarithm of the current density versus the applied potential (**Figure 59a**). From the minima of the polarization curves it was possible to interpolate the onset potentials (*i.e.* the potential at which the electrochemical process starts) for the electrocatalytic reduction of H_2O_2 with the different materials (**Table 10**). The large anticipation of the onset potential provoked by

both E1T-MoS_2 and H1T-MoS_2, compared with 2H-MoS_2 and the bare GCE, further demonstrates the influence of the 1T phase for the electrocatalytic activity of MoS_2.

After isolating the cathodic branches of the polarization curves, the overpotential (η) was plotted against the logarithm of the current density, and the linear region of the graph was fitted by linear regression (**Figure 59b**). The obtained Tafel plot is expressed by **Equation 1**:

Equation 1 $$\eta = b\ log_{10}(j) - c$$

Where b coincides with the Tafel slope, j is the current density (calculated on the geometric surface area of the modified GCEs) and c is a constant that is directly proportional to the logarithm of the exchange current density, j_0 ($c = b\ log_{10}(j_0)$).[44,45]

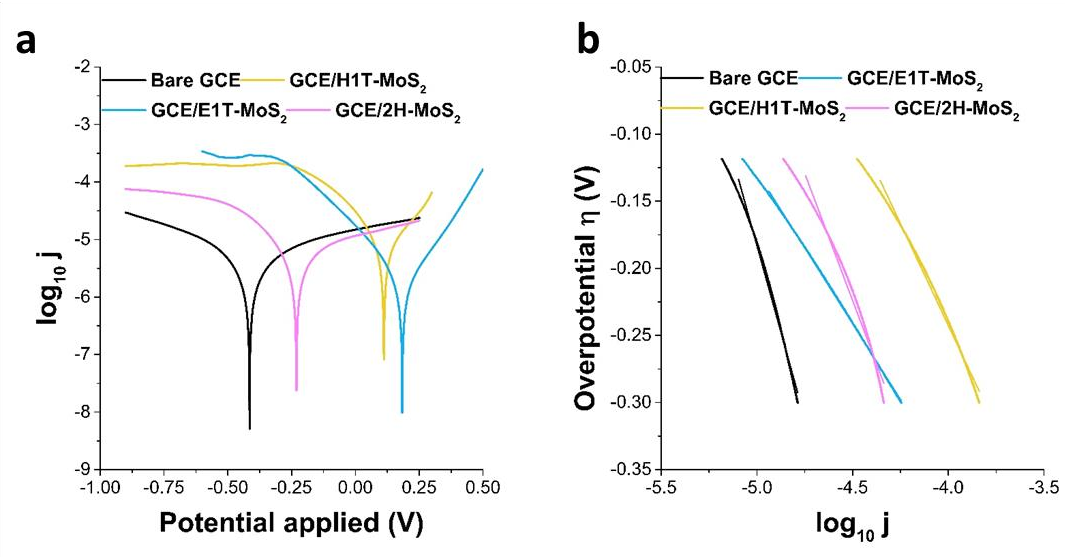

Figure 59 *a) Polarization curves obtained from linear sweep voltammetry in presence of a solution of H_2O_2 5 mmol L^{-1}; b) Tafel plots obtained for the three materials compared with bare GCE.*

The Tafel slope is a parameter describing the relation between the applied overpotential and the registered current density at the working electrode. Thus, it can be used as descriptor for the efficiency of an electrocatalyst. Since the overpotential is plotted as function of the current density, lower values of $|b|$ mean that lower overpotential must be applied in order to carry out the reaction and produce the same current density, resulting in better electrocatalytic activity.[45]

The Tafel constant ($\eta_{j=1}$) is another descriptor used to evaluate the efficiency of electrocatalysts, and is defined as the value of the overpotential η when j = 1 ($\eta_{j=1}$ =

$-b\ log_{10}(j_0)$). By definition, $\eta_{j=1}$ coincides with the value of overpotential that must be provided to yield one unit of current; thus, lower values of $\eta_{j=1}$ mean better electrocatalytic performances. This parameter is related to the Tafel slope, as the two parameters are directly proportional, but at the same time is dependent on another parameter, which is the exchange current density, j_0.[46]

Exchange current density (j_0) is another metric that must be taken into account when defining the electrocatalytic activity of a material, as it describes its activity. It is expressed as electrical current per surface area and defines the promptness of an electrode to advance with an electrochemical process. Generally, higher the exchange current density correlate with higher catalytic activity of the electrode.[47]

The values of Tafel slope, Tafel constant and exchange current density for the three materials and the negative control (bare GCE) are reported in **Table 10** and depicted as Kiviat plot in **Figure 60**.

Table 10 *Extracted parameters from polarization curves and Tafel analysis.*

	Onset Potential (V)	**Tafel Slope, *b* (mv/dec)**	**Tafel Constant, $\eta_{j=1}$ (V)**	**Exchange Current Density, j_0 (A/cm^2)**
Bare GCE	-0.413	-514	-2.754	4.38×10^{-6}
GCE/H1T-MoS_2	0.113	-303	-1.457	1.55×10^{-5}
GCE/E1T-MoS_2	0.185	-226	-1.258	2.71×10^{-6}
GCE/2H-MoS_2	-0.232	-378	-1.927	7.90×10^{-6}

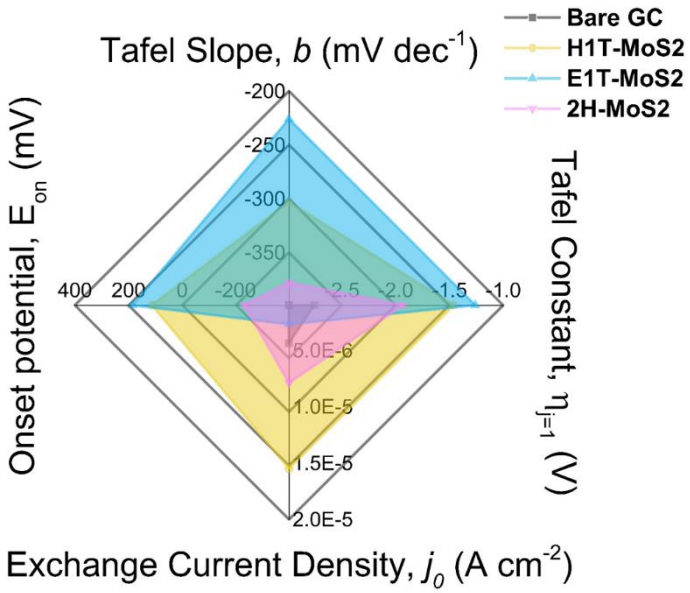

Figure 60 *Kiviat plot illustrating electrocatalytic performances of different materials.*

Based on CV and Tafel analysis, it is possible to affirm that both E1T-MoS_2 and H1T-MoS_2 are good electrocatalysts for the reduction of H_2O_2. In particular, E1T-MoS_2 stands out as the most efficient, as it presents the lowest values of Tafel slope (-226 mV dec^{-1}) and Tafel constant (-1.258 V), and a more positive onset potential (0.185 V). H1T-MoS2 has a similar onset potential (0.113 V), but higher Tafel slope (-303 mV dec^{-1}) and Tafel constant (-1.457 V). On the other hand, although 2H-MoS_2 has an electrocatalytic activity, it is not as efficient. The modified GCE/2H-MoS_2 is the electrode that registered the smallest onset potential anticipation (-0.232 V) and lowest efficiency as demonstrated by the high Tafel slope (-378 mV dec^{-1}) and Tafel constant (-1.927 V).

An important difference between E1T-MoS_2 and H1T-MoS_2 resides in the measured exchange current densities. Counterintuitively, H1T-MoS_2 presents a value of exchange current density that is higher by one order of magnitude, when compared with E1T-MoS_2. This behavior can be attributed to the different morphology of the two materials. In fact, it has been observed that in the case of HER the exchange current density is directly proportional to the edge length of MoS_2, indicating that electrocatalytic HER takes place prominently at the edge sites of MoS_2.[48] The nanoflower shape of H1T-MoS_2 presents several rough edges, which could explain the higher current density, implying that also in the case of H_2O_2 reduction the electrocatalytic sites are localized predominantly at the edges.

E1T-MoS_2 exhibits lower value of j_0 also when compared with the less active 2H-MoS_2. This could be explained by the higher affinity of E1T-MoS_2 for the substrate. Indeed, DFT

calculations have demonstrated that strong adsorption of the substrate on the surface of the catalyst may induce lower exchange current densities.[49]

3.2.3 Electrochemical Impedance Spectroscopy Study

To further study the efficiency of charge transfer and the conductivity of the materials, electrochemical impedance spectroscopy (EIS) was used. First, the reversible redox couple $[Fe(CN)_6]^{-3}/[Fe(CN)_6]^{-4}$ was used to study the conductivity of the modified electrodes: by performing EIS at the open circuit potential (OCP) it was possible to observe how the introduction of MoS_2 reduces the resistance to charge transfer (R_{CT}) with respect with the bare electrode (**Figure 60**).

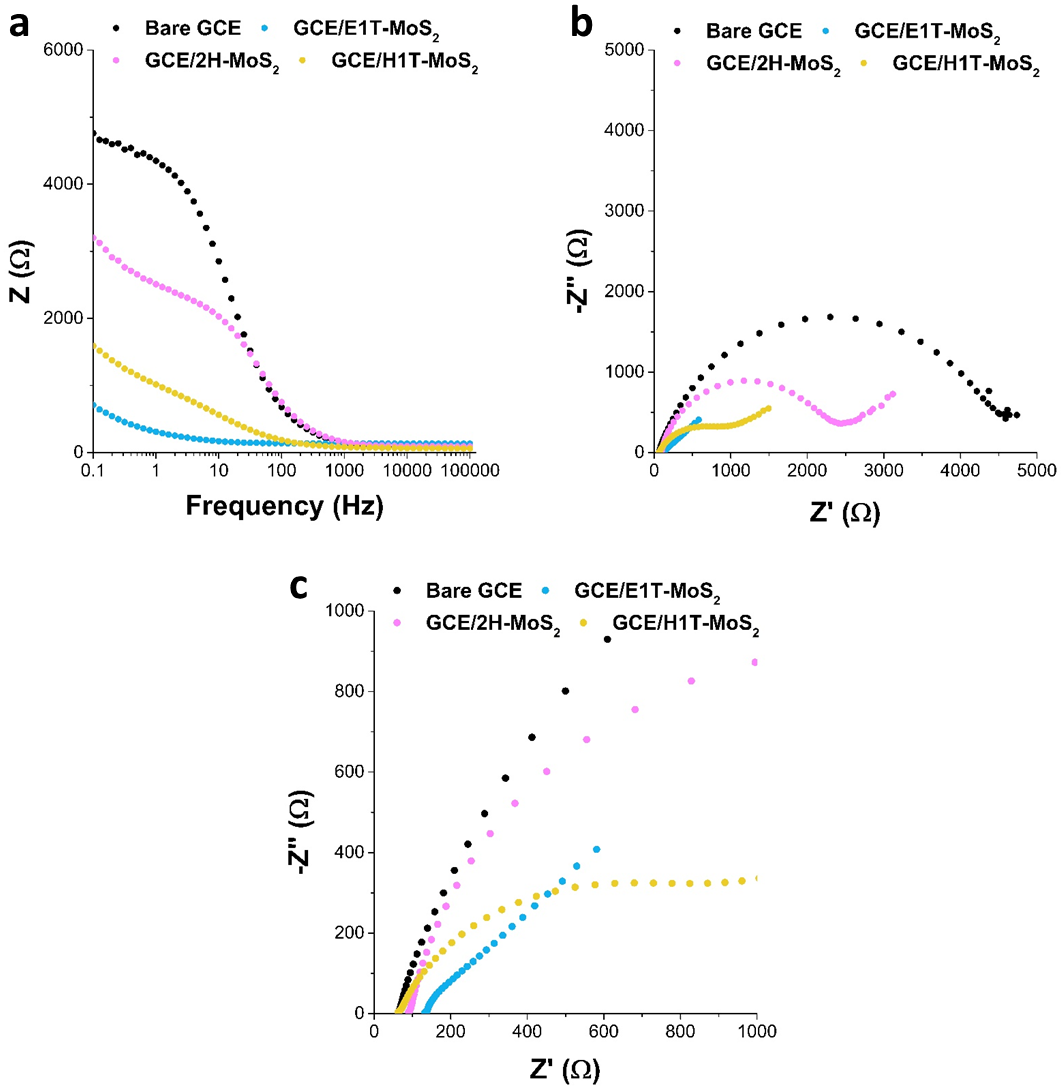

Figure 61 *a) Bode plot ad b) Nyquist plot of impedance spectra recorded in 5mM solution of $[FeCN_6]^{3-}/[FeCN_6]^{4-}$ with Bare GCE (black), E1T-MoS_2-modified GCE (light blue), H1T-MoS_2-*

modified GCE (yellow) and 2H-MoS_2-modified GCE (pink) at open circuit potential; c) magnification of the Nyquist plot in the high-frequency region.

The obtained spectra were fitted with equivalent circuits, to isolate electrical and electrochemical processes taking place at the electrode surface.

In **Table 11** are reported the equivalent circuit used to fit the data of EIS with $[Fe(CN)_6]^{3-}$/$[Fe(CN)_6]^{4-}$ redox couple for the three materials and the bare electrode as negative control.

Table 11 *Fitted parameters from EIS of modified electrodes with $[Fe(CN)_6]^{3-}$/$[Fe(CN)_6]^{4-}$ redox couple.*

Electrode	Equivalent Circuit	Fitted parameters
Bare GCE	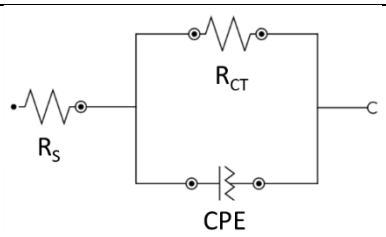	**R_S =** 63.0 Ω **R_{CT} =** 4.58 kΩ **CPE =** 8.02 µMho $s^{0.808}$
GCE/H1T-MoS_2	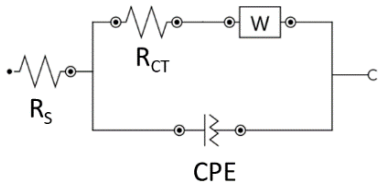	**R_S =** 62.1 Ω **R_{CT} =** 827.0 Ω **W =** 1.55 mMho $s^{0.5}$ **CPE =** 77 µMho $s^{0.717}$
GCE/E1T-MoS_2	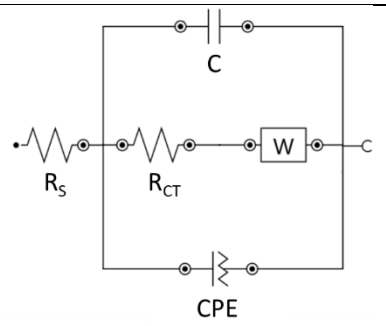	**R_S =** 135.0 Ω **C =** 137 µF **R_{CT} =** 82.2 Ω **W =** 459 µMho $s^{0.5}$ **CPE =** 1.53 mMho $s^{0.425}$
GCE/2H-MoS_2	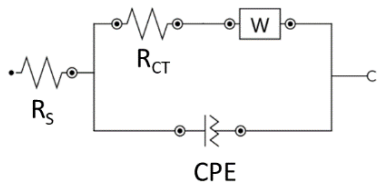	**R_S =** 91.5 Ω **R_{CT} =** 2.21 kΩ **W =** 1.16 mMho $s^{0.5}$ **CPE =** 4.90 µMho $s^{0.861}$

In all cases, the equivalent circuits include the parameter R_S, taking into account the resistance of the electrolyte buffer, with a value of resistance ranging from 62 to 135 Ω, and a CPE. For GCE/H1T-MoS_2 and GCE-2HMoS_2, a simple Randles circuit was used including an R_{CT} element, describing the resistance to the charge transfer during the electrochemical reaction, and a Warburg impedance element (W) for the mass transfer from bulk solution to electrode surface. In the case of E1T-MoS_2, a capacitor (C) was added in parallel to the Randles circuit, to account for the intrinsic capacitance of the material at negative polarizations.[50] In the case of the bare GCE, the equivalent circuit does not include a W element, as the R_{CT} is preponderant and there is no mass-transfer-dependent region in the spectrum.

Upon analyzing and fitting the impedance spectra, H1T-MoS_2 and E1T-MoS_2 outcompete the 2H phase, in terms of conductivity, thanks to their metallic nature. In particular, for the E1T-MoS_2-modified electrode R_{CT} is the lowest (82.2 Ω), and its impedance spectrum is dominated by mass diffusion (W) and capacitance. H1T-MoS_2 follows, with R_{CT} equal to 827.0, while 2H-MoS_2 presents a much higher value of 2.210 kΩ, reflecting its non-metallic nature.

The value of R_{CT} at the OCP is correlated to j_0 by **Equation 2**:[51]

$$\textbf{Equation 2} \quad j_0 = \frac{RT}{nFAR_{ct}}$$

Where R is the ideal gas constant (8.31 J mol^{-1} K^{-1}), T is the temperature (298 K), n is the number of electrons involved in the reaction, F is the Faraday constant (96485 C mol^{-1}), A is the surface of the electrode (0.19635 cm^2).

The exchange current densities calculated from the EIS experiments with $[Fe(CN)_6]^{3-}$/$[Fe(CN)_6]^{4-}$ (

Table 12) show a different trend with respect to the results from Tafel analysis, with E1T-MoS_2 having the highest value of j_0. These evidences suggest that the decrease of exchange current density for E1T-MoS_2 depends on the specific interaction between the catalyst and H_2O_2, rather than the conductivity and activity of the material.

Table 12 *Values of R_{CT} and j_0 derived from EIS measurement of with the three different materials.*

	R_{CT} (Ω)	**Exchange Current Density, j_0 (A cm^{-2})**
GCE/E1T-MoS_2	82.2	1.59×10^{-3}
GCE/H1T-MoS_2	827	1.58×10^{-4}
GCE/2H-MoS_2	2210	5.91×10^{-5}
Bare GCE	4580	2.85×10^{-5}

To verify this hypothesis and study the charge transfer during the electrocatalyzed reaction, EIS measurements were carried out in presence of 5 mmol L^{-1} solution of H_2O_2, in PBS/KCl buffer, at low and at high applied overpotential (referred to the onset potential) (**Figure 62**). The obtained spectra were all fitted with a simple equivalent circuit involving three elements that are R_S, R_{CT} and CPE (

Table 13).

Table 13 *Fitted parameters from EIS of modified electrodes with 5 mmol L^{-1} H_2O_2.*

Electrode and conditions	Equivalent Circuit	Fitted parameters
GCE/H1T-MoS_2 at the OCP	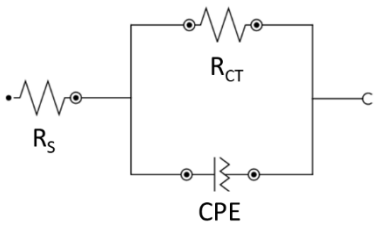	**R_S =** 51.9 Ω **R_{CT} =** 9210 Ω **CPE =** 329 µMho $s^{0.823}$
GCE/H1T-MoS_2 at -0.3 V	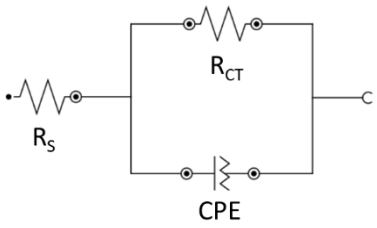	**R_S =** 89.6 Ω **R_{CT} =** 4270.0 Ω **CPE =** 602 µMho $s^{0.808}$
GCE/E1T-MoS_2 at the OCP	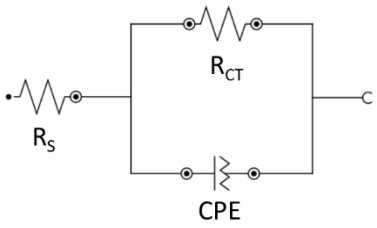	**R_S =** 113.0 Ω **R_{CT} =** 18000 Ω **CPE =** 241 µMho $s^{0.912}$
GCE/E1T-MoS_2 at -0.3 V	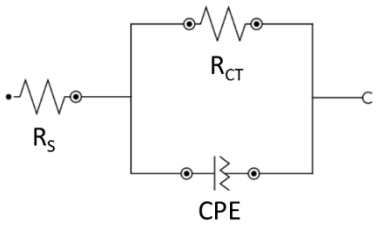	**R_S =** 111.0 Ω **R_{CT} =** 1310.0 Ω **CPE =** 521 µMho $s^{0.799}$

At low overpotential (*i.e.* at the OCP, **Figure 62a**), the fitting yielded values of R_{CT} equal to 18 kΩ for E1T-MoS_2 and 9.21 kΩ for H1T-MoS_2, which conversely result in values of j_0 of 7.26 × 10^{-6} A cm^{-2} and 1.42 × 10^{-5} A cm^{-2}, respectively (considering n = 1). These values of j_0 are compatible with data from Tafel analysis confirming the change of trend depending on the interaction of the materials with H_2O_2. However, when higher voltages are applied (-0.3 V corresponding to the position of the reduction peak in the CVs), the impedance spectra for the two materials revert and E1T-MoS2 shows better charge transfer, with an R_{CT} equal to 1.31 kΩ (j = 9.98 × 10^{-5}) (**Figure 62b**). H1T-MoS_2, is characterized by a less prominent increase of charge transfer (R_{CT} = 4.27 kΩ, j = 3.06 ×10^{-5}), which can be attributed to the lower conductivity of the material.

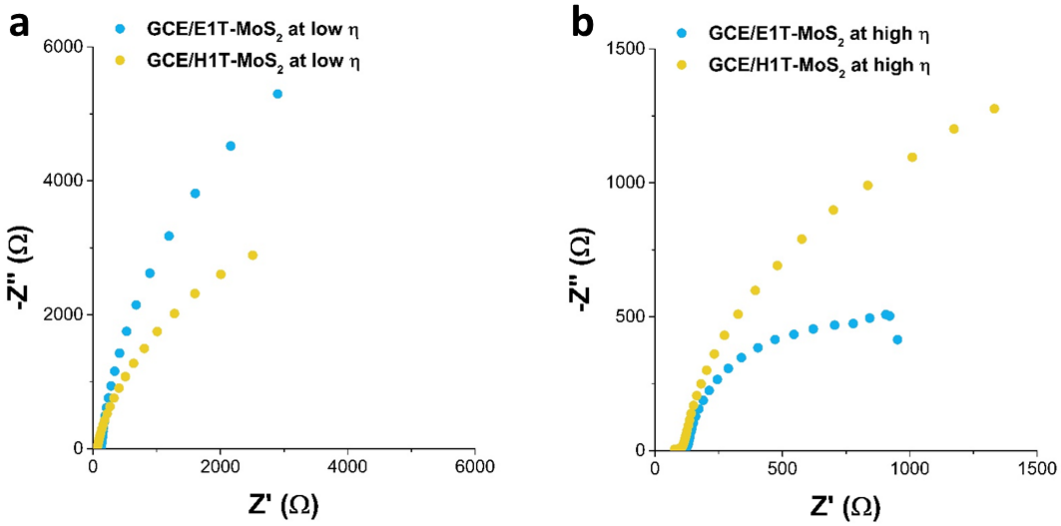

Figure 62 *Nyquist plot of impedance spectra recorded in 5mmol L^{-1} solution of H_2O_2 with E1T-MoS_2-modified GC electrode and H1T-MoS_2-modified GC electrode, at open circuit potential (a) and at -0.3 V (b).*

In the end, summing up all information from the electrochemical study, it was possible to assess that MoS_2 enriched in 1T phase is more electrocatalytically active than physically exfoliated 2H-MoS_2, and that E1T-MoS_2 and H1T-MoS_2 have a similar *j-η* dependency. H1T-MoS_2 is kinetically favored by higher j_0 and performs better at lower overpotentials, which could be attributed to higher number of active sites on the jagged edges of the nanoflowers. However, E1T-MoS_2 outcompetes H1T-MoS_2 at higher overpotential, thanks to higher conductivity and charge transfer.

Furthermore, by comparing data from EIS and Tafel, it emerged that the values of j0 calculated by the two techniques are comparable when a single-electron transfer (SET) is considered in the rate determining step (n = 1). Thus, the proposed mechanism involves the adsorption of H_2O_2 on the surface of the catalyst followed by homolytic cleavage of the O-O bond of H_2O_2, with consequent formation of free OH radicals that are subsequently reduced via charge transfer from the modified electrode. This mechanism is observed with catalytic nanomaterials based on metals of the platinum group[52] that have been implemented in colorimetric[53–55] and electrochemical sensors.[56,57] Compared with platinum, MoS_2 could be an excellent alternative thanks to its lower cost and larger availability.

3.2.4 Colorimetric Assay

A colorimetric assay based on 3,3',5,5'-tetramethylbenzidine (TMB) was used to confirm the proposed mechanism. The chromogenic substrate reacts with hydroxyl radicals formed during SET reaction catalyzed by peroxidase-mimicking catalysts, producing a blue species that strongly absorbs at 652 nm.[58,59]

Suspensions of the three materials were incubated with a 50 mmol L^{-1} solution of H_2O_2, in presence of TMB (1 mmol L^{-1}) in acetate buffer (pH = 3.5), and the absorbance was monitored over 45 minutes. As shown in **Figure 63a-b**, 2H-MoS_2 has no peroxidase-like activity under these experimental conditions, as there is no difference with the negative control. On the other hand, both E1T-MoS_2 (**Figure 63c**) and H1T-MoS_2 (**Figure 63d**) catalyze the reduction of H_2O_2 behaving as peroxidase-mimic catalysts, developing an intense blue coloration over 30 minutes (**Figure 63e**). These observations highlights again the importance of the 1T phase for the catalytic activity, not only in electrochemical setup, but also in colorimetric determination.

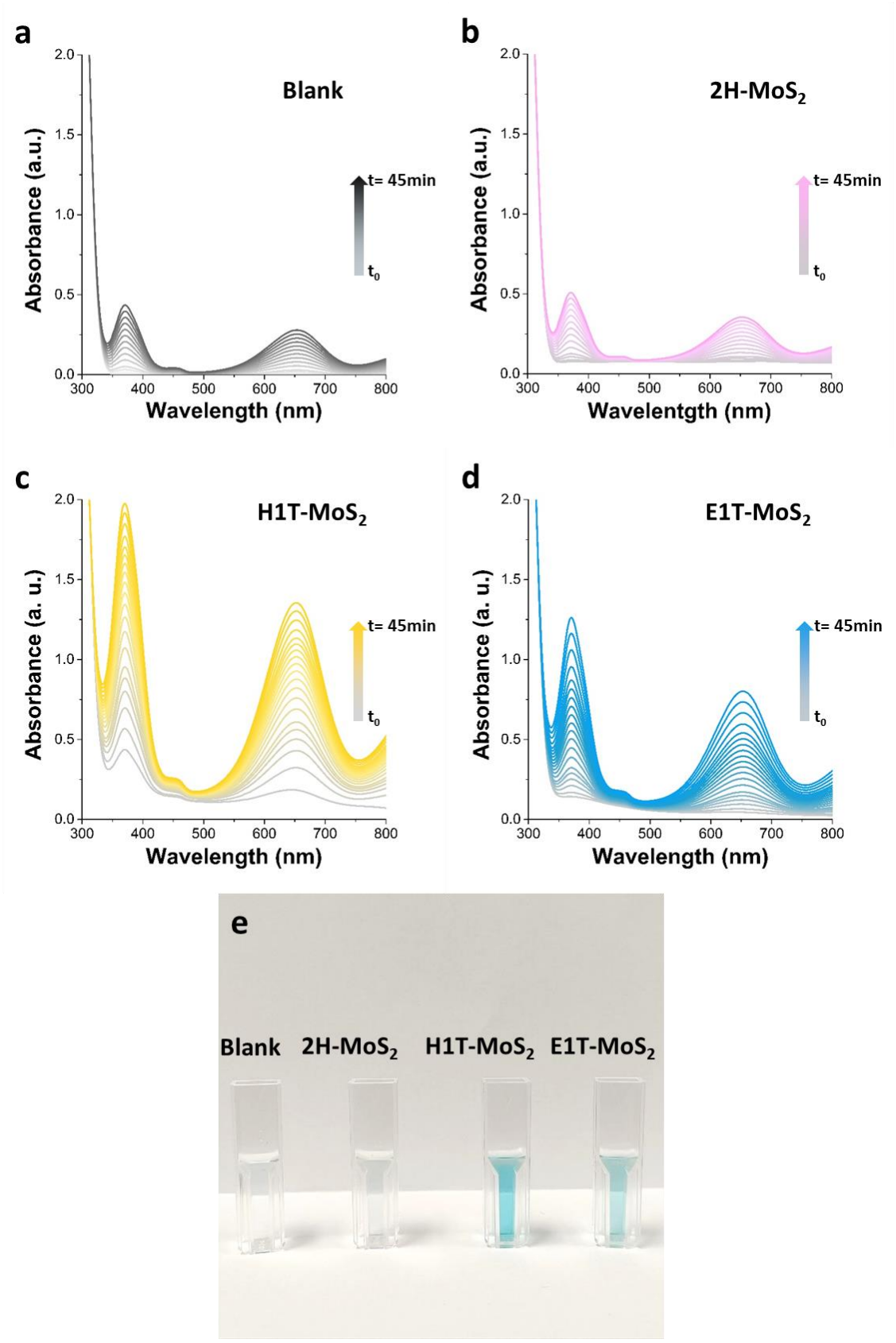

Figure 63 *a-d) UV-Vis spectra of TMB registered over 45 min in the presence of H_2O_2 50 mmol L^{-1}, with no material (a), 2H-MoS_2 (b), H1T-MoS_2 (c) and E1T-MoS_2 (d). e) Photograph of the colorimetric assay after 30 min of incubation with 50 mmol L^{-1}*

Another apparent feature from the colorimetric assay is the higher activity of H1T-MoS_2 when compared to E1T-MoS_2. By studying the kinetic of the reaction at different H_2O_2 concentrations, it was possible to observe that at low concentrations of substrate, there is no significant difference between the two 1T-MoS_2 (**Figure 64a**). However, at concentrations higher than 10 mmol L^{-1}, the trends for the reaction rate start to diverge, with E1T-MoS_2 starting to decline, possibly due to saturation of the active sites of the catalyst. On the other hand, H1T-MoS2 does not reach saturation in the investigated concentration range (**Figure 64b**).

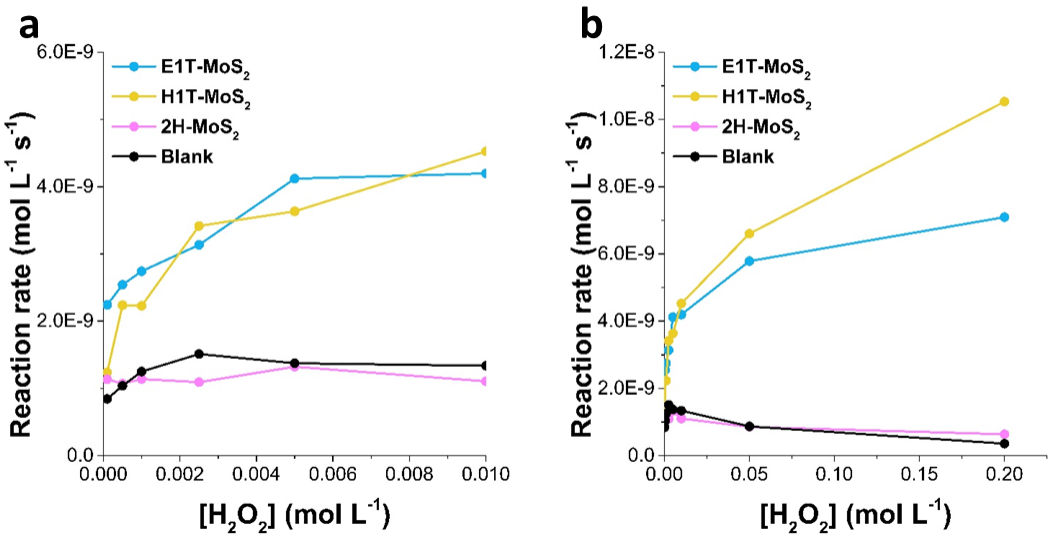

Figure 64 *Reaction rates measured in the first 300 s for all materials in the presence of H_2O_2 in a concentration range from 0 to 10 mmol L^{-1} (a) and 0 to 200 mmol L^{-1} (b).*

By comparing these data with the information obtained from the electrochemical analysis, it is possible to determine a correlation between the saturation of the active sites and a low value of j_0 for E1T-MoS_2 when compared to H1T-MoS_2. As previously stated, in absence of an applied overpotential, H1T-MoS_2 is kinetically favored, thus constitutes a better option for homogeneous catalysis in colorimetric assays.

3.2.5 Non-Covalent Functionalization of 1T-Molybdenum Disulfide

The electrocatalytic effect of 1T-MoS_2 could be extremely beneficial to design electrochemical enzymatic biosensors, using oxidoreductase enzymes as receptors. To unlock this feature, it is necessary to develop a functionalization strategy to immobilize the enzymes on the surface of the material. Ideally, the functionalization should leave the electronic and catalytic properties unchanged and at the same time allow the enzymes to retain their structure and activity.

To functionalize 1T-MoS_2 without interfering with its structure, a non-covalent approach was chosen, exploiting electrostatic interaction between the intrinsically negatively charged material and quaternary alkylammonium cations. Specifically, cholamine chloride hydrochloride ($ChNH_3$) and synthesized N',N',N'-triethylethane-1,2-diaminium salt (Et_3NEtNH_3) were used to introduce amines on the surface of 1T-MoS_2, to be subsequently used for further modification of the material surface. After synthesizing the alkylammonium salts, the functionalization is carried out by just mixing 1T-MoS_2 aqueous suspension and an aqueous solution of the alkylammonium salts and stirring.

3.2.5.1 Zeta Potential titration

The interaction between the material and the organic salts was investigated by zeta potential measurement. 1T-MoS_2 is intrinsically charged, with a zeta potential of ca -33 mV. As shown in **Figure 65a-b**, the addition of different equivalents of the organic salts determines a shift of the zeta potential towards more positive values. In particular, the addition of 1 equivalent of $ChNH_3$ determines a variation of zeta potential equal to 11.6 mV, while the addition of Et_3NEtNH_3 leads to a variation of 16.6 mV.

From the different trends, it is possible to infer that a stronger interaction occurs between Et_3NEtNH_3 and 1T-MoS_2, with respect to $ChNH_3$. This could be related to the more hydrophobic character of Et_3NEtNH_3 cation, which hinders its solvation by water molecule, favoring its adsorption on the negatively charged surface.[60,61] This feature is extremely interesting, as tuning the hydrophobicity of the alkylammonium salt could be an effective strategy to control the degree of functionalization.

In both cases, the change of surface charge of the material leads to aggregation and precipitation when the amount of added alkylammonium salt exceeds 0.5 equivalents, with total precipitation at 1 equivalent (**Figure 65c**).

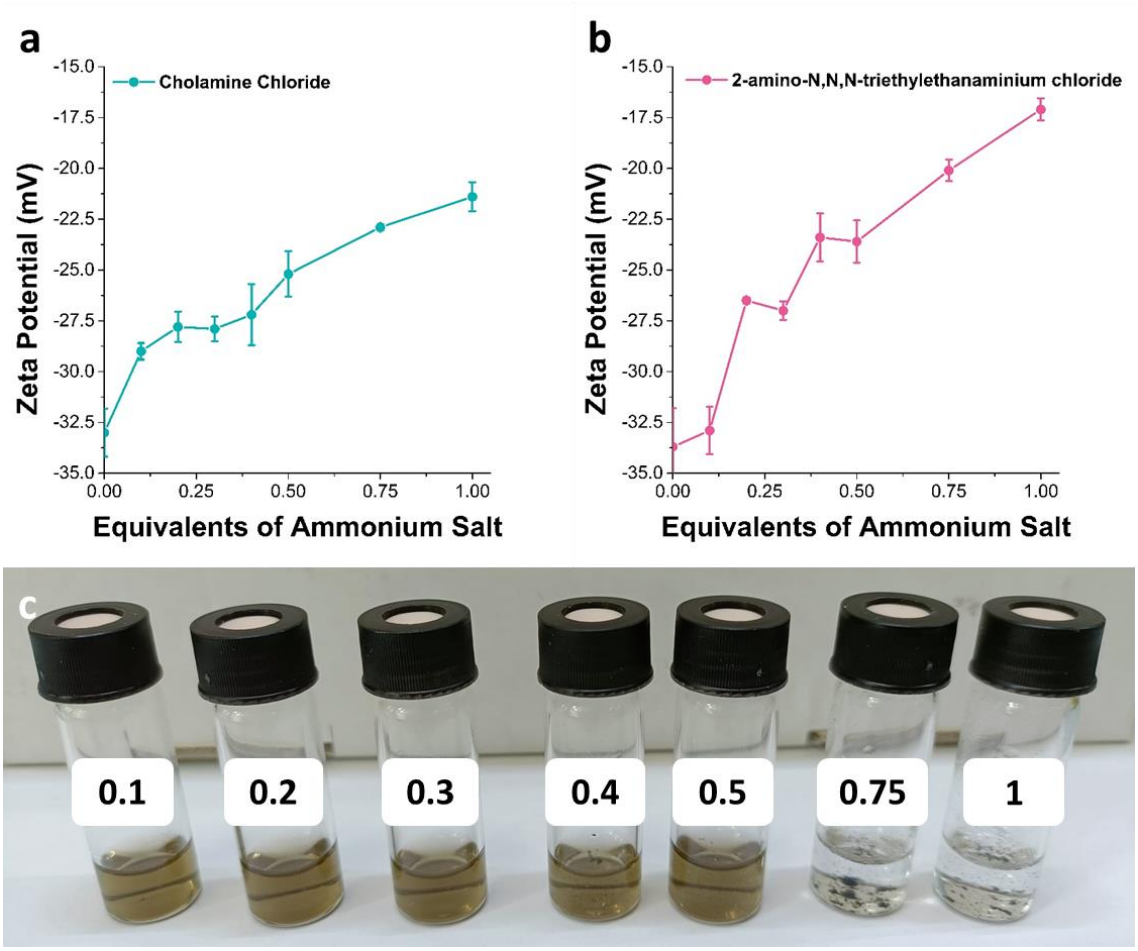

Figure 65 *a-c) Zeta potential titration of 1T-MoS_2 with $ChNH_3$ (a) and Et_3NEtNH_3 (b); c) Photograph of 1T-MoS_2 suspensions with the addition of 0.1, 0.2, 0.3, 0.4, 0.5, 0.75 and 1 equivalent of $ChNH_3$.*

3.2.5.2 Study of Surface Chemistry of the Functionalized Material

Having assessed the interaction between the material and the organic salts, the following step was to develop a procedure for functionalization and purification of the final material. The functionalization was carried out choosing 1 equivalent of organic salt, in order to guarantee a high degree of functionalization and to facilitate purification, which was performed by precipitation and washing of the precipitate. The details of the functionalization and purification protocol are reported in paragraph 3.4.5.

After functionalization, the modified materials were deposited on a SiO_2 substrate and characterized by Raman spectroscopy. **Figure 66** shows the comparison between the Raman spectra of pristine 1T-MoS_2, $ChNH_3$ and the modified material, 1T-MoS_2-$ChNH_3$.

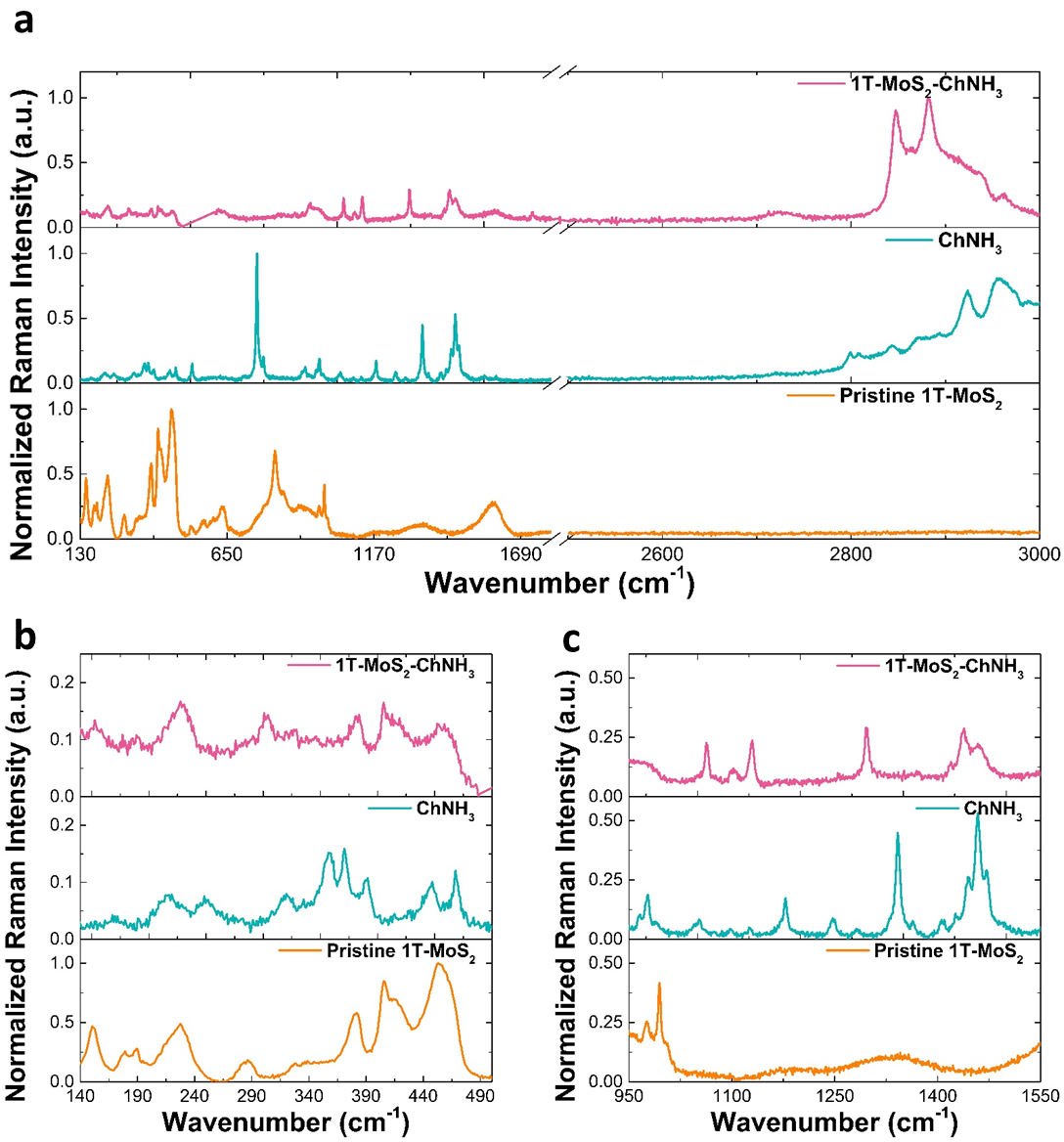

Figure 66 *a) Normalized Raman spectra of pristine 1T-MoS_2 (orange), $ChNH_3$ (teal) and 1T-MoS_2-$ChNH_3$ (magenta); b) Magnification of the spectra in the region comprised between 140 and 500 cm^{-1}; c) Magnification of the spectra in the region comprised between 900 and 1500 cm^{-1}.*

It is evident that the Raman spectrum of 1T-MoS_2-$ChNH_3$ presents peaks of the both starting materials. Specifically, in the region above 2800 cm^{-1}, signals attributable to CH_3 and CH_2 appear in the spectra of $ChNH_3$ and 1T-MoS_2-$ChNH_3$. Then, observing the range of wavenumber going from 140 to 500 cm^{-1} (**Figure 66b**), it is possible to appreciate in both pristine and modified 1T-MoS_2, peaks J_1 (151-154 cm^{-1}), J_2 (228 cm^{-1}), E_{2g} (380 cm^{-1}) and A_{1g} (405 cm^{-1}). On the other hand, in the region comprised between 950 and 1550 cm^{-1} (**Figure 66c**) it is possible to observe peaks of $ChNH_3$ (1071cm^{-1}, 1098 cm^{-1}, 1125 cm^{-1}, 1284 cm^{-1},

1445 cm^{-1}, 1459 cm^{-1}, 1471 cm^{-1}) that match peaks of 1T-MoS_2-$ChNH_3$ (1064 cm^{-1}, 1099 cm^{-1}, 1129 cm^{-1}, 1295 cm^{-1}, 1419 cm^{-1}, 1438 cm^{-1}, 1461 cm^{-1}), which are not present in the spectrum of 1T-MoS_2.

It was interesting to notice that some of the observed peaks of $ChNH_3$ experience an enhancement of their intensity in the spectrum of 1T-MoS_2-$ChNH_3$. 1T-MoS_2 is known to exhibit surface-enhanced Raman scattering (SERS) activity,[62] which is the capability of certain plasmonic materials to enhance the Raman signal of molecules adsorbed on their surface.[63] SERS is highly surface-sensitive and can be used to deduce the orientation of molecules on the surface of SERS-active materials, as the functional moieties closer to the surface experience a greater signal enhancement.[64,65] In the case of 1T-MoS_2-$ChNH_3$ it is possible to observe SERS effect for the peaks at 2849 cm^{-1} and 2883 cm^{-1} that are associable with antisymmetric stretching of CH_2 and CH_3 respectively.[66] Moreover, in the zone included between 950 and 1550 cm^{-1}, also peaks at 1062 cm^{-1} 1102 cm^{-1} and 1130 cm^{-1} experience an evident intensity enhancement. These peaks are attributable to CCNCC stretching and demonstrate the strong interaction between the surface of 1T-MoS_2 and the trimethylammonium moiety of $ChNH_3$.[66]

Similar features were observed with 1T-MoS_2-Et_3NEtNH_3 (**Figure 67**), with peaks attributable to the presence of the functionalization on the surface of the material, at 1295 cm^{-1}, 1438 cm^{-1}, and enhanced peaks at 1063 cm^{-1}, 1129 cm^{-1}, 1173 cm^{-1}, 2847 cm^{-1} and 2881 cm^{-1}.

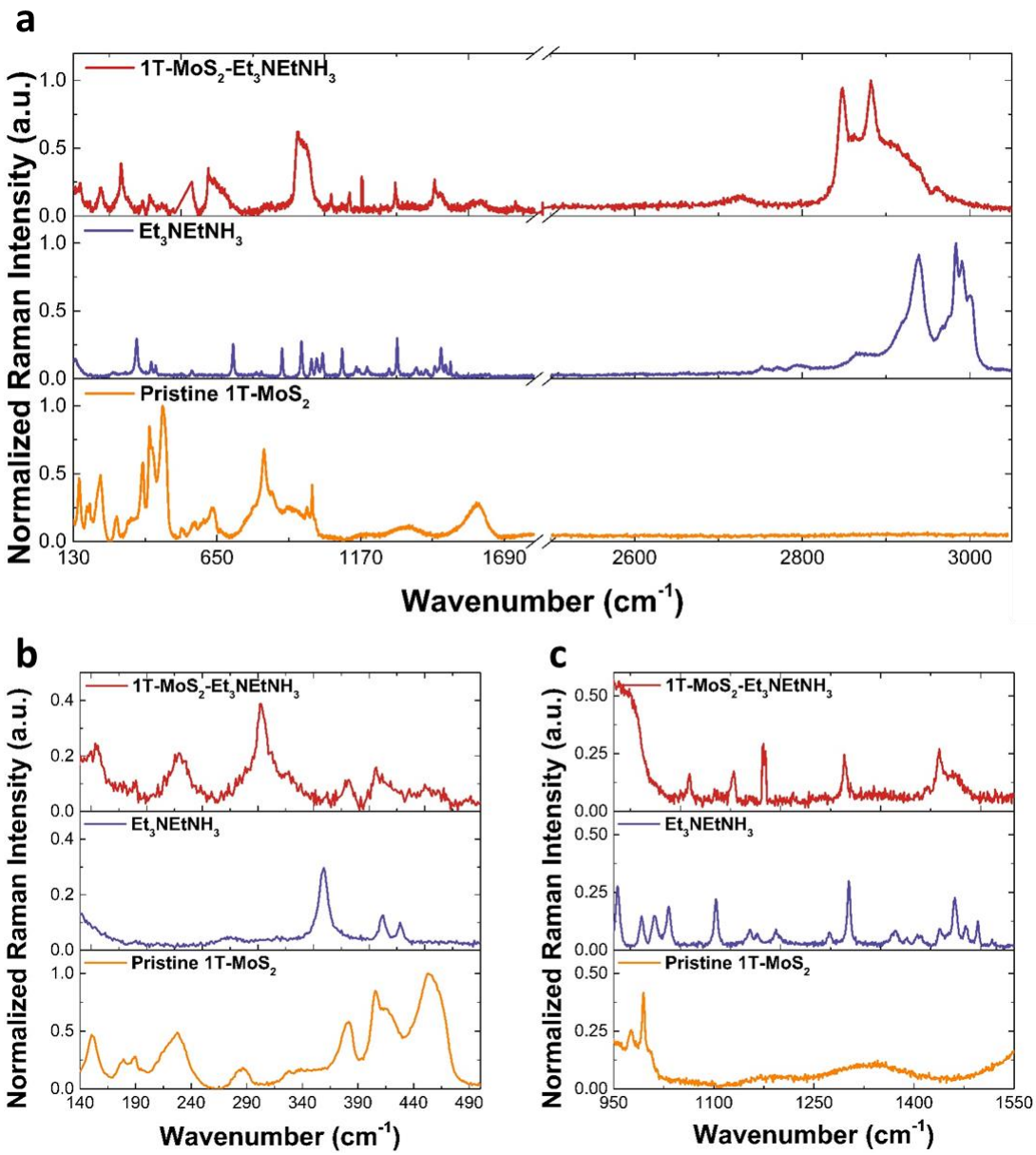

Figure 67 *a) Normalized Raman spectra of pristine 1T-MoS_2 (orange), $ChNH_3$ (blue) and 1T-MoS_2-$ChNH_3$ (red); b) Magnification of the spectra in the region comprised between 140 and 500 cm^{-1}; c) Magnification of the spectra in the region comprised between 900 and 1500 cm^{-1}.*

The surface chemistry of 1T-MoS_2-$ChNH_3$ was further investigated by XPS (**Figure 68**). The high resolution spectrum of Mo (**Figure 68a**) is quite complex, including two components at 228.19 and 231.32 eV related to 1T phase (accounting for 33.6 % of the entire region) and two components at 229.22 and 232.5 related to 2H phase (accounting for 17.74% of the entire region). A component at 234.46 eV is associated to the presence of sulfates, as can be observed also in the high-resolution spectrum of S and O (**Figure 68c, e**). Two components

for Mo at 232.60 and 235.73 eV were attributed to Mo^{6+}. These components are related partially to formation of MoO_3, as demonstrated by the spectrum of O (**Figure 68e**).

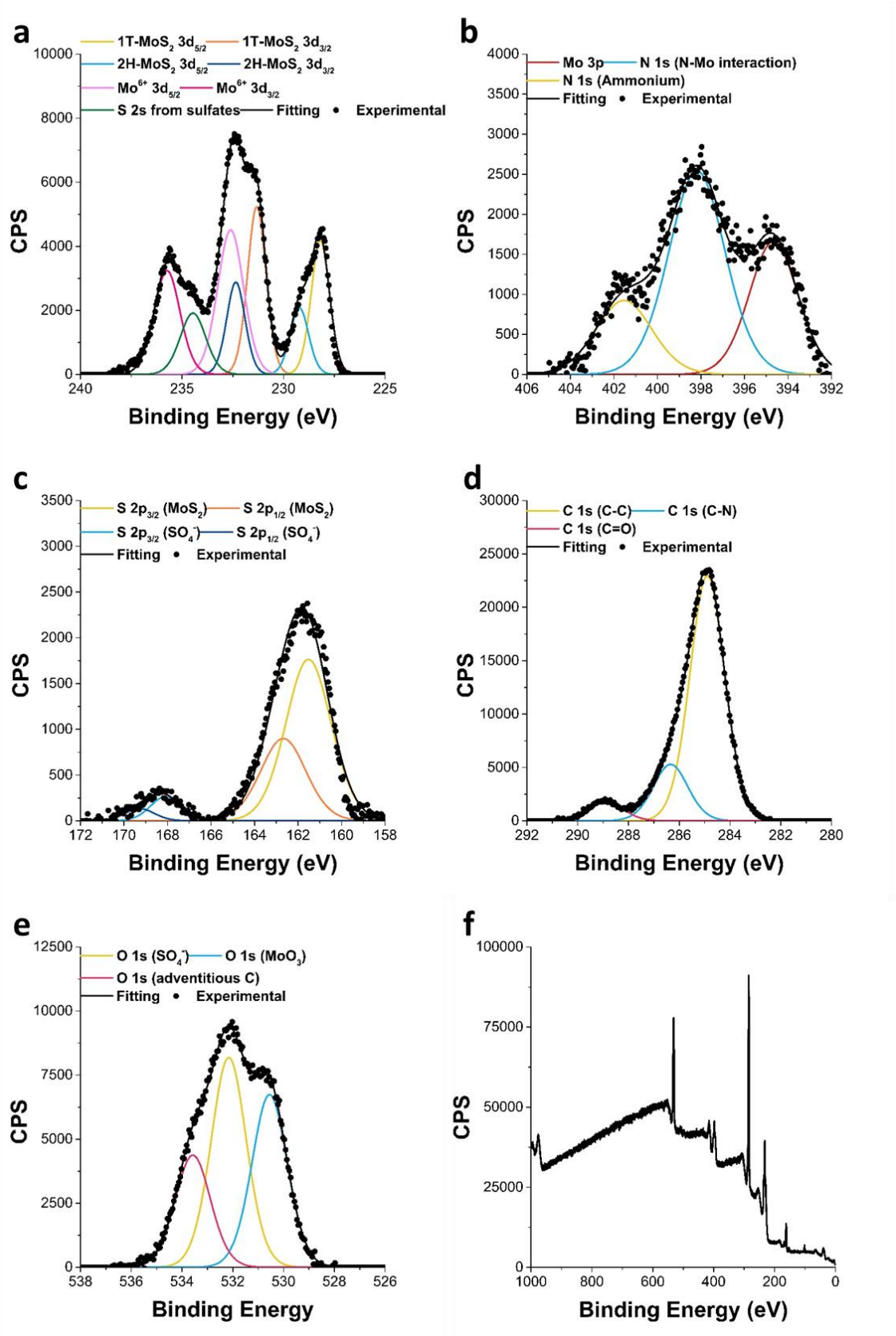

Figure 68 *High-resolution XPS spectra of a) Mo_{3d}, b) N_{1s}, c) S_{2p}, d) C_{1s} and e) O_{1s}; f) Survey spectrum of 1T-MoS_2-ChNH_3.*

However, this component can be associated with N-doping of MoS_2, as previously reported, which determines also the appearance of a peak at 398.18 eV in the high resolution spectrum of N.[67–69] Further XPS studies on the material and the ammonium salt will be useful to clarify the origin of these components.

STEM-EDX mapping allowed to observe the distribution of ammonium salts on the surface of 1T-MoS_2-$ChNH_3$. **Figure 69** shows the EDX linescan mapping of Mo, S and N of one flake of 1T-MoS2-$ChNH_3$. All three elements are co-localized and well distributed on the surface of the flake.

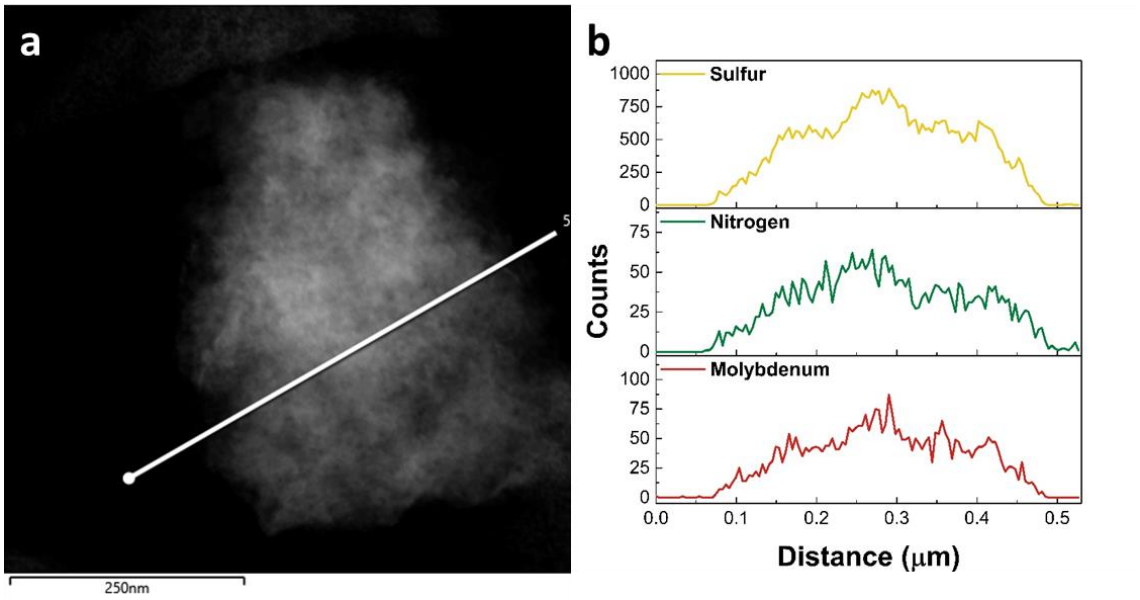

Figure 69 *STEM-EDX mapping of 1T-MoS_2-$ChNH_3$; a) STEM electron image of one nanosheet; b) linescan mapping of S (yellow), N (green) and Mo (red).*

3.2.5.3 Evaluation of Functionalization Degree by TGA

The degree of functionalization for 1T-MoS_2-$ChNH_3$ was estimated by thermogravimetric analysis (TGA) in inert atmosphere (N_2). Under these conditions, MoS_2 is stable up to 800 °C, while the organic functionalization is completely degraded.[70,71] As shown in **Figure 70**, there is a clear difference in weight loss percentage between the pristine and the functionalized material at 550 °C, which is equal to 25%. Taking into account the molecular mass of the cation (104.20 g mol^{-1}), it is possible to calculate the amount of salt to be 2.40 μmol/mg of MoS_2, which corresponds to a molar fraction $\chi = 0.38$.

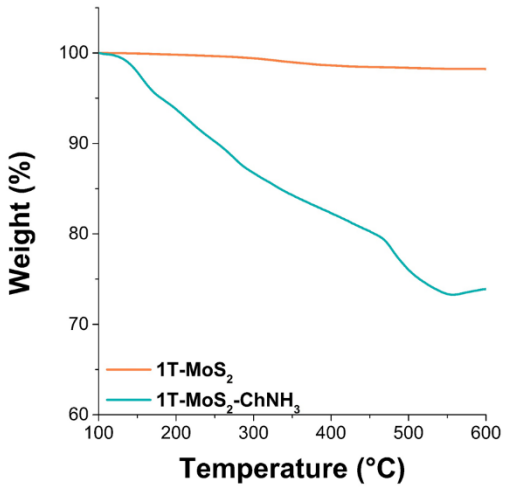

Figure 70 *TGA of 1T-MoS_2 (orange) and 1T-MoS_2-$ChNH_3$ (teal).*

3.2.5.4 Post-modification of the Composite with Fluorinated Probe

As the final goal of the functionalization is to have active primary amines on the surface of the material, it was necessary to assess if the protonated amines introduced with the salt are available after immobilization of the salt on the surface of the material. To verify it, a qualitative experiment was carried out, using p-fluorobenzaldehyde (pFBA) as fluorinated probe for the amine groups of 1T-MoS_2-$ChNH_3$ (

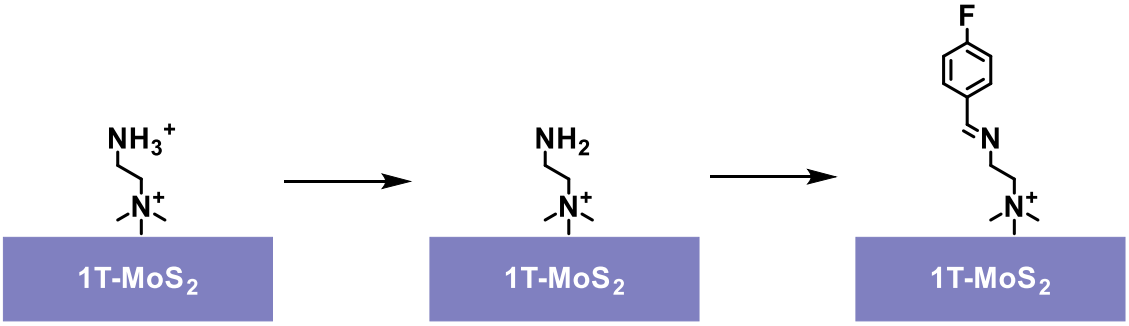

Figure 71). First, the material was suspended in methanol, by ultrasonication, adding triethylamine to deprotonate the amines. Then pFBA (1 equiv.) was added to the suspension and incubated for 1 h. Finally, the functionalized material was isolated by centrifugation and washed with methanol to eliminate the excess of pFBA.

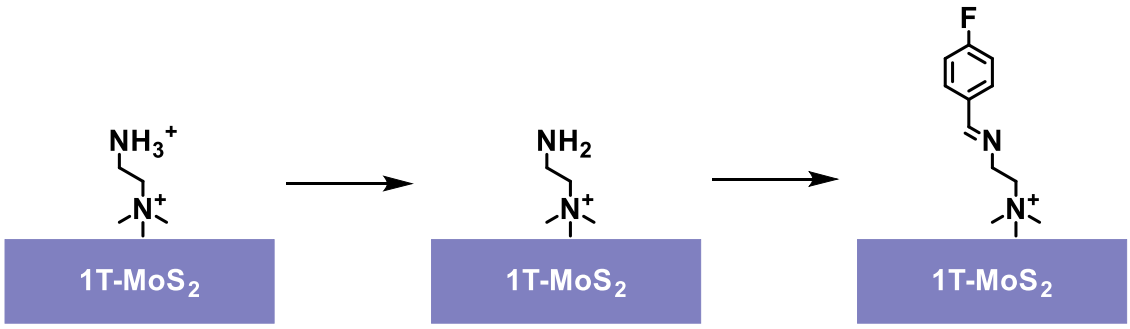

Figure 71 *Reaction scheme for imine formation on 1T-MoS2-ChNH3.*

The distribution of Fluorine was observed by STEM-EDX mapping, which shows co-localized distribution of Mo, S, N and F atoms on the nanosheets (**Figure 72**).

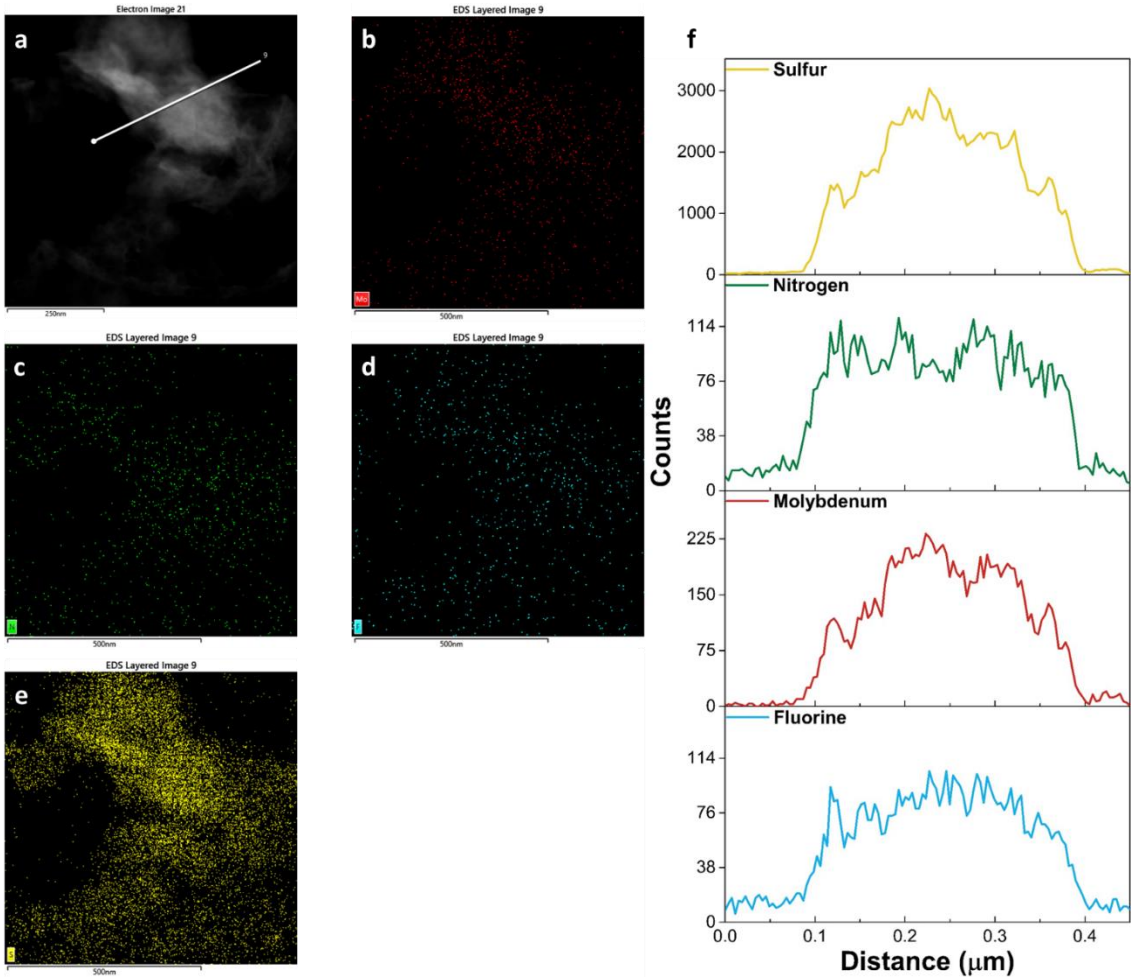

Figure 72 *a-e) STEM-EDX mapping of imine derivative of 1T-MoS2-ChNH3; STEM electron image of one nanosheets (a), and elemental mapping of Mo (b), N (c), F (d) and S (e); f) linescan mapping of the nanosheets.*

To quantify the amount of imines on the surface of 1T-MoS_2-$ChNH_3$, the material was incubated with one equivalent of pFBA for 1 h. Then, the imine derivative was washed with methanol dried and analyzed in the same conditions used for 1T-MoS_2-$ChNH_3$. As shown in **Figure 73**, the thermogram of the imine derivative presents a similar shape, but with higher weight loss (31.35%). From the difference between the thermograms of 1T-MoS_2-$ChNH_3$ and of the imine derivative (6.35%), it is possible to determine that 0.21 μmol of pFBA reacted with the material to form imines. By comparing these data with the degree of functionalization determined from **Figure 70**, it is possible to calculate the ratio between the amount of formed imines and the total amount of amines introduced on the materials, which is equal to χ_{imine} = 0.32. This value can be considered as an estimation of the available amines on the surface of the material.

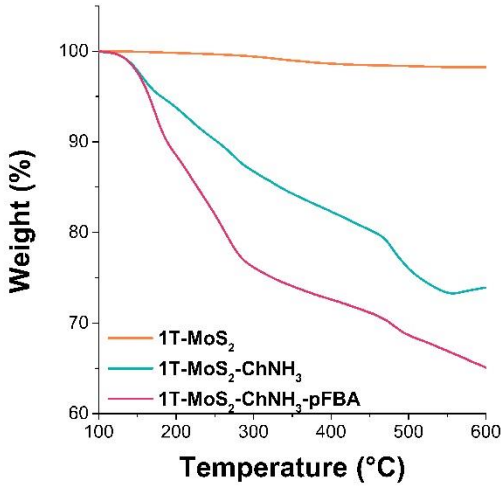

Figure 73 *TGA of pristine 1T-MoS_2 (orange), 1T-MoS_2-$ChNH_3$ (teal) and the imine derivative, 1T-MoS_2-$ChNH_3$-pFBA (purple).*

3.3 Conclusions

In conclusion, the work herein presented deepens the understanding of the electrocatalytic activity of MoS_2 for hydrogen peroxide reduction reaction, through a thorough electrochemical study and colorimetric assay, and extends its applicability for the development of enzymatic electrochemical biosensors, with a new functionalization method.

Tafel analysis highlights the superior catalytic properties of 1T-MoS_2, which shows greatly enhanced electrocatalytic properties when compared with 2H phase, thanks to it metallic character, as shown by the significant shift in overpotential and better j-η dependence. Moreover, the study shows the impact of the synthetic approach over the activity of the final material, as 1T-MoS_2 obtained from top-down and bottom-up approaches presents morphological differences, with consequences on the final catalytic activity. E1T-MoS_2 is characterized by a planar morphology, with less defects. This results in higher conductivity, but less active sites that are rapidly saturated at low overpotentials, which determine a lower exchange current density. Conversely, H1T-MoS_2 presents a rough surface with rugged edges and defects, which serve as catalytically active sites, but lead to lower conductivity.

By comparing data from Tafel analysis and EIS, it was possible to assess that the mechanism for the catalyzed reaction is based on single electron transfer with formation of hydroxyl radicals on the surface of the catalyst, similarly to Pt-based catalysts. This hypothesis was corroborated by the colorimetric assay, which in turn demonstrated that only 1T phase is effective for homogeneous catalysis of hydrogen peroxide reduction, stressing once again the importance of defining the crystalline phase of MoS_2 for its catalytic activity. Furthermore, the colorimetric assay is in agreement with the data of Tafel analysis, showing how catalytic sites of E1T-MoS_2 are saturated at concentrations of H_2O_2 higher than 50 mmol L^{-1}, whereas the activity of H1T-MoS_2 does not decrease up to 200 mmol L^{-1}.

Based on these evidences, the two morphologies of 1T-MoS_2 can be implemented for sensing of H_2O_2 either in electrochemical sensors or in colorimetric assays. E1T-MoS_2 is suggested for electrocatalytic applications and electrochemical sensing, thanks to its better conductivity and charge transfer that result in higher faradaic currents at higher overpotentials. H1T-MoS_2 is more suitable for colorimetric sensors and heterogeneous catalysis, thanks to the higher number of catalytic sites.

Non-covalent functionalization of 1T-MoS_2 nanosheets was achieved via electrostatic interaction with cholamine chloride hydrochloride and N',N',N'-triethylethane-1,2-diaminium trifluoroacetate. Raman spectroscopy showed that the interaction between the

material and the alkylammonium leads to SERS enhancement of signals related to C-H and C-N stretching, and XPS presented the appearance of new components in the high resolution spectra of Mo and N. The degree of functionalization and the availability of amines on the surface of the material was assessed by formation of imines with pFBA. The formed imines on the surface of the material were quantified by TGA, while STEM-EDX was used to demonstrate the co-localization of Mo, N, S and F.

Further studies using XPS will be needed to better understand the nature of the new component that arise in the region of N and Mo after the interaction between the material and the alkylammonium salts. Moreover, XPS and solid-state ^{19}F-NMR could be used as well to confirm the formation of the imines on the surface of the material during the post-modification with pFBA.

The work presented in this chapter, both on the electrocatalytic activity of 1T-MoS_2 and on a simple and effective strategy for its characterization, provides useful insight for the application of the material for enzymatic electrochemical sensors, paving the way for detection of various important analytes.

3.4 Experimental Section

3.4.1 Materials and Instruments

All reagents and materials were purchased from Sigma-Merck and used without further purification.

UV-Vis spectra were collected with an Agilent Cary 5000 UV-Vis spectrophotometer, at room temperature with quartz cuvettes, in a wavelength range comprised from 200 nm and 800 nm.

Raman spectra were recorded using a Renishaw inVia Raman microscope. A laser excitation wavelength of 633 nm, lens-based spectrometer with 1800 gr mm^{-1} gratings, Peltier-cooled front-illuminated CCD camera (1024 × 532 px), and a 100× objective were employed. Samples were prepared by drop-casting MoS_2 solution on a silicon oxide slide and drying it under ambient conditions. Each spectrum is derived from the average of at least 100 spectra recorded in different spots of the sample for 5 s with a laser power of 1.29 mW. Data were processed using Renishaw WiRE 4 software.

AFM images were obtained with a Nanoscope IIIa, VEECO Instruments. As a general procedure, AFM analyses were performed using tapping mode with a HQ:NSC19/ALBS probe (80 kHz; 0.6 N/m) (MikroMasch). Samples were prepared by drop cast of the aqueous suspension (concentration in the order of μg/mL) on exfoliated mica substrates. The obtained AFM images were analyzed in S3 Gwyddion 2.58.

TEM images were recorded with a Phillips CM200 transmission electron microscope equipped with Quemesa camera (Olympus Soft Imaging Solutions) and RADIUS software for image acquisition. Samples were prepared by dropcast of the aqueous suspensions (concentration 0.5 mg/mL) on Lacey Carbon 300 mesh copper grids (approx. grid hole size: 63μm), purchased from TED PELLA Inc.

STEM-EDX mapping images were recorded with a TEM – JEOL JEM – 2100F UHR transmission electron microscope equipped with a field emission electron beam FEG (Field Emission Gun) with variable acceleration between 80 and 200 kV, a 4-megapixel CMOS camera (TVIPS TemCam-F216) and two STEM detectors (VF & HAADF) in combination with an EDX detector (Oxford UltimMax).

X-ray Photoelectron Spectroscopy (XPS) spectra were registered with an XPS/UPS – SPECS SAGE HR-100 equipped with a 100 mm radius PHOIBOS analyzer, where 421 Mg Kα X-ray source was used. The samples were prepared by depositing 0.5 mg on copper tape. The

spectra were fitted using CasaXPS and calibration was performed using the major component of the C high-resolution spectrum as a reference at 284.8 eV, which is the value reported for adventitious and sp^3 C-C carbon.

Thermogravimetric analysis (TGA) measurements were carried out with a TGA Discovery (TA Instruments), where 0.4 mg of material were weighed in a Platinum HT pan and were heated in N_2 atmosphere. First, an isotherm at 100°C was applied 20 min, subsequently the samples were heated to 600°C with a ramp of 10°C/min.

3.4.2 Synthesis of 2D-Molybdenum Disulfide in different crystalline phases and morphologies

Molybdenum disulphide (MoS_2) was exfoliated in its 2H phase (2H-MoS_2) by ultrasonication of bulk MoS_2 in N-methylpyrrolidone. 150 mg of bulk MoS_2 was suspended in 150 mL of NMP (1 mg/mL), and subsequently sonicated in a sonicator bath for 4 h, at 0°C. The suspension was centrifuged and the supernatant was filtrated on PTFE membrane with 0.45 μm of pore size. The material was washed with 1 L of Milli-Q water and resuspended in 100 mL of Milli-Q water.

The exfoliated 1T phase (E1T-MoS_2) was obtained by butyllithium intercalation and exfoliation. 250 mg of MoS_2 were dried at 100°C in a Schlenck tube (with a capacity of 50 mL) for 16 h and then heated with a heat gun under vacuum to eliminate any trace of water. Under an inert atmosphere (Ar), 15 mL of dry hexane and 4 mL of butyllithium (2.5 M in hexane) were added, and the mixture was heated at 70°C for 24 h. The mixture was then cooled with an ice bath and BuLi was quenched by adding water drop by drop until the disappearance of bubbling. The crude was sonicated to disperse the material, then the material was extracted from the organic phase with Milli-Q water using a separating funnel. The aqueous phase was washed twice with hexane, was sonicated for 1 h, and subsequently centrifuged at 1000 rpm for 1.5 h at 5°C. The supernatant was filtered on PTFE filters and washed with Milli-Q water to recover the material, which was finally resuspended in Milli-Q water.

The hydrothermally synthesized MoS_2 (H1T-MoS_2) was obtained by hydrothermal reaction of molybdenum oxide with urea and thioacetamide. 36 mg of MoO_3, 360 mg of urea, and 42 mg of thioacetamide were dissolved in H_2O and introduced in an autoclave were stirred for 4 h at 35 °C. The solutions were then heated at 200 °C for 16 h. After rapid cooling, the material was recovered by filtration on PTFE filter and washed with 1 L of Milli-Q water.

After re-suspending the material in 10 mL of Milli-Q water by sonication for 1 h, the suspensions were centrifuged at 750 rpm for 30 min at 10 °C, and the supernatant was recovered.

3.4.3 Electrochemical Measurements

All electrochemical measurements were performed using an electrochemical workstation Autolab MSTAT204 potentiostat/galvanostat (Metrohm Autolab) interfaced to a PC with Nova 2.1.6 software, at laboratory room temperature (25°C). A glassy carbon electrode (GCE, diameter= 0.5 cm) was used to perform all experiments. Before each experiment, the GCE was polished on alumina 0.2 μm and sonicated in Milli-Q water and was then modified by drop casting 10 μL of 0.5 mg/mL suspensions of the materials. For CA measurements, upon drying of the MoS2 suspension, 5μL of 5% Nafion solution was drop casted on the modified electrode, to immobilize the catalyst. Ag/AgCl (3M KCl) and a platinum wire were used as reference and counter electrodes, respectively.

Before each measurement, solutions were degassed by bubbling N_2 in the solution for ten minutes. CV was performed by scanning the applied potential from 0.2 V to - 0.8 V, with a scan rate of 10 mV/s. Data were graphed without ulterior manipulation, with Origin software.

CA were carried out at a constant potential of -0.3 V, over 50 s and the signal was sampled at 15 s. The measurements were conducted with 0.5, 1, 1.5, 2, 4, 6 and 8 mmol L^{-1} solutions of H_2O_2 in PBS 0.1 mol L^{-1}, KCl 0.1 mol L^{-1}. Data were graphed, analyzed and fitted with Origin software.

For Tafel analysis, open circuit potentials were determined to identify the equilibrium potential for the reaction. Subsequently, the potential range was selected accordingly, and the potential was scanned with a scan rate of 10 mV/s in linear sweep voltammetry. By plotting the logarithm of the current against the applied potential, the polarization curve was obtained, which was then centered on the minimum individuating the onset potential of the reaction and reported against the overpotential applied over the onset potential (**Figure 74a**). From the linear fitting of the two branches of the obtained polarization curve, the exchange current density was determined as the intersection between the fitted lines. The same curve was then plotted as overpotential versus logarithm of the current, and the cathodic branch was isolated and linearly fitted (**Figure 74b**). From this linear fitting, Tafel

slope and Tafel constant were determined as the slope and the intercept of the fitted line, respectively. Data were analyzed and fitted using Origin software.

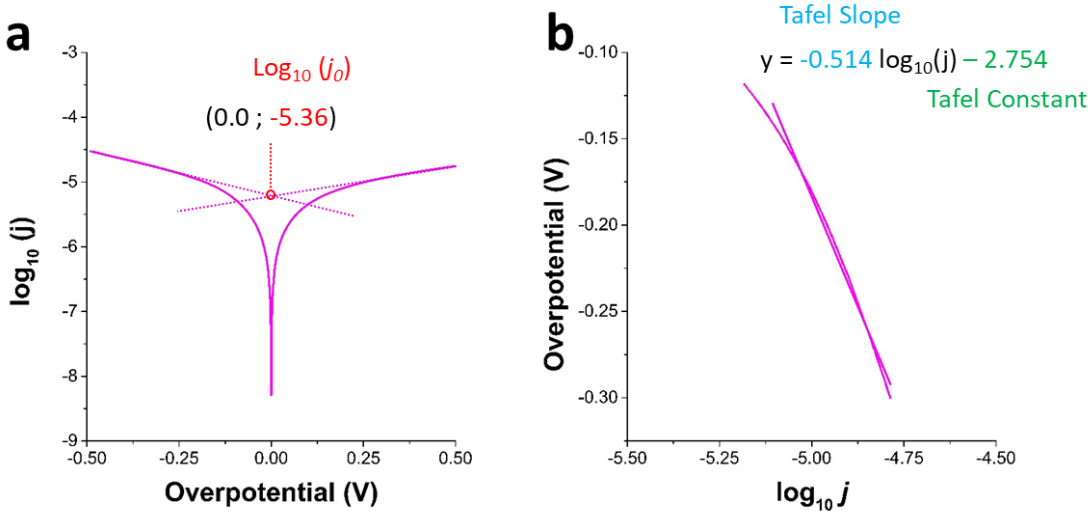

Figure 74 *Scheme highlighting the obtained parameters from Tafel analysis.*

Finally, EIS measurements were conducted at low overpotential (0.2 V) and at high overpotential (-0.3 V), with a potential amplitude of 0.01 V, scanning frequencies from 0.1 Hz to 10^5 Hz, and 10 frequencies per decade. Data were fitted using NOVA 2.1.6 software from Metrohm and subsequently graphed with Origin software.

3.4.4 Colorimetric assay

All colorimetric tests were performed in acetate buffer 0.1 mol L^{-1}, at pH 3.5. UV-Vis spectra were collected with an Agilent Cary 5000 UV-Vis spectrophotometer, at room temperature with plastic cuvettes, in a wavelength range between 300 nm and 800 nm. In each cuvette, 100 µL of MoS_2 suspension (0.1 mmol L^{-1}) were incubated with 100 µL of TMB solution (10 mmol L^{-1}, in acetate buffer 0.1 mol L^{-1}) and 50 µL of H_2O_2 (1 mol L^{-1}) in 750 µL of acetate buffer 0.1 mol L^{-1}, for a total volume of 1 mL.

The UV-Vis kinetics were registered at 652 nm with a TECAN Infinite M1000 Pro multiwell plate reader, with plastic flat base 96 multiwell plates purchased from Sarstedt. In each well, 20 µL of MoS_2 suspension (0.1 mmol L^{-1}) were incubated with 20 µL of TMB solution (10 mmol L^{-1}, in acetate buffer 0.1 mol L^{-1}) and different concentrations of H_2O_2 (0, 0.1, 0.5, 1, 2.5, 5, 10, 50 and 200 mmol L^{-1}), in acetate buffer 0.1 mol L^{-1} (total volume of 200 µL). Data from kinetic were subsequently analyzed by Origin and Excel software.

3.4.5 Non-covalent Functionalization of 1T-MoS_2

3.4.5.1 Synthesis of N-Boc-2-bromoethylamine

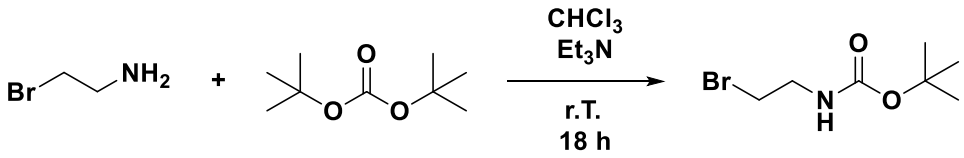

2-bromoethylamine hydrobromide (1 g, 8.06 mmol, 1 equiv.) was dissolved in chloroform (10 mL), and the resulting solution (sol. A) was left to stir at 0 °C. Subsequently, di-tert-butyl dicarbonate (1.92 g, 8.80 mmol, 1.1 equiv.) was dissolved in chloroform (10 mL) and triethylamine (2.24 mL, 16.12 mmol, 2 equiv.) was added to the resulting solution (sol. B). Sol. B was added dropwise to sol A. over 0.5 h. Once sol. B was completely added, the reaction mixture was left to stir for 18 h, at room temperature. The mixture was extracted with ethyl acetate. The organic phase was washed twice with NH_4Cl saturated solution, twice with $NaHCO_3$ saturated solution and twice with brine. Then it was dried over sodium sulfate and the solvent was removed under reduced pressure.

^{1}H-NMR (400 MHz, $CDCl_3$): δ 1.40 (s, 9H), 3.40 (m, 2H), 3.48 (m, 2H), 5.03 (s, 1H).

3.4.5.2 Synthesis of 2-((tert-butoxycarbonyl)amino)-N,N,N-triethylethanaminium bromide

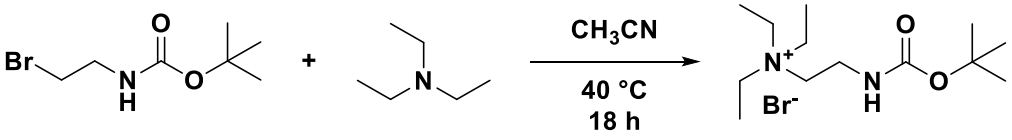

According to a modified reported procedure,[74] N-Boc-bromoethylamine (2.282 g, 10 mmol, 1 equiv.) was dissolved in acetonitrile (10 mL), then triethylamine (4.17 mL, 30 mmol, 3 equiv.) was added. The mixture was stirred at 40 °C for 18 h. The solvent was removed under reduced pressure and the product was recovered by precipitation in ethyl acetate.

1H-NMR (400 MHz, D_2O): δ 1.30 (t, 9H), 1.45 (s, 9H), 3.35 (m, 8H), 3.50 (t, 2H).

3.4.5.3 Synthesis of N',N',N'-triethylethane-1,2-diaminium (Et_3NEtNH_3)

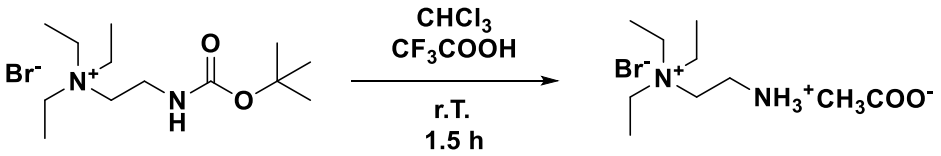

2-((tert-butoxycarbonyl)amino)-N,N,N-triethylethanaminium (924 mg, 2.84 mmol, 1 equiv.) was dissolved in $CHCl_3$ (7 mL) and cooled to 0 °C, then trifluoroacetic (5 mL, 91 mmol, 32 equiv.) was added dropwise. The reaction mixture was stirred at room temperature for 1.5 h. The solvent was removed under reduced pressure, yielding the product as a white solid. ^{1}H-NMR (400 MHz, D_2O): δ 1.35 (t, 9H), 3.42 (q, 6H), 3.54 (m, 4H).

3.4.5.4 Functionalization of 1T-MoS_2 with alkylammonium salts

1T-MoS_2 aqueous suspension (2 mL of 0.5 mg/mL solution, 6.25 μmol, 1 equiv.) was sonicated in ice bath for 15 min. The alkylammonium salt (6.25 μmol, 1 equiv.) is solubilized in 100 μL of milliQ water and added to the 1T-MoS_2 suspension (**Figure 75a**). The mixture is stirred for 30 min (**Figure 75b**), then sonicated for 5 min in ice bath (**Figure 75c**), and finally stirred for other 30 min (**Figure 75d**).

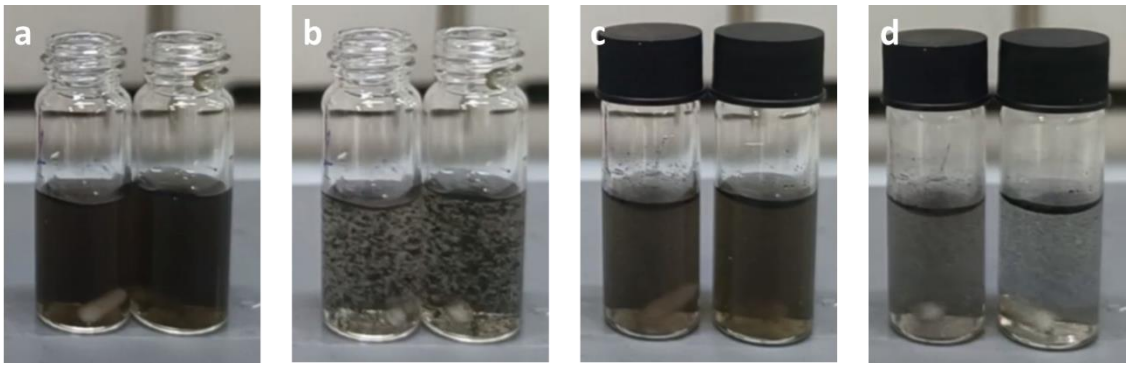

Figure 75 *Photographs of different steps of functionalization of 1T-MoS_2.*

Then, the precipitate is separated by centrifugation (2000 rpm, 30 min). The solid is washed twice with 1 mL of milliQ water, each time sonicating for 5 min and centrifuging at 2000 rpm for 30 min. Finally, water is removed by lyophilization (72 h), to isolate the dry material.

3.4.5.5 Fluorine Tagging of Amines with p-Fluorobenzaldehyde

The obtained 1T-MoS_2-$ChNH_3$ was suspended in methanol (1 mL), by adding 20 μL of triethylamine 0.72 mol L^{-1} (14.4 μmol, 4.6 equiv. relative to the starting ammonium salt), and sonicating for 10 min in ice bath. Then, p-fluorobenzoaldehyde (8.7 μL of a 10% solution in methanol, 6.25 μmol, 1 equiv. relative to the starting ammonium salt) was added and the mixture was sonicated for 5 min and then incubated for 1 h. Finally, the imine derivative was isolated by centrifugation (6000 rpm, 10 min), resuspending and washing twice with methanol (1mL).

3.4.5.6 TGA quantification of available amines

The TGA measurement were carried out as described in paragraph 3.4.1. The degree of functionalization was calculated from the weight loss derived from thermograms of 1T-MoS_2 and 1T-MoS_2-$ChNH_3$ (**Figure 70**), as follows:

$$\%W_{ChNH3} = \%WL_{(1T-MoS_2-ChNH_3)} - \%WL_{(1T-MoS_2)}$$

$$W_{ChNH_3} = \%W_{ChNH_3} \times W_i$$

$$W_{1T-MoS_2} = W_i - (\%W_{ChNH_3} \times W_i)$$

$$d_{F\ ChNH3} = \frac{W_{ChNH_3}}{MW_{ChNH_3} \times W_{1T-MoS_2}}$$

$$\chi_{ChNH3} = \frac{W_{ChNH_3} \times MW_{MoS2}}{MW_{ChNH_3} \times W_{1T-MoS_2}}$$

Where:

$\%W_{ChNH3}$: percentage mass of $ChNH_3$ cation in the composite 1T-MoS_2-$ChNH_3$;

$\%WL_{(1T\text{-}MoS2\text{-}ChNH3)}$: weight loss at 550 °C recorded for the composite 1T-MoS_2-$ChNH_3$;

$\%WL_{(1T\text{-}MoS2)}$: weight loss at 550 °C recorded for pristine 1T-MoS_2;

W_{ChNH3}: mass of $ChNH_3$ cation in the composite 1T-MoS_2-$ChNH_3$;

W_i: total initial mass of the sample of 1T-MoS_2-$ChNH_3$;

$W_{1T\text{-}MoS2}$: mass of pristine 1T-MoS_2 in the composite 1T-MoS_2-$ChNH_3$;

MW_{ChNH3}: molecular mass of $ChNH_3$ cation;

MW_{MoS2}: molecular mass of MoS_2;

$d_{F\ ChNH3}$: degree of functionalization expressed in $\mu mol_{ChNH3}\ mg_{MoS2}^{-1}$;

χ_{ChNH3}: molar fraction of $ChNH_3$ cation in the composite 1T-MoS_2-$ChNH_3$.

Then, the amount of amines reacted with pFBA to form the imine derivative was calculated from the thermograms of 1T-MoS_2, 1T-MoS_2-$ChNH_3$ and 1T-MoS_2-$ChNH_3$-pFBA (**Figure 73**), as follows:

$$\%W_{imine} = \%WL_{(1T-MoS_2-ChNH_3-pFBA)} - \%WL_{(1T-MoS_2-ChNH_3)}$$

$$W_{imine} = \%W_{imine} \times W_i$$

$$d_{F\ imine} = \frac{W_{imine}}{MW_{imine} \times W_{1T-MoS_2}}$$

$$\chi_{imine} = \frac{d_{F\ imine}}{d_{F\ ChNH3}}$$

Where:

$\%W_{imine}$: percentage mass increment of the composite 1T-MoS_2-$ChNH_3$ after imine formation with pFBA;

$\%WL_{(1T\text{-}MoS2\text{-}ChNH3\text{-}pFBA)}$: weight loss at 550 °C recorded for the imine derivative 1T-MoS_2-$ChNH_3$-pFBA;

$\%WL_{(1T\text{-}MoS2\text{-}ChNH3)}$: weight loss at 550 °C recorded for the composite 1T-MoS_2-$ChNH_3$;

W_{imine}: mass increment of the composite 1T-MoS_2-$ChNH_3$ after imine formation with pFBA;

W_i: total initial mass of the sample of 1T-MoS_2-$ChNH_3$-pFBA;

$W_{1T\text{-}MoS2}$: mass of pristine 1T-MoS_2 in the composite 1T-MoS_2-$ChNH_3$;

MW_{imine}: molecular mass increment of the ChN_3 cation after imine formation with pFBA;

$d_{F\ imine}$: degree of functionalization expressed in $\mu mol_{imine}\ mg_{MoS2}^{-1}$;

$d_{F\ ChNH3}$: degree of functionalization expressed in $\mu mol_{ChNH3}\ mg_{MoS2}^{-1}$;

χ_{imine}: molar fraction amines that reacted to form imines with pFBA in the composite 1T-MoS_2-$ChNH_3$.

3.5 References

(1) Nicolosi, V.; Chhowalla, M.; Kanatzidis, M. G.; Strano, M. S.; Coleman, J. N. Liquid Exfoliation of Layered Materials. *Science* **2013**, *340* (6139), 1226419. https://doi.org/10.1126/science.1226419.

(2) Acerce, M.; Akdoğan, E. K.; Chhowalla, M. Metallic Molybdenum Disulfide Nanosheet-Based Electrochemical Actuators. *Nature* **2017**, *549* (7672), 370–373. https://doi.org/10.1038/nature23668.

(3) Xu, M.; Liang, T.; Shi, M.; Chen, H. Graphene-Like Two-Dimensional Materials. *Chem. Rev.* **2013**, *113* (5), 3766–3798. https://doi.org/10.1021/cr300263a.

(4) Wang, H.; Li, C.; Fang, P.; Zhang, Z.; Zhang, J. Z. Synthesis, Properties, and Optoelectronic Applications of Two-Dimensional MoS2 and MoS2-Based Heterostructures. *Chem. Soc. Rev.* **2018**, *47* (16), 6101–6127. https://doi.org/10.1039/C8CS00314A.

(5) Tsai, P.-C.; Huang, C.-W.; Chang, S.-J.; Chang, S.-W.; Lin, S.-Y. Charge Storage of Isolated Monolayer Molybdenum Disulfide in Epitaxially Grown MoS2/Graphene Heterostructures for Memory Device Applications. *ACS Appl. Mater. Interfaces* **2021**, *13* (38), 45864–45869. https://doi.org/10.1021/acsami.1c12064.

(6) Tsai, P.-C.; Yan, C.-R.; Chang, S.-J.; Chang, S.-W.; Lin, S.-Y. Persistent Charge Storage and Memory Operation of Top-Gate Transistors Solely Based on Two-Dimensional Molybdenum Disulfide. *Nanotechnology* **2023**, *34* (30), 305701. https://doi.org/10.1088/1361-6528/acd064.

(7) Al-Ghiffari, A. D.; Ludin, N. A.; Davies, M. L.; Yunus, R. M.; Suait, M. S. Systematic Review of Molybdenum Disulfide for Solar Cell Applications: Properties, Mechanism and Application. *Materials Today Communications* **2022**, *32*, 104078. https://doi.org/10.1016/j.mtcomm.2022.104078.

(8) Guo, S.; Wu, K.; Li, C.; Wang, H.; Sun, Z.; Xi, D.; Zhang, S.; Ding, W.; Zaghloul, M. E.; Wang, C.; Castro, F. A.; Yang, D.; Zhao, Y. Integrated Contact Lens Sensor System Based on Multifunctional Ultrathin MoS2 Transistors. *Matter* **2021**, *4* (3), 969–985. https://doi.org/10.1016/j.matt.2020.12.002.

(9) Silvestri, A.; Wetzl, C.; Alegret, N.; Cardo, L.; Hou, H.-L.; Criado, A.; Prato, M. The Era of Nano-Bionic: 2D Materials for Wearable and Implantable Body Sensors. *Advanced Drug Delivery Reviews* **2022**, *186*, 114315. https://doi.org/10.1016/j.addr.2022.114315.

(10) Escalera-López, D.; Iffelsberger, C.; Zlatar, M.; Novčić, K.; Maselj, N.; Van Pham, C.; Jovanovič, P.; Hodnik, N.; Thiele, S.; Pumera, M.; Cherevko, S. Allotrope-Dependent Activity-Stability Relationships of Molybdenum Sulfide Hydrogen Evolution Electrocatalysts. *Nat Commun* **2024**, *15* (1), 3601. https://doi.org/10.1038/s41467-024-47524-w.

(11) Manyepedza, T.; Courtney, J. M.; Snowden, A.; Jones, C. R.; Rees, N. V. Impact Electrochemistry of MoS2: Electrocatalysis and Hydrogen Generation at Low Overpotentials. *J. Phys. Chem. C* **2022**, *126* (42), 17942–17951. https://doi.org/10.1021/acs.jpcc.2c06055.

(12) Tian, L.; Zhao, J.; Ren, X.; Sun, X.; Wei, Q.; Wu, D. MoS2-Based Catalysts for N2 Electroreduction to NH3 – An Overview of MoS2 Optimization Strategies. *ChemistryOpen* **2021**, *10* (10), 1041–1054. https://doi.org/10.1002/open.202100196.

(13) He, C.; Cui, L.; Wu, X.; Cai, Y.; Ma, Z.; Zhong, X.; Wang, H.; Li, Q.; Huang, Y.; Pan, Q. Oxygen Reduction Reaction Promoted by the Strong Coupling of MoS2 and SnS. *ACS Appl. Energy Mater.* **2021**, *4* (9), 9498–9506. https://doi.org/10.1021/acsaem.1c01677.

(14) Sies, H. Hydrogen Peroxide as a Central Redox Signaling Molecule in Physiological Oxidative Stress: Oxidative Eustress. *Redox Biology* **2017**, *11*, 613–619. https://doi.org/10.1016/j.redox.2016.12.035.

(15) Cadenas, E.; Davies, K. J. A. Mitochondrial Free Radical Generation, Oxidative Stress, and Aging1. *Free Radical Biology and Medicine* **2000**, *29* (3), 222–230. https://doi.org/10.1016/S0891-5849(00)00317-8.

(16) Görlach, A.; Brandes, R. P.; Nguyen, K.; Amidi, M.; Dehghani, F.; Busse, R. A Gp91phox Containing NADPH Oxidase Selectively Expressed in Endothelial Cells Is a Major Source of Oxygen Radical Generation in the Arterial Wall. *Circulation Research* **2000**, *87* (1), 26–32. https://doi.org/10.1161/01.RES.87.1.26.

(17) Forman, H. J.; Bernardo, A.; Davies, K. J. A. What Is the Concentration of Hydrogen Peroxide in Blood and Plasma? *Archives of Biochemistry and Biophysics* **2016**, *603*, 48–53. https://doi.org/10.1016/j.abb.2016.05.005.

(18) Sheng, Y.; Abreu, I. A.; Cabelli, D. E.; Maroney, M. J.; Miller, A.-F.; Teixeira, M.; Valentine, J. S. Superoxide Dismutases and Superoxide Reductases. *Chem. Rev.* **2014**, *114* (7), 3854–3918. https://doi.org/10.1021/cr4005296.

(19) García-Santamarina, S.; Boronat, S.; Hidalgo, E. Reversible Cysteine Oxidation in Hydrogen Peroxide Sensing and Signal Transduction. *Biochemistry* **2014**, *53* (16), 2560–2580. https://doi.org/10.1021/bi401700f.

(20) Marinho, H. S.; Real, C.; Cyrne, L.; Soares, H.; Antunes, F. Hydrogen Peroxide Sensing, Signaling and Regulation of Transcription Factors. *Redox Biology* **2014**, *2*, 535–562. https://doi.org/10.1016/j.redox.2014.02.006.

(21) Wang, X.; Fu, J.; Jiang, C.; Liao, X.; Chen, Y.; Jia, T.; Chen, G.; Feng, X. Specific and Long-Term Luminescent Monitoring of Hydrogen Peroxide in Tumor Metastasis. *Advanced Materials* **2023**, *35* (20), 2210948. https://doi.org/10.1002/adma.202210948.

(22) Milton, N. G. N. Role of Hydrogen Peroxide in the Aetiology of Alzheimer's Disease. *Drugs Aging* **2004**, *21* (2), 81–100. https://doi.org/10.2165/00002512-200421020-00002.

(23) Tabner, B. J.; El-Agnaf, O. M. A.; Turnbull, S.; German, M. J.; Paleologou, K. E.; Hayashi, Y.; Cooper, L. J.; Fullwood, N. J.; Allsop, D. Hydrogen Peroxide Is Generated during the Very Early Stages of Aggregation of the Amyloid Peptides Implicated in Alzheimer Disease and Familial British Dementia *. *Journal of Biological Chemistry* **2005**, *280* (43), 35789–35792. https://doi.org/10.1074/jbc.C500238200.

(24) Chang, K.-H.; Chen, C.-M. The Role of Oxidative Stress in Parkinson's Disease. *Antioxidants* **2020**, *9* (7), 597. https://doi.org/10.3390/antiox9070597.

(25) Percário, S.; da Silva Barbosa, A.; Varela, E. L. P.; Gomes, A. R. Q.; Ferreira, M. E. S.; de Nazaré Araújo Moreira, T.; Dolabela, M. F. Oxidative Stress in Parkinson's Disease: Potential Benefits of Antioxidant Supplementation. *Oxidative Medicine and Cellular Longevity* **2020**, *2020* (1), 2360872. https://doi.org/10.1155/2020/2360872.

(26) Tabner, B. J.; Turnbull, S.; El-Agnaf, O. M. A.; Allsop, D. Formation of Hydrogen Peroxide and Hydroxyl Radicals from Aβ and α-Synuclein as a Possible Mechanism of Cell Death in Alzheimer's Disease and Parkinson's Disease1, 2. *Free Radical Biology and Medicine* **2002**, *32* (11), 1076–1083. https://doi.org/10.1016/S0891-5849(02)00801-8.

(27) Minzaghi, D.; Pavel, P.; Kremslehner, C.; Gruber, F.; Oberreiter, S.; Hagenbuchner, J.; Frari, B. D.; Blunder, S.; Gruber, R.; Dubrac, S. Excessive Production of Hydrogen Peroxide in Mitochondria Contributes to Atopic Dermatitis. *J Invest Dermatol* **2023**, *143* (10), 1906-1918.e8. https://doi.org/10.1016/j.jid.2023.03.1680.

(28) Bertino, L.; Guarneri, F.; Cannavò, S. P.; Casciaro, M.; Pioggia, G.; Gangemi, S. Oxidative Stress and Atopic Dermatitis. *Antioxidants* **2020**, *9* (3), 196. https://doi.org/10.3390/antiox9030196.

(29) Lipińska, W.; Siuzdak, K.; Karczewski, J.; Dołęga, A.; Grochowska, K. Electrochemical Glucose Sensor Based on the Glucose Oxidase Entrapped in Chitosan Immobilized onto

Laser-Processed Au-Ti Electrode. *Sensors and Actuators B: Chemical* **2021**, *330*, 129409. https://doi.org/10.1016/j.snb.2020.129409.

(30) Kang, X.; Wang, J.; Wu, H.; Aksay, I. A.; Liu, J.; Lin, Y. Glucose Oxidase–Graphene–Chitosan Modified Electrode for Direct Electrochemistry and Glucose Sensing. *Biosensors and Bioelectronics* **2009**, *25* (4), 901–905. https://doi.org/10.1016/j.bios.2009.09.004.

(31) Silvestri, A.; Criado, A.; Poletti, F.; Wang, F.; Fanjul-Bolado, P.; González-García, M. B.; García-Astrain, C.; Liz-Marzán, L. M.; Feng, X.; Zanardi, C.; Prato, M. Bioresponsive, Electroactive, and Inkjet-Printable Graphene-Based Inks. *Advanced Functional Materials* **2022**, *32* (2), 2105028. https://doi.org/10.1002/adfm.202105028.

(32) Wang, T.; Zhu, H.; Zhuo, J.; Zhu, Z.; Papakonstantinou, P.; Lubarsky, G.; Lin, J.; Li, M. Biosensor Based on Ultrasmall MoS2 Nanoparticles for Electrochemical Detection of H2O2 Released by Cells at the Nanomolar Level. *Anal. Chem.* **2013**, *85* (21), 10289–10295. https://doi.org/10.1021/ac402114c.

(33) Guo, X.; Wang, Y.; Wu, F.; Ni, Y.; Kokot, S. A Colorimetric Method of Analysis for Trace Amounts of Hydrogen Peroxide with the Use of the Nano-Properties of Molybdenum Disulfide. *Analyst* **2015**, *140* (4), 1119–1126. https://doi.org/10.1039/C4AN01950D.

(34) Cao, P.; Wang, N.; Dai, H.; Ma, H.; Lin, M. Molybdenum-Containing Polypyrrole Self-Supporting Hollow Flexible Electrode for Hydrogen Peroxide Detection in Living Cells. *Analytica Chimica Acta* **2021**, *1151*, 338251. https://doi.org/10.1016/j.aca.2021.338251.

(35) Shu, Y.; Zhang, W.; Cai, H.; Yang, Y.; Yu, X.; Gao, Q. Expanding the Interlayers of Molybdenum Disulfide toward the Highly Sensitive Sensing of Hydrogen Peroxide. *Nanoscale* **2019**, *11* (14), 6644–6653. https://doi.org/10.1039/C9NR00333A.

(36) Coleman, J. N.; Lotya, M.; O'Neill, A.; Bergin, S. D.; King, P. J.; Khan, U.; Young, K.; Gaucher, A.; De, S.; Smith, R. J.; Shvets, I. V.; Arora, S. K.; Stanton, G.; Kim, H.-Y.; Lee, K.; Kim, G. T.; Duesberg, G. S.; Hallam, T.; Boland, J. J.; Wang, J. J.; Donegan, J. F.; Grunlan, J. C.; Moriarty, G.; Shmeliov, A.; Nicholls, R. J.; Perkins, J. M.; Grieveson, E. M.; Theuwissen, K.; McComb, D. W.; Nellist, P. D.; Nicolosi, V. Two-Dimensional Nanosheets Produced by Liquid Exfoliation of Layered Materials. *Science* **2011**, *331* (6017), 568–571. https://doi.org/10.1126/science.1194975.

(37) Fan, X.; Xu, P.; Li, Y. C.; Zhou, D.; Sun, Y.; Nguyen, M. A. T.; Terrones, M.; Mallouk, T. E. Controlled Exfoliation of MoS2 Crystals into Trilayer Nanosheets. *J. Am. Chem. Soc.* **2016**, *138* (15), 5143–5149. https://doi.org/10.1021/jacs.6b01502.

(38) Geng, X.; Sun, W.; Wu, W.; Chen, B.; Al-Hilo, A.; Benamara, M.; Zhu, H.; Watanabe, F.; Cui, J.; Chen, T. Pure and Stable Metallic Phase Molybdenum Disulfide Nanosheets for Hydrogen Evolution Reaction. *Nat Commun* **2016**, *7* (1), 10672. https://doi.org/10.1038/ncomms10672.

(39) Rukelj, Z.; Štrkalj, A.; Despoja, V. Optical Absorption and Transmission in a Molybdenum Disulfide Monolayer. *Phys. Rev. B* **2016**, *94* (11), 115428. https://doi.org/10.1103/PhysRevB.94.115428.

(40) Kaur, J.; Singh, M.; Dell'Aversana, C.; Benedetti, R.; Giardina, P.; Rossi, M.; Valadan, M.; Vergara, A.; Cutarelli, A.; Montone, A. M. I.; Altucci, L.; Corrado, F.; Nebbioso, A.; Altucci, C. Biological Interactions of Biocompatible and Water-Dispersed MoS2 Nanosheets with Bacteria and Human Cells. *Sci Rep* **2018**, *8* (1), 16386. https://doi.org/10.1038/s41598-018-34679-y.

(41) Li, H.; Zhang, Q.; Yap, C. C. R.; Tay, B. K.; Edwin, T. H. T.; Olivier, A.; Baillargeat, D. From Bulk to Monolayer MoS2: Evolution of Raman Scattering. *Advanced Functional Materials* **2012**, *22* (7), 1385–1390. https://doi.org/10.1002/adfm.201102111.

(42) Nayak, A. P.; Pandey, T.; Voiry, D.; Liu, J.; Moran, S. T.; Sharma, A.; Tan, C.; Chen, C.-H.; Li, L.-J.; Chhowalla, M.; Lin, J.-F.; Singh, A. K.; Akinwande, D. Pressure-Dependent Optical and Vibrational Properties of Monolayer Molybdenum Disulfide. *Nano Lett.* **2015**, *15* (1), 346–353. https://doi.org/10.1021/nl5036397.

(43) Zhao, Y.; Ouyang, G. Thickness-Dependent Photoelectric Properties of MoS2/Si Heterostructure Solar Cells. *Sci Rep* **2019**, *9* (1), 17381. https://doi.org/10.1038/s41598-019-53936-2.

(44) Wu, W.; Lu, Q.; Li, G.; Wang, Y. How to Extract Kinetic Information from Tafel Analysis in Electrocatalysis. *The Journal of Chemical Physics* **2023**, *159* (22), 221501. https://doi.org/10.1063/5.0175156.

(45) Voiry, D.; Chhowalla, M.; Gogotsi, Y.; Kotov, N. A.; Li, Y.; Penner, R. M.; Schaak, R. E.; Weiss, P. S. Best Practices for Reporting Electrocatalytic Performance of Nanomaterials. *ACS Nano* **2018**, *12* (10), 9635–9638. https://doi.org/10.1021/acsnano.8b07700.

(46) Anantharaj, S.; Noda, S. How Properly Are We Interpreting the Tafel Lines in Energy Conversion Electrocatalysis? *Materials Today Energy* **2022**, *29*, 101123. https://doi.org/10.1016/j.mtener.2022.101123.

(47) Barbir, F. Chapter Three - Fuel Cell Electrochemistry. In *PEM Fuel Cells (Second Edition)*; Barbir, F., Ed.; Academic Press: Boston, 2013; pp 33–72. https://doi.org/10.1016/B978-0-12-387710-9.00003-5.

(48) Sharma, U.; Karazhanov, S.; Alonso-Vante, N.; Das, S. Metallic-Phase of MoS2 as Potential Electrocatalyst for Hydrogen Production via Water Splitting: A Brief Review. *Current Opinion in Electrochemistry* **2022**, *35*, 101067. https://doi.org/10.1016/j.coelec.2022.101067.

(49) Antipin, D.; Risch, M. Calculation of the Tafel Slope and Reaction Order of the Oxygen Evolution Reaction between pH 12 and pH 14 for the Adsorbate Mechanism. *Electrochemical Science Advances* **2023**, *3* (6), e2100213. https://doi.org/10.1002/elsa.202100213.

(50) Chen, J.; Walker, W. R.; Xu, L.; Krysiak, O.; She, Z.; Pope, M. A. Intrinsic Capacitance of Molybdenum Disulfide. *ACS Nano* **2020**, *14* (5), 5636–5648. https://doi.org/10.1021/acsnano.9b10182.

(51) Swamy, T.; Chiang, Y.-M. Electrochemical Charge Transfer Reaction Kinetics at the Silicon-Liquid Electrolyte Interface. *J. Electrochem. Soc.* **2015**, *162* (13), A7129. https://doi.org/10.1149/2.0181513jes.

(52) Biby, A.; Crawford, H.; Xia, X. Platinum-Group Metal Nanoparticles as Peroxidase Mimics: Implications for Biosensing. *ACS Appl. Nano Mater.* **2022**, *5* (12), 17622–17631. https://doi.org/10.1021/acsanm.2c03365.

(53) Kora, A. J.; Rastogi, L. Peroxidase Activity of Biogenic Platinum Nanoparticles: A Colorimetric Probe towards Selective Detection of Mercuric Ions in Water Samples. *Sensors and Actuators B: Chemical* **2018**, *254*, 690–700. https://doi.org/10.1016/j.snb.2017.07.108.

(54) Wang, Z.; Yang, X.; Yang, J.; Jiang, Y.; He, N. Peroxidase-like Activity of Mesoporous Silica Encapsulated Pt Nanoparticle and Its Application in Colorimetric Immunoassay. *Analytica Chimica Acta* **2015**, *862*, 53–63. https://doi.org/10.1016/j.aca.2014.12.046.

(55) Xi, Z.; Wei, K.; Wang, Q.; Kim, M. J.; Sun, S.; Fung, V.; Xia, X. Nickel–Platinum Nanoparticles as Peroxidase Mimics with a Record High Catalytic Efficiency. *J. Am. Chem. Soc.* **2021**, *143* (7), 2660–2664. https://doi.org/10.1021/jacs.0c12605.

(56) Mazzotta, E.; Di Giulio, T.; Mastronardi, V.; Pompa, P. P.; Moglianetti, M.; Malitesta, C. Bare Platinum Nanoparticles Deposited on Glassy Carbon Electrodes for Electrocatalytic

Detection of Hydrogen Peroxide. *ACS Appl. Nano Mater.* **2021**, *4* (8), 7650–7662. https://doi.org/10.1021/acsanm.1c00754.

(57) Bahshi, L.; Frasconi, M.; Tel-Vered, R.; Yehezkeli, O.; Willner, I. Following the Biocatalytic Activities of Glucose Oxidase by Electrochemically Cross-Linked Enzyme−Pt Nanoparticles Composite Electrodes. *Anal. Chem.* **2008**, *80* (21), 8253–8259. https://doi.org/10.1021/ac801398m.

(58) Ma, M.; Zhang, Y.; Gu, N. Peroxidase-like Catalytic Activity of Cubic Pt Nanocrystals. *Colloids and Surfaces A: Physicochemical and Engineering Aspects* **2011**, *373* (1), 6–10. https://doi.org/10.1016/j.colsurfa.2010.08.007.

(59) Pedone, D.; Moglianetti, M.; Lettieri, M.; Marrazza, G.; Pompa, P. P. Platinum Nanozyme-Enabled Colorimetric Determination of Total Antioxidant Level in Saliva. *Anal. Chem.* **2020**, *92* (13), 8660–8664. https://doi.org/10.1021/acs.analchem.0c01824.

(60) de Jesus, A. J.; Yin, H. 5.14 - Supramolecular Membrane Chemistry. In *Comprehensive Supramolecular Chemistry II*; Atwood, J. L., Ed.; Elsevier: Oxford, 2017; pp 311–328. https://doi.org/10.1016/B978-0-12-409547-2.12572-7.

(61) van der Post, S. T.; Scheidelaar, S.; Bakker, H. J. Water Dynamics in Aqueous Solutions of Tetra-n-Alkylammonium Salts: Hydrophobic and Coulomb Interactions Disentangled. *J. Phys. Chem. B* **2013**, *117* (48), 15101–15110. https://doi.org/10.1021/jp4085734.

(62) Er, E.; Hou, H.-L.; Criado, A.; Langer, J.; Möller, M.; Erk, N.; Liz-Marzán, L. M.; Prato, M. High-Yield Preparation of Exfoliated 1T-MoS2 with SERS Activity. *Chem. Mater.* **2019**, *31* (15), 5725–5734. https://doi.org/10.1021/acs.chemmater.9b01698.

(63) Moon, J.; Li, M.; Ramirez-Cuesta, A. J.; Wu, Z. Raman Spectroscopy. In *Springer Handbook of Advanced Catalyst Characterization*; Wachs, I. E., Bañares, M. A., Eds.; Springer International Publishing: Cham, 2023; pp 75–110. https://doi.org/10.1007/978-3-031-07125-6_4.

(64) Michota, A.; Bukowska, J. Surface-Enhanced Raman Scattering (SERS) of 4-Mercaptobenzoic Acid on Silver and Gold Substrates. *Journal of Raman Spectroscopy* **2003**, *34* (1), 21–25. https://doi.org/10.1002/jrs.928.

(65) Brolo, A. G.; Jiang, Z.; Irish, D. E. The Orientation of 2,2′-Bipyridine Adsorbed at a SERS-Active Au(1 1 1) Electrode Surface. *Journal of Electroanalytical Chemistry* **2003**, *547* (2), 163–172. https://doi.org/10.1016/S0022-0728(03)00215-8.

(66) Gamer, G.; Wolff, H. Raman and Infrared Spectra of Gaseous Secondary Aliphatic Amines [(CH32NH, (CH3)2ND, (C2H5)2NH and C2H5NHCH3]. *Spectrochimica Acta Part A:*

Molecular Spectroscopy **1973**, *29* (1), 129–137. https://doi.org/10.1016/0584-8539(73)80015-7.

(67) Yang, Q.; Wang, Z.; Dong, L.; Zhao, W.; Jin, Y.; Fang, L.; Hu, B.; Dong, M. Activating MoS2 with Super-High Nitrogen-Doping Concentration as Efficient Catalyst for Hydrogen Evolution Reaction. *J. Phys. Chem. C* **2019**, *123* (17), 10917–10925. https://doi.org/10.1021/acs.jpcc.9b00059.

(68) Tao, P.; He, J.; Shen, T.; Hao, Y.; Yan, J.; Huang, Z.; Xu, X.; Li, M.; Chen, Y. Nitrogen-Doped MoS2 Foam for Fast Sodium Ion Storage. *Advanced Materials Interfaces* **2019**, *6* (13), 1900460. https://doi.org/10.1002/admi.201900460.

(69) Polumati, G.; Kolli, C. S. R.; Selamneni, V.; Salazar, M. F.; De Luna Bugallo, A.; Sahatiya, P. Modulation of Schottky Barrier Height by Nitrogen Doping and Its Influence on Responsivity of Monolayer MoS2 Photodetector. *Advanced Materials Interfaces* **2023**, *10* (9), 2202108. https://doi.org/10.1002/admi.202202108.

(70) Jiang, Y.; Wang, J.; Wu, J.; Zhang, Y. Preparation of High-Performance Natural Rubber/Carbon Black/Molybdenum Disulfide Composite by Using the Premixture of Epoxidized Natural Rubber and Cysteine-Modified Molybdenum Disulfide. *Polym. Bull.* **2021**, *78* (3), 1213–1230. https://doi.org/10.1007/s00289-020-03157-9.

(71) Song, Y.; Yang, D.; Li, Y.; Tian, S.; Deng, Q.; Liu, R.; Wang, Z.; Wang, X.; Hu, H.; Wang, Y.; Zhao, J. Dodecylation of Molybdenum Disulfide and Its Electrochemical Properties for Hydrogen Evolution Reaction. *Nanotechnology* **2023**, *34* (48), 485601. https://doi.org/10.1088/1361-6528/acf1a8.

(72) Bartolomei, B.; Sbacchi, M.; Rosso, C.; Günay-Gürer, A.; Zdražil, L.; Cadranel, A.; Kralj, S.; Guldi, D. M.; Prato, M. Synthetic Strategies for the Selective Functionalization of Carbon Nanodots Allow Optically Communicating Suprastructures. *Angewandte Chemie* **2024**, *136* (5), e202316915. https://doi.org/10.1002/ange.202316915.

(73) Gentile, G.; Mamone, M.; Rosso, C.; Amato, F.; Lanfrit, C.; Filippini, G.; Prato, M. Tailoring the Chemical Structure of Nitrogen-Doped Carbon Dots for Nano-Aminocatalysis in Aqueous Media. *ChemSusChem* **2023**, *16* (7), e202202399. https://doi.org/10.1002/cssc.202202399.

(74) Zhu, Q.; Yuan, Z.; Qian, W.; Li, Y.; Qiu, Z.; Tang, W.; Wang, J.; Ding, Y.; Hu, A. Spherical Polyelectrolyte Brushes as a Novel Platform for Paramagnetic Relaxation Enhancement and Passive Tumor Targeting. *Advanced Healthcare Materials* **2017**, *6* (12), 1700071. https://doi.org/10.1002/adhm.201700071.

Chapter IV

Ultrasound-aided Exfoliation of Few-layered Graphene in a Sustainable Alternative Solvent

Abstract

Liquid phase exfoliation (LPE) is one of the most promising processes for the scalable production of graphene. However, the traditional solvents used for LPE, namely N-Methylpyrrolidone, and N,N-Dimethylformamide, are highly toxic and harmful to the environment. In the last 7 years, greener alternatives for LPE have been explored. Among those, Cyrene (dihydrolevoglucosenone) emerged as an ideal candidate thanks to its physical-chemical properties, wide availability, and negligible toxicity.

In this chapter, the influence of several operational parameters of LPE processes over the final quality of exfoliated graphene has been investigated. The study aims to set up guidelines to design a sustainable laboratory protocol for producing high-quality graphene for conductive solutions.

4.1 Introduction

4.1.1 Cyrene as a Sustainable Alternative Solvent for Graphene Exfoliation

Liquid phase exfoliation (LPE) of 2D materials, and specifically graphene, unlocks large-scale production of colloidal graphene, which finds application in several fields, from sustainable liquid lubrication for industrial machinery[1] to heat transfer fluids,[2] from anti-corrosion coatings[3] to printable electronics[4] and optoelectronics.[5]

LPE methods are economical, versatile, and easily scalable, but come with two main drawbacks, which are the low quality of graphene and the use of large amounts of organic solvents, surfactants and oxidants. Typical solvents used for exfoliation of graphene are NMP[6] and DMF[7], which are known to be highly toxic and oncogenic.[8–11] As a matter of fact, both solvents have been included in the list of "Substances of Very High Concern" (SVHC), which is propaedeutic to restriction of any substance under European REACH regulation [Regulation (EC) no. 1907/2006], and the use of DMF has been recently restricted by the European Commission, because of its acute toxicity.[12]

Therefore, it is urgent to identify valid alternatives for sustainable processing of exfoliated graphene. A study by H. J. Salavagione et al. in 2017, presented Cyrene

(dihydrolevoglucosenone) as a promising solvent for exfoliation of graphene.[13] In their work, they used computational methods to perform a screening of over 10,000 solvents as candidates for liquid processing of graphene. In a multi-phase selection, they first isolated a group of suitable solvents based on their physical chemical properties (*i.e.* polarity, surface tension and viscosity), and then applied toxicity and environmental persistency check to exclude harmful species. In the end, Cyrene emerged as the best solvent for LPE of graphene, outcompeting even traditional NMP and DMF, both in terms of yield and flake quality. Since then, Cyrene was reported in the literature as an efficient medium for preparation of graphene-based conductive inks for screen-printing flexible electronics,[14–16] graphene coatings for fabric[17] and inks for 3D extrusion printing.[18]

The potential of Cyrene is not limited to graphene LPE, as this solvent can serve as a reaction medium for organic synthesis, materials chemistry and biocatalysis.[19] Thus, the extreme versatility of this solvent opens to the possibility of post-modification of highly concentrated graphene suspensions, which is a game changer for the industrial scale-up of graphene inks.

The academic interest in Cyrene has been growing sensitively in the last few years (**Figure 76 a**). However, few works focused on its use for graphene LPE (**Figure 76b**) and research in this field is still at an initial state. Moreover, LPE efficiency is strongly dependent on the specific equipment,[20] and many operational parameters and variables are to be taken into account to optimize the quality of the final material.

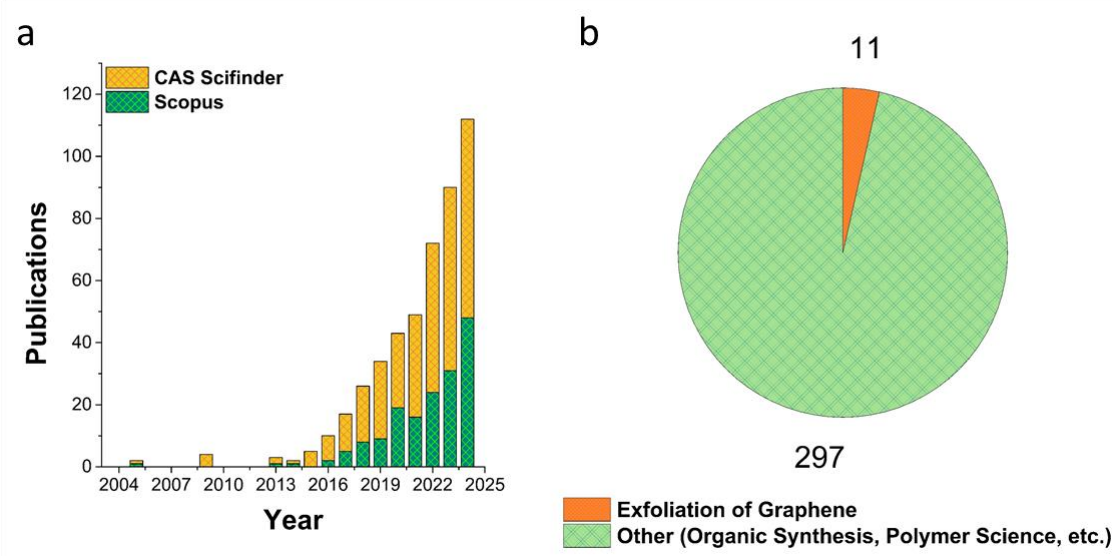

Figure 76 *a) Histogram illustrating the number of publications related to Cyrene from 2004 to 2024; b) Pie chart illustrating the number of pubblications related to Cyrene-mediated graphene LPE vs other publications presenting Cyrene for different applications.*

4.1.2 Aim of the Project

This project aimed to study the influence of various operational parameters on the LPE of graphene, to establish an operational protocol for the production of high quality graphene nanosheets for printable formulations. Specifically, the importance of operational amplitude, reactor size and pulsed sonication were investigated, as well as the suitability of different types of graphite for LPE. The project was carried out under the supervision of Dr. Alessandro Silvestri and Prof. Maurizio Prato.

4.2 Results and Discussion

In first instance, it was necessary to define a set of experimental variables and parameters. LPE was carried out with a tip sonicator that allows setting amplitude of the sonic waves, to modulate the power of the used radiation, sonication time and sonication mode (continuous sonication or pulsed sonication). Sonication time was maintained constant during the study. Indeed, long times of sonication can be detrimental for the quality of exfoliated graphene, as they lead to formation of more defects.[21,22] Moreover, the principles of green chemistry and green engineering require to minimize the energy input of chemical processes, which results in the minimization of operational time.[23] As a consequence, a short time of sonication (15 minutes) was preferred, to prioritize the quality of graphene flakes over the yield.

4.2.1 Effect of the Amplitude

In tip sonicators, the power is set in terms of amplitude, which is the distance of one movement up and down of the piezoelectric crystal. The amplitude is expressed in percentage with respect to the diameter of the probe. Exfoliation of graphene was performed on 25 mg of graphite in 25 mL flasks, at 20%, 30%, and 40% amplitude. Higher amplitudes were excluded because of instrumental limits and poor control over the temperature. To evaluate the efficiency of graphene exfoliation, absorbance at 660 nm was used as a rapid quantitative response, as in this region of the spectrum the absorbance is dependent on the scattering of dispersed nanoparticles, and therefore on their concentration.[13,24] **Figure 77** illustrates the obtained spectra for the graphene suspensions exfoliated at different amplitudes.

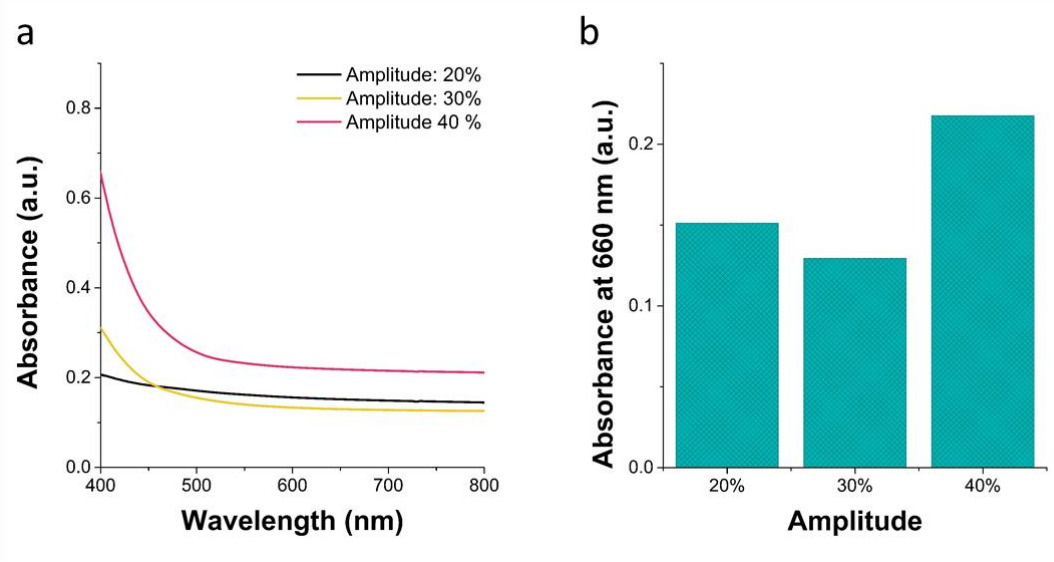

Figure 77 *a) UV-Vis spectra recorded for graphene exfoliated in Cyrene at 20% (black), 30% (yellow), and 40% (magenta) amplitude; b) histogram comparing absorbance at 660 nm for the different batches.*

In the range of investigated amplitudes, 40% amplitude resulted to be the most efficient. Using the value of absorptivity reported by Salavagione et al.,[13] the concentration of the suspension can be estimated to be 0.05 mg/mL, with an exfoliation yield of 3.2%.

4.2.2 Effect of the Flask Size

The subsequent step was to compare LPE efficiency at 40% amplitude with different reactor sizes. To understand the impact of the flask size on LPE, two different flasks, 25 mL and 50 mL, were used to carry out the exfoliation, while maintaining constant the ratio between the volume of solvent and the volume of the flask (3:5) and the graphite to Cyrene ratio (3:2). **Figure 78** illustrates the obtained spectra for the graphene suspensions exfoliated in a 25 mL round bottom flask, with 25 mg of graphite and 16 mL of Cyrene, and in a 50 mL round bottom flask, with 45 mg of graphite and 30 mL of Cyrene.

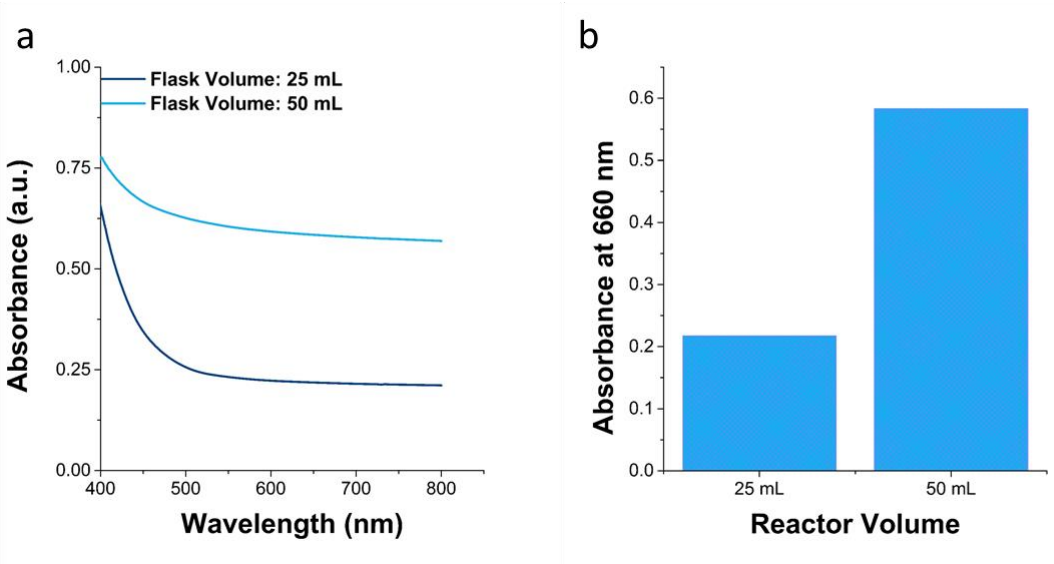

Figure 78 *a) UV-Vis spectra recorded for graphene exfoliated in Cyrene in 25 mL flask (black) and in 50 mL flask (light blue); b) histogram comparing absorbance at 660 nm for the different batches.*

The exfoliation yield increases at a larger volume, from 3.2% to 10%, with a final concentration of graphene of 0.15 mg/mL. The volume of solvent and the reactor exert an influence on the process in terms of efficiency and heat dispersion.[25] Typically, larger volumes of solvent lead to attenuation of the energy of the mechanical wave,[26] with formation of "dead zones" in which the efficiency of sonication is sensitively lower.[27] Indeed, attenuation of ultrasounds in fluids is governed by **Equation 1** and **Equation 2**:[28–31]

$$\textbf{Equation 1} \quad I = I_0 e^{-2\alpha d}$$

$$\textbf{Equation 2} \quad \alpha_f = \frac{8\pi^2\omega^2\mu}{3\rho C^3}$$

Where:

- I is the acoustic intensity at a distance d (m) from the source;

- I_0 is the intensity at the source;

- α_f is the attenuation coefficient;

- ω is the angular frequency of irradiation;

- μ is the viscosity of the medium (kg m s^{-2});

- ρ is the density of the medium (kg/m^3);

-C is the speed of sound in the liquid (m/s);

From physical-chemical properties of Cyrene, it is possible to approximate a value of α_f = 1.41×10^{-3} m^{-1}, so that intensity at maximum distance from the source (20 mm) at the center of the reactor is equal to 99.99% of the intensity at the source. Consequently, attenuation is not an issue in the case of the used reactors.

On the other hand, for some reactions in sonochemical setups, larger volumes have been associated with higher efficiency,[32] and can help with the temperature control, which could explain the higher exfoliation yield with the larger reactor.

4.2.3 Comparison with NMP

Once the best operational amplitude and reactor size were identified, LPE of graphene was carried out with NMP in the same conditions, to compare the performances of the two solvents. **Figure 79** reports the UV-Vis spectra obtained for the obtained suspensions and the calculated concentrations of the final suspensions.

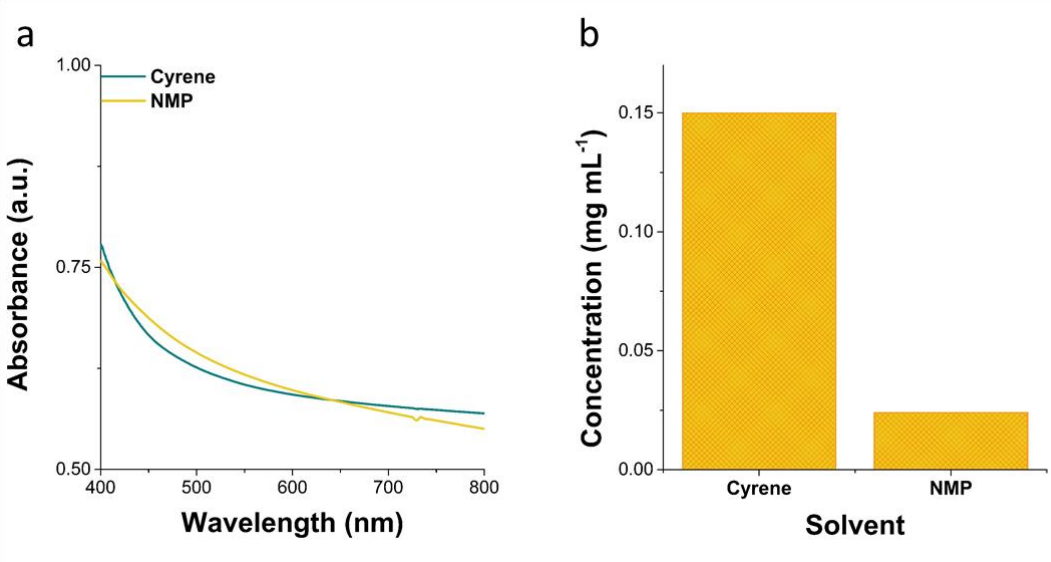

Figure 79 *a) UV-Vis spectra recorded for graphene exfoliated in Cyrene (green) and in NMP (yellow) in 50 mL flask at 40% amplitude; b) histogram comparing concentrations of the different batches.*

While the two suspensions present similar values of absorbance at 660 nm (0.583 for Cyrene and 0.581 for NMP), the absorptivity reported for NMP suspensions of graphene (2460 L g^{-1} m^{-1}), which is more than 6 times higher than that of graphene in Cyrene, so that the concentration calculated for graphene exfoliated in graphene is equal to 0.024 mg mL^{-1}.

To further characterize the obtained exfoliated graphenes, the suspension was filtrated on PTFE, and after multiple washing with ethanol to remove excess of Cyrene, graphene was suspended in isopropanol. The isopropanol suspension was used to prepare samples for transmission electron microscopy.

TEM micrographs of graphene exfoliated in Cyrene (**Figure 80a-b**) show small aggregated multi-layered graphene nanosheets. On the other hand, micrographs of graphene exfoliated in NMP (**Figure 80c-d**) present multi-layered graphite, with irregular edges.

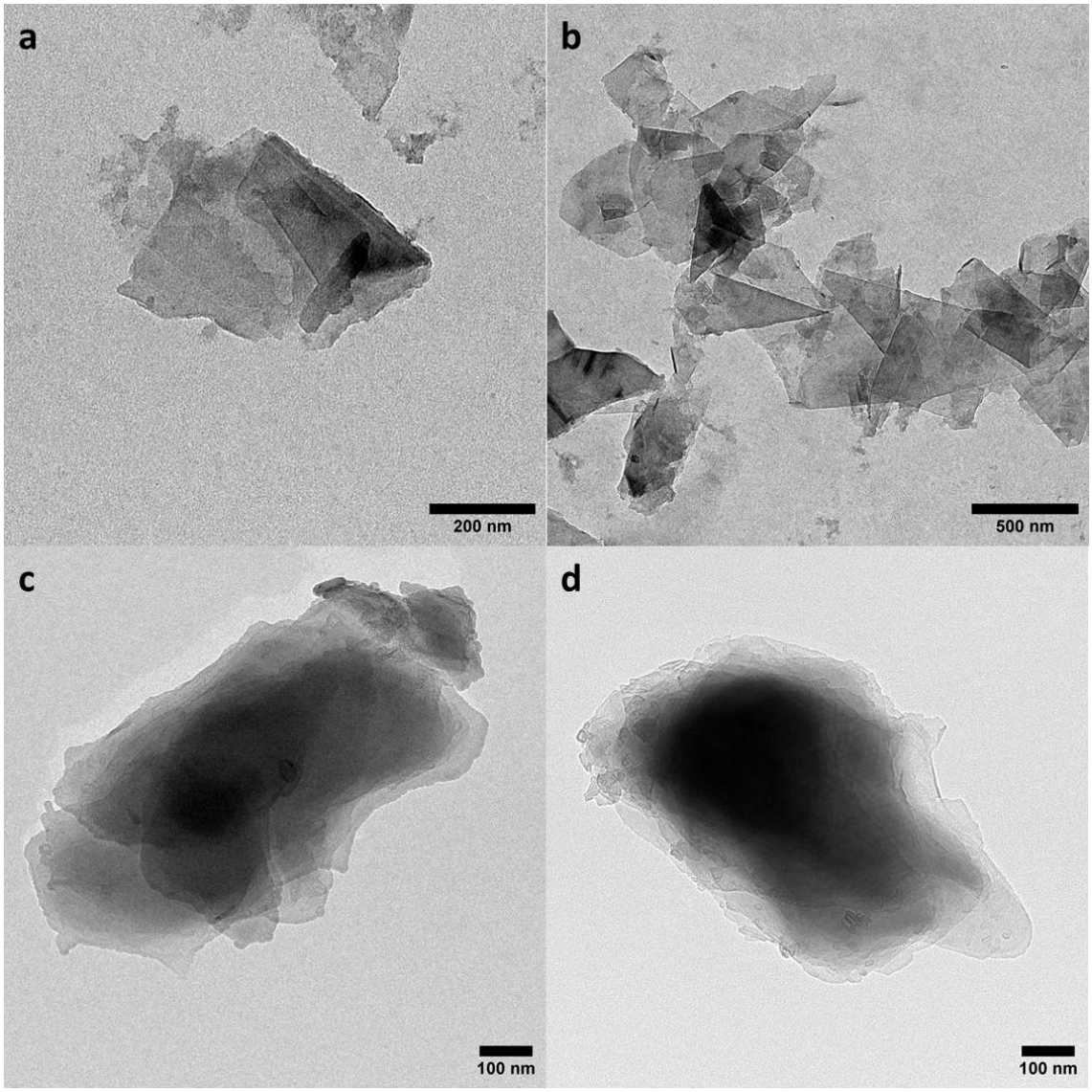

Figure 80 *TEM micrographs of graphene exfoliated in Cyrene (a-b) and in NMP (c-d) in 50 mL reactor at 40% amplitude.*

These evidences suggest that Cyrene outcompetes NMP not only for the yield of final graphene (10% in Cyrene and 1.6% in NMP) but also for the exfoliation efficacy.

4.2.4 Pulsed Sonication

To increase the degree of exfoliation, and improve the quality of final graphene, the effect of slow pulsed sonication on LPE was investigated. LPE was carried out with a sequence of pulses of 1 s at 40 %, alternating to silent periods of 1 s. The use of pulsed sonication determines higher efficiency, as it helps controlling the size of cavitation bubbles[33] and preventing energy-loss phenomena, such as the formation of degassing bubbles.[34] The result of pulsed sonication was a clear improvement over the morphology of graphene flakes, as shown in **Figure 81**.

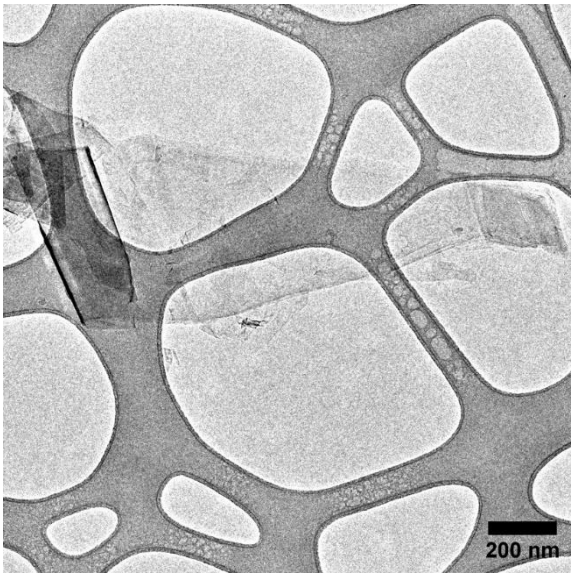

Figure 81 *TEM micrograph of graphene exfoliated with pulsed sonication in Cyrene, with 50 mL reactor at 40% amplitude.*

The pulsed sonication produced wider graphene nanosheets, with more regular edges and lower thickness. However, the quantitative yield was sensitively lower (2.80%).

4.2.5 Comparison of Different Graphite Types

Finally, the developed protocol was tested on three different types of graphite, to assess the influence of the graphite morphology over the final graphene nanosheets. Besides graphite flakes, graphite powder and spherical graphite were used for this purpose.

Graphite flakes are a type of natural macro crystalline graphite, consisting of large crystals, uniformly oriented into scaly or lamella forms.[35]

Graphite powder can be either natural or artificial. The main difference with graphite flakes is the size of the particles constituting the material, with graphite powder being composed of smaller particles (<20 μm).

Spherical graphite is unstructured form of graphite[35] formed of well-rounded spherules of few μm of diameter (<23 μm) with low specific surface area, typically used for batteries and energy storage.[36]

TEM micrographs of the obtained graphene batches are reported in **Figure 82**.

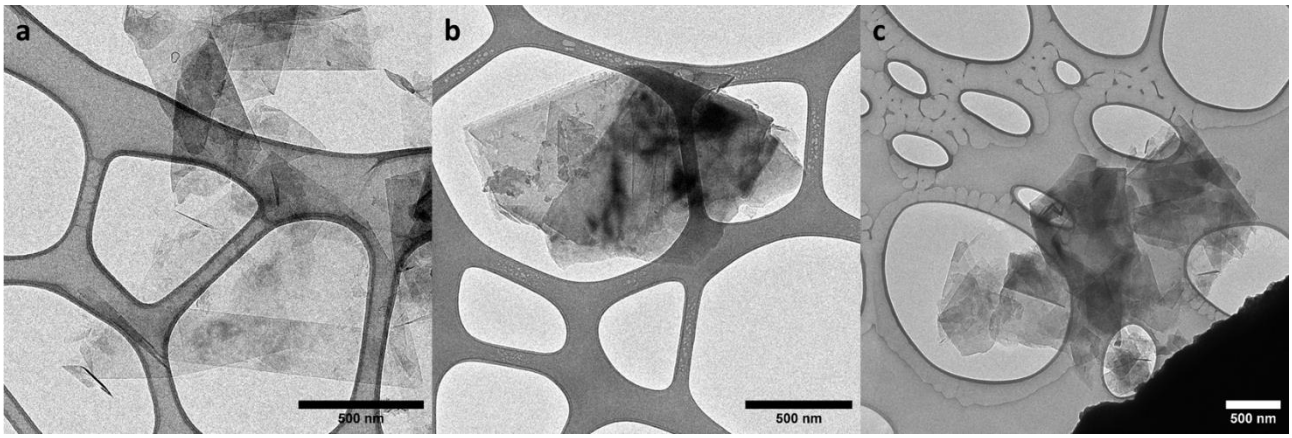

Figure 82 *TEM micrographs of graphene exfoliated from pulsed sonication of graphite flakes (a), graphite powder (b) and spherical graphite (c), in Cyrene in 50 mL reactor at 40% amplitude.*

In the used conditions, graphite flakes prove to be the best type of graphite for LPE of high quality graphene, with wider nanosheets and lower number of stacked layers. Graphite powder and spherical graphite yielded smaller nanoflakes, with irregular edges and various layers.

The graphene obtained from graphite flakes was further characterized by XPS and Raman spectroscopy (**Figure 83**).

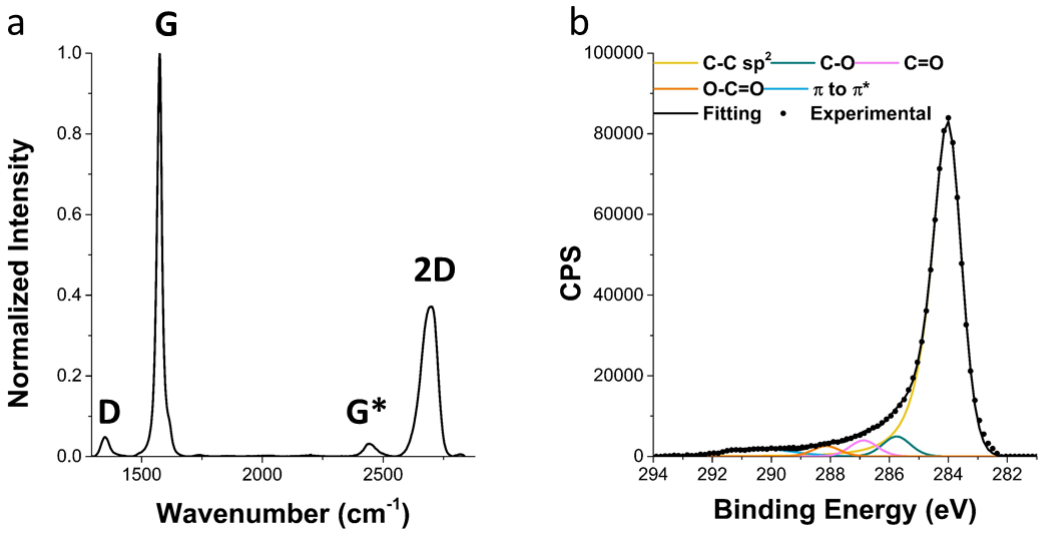

Figure 83 *a) Raman spectrum and b) high resolution XPS spectrum of C of graphene exfoliated from pulsed sonication of graphite flakes in Cyrene in 50 mL reactor at 40% amplitude. Raman spectrum was normalized for the highest peak that is the G band.*

Specifically, from Raman spectrum it was possible to determine the ratio between the intensity of the G band and the D band, which is an indicator of the defectiveness of graphene.[37] Moreover, information on the number of layers was extrapolated from the 2D band, from the ratio I_{2D}/I_G,[38,39] its Raman shift,[38] and line-shape.[40,41]

The I_D/I_G ratio is equal to 0.04, which indicates a very low amount of defects on the surface of the obtained flakes. The I_{2D}/I_G ratio was calculated to be 0.41, which indicates the presence of few-layer and multilayer graphene flakes.[38,39] The spectrum of LPE graphene was compared with data retrieved from a CVD graphene in the same conditions (**Figure 84**). The FWHM determined for LPE graphene is approximately two times the value found for CVD graphene, which is consistent with few-layer graphene (**Figure 84b**).[41,42] Finally, the position of 2D band of LPE graphene is in agreement with an average thickness between three and five layers.[38]

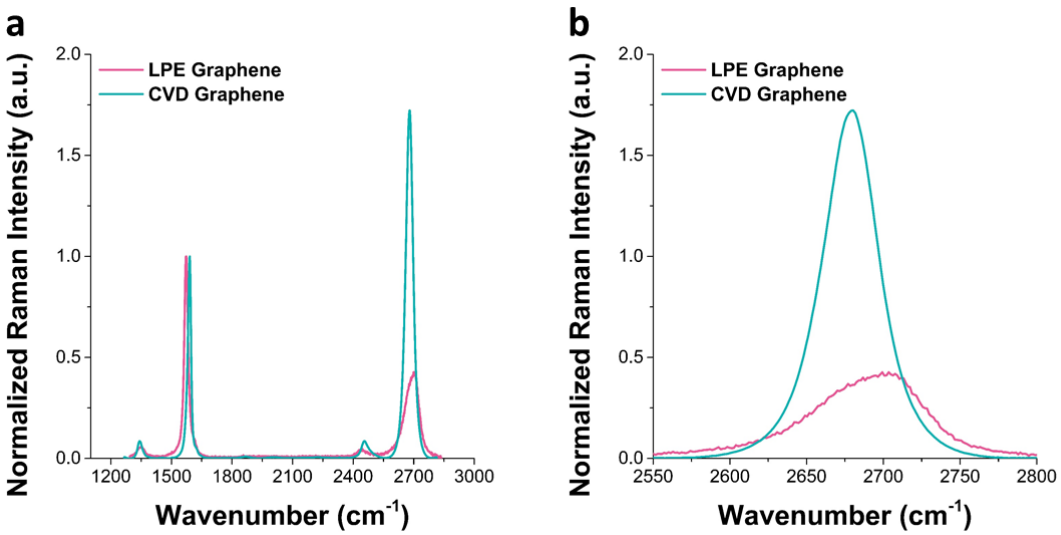

Figure 84 *a) Raman spectra of LPE graphene (magenta) and CVD graphene (teal); b) magnification of the 2D bands.*

From XPS, the ratio between O and C atomic percentage was extrapolated to assess the lack of oxidation and the efficiency of purification from Cyrene.[24] These parameters were used to compare the quality of the obtained graphene with other examples from literature (**Table 14**). The obtained graphene is competitive with other examples reported in literature, with the lowest value of ID/IG, a good value of I2D/IG and %O/%C.

Table 14 *Comparison of different exfoliated graphenes from literature, based on Raman and XPS analysis.*

Solvent	Exfoliation Method	I_D/I_G (Raman)	I_{2D}/I_G (Raman)	%O/%C (XPS)	Reference
DMF	LPE (sonication)	0.06	0.44	-	[43]
Ethanol	LPE (sonication)	0.08	0.35	-	[43]
Water	LPE (sonication)	0.27-0.49	0.68-0.70	-	[20]
Water (surfactants)	LPE (sonication)	-	Average over mapping = 0.5	-	[44]
Aqueous H2SO4 + KMnO4, H2O2	LPE (oxidation + FeCl3 intercalation +	0.21	-	0.091	[45]
Argon Gas	Plasma Spray	0.17-0.23	-	0.047	[46]
Cyrene	LPE (sonication)	0.25	0.036	0.05	[14]
Cyrene	LPE (sonication)	0.2	-	-	[13]
Cyrene	LPE (sonication)	0.04	0.41	0.09	This work

4.3 Conclusions

In conclusion for this chapter, the set of preliminary data obtained from the study allowed us to understand the influence of various operational parameters on the efficiency of LPE to produce high-quality graphene nanosheets. Amplitude and reactor size influence the exfoliation efficiency, as the maximum yield was obtained at 40% amplitude in the larger reactor. Pulsed sonication allowed increasing the sonication efficiency and the exfoliation efficacy, leading to exfoliation of few-layer graphene nanosheets. The protocol gave the best results with crystalline graphite flakes. From Raman spectroscopy, the low value for the I_D/I_G ratio (0.04) indicates extremely low amount of defects, while from the 2D band the thickness of the exfoliated graphene was estimated to be in the range of three to five layers. XPS showed an extremely low content of oxygenated moieties (0.09 O/C) attributable to defects or the presence of solvent residues after the purification.

Further studies will be needed to optimize the process, especially in terms of yield. However, the experimental protocol allowed the obtaining of high-quality few-layered graphene nanosheets that outcompete other exfoliated graphenes from the literature.

Once optimized, the process can be used on a laboratory scale for the sustainable production of highly conductive printable formulations.

4.4 Experimental Section

4.4.1 Materials and Instruments

Cyrene™ Biorenewable (#807796-2.5L), graphite flakes (#808067-2.5KG) and graphite powder (#282863-1KG) were purchased from Sigma Aldrich and used without further purification. Spherical graphite (#PG1112) was purchased from ProGraphiteShop.

All exfoliation experiments were carried out using a Fisher Scientific Sonic Dismembrator, operating at 20 kHz, with an Aluminum alloy converter (183 mm × 63.5 mm) and a Titanium alloy horn (136 mm ×13 mm).

UV-Vis spectra were collected with an Agilent Cary 5000 UV-Vis spectrophotometer, at room temperature with plastic cuvettes, in a wavelength range comprised from 300 nm and 800 nm.

TEM images were recorded with a Phillips CM200 transmission electron microscope equipped with Quemesa camera (Olympus Soft Imaging Solutions) and RADIUS software for image acquisition. Samples were prepared by dropcast of the aqueous suspensions (concentration 0.5 mg/mL) on Lacey Carbon 300 mesh copper grids (approx. grid hole size: 63μm), purchased from TED PELLA Inc.

Raman spectra were recorded using a Renishaw inVia Raman microscope. A laser excitation wavelength of 633 nm, lens-based spectrometer with 1800 gr mm^{-1} gratings, Peltier-cooled front-illuminated CCD camera (1024 × 532 px), and a 100× objective were employed. Samples were prepared by drop-casting MoS_2 solution on a silicon oxide slide and drying it under ambient conditions. Each spectrum is derived from the average of at least 100 spectra recorded in different spots of the sample for 5 s with a laser power of 1.29 mW. Data were processed using Renishaw WiRE 4 software.

X-ray Photoelectron Spectroscopy (XPS) spectra were registered with an XPS/UPS – SPECS SAGE HR-100 equipped with a 100 mm radius PHOIBOS analyzer, where 421 Mg Kα X-ray source was used. The samples were prepared by drop-casting 80 μL of a 0.5 mg/mL suspension of material in Milli-Q water, on a gold-coated substrate. The samples were then let dry under vacuum. The spectra were fitted using CasaXPS and calibration was performed using the major component of the C high-resolution spectrum as a reference at 284.0 eV, which is the value reported for sp^2 carbon for graphene.

4.4.2 Exfoliation of Graphene

Graphite flakes (45 mg) were ground with porcelain mortar and pestle for 10 minutes (**Figure 85a**). Subsequently 15 mL of Cyrene were added and the mixture was ground for other 2 minutes (**Figure 85b**).

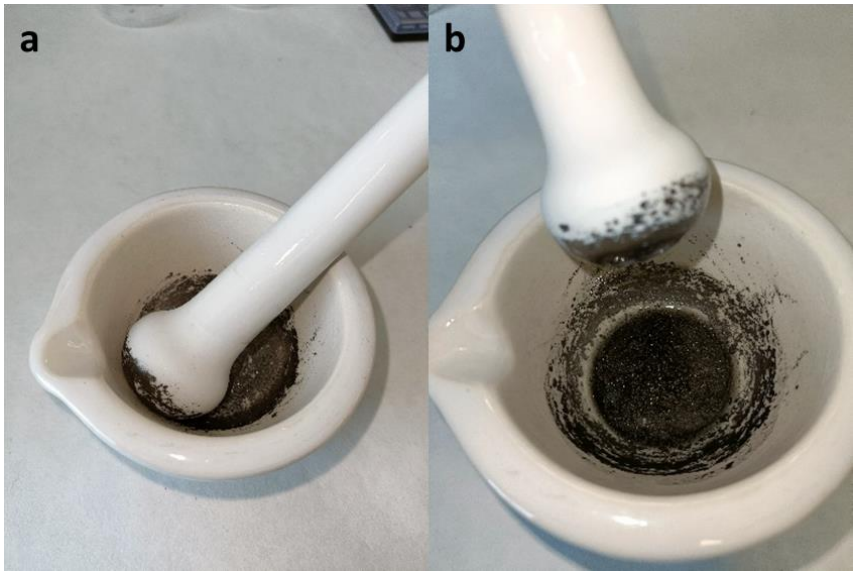

Figure 85 *a) Graphite grinding; b) grinding of graphite + Cyrene.*

The mixture was then transferred to a round bottom flask (50 mL) and Cyrene was added, reaching a final volume of 30 mL.

Pulsed sonication was applied at 40% amplitude, with a sequence of pulses of 1 s alternated to silent periods of 1 s, for 30 minutes (15 minutes of active sonication). The flask was kept in ice during the whole procedure.

After sonication, the suspension was centrifuged at 5000 rpm for 10 min at 25 °C. The supernatant was collected and stored at 4 °C.

To prepare samples for TEM, XPS and Raman analysis, graphene flakes were filtrated on PTFE filter (0.45 μm), and washed by resuspending in ethanol (100 mL) for five times.

The final material was resuspended in isopropanol.

4.5 References

(1) Dhanola, A.; Gajrani, K. K. Novel Insights into Graphene-Based Sustainable Liquid Lubricant Additives: A Comprehensive Review. *Journal of Molecular Liquids* **2023**, *386*, 122523. https://doi.org/10.1016/j.molliq.2023.122523.

(2) Sadeghinezhad, E.; Mehrali, M.; Saidur, R.; Mehrali, M.; Tahan Latibari, S.; Akhiani, A. R.; Metselaar, H. S. C. A Comprehensive Review on Graphene Nanofluids: Recent Research, Development and Applications. *Energy Conversion and Management* **2016**, *111*, 466–487. https://doi.org/10.1016/j.enconman.2016.01.004.

(3) Kousalya, A. S.; Kumar, A.; Paul, R.; Zemlyanov, D.; Fisher, T. S. Graphene: An Effective Oxidation Barrier Coating for Liquid and Two-Phase Cooling Systems. *Corrosion Science* **2013**, *69*, 5–10. https://doi.org/10.1016/j.corsci.2012.12.014.

(4) Saidina, D. S.; Zubir, S. A.; Fontana, S.; Hérold, C.; Mariatti, M. Synthesis and Characterization of Graphene-Based Inks for Spray-Coating Applications. *J. Electron. Mater.* **2019**, *48* (9), 5757–5770. https://doi.org/10.1007/s11664-019-07376-3.

(5) Lin, F.; Tong, X.; Wang, Y.; Bao, J.; Wang, Z. M. Graphene Oxide Liquid Crystals: Synthesis, Phase Transition, Rheological Property, and Applications in Optoelectronics and Display. *Nanoscale Res Lett* **2015**, *10* (1), 435. https://doi.org/10.1186/s11671-015-1139-1.

(6) Barwich, S.; Khan, U.; Coleman, J. N. A Technique To Pretreat Graphite Which Allows the Rapid Dispersion of Defect-Free Graphene in Solvents at High Concentration. *J. Phys. Chem. C* **2013**, *117* (37), 19212–19218. https://doi.org/10.1021/jp4047006.

(7) Gambhir, S.; Murray, E.; Sayyar, S.; Wallace, G. G.; Officer, D. L. Anhydrous Organic Dispersions of Highly Reduced Chemically Converted Graphene. *Carbon* **2014**, *76*, 368–377. https://doi.org/10.1016/j.carbon.2014.04.088.

(8) Malley, L. A.; Slone, T. W.; Van Pelt, C.; Elliott, G. S.; Ross, P. E.; Stadler, J. C.; Kennedy, G. L. Chronic Toxicity/Oncogenicity of Dimethylformamide in Rats and Mice Following Inhalation Exposure. *Fundamental and Applied Toxicology* **1994**, *23* (2), 268–279. https://doi.org/10.1006/faat.1994.1105.

(9) Saillenfait, A. M.; Gallissot, F.; Morel, G. Developmental Toxicity of *N*-Methyl-2-Pyrrolidone in Rats Following Inhalation Exposure. *Food and Chemical Toxicology* **2003**, *41* (4), 583–588. https://doi.org/10.1016/S0278-6915(02)00300-9.

(10) Lee, K. P.; Chromey, N. C.; Culik, R.; Barnes, J. R.; Schneider, P. W. Toxicity of *N*-Methyl-2-Pyrrolidone (NMP): Teratogenic, Subchronic, and Two-Year Inhalation Studies.

Fundamental and Applied Toxicology **1987**, *9* (2), 222–235. https://doi.org/10.1016/0272-0590(87)90045-5.

(11) Campbell, H. L.; Striebig, B. A. Evaluation of N-Methylpyrrolidone and Its Oxidative Products Toxicity Utilizing the Microtox Assay. *Environ. Sci. Technol.* **1999**, *33* (11), 1926–1930. https://doi.org/10.1021/es981061o.

(12) *Regulation - 2021/2030 - EN - EUR-Lex*. https://eur-lex.europa.eu/eli/reg/2021/2030/oj (accessed 2024-10-22).

(13) Salavagione, H. J.; Sherwood, J.; Bruyn, M. D.; Budarin, V. L.; Ellis, G. J.; Clark, J. H.; Shuttleworth, P. S. Identification of High Performance Solvents for the Sustainable Processing of Graphene. *Green Chem.* **2017**, *19* (11), 2550–2560. https://doi.org/10.1039/C7GC00112F.

(14) Tkachev, S.; Monteiro, M.; Santos, J.; Placidi, E.; Hassine, M. B.; Marques, P.; Ferreira, P.; Alpuim, P.; Capasso, A. Environmentally Friendly Graphene Inks for Touch Screen Sensors. *Advanced Functional Materials* **2021**, *31* (33), 2103287. https://doi.org/10.1002/adfm.202103287.

(15) Zhou, X.; Leng, T.; Pan, K.; Liu, Y.; Zhang, Z.; Li, J.; Novoselov, K. S.; Hu, Z. A Sustainable Approach towards Printed Graphene Ink for Wireless RFID Sensing Applications. *Carbon* **2024**, *218*, 118693. https://doi.org/10.1016/j.carbon.2023.118693.

(16) Fernandes, J.; Nemala, S. S.; De Bellis, G.; Capasso, A. Green Solvents for the Liquid Phase Exfoliation Production of Graphene: The Promising Case of Cyrene. *Front. Chem.* **2022**, *10*. https://doi.org/10.3389/fchem.2022.878799.

(17) Kukle, S.; Bake, I.; Abele, L. Graphene-Containing Para Aramid Fabric Coating via Surfactant Assisted Exfoliation of Graphite. *Materials Today: Proceedings* **2024**, *97*, 44–51. https://doi.org/10.1016/j.matpr.2023.09.131.

(18) Hassan, K.; Tung, T. T.; Stanley, N.; Yap, P. L.; Farivar, F.; Rastin, H.; Nine, M. J.; Losic, D. Graphene Ink for 3D Extrusion Micro Printing of Chemo-Resistive Sensing Devices for Volatile Organic Compound Detection. *Nanoscale* **2021**, *13* (10), 5356–5368. https://doi.org/10.1039/D1NR00150G.

(19) Stini, N. A.; Gkizis, P. L.; Kokotos, C. G. Cyrene: A Bio-Based Novel and Sustainable Solvent for Organic Synthesis. *Green Chem.* **2022**, *24* (17), 6435–6449. https://doi.org/10.1039/D2GC02332F.

(20) Tyurnina, A. V.; Tzanakis, I.; Morton, J.; Mi, J.; Porfyrakis, K.; Maciejewska, B. M.; Grobert, N.; Eskin, D. G. Ultrasonic Exfoliation of Graphene in Water: A Key Parameter Study. *Carbon* **2020**, *168*, 737–747. https://doi.org/10.1016/j.carbon.2020.06.029.

(21) Khan, U.; O'Neill, A.; Lotya, M.; De, S.; Coleman, J. N. High-Concentration Solvent Exfoliation of Graphene. *Small* **2010**, *6* (7), 864–871. https://doi.org/10.1002/smll.200902066.

(22) Baig, Z.; Mamat, O.; Mustapha, M.; Mumtaz, A.; Munir, K. S.; Sarfraz, M. Investigation of Tip Sonication Effects on Structural Quality of Graphene Nanoplatelets (GNPs) for Superior Solvent Dispersion. *Ultrasonics Sonochemistry* **2018**, *45*, 133–149. https://doi.org/10.1016/j.ultsonch.2018.03.007.

(23) Anastas, P.; Eghbali, N. Green Chemistry: Principles and Practice. *Chem. Soc. Rev.* **2009**, *39* (1), 301–312. https://doi.org/10.1039/B918763B.

(24) Hernandez, Y.; Nicolosi, V.; Lotya, M.; Blighe, F. M.; Sun, Z.; De, S.; McGovern, I. T.; Holland, B.; Byrne, M.; Gun'Ko, Y. K.; Boland, J. J.; Niraj, P.; Duesberg, G.; Krishnamurthy, S.; Goodhue, R.; Hutchison, J.; Scardaci, V.; Ferrari, A. C.; Coleman, J. N. High-Yield Production of Graphene by Liquid-Phase Exfoliation of Graphite. *Nature Nanotech* **2008**, *3* (9), 563–568. https://doi.org/10.1038/nnano.2008.215.

(25) Contamine, R. F.; Wilhelm, A. M.; Berlan, J.; Delmas, H. Power Measurement in Sonochemistry. *Ultrasonics Sonochemistry* **1995**, *2* (1), S43–S47. https://doi.org/10.1016/1350-4177(94)00010-P.

(26) Luo, J.; Fang, Z.; Smith, R. L.; Qi, X. Fundamentals of Acoustic Cavitation in Sonochemistry. In *Production of Biofuels and Chemicals with Ultrasound*; Fang, Z., Smith, Jr., Richard L., Qi, X., Eds.; Springer Netherlands: Dordrecht, 2015; pp 3–33. https://doi.org/10.1007/978-94-017-9624-8_1.

(27) Servant, G.; Laborde, J.-L.; Hita, A.; Caltagirone, J.-P.; Gérard, A. Spatio-Temporal Dynamics of Cavitation Bubble Clouds in a Low Frequency Reactor: Comparison between Theoretical and Experimental Results. *Ultrasonics Sonochemistry* **2001**, *8* (3), 163–174. https://doi.org/10.1016/S1350-4177(01)00074-8.

(28) Majumdar, S.; Kumar, P. S.; Pandit, A. B. Effect of Liquid-Phase Properties on Ultrasound Intensity and Cavitational Activity. *Ultrasonics Sonochemistry* **1998**, *5* (3), 113–118. https://doi.org/10.1016/S1350-4177(98)00019-4.

(29) Gogate, P. R.; Sutkar, V. S.; Pandit, A. B. Sonochemical Reactors: Important Design and Scale up Considerations with a Special Emphasis on Heterogeneous Systems. *Chemical Engineering Journal* **2011**, *166* (3), 1066–1082. https://doi.org/10.1016/j.cej.2010.11.069.

(30) Lupacchini, M.; Mascitti, A.; Giachi, G.; Tonucci, L.; d'Alessandro, N.; Martinez, J.; Colacino, E. Sonochemistry in Non-Conventional, Green Solvents or Solvent-Free

Reactions. *Tetrahedron* **2017**, *73* (6), 609–653. https://doi.org/10.1016/j.tet.2016.12.014.

(31) Eckart, C. Vortices and Streams Caused by Sound Waves. *Phys. Rev.* **1948**, *73* (1), 68–76. https://doi.org/10.1103/PhysRev.73.68.

(32) Nanzai, B.; Okitsu, K.; Takenaka, N.; Bandow, H.; Tajima, N.; Maeda, Y. Effect of Reaction Vessel Diameter on Sonochemical Efficiency and Cavitation Dynamics. *Ultrasonics Sonochemistry* **2009**, *16* (1), 163–168. https://doi.org/10.1016/j.ultsonch.2008.05.016.

(33) Lee, J.; Ashokkumar, M.; Kentish, S.; Grieser, F. Determination of the Size Distribution of Sonoluminescence Bubbles in a Pulsed Acoustic Field. *J. Am. Chem. Soc.* **2005**, *127* (48), 16810–16811. https://doi.org/10.1021/ja0566432.

(34) Tuziuti, T.; Yasui, K.; Lee, J.; Kozuka, T.; Towata, A.; Iida, Y. Mechanism of Enhancement of Sonochemical-Reaction Efficiency by Pulsed Ultrasound. *J. Phys. Chem. A* **2008**, *112* (22), 4875–4878. https://doi.org/10.1021/jp802640x.

(35) Wissler, M. Graphite and Carbon Powders for Electrochemical Applications. *Journal of Power Sources* **2006**, *156* (2), 142–150. https://doi.org/10.1016/j.jpowsour.2006.02.064.

(36) Huang, S.; Wang, W.; Cui, Q.; Song, W.-L.; Jiao, S. Assessment of Spherical Graphite for Lithium-Ion Batteries: Techniques, China's Status, Production Market, and Recommended Policies for Sustainable Development. *Advanced Sustainable Systems* **2022**, *6* (11), 2200243. https://doi.org/10.1002/adsu.202200243.

(37) Dresselhaus, M. S.; Jorio, A.; Hofmann, M.; Dresselhaus, G.; Saito, R. Perspectives on Carbon Nanotubes and Graphene Raman Spectroscopy. *Nano Lett.* **2010**, *10* (3), 751–758. https://doi.org/10.1021/nl904286r.

(38) Papanai, G. S.; Sharma, I.; Gupta, B. K. Probing Number of Layers and Quality Assessment of Mechanically Exfoliated Graphene via Raman Fingerprint. *Materials Today Communications* **2020**, *22*, 100795. https://doi.org/10.1016/j.mtcomm.2019.100795.

(39) Ciesielski, A.; Samorì, P. Graphene via Sonication Assisted Liquid-Phase Exfoliation. *Chem. Soc. Rev.* **2013**, *43* (1), 381–398. https://doi.org/10.1039/C3CS60217F.

(40) Roscher, S.; Hoffmann, R.; Ambacher, O. Determination of the Graphene–Graphite Ratio of Graphene Powder by Raman 2D Band Symmetry Analysis. *Anal. Methods* **2019**, *11* (9), 1224–1228. https://doi.org/10.1039/C8AY02619J.

(41) Ferrari, A. C.; Meyer, J. C.; Scardaci, V.; Casiraghi, C.; Lazzeri, M.; Mauri, F.; Piscanec, S.; Jiang, D.; Novoselov, K. S.; Roth, S.; Geim, A. K. Raman Spectrum of Graphene and

Graphene Layers. *Phys. Rev. Lett.* **2006**, *97* (18), 187401. https://doi.org/10.1103/PhysRevLett.97.187401.

(42) Hao, Y.; Wang, Y.; Wang, L.; Ni, Z.; Wang, Z.; Wang, R.; Koo, C. K.; Shen, Z.; Thong, J. T. L. Probing Layer Number and Stacking Order of Few-Layer Graphene by Raman Spectroscopy. *Small* **2010**, *6* (2), 195–200. https://doi.org/10.1002/smll.200901173.

(43) Vacacela Gomez, C.; Guevara, M.; Tene, T.; Villamagua, L.; Usca, G. T.; Maldonado, F.; Tapia, C.; Cataldo, A.; Bellucci, S.; Caputi, L. S. The Liquid Exfoliation of Graphene in Polar Solvents. *Applied Surface Science* **2021**, *546*, 149046. https://doi.org/10.1016/j.apsusc.2021.149046.

(44) Large, M. J.; Ogilvie, S. P.; Amorim Graf, A.; Lynch, P. J.; O'Mara, M. A.; Waters, T.; Jurewicz, I.; Salvage, J. P.; Dalton, A. B. Large-Scale Surfactant Exfoliation of Graphene and Conductivity-Optimized Graphite Enabling Wireless Connectivity. *Advanced Materials Technologies* **2020**, *5* (7), 2000284. https://doi.org/10.1002/admt.202000284.

(45) Tao, R.; Li, F.; Lu, X.; Liu, F.; Xu, J.; Kong, D.; Zhang, C.; Tan, X.; Ma, S.; Shi, W.; Mo, R.; Lu, Y. High-Conductivity–Dispersibility Graphene Made by Catalytic Exfoliation of Graphite for Lithium-Ion Battery. *Advanced Functional Materials* **2021**, *31* (6), 2007630. https://doi.org/10.1002/adfm.202007630.

(46) Islam, A.; Mukherjee, B.; Pandey, K. K.; Keshri, A. K. Ultra-Fast, Chemical-Free, Mass Production of High Quality Exfoliated Graphene. *ACS Nano* **2021**, *15* (1), 1775–1784. https://doi.org/10.1021/acsnano.0c09451.